Ion Beam Modification of Thin Film Barrier Layer and Deposition of Transparent Conductive Oxides on Polymer Substrate for Flexible Display

by

Shih-Hsiu Hsiao

Supervised by

Professor Dr. Ari Ide-Ektessabi

Department of Mechanical Engineering and Science

Graduate School of Engineering

Kyoto University, Japan

February 2008

Acknowledgements

First, I would like to express my gratitude and thank to Professor Ari Ide-Ektessabi for being my dissertation supervisor. It is my great pleasure to work with him. He provided me the ability of engineering thinking in this study. This will be a treasure for my entire professional career. He also guided me to approach the important problem in the field. I thank him for all the effort to enhance my sense in theoretical fields.

Also, I would like to thank Professor Kimura of Micro Engineering department and Professor Kawai of Materials Science and Engineering department. They gave me great support and guidance in this research. Professor Kimura and Professor Kawai provided me valuable advice on the research direction of RBS measurement and XPS analysis.

I would like to thank my senior lab-mate Mr. Tanaka. He gave me a great support and guidance in a lot of experiments, and the warm encouragement when we faced problems in this study. Specially, in the deposition process of electron beam evaporation and sputtering method, he guided me a lot and provides many precise experiences in the process.

I would like to thank my group mates, Mr. Yamaguchi for assistance and support in the implementation of linear ion source and electron beam evaporation chamber, and Mr. Kobayakawa for making the transparent conductive oxide targets and sputtering techniques. I also acknowledge Mr. Sawada and Mr. Mori in the factory for the sample holder and some mechanical device production.

For the machine used for the thin films properties evaluation, I wish to express gratitude and thanks to Mr. Kinoshita for his kind advice on AFM and SEM analysis. I acknowledge Mr. Nakamura and Mr. Haragughi at Kyoto Prefectural Technology Center for Small and Medium Enterprises for the guidance in using the Shimadzu scratch tester for adhesion and NIR spectrum measurement. Thanks a lot for the guidance from Ishikawa lab for the XPS utilization in Kyoto University Katsura campus. And Prof Tsuchida for the RBS analysis performed at Quantum Science Engineering Center, and XRD measurement from Fujita lab.

Abstract

The flat panel display industry is a fast growing electronics industry today, and the flexible display is expected to be the next-generation flat panel display. These flexible displays are made of thin substrates which can be bent without losing their functionality, compared to the rigid glass commonly used in the display industry. The thin substrates are constructed with multilayered, thin film structures. In these layers, the properties of transparent conductive oxides layers and the barrier layers affect the performance of displays significantly.

The purposes of this research are to: (1) Develop a new ion beam irradiation system for surface modification of PET substrate; (2) Investigate new approaches in preparing the materials for transparent conductive oxides (TCOs) layers that can be deposited at room temperature and under low temperature thermal process with the high optical transmittance and surface conductivity; (3) Deposit the optimal barrier thin film on PET substrate to decrease the water vapor permeation rate.

This study has a total of seven chapters. A background and some introduction about the study can be found in Chapter 1. Chapter 2 introduces a new system including the linear ion source and the electron-beam evaporation developed in a vacuum system. The linear ion source was used to assist the modification of the PET surface. The electron cyclotron resonance ion source was used as a comparison to the linear ion source. The linear ion source can provide a large area, uniform ion beam irradiation, and is suitable for the production scale.

Chapter 3 introduces the polymer-based substrate of polyethylene terephthalate (PET) used in this study. PET is light weight and has a good transparency. It is widely used as a good candidate for flexible display. One should note that the PET substrate has the additional restrictions on the sensitivity to heat treatment and suffers from dimensional and structural instability when exposed to heat. Two kinds of typical physical vapor deposition methods, namely electron-beam evaporation and sputtering deposition, were used to deposit TCOs onto the PET substrate. This study showed the indium tin oxide (ITO) thin film could not be successfully deposited at room temperature by electron beam evaporation. Depending on the substrate temperature, the ITO thin films deposited by electron beam evaporation had much better optical and electrical properties at higher temperature. When the substrate temperature was 280 ℃, the light transmittance and surface resistivity of ITO thin films reached over 85 % transmittance and 56 Ω/cm^2, close to the values of the expected specification. However, this high substrate temperature process is not feasible for the PET substrate. Thus, we used sputtering deposition for the TCOs thin films.

Chapter 4 demonstrated that the argon and oxygen ion irradiation alters the chemical and physical

properties of the PET surface, and thus improves the adhesion of the thin films deposited onto the PET substrate. X-ray photoelectron spectroscopy (XPS), atomic force microscopy (AFM), and scanning electron microscopy (SEM) were used to analyze the modifications of the surface.

As a result of experiments, when the ion energy was less than 500 eV, the ion beam irradiation mainly had the cleaning effect. With the increase in irradiation dose and ion energy, its primary effect became sputtering. In the XPS analysis of the different irradiation conditions on the surface, the carbon to oxygen concentration was increased either by argon ion or oxygen ion irradiation, and it increased more when the irradiated ion energy was higher. This increase may be due to a part of the sputtered oxygen diffused in vacuum and the carbon remained on the surface when the bonding was broken by irradiated ions. When the ion irradiation dose increased, the chemical structure modification was similar under the same irradiated ion energy. However, it is a little different for surface morphology and roughness detected by AFM and SEM. The surface became smooth and flat at the initial ion irradiation, and it was considered as the cleaning effect. When we extended the irradiation exposure of oxygen ions, the surface became rougher and RMS roughness became larger. The oxygen ion beam irradiation was shown to be more effective in modifying the surface morphology. Finally, the scratch testing was applied for the adhesion testing between PET surface and TCOs layer.

In Chapter 5, we illustrate that eight types of TCOs, which include ITO, ZnO, In_2O_3 (IZO), MgO (MZO), Al_2O_3 (AZO), Ga_2O_3 (GZO) doped ZnO, Al_2O_3 doped MZO (AMZO), and Ga_2O_3 doped MZO (GMZO), were deposited by RF magnetron sputtering method at room temperature, 100 ℃ substrate temperature during the deposition and 150 ℃ post annealing process. Rutherford backscattering spectroscopy (RBS), X-ray diffraction (XRD), XPS and AFM were used to detect the properties of thin films. ITO deposited at room temperature had light transmittance over 90 % and surface resistivity near 20 Ω/cm^2. IZO had the premium optical and electrical properties among the ZnO with a few metal oxide doping. It also had over 90 % light transmission and the surface resistivity below 60 Ω/cm^2. Other ZnO with dopants and ZnO deposited at room temperature had good optical properties but poor conductivity, especially ZnO and MZO. The doped MgO was found to be effective in improving the band gap, and thus it can improve the light transmission in short wavelength.

Organic luminescent emitting materials are easily oxidized and degrade fast due to water and oxygen permeation. Chapter 6 focuses on the SiO_x thin film as a barrier layer which was deposited by the electron beam evaporation method. Calcium oxide was used as a detector for water vapor transmission rate measurement. The PET film with a 100 nm SiO_x barrier layer was operative in moisture transmission rate improvement, and the rate decreased to approximately 10 % of it without coating. Moreover, ion beam assisted deposition process was used to increase the density of barrier thin films, and it enhanced the waterproof barrier function of the deposited SiO_x thin films.

Table of Contents

Chapter 1

Introduction

1.1 Overview

The evolution of display technology away from the bulky CRT display to the thin LCD monitor used for desktop computer has had a significant influence on space saving and power consumption. In the progress of the recent 30 years, Flat-Panel Displays (FPDs) have become one of the fastest growing electronic products in industry, and is expected to be a major marketing force in the coming future. Flat panel displays encompass the technologies that enable video displays that are lighter and much thinner than traditional television or video displays used with cathode ray tubes. They are usually less than 100 mm in thickness. Moreover, the future FPDs products will be designed and made more space conserving, power consumer saving, and more lightweight for its mobility. They have become a significant and indispensable commodity in our daily lives.

For the basic structure of FPDs, it can be described as thin, multilayered sandwiches that operate light. Figure 1-1 shows one of the examples for the basic structure of emissive display cell. The three different yet basic modes of FPDs operation can be considered as transmissive, reflective and emissive. Transmissive and reflective modes can be combined in transflective modes shown in Figure 1-2. There are many ways to approach flat panel displays like the liquid crystal display (LCD) and plasma display panel (PDP) as those are well known for their use in televisions. They can be roughly separated into emissive and non-emissive types as shown in Figure 1-3. The former generates dots of the light, the latter reflects or modulates light.

One of the flat panel displays, the flexible display, is expected to be a part of the next generation of FPDs. The flexible display technologies are developed to make display more lightweight and more flexible, much like how a piece of paper can be folded without losing its functionality. It can be widely utilized in many applications, specifically modern portable devices such as laptops, cellular phones, digital cameras, electronic paper display, electronic books, depending on its portability requirements. Figure 1-4 shows an example of image from the “take anywhere, read anywhere” plastic logic flexible displays using E ink imaging film [1]. The term “flexible display” sometimes means different things to different people. The broad definition of a flexible flat panel display is given by Slikkerveer (2003)

A flat panel display constructed of thin (flexible) substrates that can be bent, flexed, conformed, or rolled to a radius of curvature of a few centimeters without losing functionality.

Defining a flexible display is similar to defining modern art, which shows why the diversity of the application for flexible display technology is so great [2]. There are many companies and new entrants who are currently active in the research of flexible displays presently based primarily on liquid crystal displays (LCD), organic light-emitting diodes (OLED) [3]. The ability to flex a display has attracted the attention of researchers for many years, and they have paid a lot of effort and spent a lot of resources dedicated to the development of flexible display configurations [4]. The convergence of these technologies includes the robust flexible substrates, barrier layer, optical layers, thin film transistors, conducting layer, inorganic and organic electronics and packaging technologies etc. This study placed a larger focus on the transparent conducting layer and barrier layers used on plastic substrates.

A flexible or an engineered substrate is a key platform in the establishment of a flexible displays industry. This flexible substrate must be used to replace conventional glass substrates used in displays. Glass is regarded as the standard substrate material for display and is widely used in the flat panel displays industry due to its rigid, wearable and optical characteristic. Moreover, glass has the mechanical properties of smoothness and dimensional stability. For flexible display, it offers substantial rewards in terms of being able to develop displays that are thinner, lighter, robust, and can be rolled away. There are two choices for flexible substrates, polymeric and thin glass. In this study, the polymeric substrate is used as the flexible substrates, and polyethylene terephthalate (PET) is a good candidate for the flexible substrate.

Consequently, the robust flexible substrates with transparent conducting electrodes play an important role in flexible displays technology. Transparent conducting oxides (TCOs) layers are necessary for displays regardless of whether it is used in the liquid crystal display or in the organic light-emitting diodes display [5]. The various materials were experimented for transparent conductive electrodes and indium tin oxide (ITO) was the typical conducting layer widely used for TCOs [6]. ITO is entirely used in the majority of display applications due to its superior combination of environmental stability, relatively low electrical resistivity, and high light transmittance. However, the principal ingredient in ITO, indium, is very hard to obtain because it is an expensive and scarce metal. When we reviewed the selection of TCO materials at present, we found that TCOs require the properties of high electronic conductivity and high optical transparency in the visible region. There is, however, a belief that high optical transparency is incompatible with high electronic conduction. The alternative TCO materials based on mixed binary and ternary oxides of the Cd^{+2}, Zn^{+2}, In^{+3}, and Sn^{+4} were under development, and numerous studies on binary, ternary compound oxides composed of combination of In, Zn, Sn and Ga have been reported [7-10].

Indium zinc oxide, and zinc oxide were known to be transparent in the visible region of about 400 nm to 700 nm and exhibit high conductivity [11]. Moreover, the use of the suitable impurity doped ZnO has garnered much attention as an alternative to the use of ITO.

For flexible displays, polymer based substrates impose additional restrictions on their sensitivity to heat treatment and the displays suffer from dimensional and structural instability when they are exposed to heat. Even at modest substrate temperatures of 100 ℃ to 150 ℃, the dimensional stability of many polymers are poor and may lead to increased film stress and failure by cracking. The primary consideration in the selection of a transparent conductor and the processing methods for use is the ability to deposit material with adequate optical and electrical properties, according the polymers substrates with an additional set of restrictions. As such, the deposition of transparent conductive oxides onto polymeric substrates requires a process that uses minimal exposure to energetic radiation and negligible substrate heating. In this study, the electron beam evaporation and sputtering deposition were both used for TCOs thin films deposition. Additionally, ion beam irradiation was used to improve the surface properties and enhance the thin film properties through ion beam assisted deposition.

Another particular challenge for flexible display is barrier thin films. OLED material is very environmentally sensitive and plastic is very porous. When polymeric substrates are employed in flexible display applications, a barrier layer is required to protect the enclosed functional materials and layers from oxygen and water permeation. OLED devices deposited on PET substrates survive only a matter of hours when exposed to atmospheric conditions due to the high diffusion of oxygen and water vapor through the native polymeric substrate. Without good barriers, the flexible OLED industry cannot be the industry it could potentially become. Transparent silicon oxide thin films are extensively used as barrier layers, and can also be utilized on polymeric substrates. In this study, SiO_x thin film was used as the barrier layer to behave as protection of the enclosed functional materials like the extreme sensitivity of OLED materials from water vapor permeation. The chemical reaction and absorption of the calcium oxide to water was used to evaluate water vapor permeation properties.

A few analysis and measurement methods including X-ray photoelectron spectroscopy (XPS), atomic force microscopy (AFM), scanning electron microscopy (SEM), Rutherford backscattering spectroscopy (RBS) and X-ray diffraction (XRD) were used to investigate the various properties of the surface and properties of thin films.

1.2 Scope of the Present Work

In this study, the experiments were focused on two layers including the transparent conducting

layer and the barrier layer on polymeric substrate used for flexible display. Ion beam irradiation was used for the surface modification and ion beam assisted deposition to improve the density of the barrier layers. In Chapter 2, a new system including linear ion source and electron-beam evaporation was developed in a vacuum system for thin film deposition and surface modification. The electron cyclotron resonance (ECR) ion source was used as a comparison to the linear ion source. The linear ion source can provide a large area, uniform ion beam irradiation, and is suitable for the production scale.

Chapter 3 introduces the polymeric substrate used in this study. It is polyethylene terephthalate (PET), and is widely used as the flexible substrate. However, PET has some additional restrictions on the sensitivity to heat treatment and suffers from dimensional and structural instability when it's exposed to heat. Two kinds of typical physical vapor deposition methods including electron-beam evaporation and sputtering deposition were used for transparent conducting oxides (TCO) deposited. At last, according to the different Young's module between TCOs materials and substrate, the mechanical limitation of TCOs layers used on flexible substrates was experimented on and evaluated.

Chapter 4 concentrates on the surface modification of PET substrates treated by argon ions and oxygen ions irradiation. X-ray photoelectron spectroscopy (XPS), atomic force microscopy (AFM), and scanning electron microscopy (SEM) were used to analyze the modifications of the surface. Finally, the scratch testing was applied for the adhesion testing between PET surface and TCOs layer.

In Chapter 5, the TCOs materials used in this study, including indium tin oxide and zinc oxide with the dopants, were deposited by RF magnetron sputtering method. Rutherford backscattering spectroscopy (RBS), X-ray diffraction (XRD), XPS and AFM were used to detect the properties of their thin films. They were discussed and a correlation was found with the optical and electronic properties as the transparent conducting layers used for flexible display.

Organic luminescent emitting materials are easily oxidized and degrade fast when water and oxygen permeation, Chapter 6 focused on the SiO_x as barrier layer which was deposited by the electron beam evaporation method. Calcium oxide was used as detector for water vapor transmission rate. The ion beam assisted deposition was used to increase the density of the barrier layers and it is expected to improve the water vapor permeation property.

Chapter 7 gives some conclusions from studies and future outlook. The appendix includes a brief introduction and the condition of five equipments and methods used in this study.

Reference

1. http://www.plasticlogic.com/
2. P. J. Slikkerveer, Information Display 3, 20-24 (2003).
3. A. Sugimoto, H. Ochi, S. Fujimura, A. Yoshida, T. Miyadera, M. Tsuchida, IEEE J. Selected Topics in Quantum Electronics, 10, 1 (2004).
4. Howard, W. E, Scientific American 290, 76-81 (2004).
5. H. Hosono, Thin Solid Films, 515, 15, 6000-6014 (2007).
6. O. A. Ghandour, D. Constantinide, R. Sheets, Society of Photo Optical Instrumentation Engineers (2002).
7. I. Sieber, N. Wanderka, I. Urban, I. Dorfel, E. Schierbhorn, F. Fenske, W. Fuhs, Thin Solid Films 330, 108 (1998).
8. Z. C. Jin, I. Hamberg, C. G. Granqvist, J. Appl. `Phys. 64(10), 5117 (1988).
9. J. Cho, J. Nah, M. S. Oh, J. H. Song, K. H. Yoon, H. J. Jung, W. K. Choi, Jpn. J. Appl. Phys. 40, L1040 (2001).
10. M. Miyazaki, K. Sato, A. Mitsui, H. Nishimura, J. Non-Cryst. Solids 218, 323 (1997).
11. A. Kaijo, K. Inoue, S. Matsuzaki, Y. Shigesato, In Proceedings of the Fourth Pacific Rim International Conference on Advanced Material Processing. (2001).

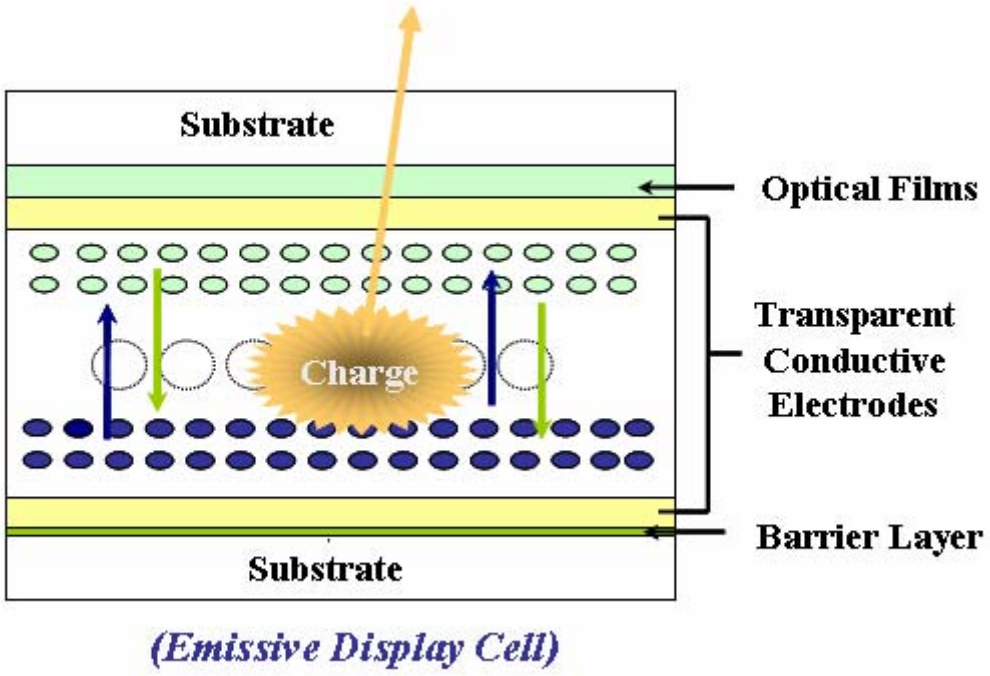

Figure 1-1. Basic structure of emissive display cell

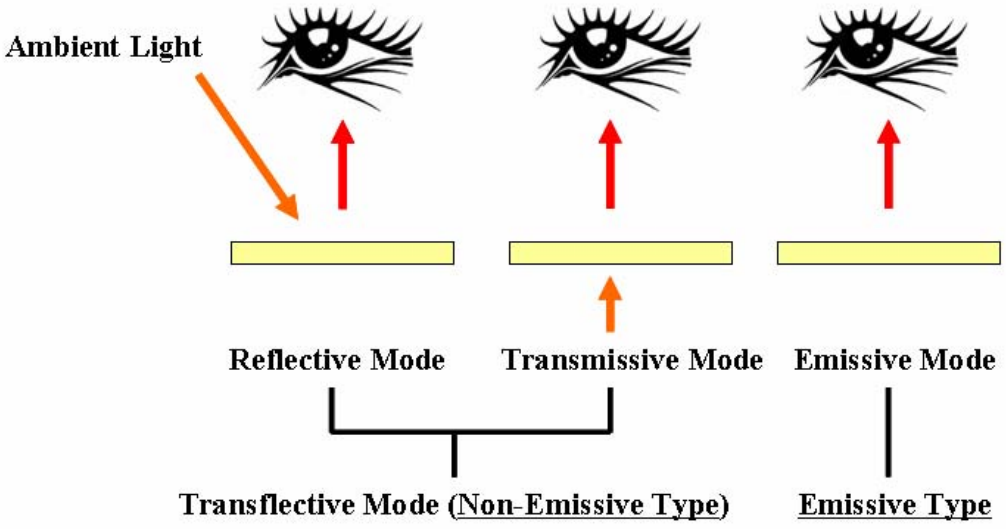

Figure 1-2. Reflective, transmissive and emissive modes of displays

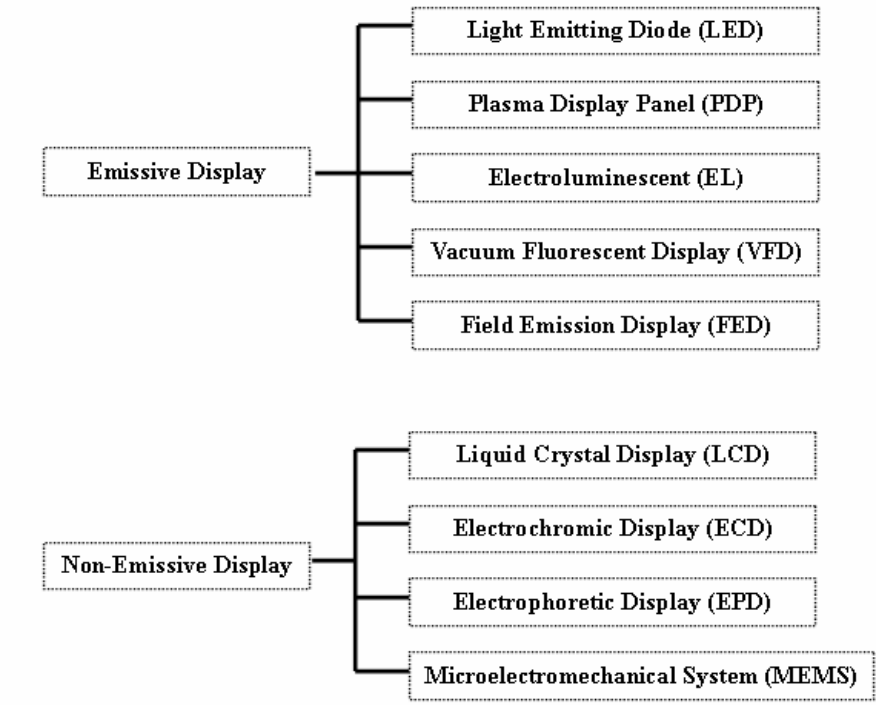

Figure 1-3. Emissive and non-emissive types of display category

Figure 1-4. Image of "take anywhere, read anywhere" from Plastic Logic flexible display

Chapter 2

System Development with Linear Ion Source

2.1 Introduction

Ion beam irradiation offers the various purposes for surface modification such as surface cleaning by sputtering, implantation of trace elements, thin films deposition, and the chemical or structural morphological changes on surface [1, 2]. Consequently, there is a strong demand for the use of a high performance ion beam that can provide stable, large area irradiation capability, that is specially applied in the industry [3]. The ion source was used for surface modification of polymer substrates and in some cases, ion beam assisted deposition [4-7]. The electron cyclotron resonance ion source was used and used properly,, but its radiation area is small. Here, we developed a new ion beam irradiation system. This system, included with the linear ion source and electron beam evaporation, can be utilized for the surface modification and thin film deposition.

2.2 ECR Ion Source

The electron cyclotron resonance (ECR) ion source was used as a comparison in this experiment. The use of ECR ion sources for the production of intense beams of highly charged ions has significantly grown in recent years. ECR ion sources are used as injectors into linear accelerators, Van-de-Graaff generators or cyclotrons, in nuclear and elementary particle physics. In atomic and surface physics, ECR ion sources deliver intense beams of highly charged ions either for collision experiments or the investigation of surfaces. One main advantage of this kind of ion source is that ions of all elements can be produced. Furthermore, there are practically no wearing parts, like filaments, in the ion source. Therefore, stable ion beams can be utilized for a long period of time, from days to weeks.

The ECR ion source used as the comparison to the linear ion source in this experiment is located at the Kyoto Thin Film Materials Institute. The ion beam from ECR ion source has the 45 ℃ incident irradiated angle to sample holder, but this sample holder can be rotated at the constant speed to receive the uniform irradiation. Figure 2-1 shows the schematic of the ECR chamber and sample holder. When the oxygen or argon gas was introduced into the ECR ion source, it generated an ion beam to irradiate the target samples. The ECR ion source has the advantage of being compact

and effective. However, in comparison, the linear ion source can provide a much larger irradiation area for production scale, and the ECR ion source used was focused on small area high ion irradiation. The ECR type ion source employed in this study is from ULVAC Inc. It has the capability of supplying a stable high-density beam. The acceleration voltage in the ECR type ion source was used as an indicator of the energy of incident ions.

When we compared the surface modification effect between the ECR ion source and the linear ion source, the ECR ion source was operated with oxygen and 8 ccm of argon gas, and the ion accelerated voltages of 500 V, 1000 V and 1500 V charge were utilized. The dose value of ECR was measured by using the detector with dimensions of 20 mm x 20 mm square stainless thin plate as the current meter attracted on Teflon insulator substrate. Figure 2-2 shows the measured current to the ion accelerated voltage of oxygen ions and argon ions. It indicates that when the accelerated voltage reached or went past 1000 kV, the necessary measured current to achieve stability is approximately 10 uA/ cm^2. On the other hand, the dose value can be calculated to be 6.24 x 10^{13} ions/ cm^2 sec for oxygen and argon ions, at an accelerated voltage of 1000 V.

2.3 Linear Ion Source

The linear ion source consisted of a closed drift ion beam source that was applied as the reliable, robust ion source for the industrial scale vacuum system [8]. The linear ion sources deliver low-maintenance, high-yield functionality with high performance quality. Moreover, it has the features of no filaments or hollow cathodes by eliminating the hot filament cathodes and the emitters used in other designs. The level of maintenance is minimized, as its gridless ion source technology avoids the expenses, maintenance, and alignment problems that come with grid sources [9]. Also, it is compatible with a wide variety of gases and allows material to be processed in a reactive gas environment. It is easily flange mountable as it mounts directly to the chamber wall through existing ports in this system.

In this experiment, the linear ion source, mounted to the upper flange of chamber, works to irradiate ions which are used for surface modification of samples that are put on the sample holder at 250 mm below. Additionally, the height of the sample holder can be adjusted to any distance between 300 mm to 100 mm from the linear ion source. This cylinder-type chamber has dimensions of 250 mm in radius and 500 mm in height. In this vacuum system, we designed a linear ion beam and an electron beam evaporation upside and downside. Consequently, the sample holder cannot be located too far from the linear ion source, when the electron beam evaporation device is set on the downside of the chamber. We made three kinds of sample holders for the different purposes, and their rotation or movement can be easily controlled from outside of the chamber. The electron beam

evaporation was used to deposit thin film on the samples after ion processing. The distance between the electron-beam evaporated target and sample was approximate 150 mm.

2.3.1 Operating Principle of Linear Ion Source

The linear ion source used in this experiment was purchased from Advanced Energy Industries, Inc. It is a LIS 38 cm type with the assembly dimensions of 7.7 cm x 10.2 cm x 38 cm and 16.8 Kg in weight. It is connected to the high voltage power supply, cooling water in/out system, and with two adjustments of gas adjustment and input power adjustment shown in Figure 2-3(a). The basic operation was the linear ion source being mounted in the upper flange of chamber, faced downward in a vacuum chamber, and pumped down to base pressure. The permanent magnet creates a magnetic field between the magnetic poles. The cathode material is the steel that is magnetized by the permanent magnet. This creates a magnetic field around the cathode. Gas is evenly distributed throughout the gas box and introduced from a slit beneath the cathode. The cathode parts are grounded. When a positive voltage is applied to the anode, it creates a discharge between the anode and the cathode in the magnetic field [10-12]. Ions in the discharge plasma are repelled by the positive anode and accelerate away from the source. Across the extraction slit, the electric field is perpendicular to the magnetic field. Hence, the ions are accelerated and extracted in the direction of the electric field whereas almost all electrons are confined inside the ion source. A diagram of the linear ion source is shown in Figure 2-3(b), and a photograph is shown in Figure 2-4.

This linear ion source has two ion emission slits which are 286 mm in length and 76.2 mm in the distance between both parallel straight slits. When oxygen and argon gas were injected into the linear ion source and discharge high voltage, electrons are released from the cathode and subject to the effects of the cross electromagnetic field. The linear ion source can work in two distinct modes: high-voltage, discharge voltage from 600 V to 3000 V and low-voltage from 250 V to 500 V, respectively, and collimated and diffused beam modes [13]. High voltage mode could be achieved at a low gas flow and in this mode, discharge voltage increases with increasing discharge current. In high voltage mode, it is considered that there is a circulating Hall current, where the electron space charge isn’t compensated by ions. This current increase with increasing discharge voltage causes increased ionization and an increase in the discharge current. In a low-voltage mode, the electron space charge is compensated by ions, so the discharge current is not limited by space charge. The operations of these two modes are related to the working discharge provided and gas feed. We used the collimated mode in this study, the discharge voltage operated from 500 V to 1500 V, and the gas feed had a flow rate below 20 ccm.

2.3.2 Sample Holder development

There are three kinds of sample holders designed for this study. The first one is the flat-plane type with a simple structure, and it can be rotated at different kinds of angles as shown in Figure 2-5(a) with dimensions of 200 mm x 300 mm. The samples can be put on both sides of the flat-plate for ion irradiation and thin films deposition. The flat-plate can be set up at any angle as the ion beam incident angle. The different ion beam incident angle results in the various sputtering yield for the surface modification, and it is discussed in Chapter 4. This flat-plate sample holder was used for the basic analysis of surface ion beam modification and the evaluation of the deposition for thin films properties. The second one is shown in Figure 2-5(b) as the rolling type, the samples were put on these two cylinder-type holders. They can be rolled at constant speed from the motor outsides of the chamber. It is the model designed for the roll to roll fabrication holder. The ion irradiation and the deposition rate were uniform during the processing and the size can be extended when it was applied in a big chamber for the production scale.

At this rolling type sample holder, the two cylinder holders with equivalent diameters of 38 mm, were designed at the 35 mm between the two center axes and located at right-center and right-below of two slits of the linear ion source where the maximum ion irradiation will be described later. The third one is shown in Figure 2-6, and it is used to measure the ion distribution and ion irradiation dose of the linear ion source. The detector is the 20 mm x 20 mm square stainless thin plane as the current meter is attracted on Teflon insulator substrate. When the ion beam bombarded the stainless thin plane, the occurred current was measured. The current in uA was calculated from the detector connected to 1000 ohm resistance and the voltage in mV measured during the ion beam irradiation. As Figure 2-6 shows, the six detectors holders can be moved in y-axis direction by a ball-screw. Moreover, it can be adjusted in height by the z-axis to measure different positions from the ion-emitted part. Using this sample holder, we can measure three dimensions of ion beam current distribution of the linear ion source.

2.3.3 Ion Beam Distribution and Energy

The ion beam distribution and the energy of the linear ion source was measured in this chapter. The ion irradiated Dose (ions/m^2) D can be derived from the equation (2-1):

$$D = \frac{Jt}{eN} \tag{2-1}$$

Where J is the current density (A/m^2), e is 1.60219 x 10^{-19} (C) and t is the irradiated time (sec)

and *N* is the valence of ions. This linear ion source has two ion emission slits and they are 286 mm in length. The distance between both parallel straight slits is 76.2 mm. The sample holder previously described was used to measure the currency of each location to detect the ion beam distribution in spacing, below the linear ion source. Oxygen and argon were introduced through a gas feed manifold as the ion gas, and the flow rate that was set up from 5 ccm to 20 ccm, behaved as the collimated mode. Also, the discharge voltage was operated at 750 V, 1000 V, 1250 V and 1500 V. When glowing discharge voltage was provided between the anode and the cathode, the plasma was captured by the magnetic field and turned in a spiral motion from both straight slits.

Under the collimated mode, the ion beam was focused, and current was measured by the detector in uA. The coordinates were defined as the x-axis was parallel and the y-axis was perpendicular to the slit direction of the linear ion source. On the sample holder, there were six detectors in the x-axis direction. They were moved and directed in the y- axis direction in an 5 mm interval. The ion beam's current distribution in the x-y plane was measured. The initiated x-y plane measured points were located at 250 mm below the linear ion source. After that, we repeated the same measurement process to adjust the detectors in z-axis height. Figure 2-7 shows one of the ion beam distributions on the x-y plane in the conditions of 20 ccm of argon and discharge voltages at 500 V, 1000 V and 1500 V. Figure 2-8 shows the oxygen ion current density measured in the same condition. In Figure 2-7 and Figure 2-8, the current density distribution of the ion beam has two peaks, and all the curve lines measured had two peaks with maximum current measured in the y-axis direction perpendicular to the linear ion source slit. These two peaks were located at right-center and right-below with respect to the two emitting slits. The measured current densities were uniform in the direction parallel to the extraction slit.

Figure 2-9 shows the ion current distribution measured at the x-y plane, and its contour mapping is shown in Figure 2-10. It is very clear that the pink part of contour mapping received the maximum ion beam irradiation. It indicated the target substrates posited on the pink part. The peaks location of the y-axis along to the x-axis can obtain the maximum and regular ion beam irradiation. We adjusted the height in the z-axis, and measured the ion current distribution at distances of 50 mm, 100 mm, and 150 mm from the emitting slits. Figure 2-11 shows the current distribution when argon discharged at 1000 V and 20 ccm. It also shows two peaks at the slit position, and it was considerable that the peak current was increasing when it was closer to the emitting slits. Figure 2-12 shows the argon and oxygen maximum current densities when it charged in the various voltage from 500 V to 1500 V and at distances of 50 mm, 100 mm and 150 mm. The maximum current increased depending on the increasing discharge and the closer proximity in position to the emitting slits. From the ion beam current distribution measured in the different kinds of conditions, we can calculate the irradiated ion dose. The sample was usually put at a distance of 250 mm and at the maximum ion irradiation location for surface medication. The dose rate was from 8×10^{13} ions/ cm^2

sec to 4 x 10^{14} ions/ cm^2 sec operated in the various discharge voltages. Therefore, the individual irradiated dose can be estimated by irradiated time.

The ion energy profile of the linear ion source was measured using the ion beam energy analyzer designed by a senior associate, Mr. Yasui in 2003 [14]. The schematic was shown in Figure 2-13. This analyzer is made by stainless composed of two parts and the voltage supply circuit. One of the parts is the collector where the voltage Φ_0 can be applied. Ion beam comes into the collector part through a hole on the upside of the collector. The current occurred in the collector when the ion beam irradiated was measured as $I_{collector.}$. When the retarding potential voltage was applied, the ions couldn't reach to the collector when the energy was smaller than the potential energy $e\Phi_0$. When the energy E is equal or bigger than $e\Phi_0$, the differential of $I_{collector}$ with respect to E is as the equation (2-2) indicates:

$$-dI_{collector} = e\rho(E)dE \tag{2-2}$$

where ρ (E) [ions/eV] is the number of ions whose energy is E. From equation (2-2), ion energy distribution can be calculated by measuring the ion beam current and the retarding voltage.

During the ion beam irradiation, there were various electrons generated in the different conditions. In one of the cases, when the collector potential was more than 50 eV, the secondary electron ejection from the collector was inhibited, holding the fact that the energy of the secondary electrons was generally less than 50 eV . In this experiment, the current of collector is given by

$$I_{collector} = I_{ion} + I_{electron} \tag{2-3}$$

where I_{ion} and $I_{electron}$ make up the current caused by positive ions and electrons in the processes. For the electrons in the process, some ions collided with residual atoms or molecules, ionizing them to ions and electrons. The collisions that occurred on this stainless steel device, may create electrons as the secondary electrons.

At the proper retarding potential voltage provided, the ions were kept from colliding with the collector. Above all, the ion's energy of the linear ion source can be derived from measuring the beam current at the collector, when the potential is more than 50eV following the equation (2-3). It is then noted that ion energy distribution couldn't be obtained if the ions energy is less than 50 eV. The energy distribution of the linear ion source was measured when argon and oxygen gas are introduced in. The ion operated voltages were at 500 V, 1000 V and 1500 V. The analyzer was located at a distance of 280 mm below the slit of the linear ion source. The collector potential was adjusted from 0 V to 1500 V.

Figure 2-14 shows the relationship between the ion current and retarding potential at the argon

gas discharge voltages of 500 V, 1000 V, and 1500 V. The ion beam current reached the saturation point for argon ion beams at the discharge voltages of 500 and 1000 V. However, at the 1500 V discharge voltage, the ion beam current decreased gradually. The ion beam distribution ρ(E) can be calculated and normalized by the measured beam current, as the current was differentiated with respect to E in equation (2-2). Figure 2-15 shows the plot of the ion beam distribution density ρ(E) ion beam energy. For the ion energy, when the linear ion source was operated at a discharge voltage of 500 V, it was at a high in density at 200 eV. 1000 V Discharge voltage was at 350 eV, and the 1500 V discharge was roughly located at 500 eV. These are the most probable values of the ion energy that indicated the ion energy with the largest value of the ion distribution function ρ(E). The most probable value of the ion energy increased almost linearly with increasing discharge voltage, and it was approximately 35 % of the discharge voltage. The ion beam distributions were all measured under the collimated mode, and this mode was utilized for ion beam surface modification later.

2.4 Electron-Beam Evaporation Developed for the Simultaneous Process

Electron beam evaporation is the preferred vacuum evaporation technique for depositing films. It is a popular method, unique in the sense that it can be used to evaporate high-melting-point materials at appreciable rates. The oxide materials with high-melting-points used in this study can be evaporated by this method. In this system, the linear ion source can provide the large area surface modification. In addition, an electron-beam evaporator was installed on the downside of the chamber to deposit the thin film when the sample rotated 180 degrees to face downward, as shown in Figure 2-16. The ion beam surface modification and thin films deposition can be combined in the simultaneous process.

For electron beam evaporation, electrons are thermionically emitted from heated filaments that are shielded from direct line of sight of both the evaporant and the substrate. The cathode potential is negatively biased with respect to a nearby grounded anode from 4 to 20 kilovolts, and this serves to accelerate the electrons. In addition, a transverse magnetic field is applied, which serves to deflect the electron beam in a 270 ℃ circular arc and focus it on the hearth and evaporant charge at ground potential. The electron beam evaporation used in this study was 4 kW, single E-type electron-beam gun from ANELVA Corp., and the connected power supply and control unit was also from ANELVA corp. The distance between the sample holders to the electron beam evaporation crucible was 150 mm.

This vacuum chamber, including the linear ion source and electron beam evaporation, can provide the simultaneous processing of ion beam and deposition. However, the linear ion source

was aligned with the electron beam evaporation device, and the ion beam irradiation was at the opposite side of the thin films deposited side. Ion beam assisted deposition cannot be applied in this system. However, the linear ion source can provide the premium pre- or post- treatment of surface covering films, adhesion improvement, and film contamination reduction by removing hydrocarbon and other residuals.

References

1. A. M. Ektessabi, K. Yamaguchi, Thin Solid Films 377-378, 793-797 (2000).
2. A. M. Ektessabi, S. Hakamada, Thin Solid Films 377-378, 621-625 (2000).
3. A. Anders, Surf. Coat. Technol. 200, 1893-1906 (2005).
4. S. Mohan, M. Ghanashyam, Vacuum 46, 7, 645-659 (1995).
5. R. Flitsch, D. Y. Shih, J. Adhesion Sci. Technol. 10 (12), 1241-1253 (1996).
6. J. Ge, J. K. Kivilahti, J. Appl. Phys. 92 (6), 3007-3015 (2002).
7. S. Kim, K. J. Lee, Y. Seo, Lamgmuir 20, 157-163 (2004).
8. A. Ide-Ektessabi, N. Yasui, Review of Scientific Instruments, 73, 2 (2002).
9. http://www.advanced-energy.com/
10. A. Lazurenkom V. Kim, A. Bishaev, M. Auweter-Kurtz, J. Appl. Phys. 98, 043303 (2005).
11. J. P. Boeul, L. Garrigues, J. Appl. Phys. 84 (7), 3541-3554 (1998).
12. G. J. M. Hagelaar, J. Bareilles, L. Garrigues, J. Boeuf, J. Appl. Phys. 91 (9), 5592-5598 (2002).
13. Advanced Energy, “User Manual for Linear Ion Beam Source”, (1999).
14. Yasui, Kyoto University, Master Thesis (2003).

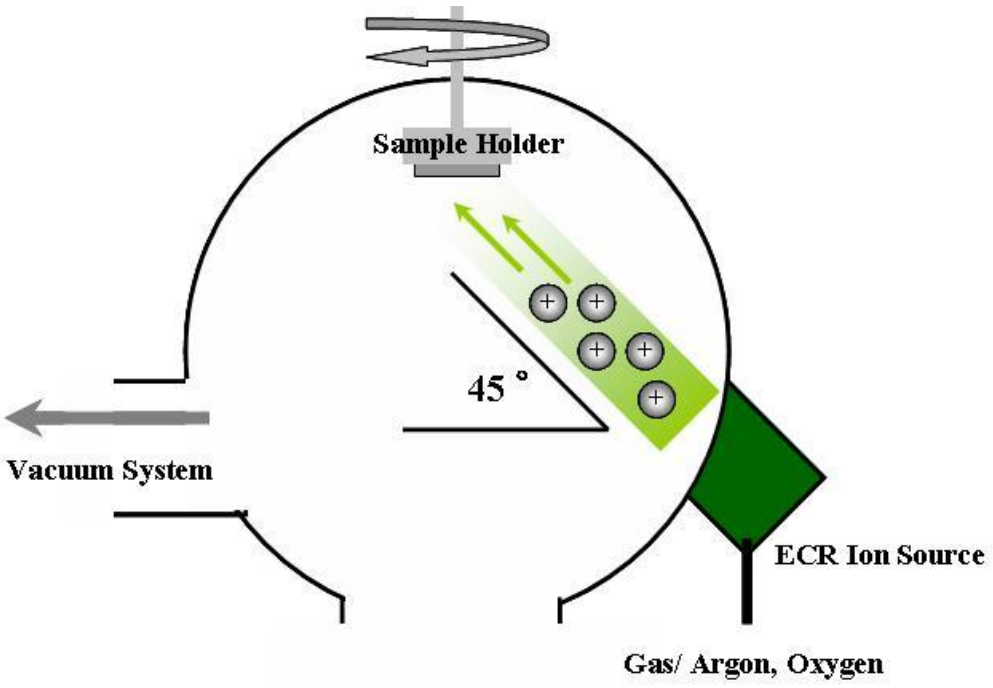

Figure 2-1. Schematic of ECR Chamber

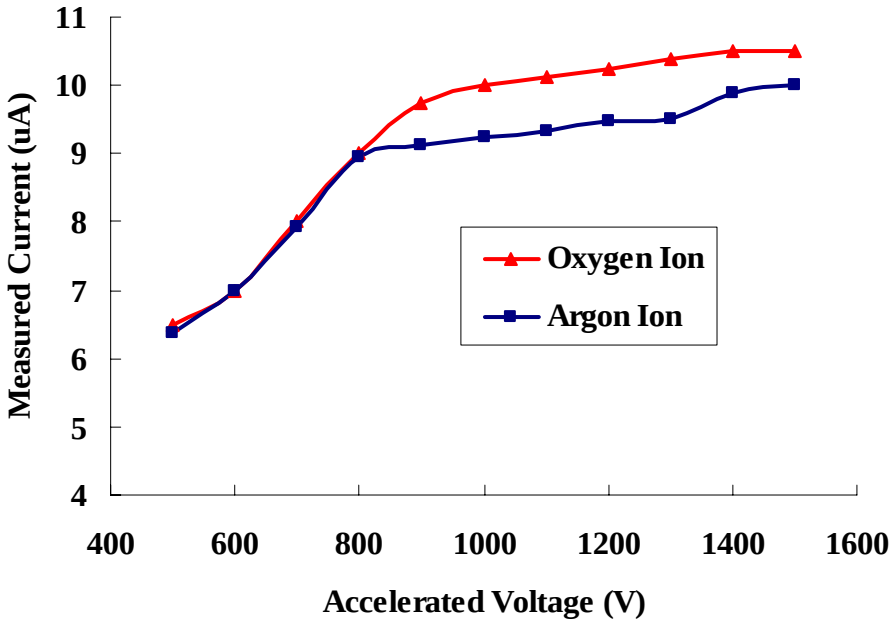

Figure 2-2. Measured current to accelerated voltage of oxygen and argon ions (ECR)

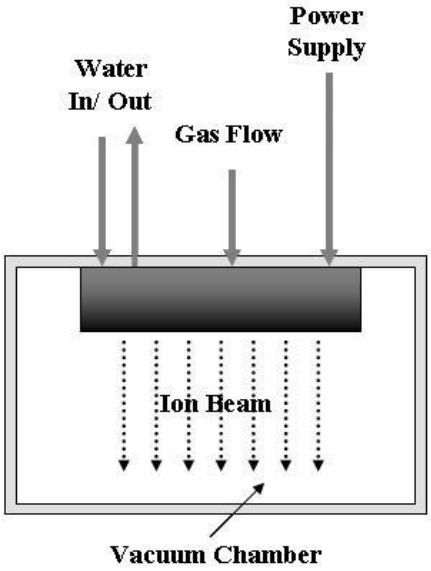

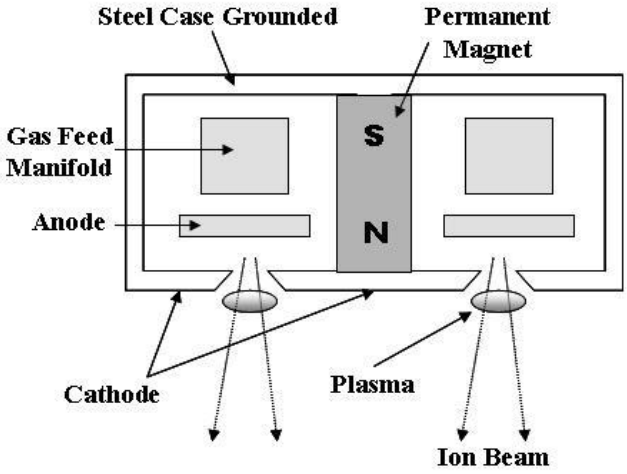

Figure 2-3(a). System of linear ion source

Figure 2-3(b). A diagram of linear ion source

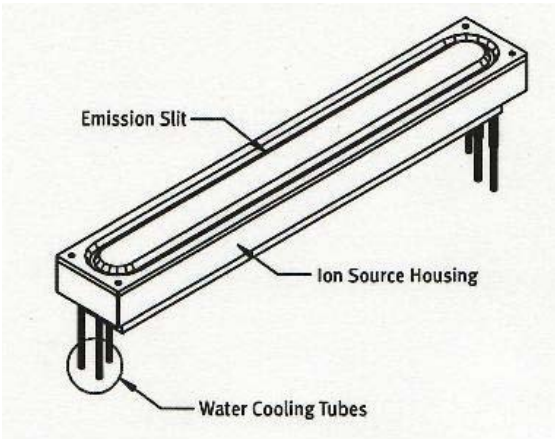

Figure 2-4. Appearance of linear ion source

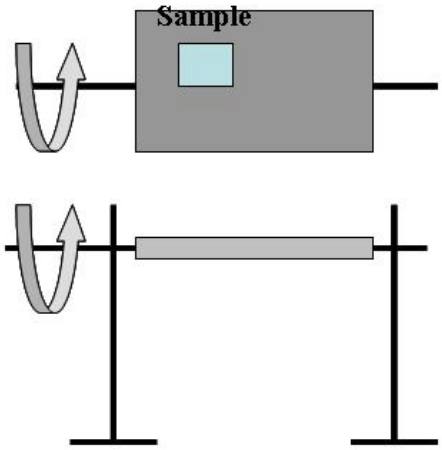

Figure 2-5(a). Flat-plate type

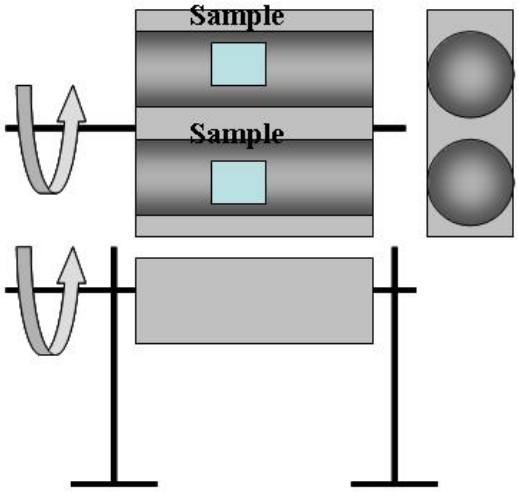

Figure 2-5(b). Rolling type

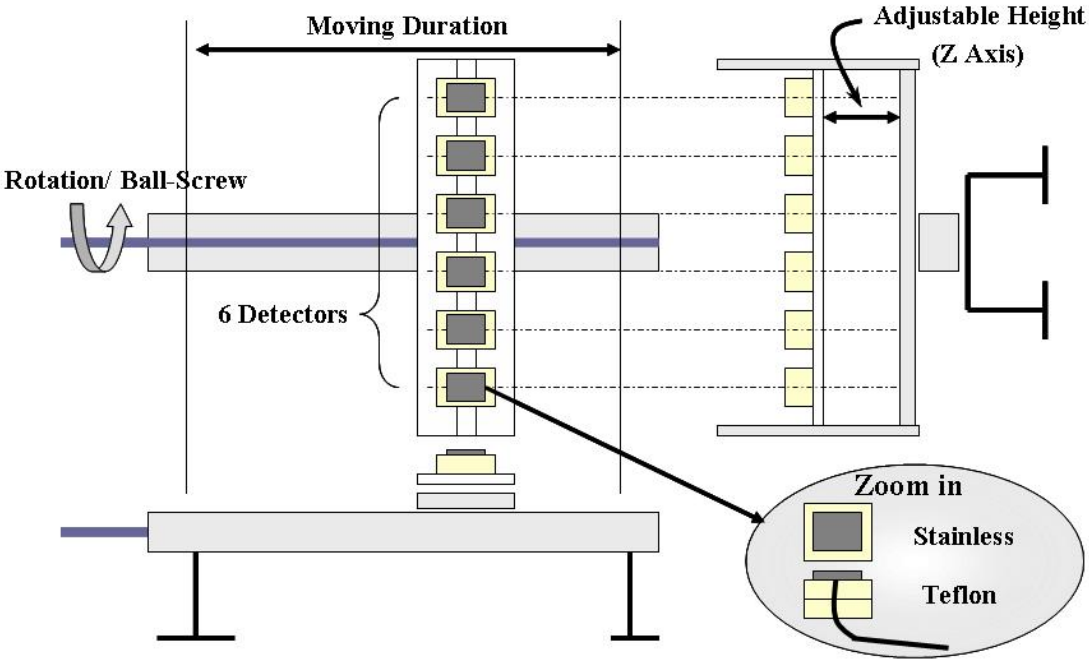

Figure 2-6. Ion distribution measurement type

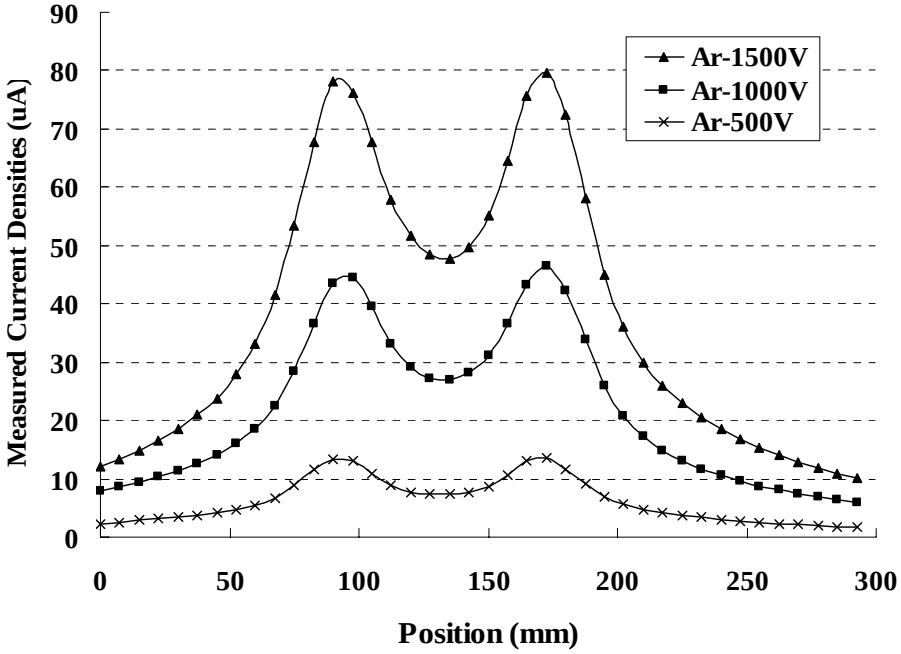

Figure 2-7. Argon irradiation at the discharge voltage 500 V, 1000 V and 1500V

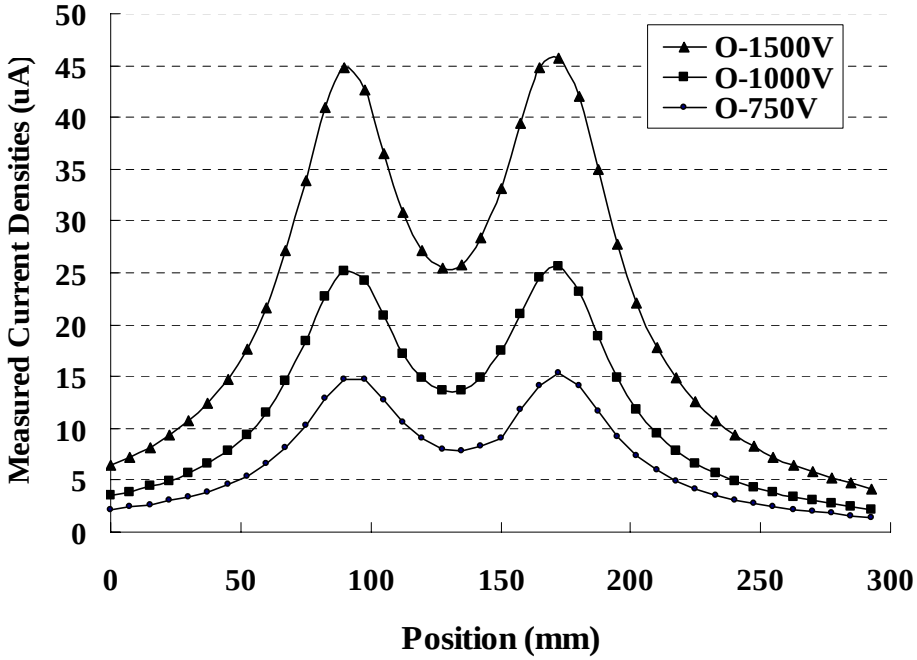

Figure 2-8. Oxygen irradiation at the discharge voltage 750V, 1000V and 1500V

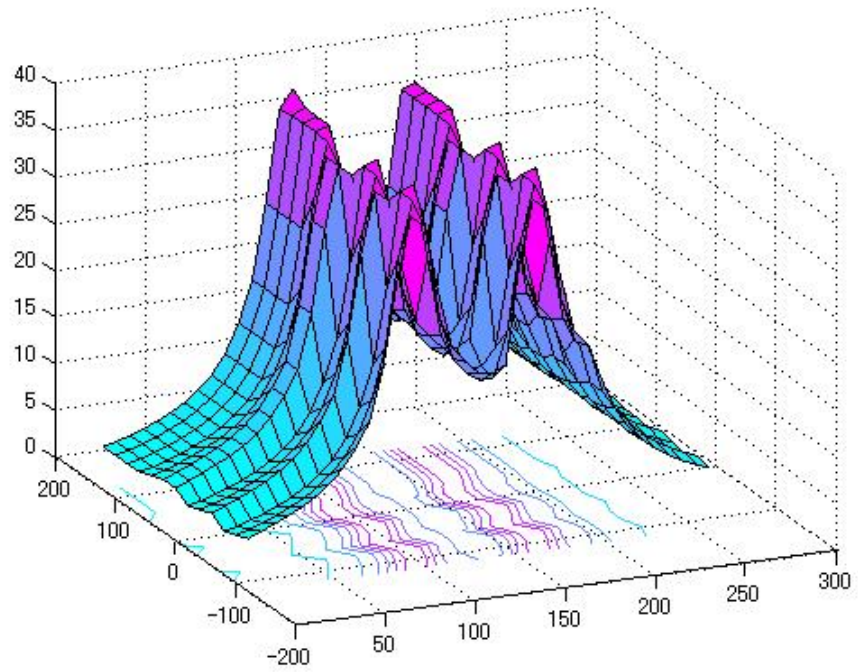

Figure 2-9. 3-D ion current distribution measured at the x-y plane

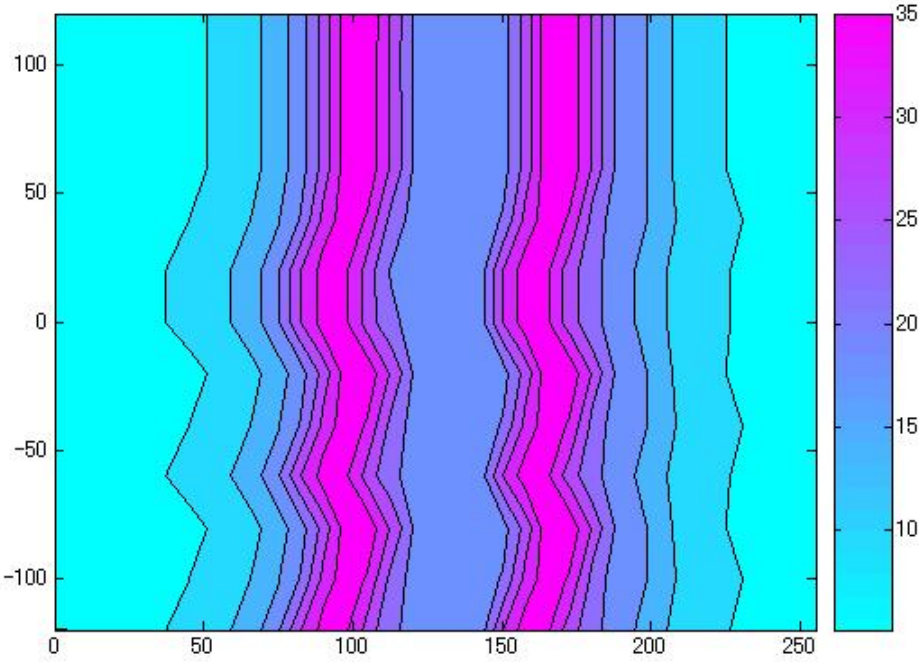

Figure 2-10. Contour mapping of Figure 2-9

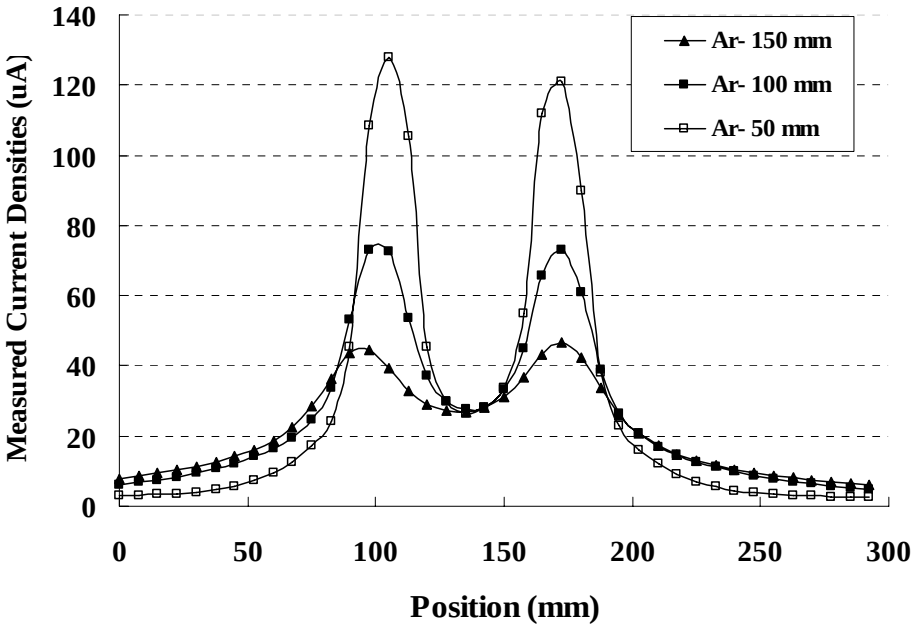

Figure 2-11. Current distribution at different distance. (Ar 1000V)

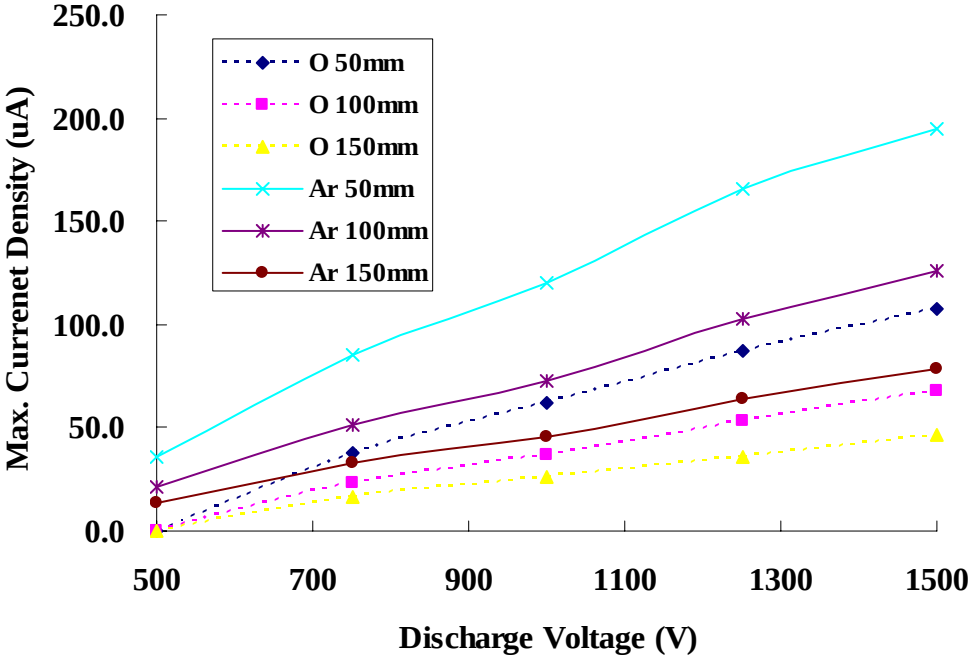

Figure 2-12. Max. current density of oxygen and argon ions at different distance

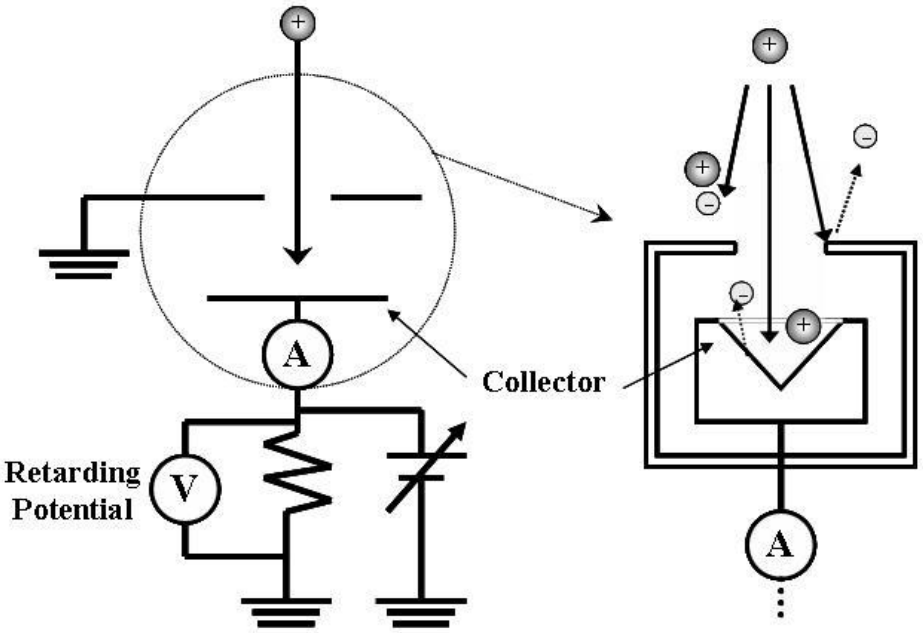

Figure 2-13. Ion Energy detector

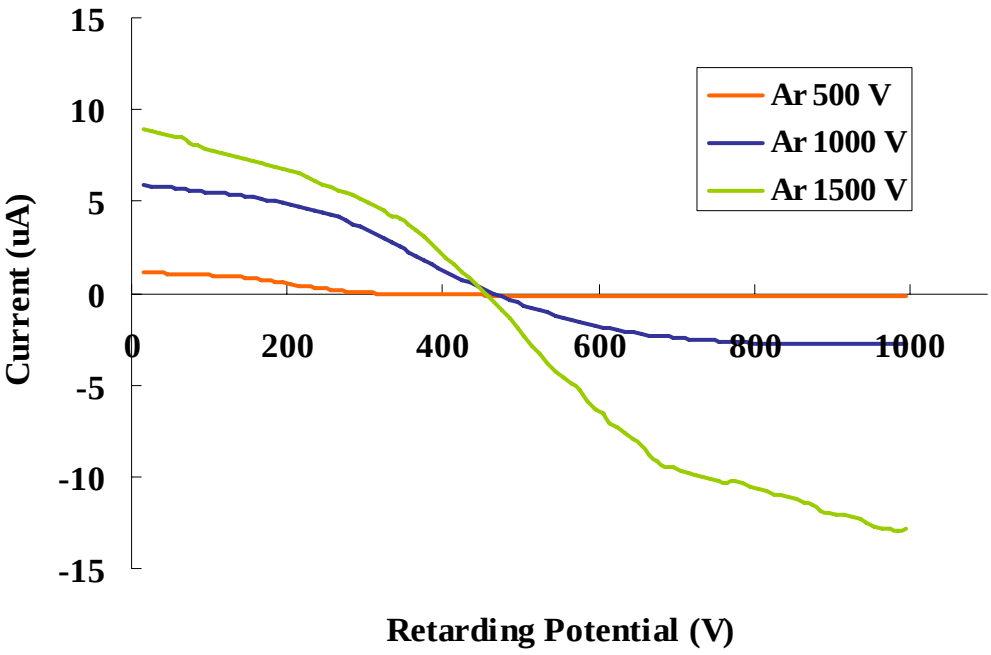

Figure 2-14. Retarding Potential to Current

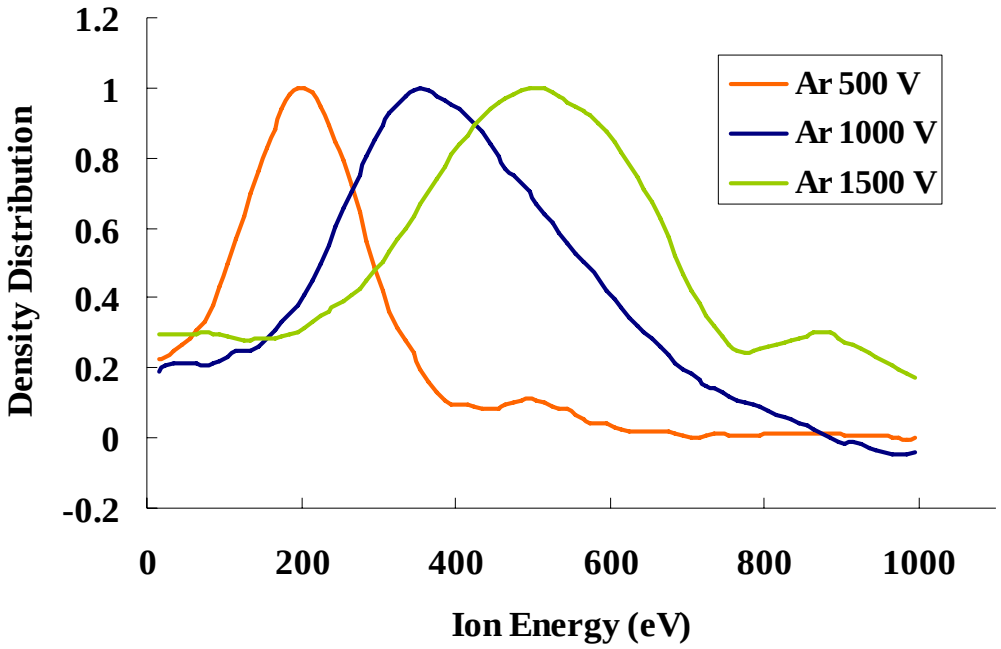

Figure 2-15. Ion energy and Density distribution

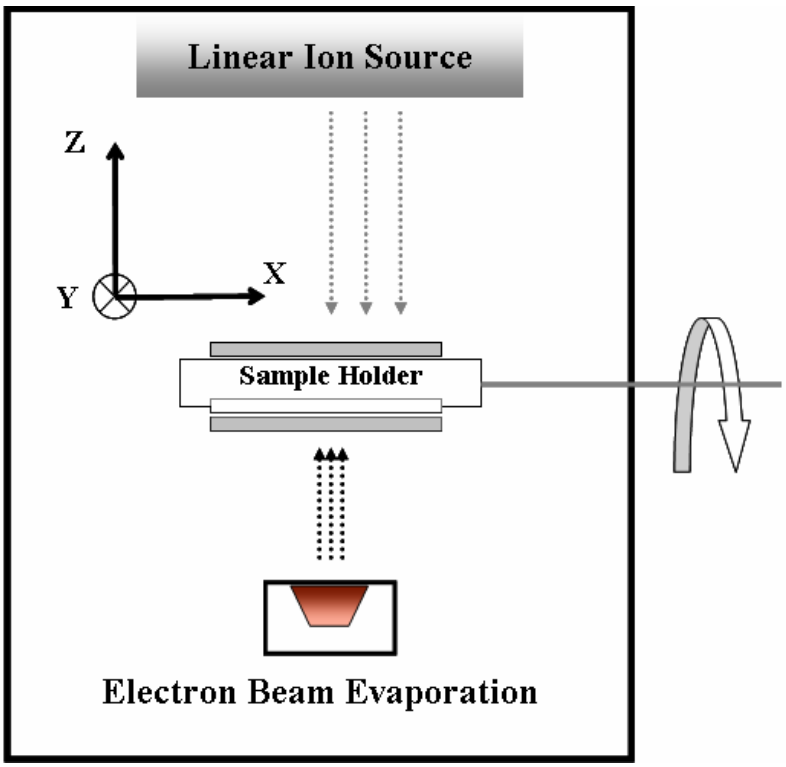

Figure 2-16. Linear ion source and electron beam evaporation chamber

Chapter 3

Transparent Conducting Oxide Deposition on Polymer

3.1 Substrate – Polyethylene Terephthalate (PET)

For the substrates used in display applications, glass is widely popular in the flat panel displays industry because of its rigid, wearable and optical characteristic. Furthermore, glass has mechanical properties of smoothness, dimensional stability, and it is regarded as the standard substrate material for flat panel displays. For flexible displays, glass offers substantial rewards in terms of being able to develop displays that are thinner, lighter and capable of being rolled away when not needed. There are two choices for flexible substrates, which include polymeric and thin glass. In this study, polymeric substrate was used. In order to replace glass, a plastic substrate needs to be able to offer the properties of glass. This includes clarity, dimensional stability, thermal stability, barrier, solvent resistance, as well as a low coefficient of thermal expansion coupled with a smooth surface.

Polymers are the ubiquitous materials in modern manufacturing process and offer a wide variety of chemical and mechanical properties applicable to numerous problems [1]. From polymers used for structural purpose to plastics compatible with biological tissue, the used of polymeric species continue to grow. Polymers substrates are considered good substitutes for glass substrates used in display applications [2, 3]. Despite the versatility of many polymeric materials, there are limitations to their applications. The surface properties of a polymer will preclude its use in an application to which its mechanical properties may be very well-suited. However, the polymer surface modification can offer significant benefits by allowing the surface properties to be tailored to meet a specific requirement while retaining beneficial mechanical properties. The next chapter will discuss how to modify surface properties by ion beam irradiation.

In polymer materials, polyethylene terephthalate (PET) is a good candidate used as a flexible substrate. PET is a thermoplastic polymer resin of the polyester family that is used in synthetic fibers, beverage, food and other liquid containers [4]. PET has good barrier properties against oxygen and carbon dioxide. Therefore, it is utilized in bottles for mineral water. Other applications include food trays for oven use, roasting bags, as well as mechanical components. PET exists both as an amorphous (transparent) and as a semi-crystalline (opaque and white) thermoplastic material depending on its processing and thermal history. Generally, it has good resistance to mineral oils, solvents and acids. PET is a hard, stiff, strong, dimensionally stable material that absorbs very little water. It has good gas barrier properties and good chemical resistance. In the industry and electrical

field, PET can be widely used in electrical insulation, lamination, OHP sheet, ID card, ITO coating, solar film and optical films. PET is usually made through two step condensation polymerization of the dimethyl ester of terephthalic acid and ethylene glycol. It includes an ester bond (-O=C-O-), a methylene (C_2H_4) and a benzyne (C_6H_4) internally. The chemical constitution of PET ($C_{10}H_8O_4$) is shown in Figure 3-1. The PET film used in this study has the density of 1400 Kg/m^3, and Young Modulus of 5 GPa. Its melting point is 258 ℃ and glass transition temperature is 78 ℃. The specific heat is 1.05 KJ/ Kg K, and the coefficient of heat transfer is 0.24 W/m K. The light transmission of 125 um PET thickness used was over 85 % from 400 nm to 700 nm in viable wavelength.

The biggest challenge for polymer substrates used in the flexible display is the process temperature required by subsequent display layers. Thermal and dimensional stability are critical in enabling a film to withstand the high temperature of deposition of the barrier and indium thin oxide coatings; to ensure precision registration of the different layers in the final device, plastic films undergo a variable and undesirable change in dimensions at the T_g. This is due to both molecular relaxation events associated with the increased mobility of the polymer chains and also shrinkage or expansion associated with relaxation of residual strain within the oriented parts of the film structure. However, when considering what the required temperature is for device manufacture. the glass transition temperature T_g is an obvious characteristic to focus on. Polymers undergo a change in physical and mechanical properties at the glass transition T_g, and the PET films used in this experiments have T_g of 78 ℃. Sometimes, it is considered to have too low T_g to impart the thermal and dimensional stability necessary to support some deposition process. And below the T_g 78 ℃, we could not achieve the thin film properties expected.

We tried to increase the temperature, because the PET films T_g of 78 ℃ is too low for thin film deposition process. The dimensional stability of PET could be enhanced by a heat stabilization process, in which the internal strain in the film was relaxed through exposure to high temperature while under minimum line tension. The majority of polymer film, when heated to temperatures above the nominal T_g, showed some tendency to shrink or expand along selected axes. When the shrinkage at a given temperature is measured by placing the sample in a heated oven for a given a period of time, and the percentage of shrinkage was calculated as the % change of dimension of the film before and after the heating process. Heat-stabilized PET film exhibits minimal shrinkage in the order of < 0.1 % and typically < 0.05 % when exposed to temperatures of up to 140 ℃ [5]. In addition, once heat stabilized, the Tg effects described above were essentially negated and the PET film remained a dimensionally reproducible substrate up to 150 ℃. Figure 3-2 shows the dimension change with temperature and time from William A. MacDonald (2003), detected by the thermal mechanical analysis [1]. In this experiment, we deposited the transparent conducting oxides thin films at room temperature, and in some cases increased the substrate temperature to 100 ℃ during

the deposition processing and 150 ℃ during the post-annealing process. The thermal process affected some properties of thin films and it is discussed in following chapter.

3.2 Electron beam evaporation

The chamber including the linear ion source and the electron beam evaporation described in Chapter 2.4 was used to deposit indium tin oxide (ITO) as the transparent conducting oxide (TCO) thin films in this experiment. ITO has been commonly used as the TCO in the display industry, because of its excellent optical and electrical properties. However, when it was utilized on polymeric based substrates for the flexible display, the process temperature had some restrictions, set by the sensitivity of polymer substrate. In Chapter 2.4, the electron beam evaporation equipment was developed in the same chamber with the linear ion source shown in Figure 3-3. It was used after the surface modification process of PET substrate when the sample holder was rotated 180 degree to face downward. In this experiment, the ITO material used as the evaporated target were at 2 wt % SnO_2 doped with In_2O_3.

At first, the ITO was deposited at room temperature by the electron beam evaporated, all without any gas injected within it. The thickness of thin film was approximately 150 um. The transmission rate of this deposited thin film was below 30 %, and it was nearly opaque. It could not be used for part of device to display. This thin film was not transparent that can be considered indium and tin cannot fully be oxidized when it deposited on substrates. It is called as metal-rich discolored deposit [6]. After Rutherford backscattering spectroscopy (RBS) was used in detection for the thin films composition, it was revealed to have poor oxygen ratio in it. As we know, very few inorganic compounds evaporate without molecular change and therefore the vapor composition is usually different from that of the original solid or liquid source. As a consequence, the stoichiometry of the film deposited generally differs from that of the source. The troublesome decomposition of multivalent metal oxides to lower oxides like metal-rich discolored deposits can be compensated by reactive evaporation in active oxygen ambient. In this case, the expected TCO thin films cannot be performed by the electron beam evaporation processing without oxygen gas introduced within the system. For this reason, the improved way was proposed to introduce a gas pipe near the substrate for the reactive evaporation. When additional 5 ccm oxygen flow was injected into the system which is closed to the substrate during the deposition process, the optical properties of the expected ITO thin film improved little, but the light transmission rate was still below 50 %. It is still unusable as the transparent thin films for display.

Figure 3-5 shows the RBS spectrum of the ITO thin film deposited at room temperature with 5 ccm oxygen gas. In this RBS spectrum, it is difficult to calculate the composition of indium and tin

to oxygen ratio using the method described in Appendix 3 RBS part. This is because the peak of indium and tin are overlapping. Through the process in analyzing the element concentration described in Appendix 3, we know the exact area of peak for each element and respective cross sections. A software named RUMP designed for analysis and simulation of Rutherford backscattering spectrometry (RBS) spectrum was used. By using this software, we can simulate the composition of the compound and let the simulation data curve to fit the spectrum measured. Figure 3-6 shows the simulation fitting to the spectrum of Figure 3-5. The green curve is the tin peak, the blue curve is the indium peak, and red curve is the curve fitting to the measured data. The simulated data shows that the indium ratio was higher. It was about 41%, 1 % and 58 % to indium, tin and oxygen, respectively. It was thought the thin films included too much metal content and resulted in the opaque films. Introducing more active oxygen gas was hypothesized to improve the properties of ITO thin films. However, following the increase of ambient oxygen gas flow in chamber, working pressure actually increased. The electron beam evaporation apparatus installed in this chamber had a recommended working pressure of 6.7×10^{-3} Pa, and was limited to use only when the pressure was beyond 10^{-2} Pa; otherwise the filament might break down.

Because the electron beam evaporation apparatus used in the linear ion source chamber cannot meet the higher working pressure, the alternative method was considered: using the other electron beam evaporation located in the different chamber. This experiment included depositing ITO thin films. This electron beam evaporation apparatus can be operated at a much higher ambient pressure with the ECR ion source shown in Figure 3-7. Moreover, the sample holder can be heated during the deposition processing. The oxygen composition of the ITO evaporant target in crucible was medium. The low oxygen target ($In_2O_{3-\delta}$) appeared yellow [7]. When δ approaches zero, the color changed from green to grey to black, as shown in Figure 3-4. The deposition conditions were applied in higher oxygen pressure at 8 ccm flow. It was expected that the ion bombard and more active oxygen ambient contributed to the dynamic oxidation and improve the ITO properties.

The experiment results show the light transmittance improved, but not enough to be a transparent film. At the second stage, we tried to add the thermal processing and heated up the substrate temperature during the deposition. The substrates were heated to 280 ℃, 250 ℃ for glass, and 150 ℃ for PET films, and it was effective and resulted in improved properties of the ITO films. The experimental results demonstrated the oxygen flow rate and showed that the oxygen ion beam assisted the deposition affect very little for the transparency of ITO thin films. Either an increase in oxygen gas flow rate to 8 ccm or using oxygen ion beams assisted deposition resulted in the low light transmission below 50 %. The substrate temperature during the deposition served as a key factor to enhance the properties of ITO thin films. The transparency improved significantly when the substrates temperature was varied from room temperature to 250 ℃ and 280 ℃. Figure 3-8 shows the photograph of different substrate deposited on ITO in (a) room temperature, (b) 150 ℃

and (c) 250 ℃, (d) 280 ℃, (e) room temperature by sputtering method, and (f) no film on glass slide substrate. The color was changed. The light transmittance measured was modified from 41 %, 61 % to 74 %, 80 % on average in the visible wavelength for (a), (b), (c), (d) of Figure 3-8 respectively.

The optical properties improved significantly when the substrate temperature increased. Moreover, another important property for the transparent conductive electrodes is its surface resistivity. Figure 3-11 shows the light transmission and surface resistivity for each condition applied in this experiment. When the substrate temperature increased to 150 ℃, the surface resistivity decreased from 1700 Ω/cm^2 deposited at room temperature with IBAD to 120 Ω/cm^2, and decreased to 57 Ω/cm^2 at the condition of 250 ℃ substrate temperature. Although it was still worse than the ITO deposited by sputtering described later, it was very close to the target specification. The thermal process not only improved the optical property but also the electrical property of ITO thin films.

When we analyzed the composition of ITO films deposited at each condition, Figure 3-9 and Figure 3-10 show the RBS spectrums of the sample deposited at 150 ℃ and 250 ℃. and simulated fitting by RUMP. The oxygen composition ratio was increased from 58 % at room temperature to 59.1 % at 150 ℃ and 59.7 % at 250 ℃ . The indium ratio was relatively decreased with substrate temperature increase.

In summary, the complicated decomposition of metal oxides occurred at the electron beam evaporated processing and resulted in the lower oxide-like metal-rich discolored deposition on substrates. Even with the increased active oxygen ambient gas, it resulted in little improvement of ITO thin films. Consequently, heating the substrate showed obvious improvement. However, the plastic substrate like PET used in this study has the thermal sensitivity as its restriction. In other words, the deposition of these brittle inorganic materials on plastic while achieving the highest possible optical, electrical and mechanical performance presents a new set of challenges to the thin film deposition and processing community. At the modest substrate temperature, from room temperature to 150 ℃, the PET substrate cannot achieve the expected ITO thin films. The advanced processing method should be considered.

3.3 Sputtering deposition

The various physical vapor deposition (PVD) methods have been used for the transparent conducting oxides within the industry and include the pulsed laser deposition (PLD) method [8, 9], molecular beam epitaxy (MBE) method [10, 11], Ion Plating (IP) method [12-15], and RF sputtering method. The RF sputtering method was utilized as the alternative in this study. It is

advantageous since it can be applied applied in large areas for industry, and can easily control the composition of thin films. Since the sputter yields are essentially similar for the target materials, sputtering of a dielectric cathode in an plasma should be feasible. Moreover, the AC RF sputtering method can be operated at room temperature, and is suitable for the polymeric based substrates that cannot endure the high temperature processing.

The RF magnetron sputtering device was used alternatively for transparent conducting oxides deposition. The substrate was located in a low-pressure chamber between two electrodes, and these electrodes were driven by an RF power source, which generates the plasma and ionizes the gas between the electrodes. A potential drives the ions towards the target surface as the cathode causing atoms to be knocked off the target surface from ion bombardment. The target materials were sputtered out and deposited on the substrate surface. A magnetic field is applied to contain the plasma near the surface of the target to increase the deposition rate. The schematic of magnetron sputtering equipment was shown in Figure 3-12.

The RF sputtering essentially works because the target self-biases to a negative potential. Once this happens, it behaves where positive ion-bombardment sputters away atoms for subsequent deposition. The target used in the sputtering method played an important role for the thin film composition. The targets come in a variety of shapes: rectangular, triangular and circular plates etc, and targets range in size from 10 cm dimensions for laboratory purposes to several meters for industry. The circular plate with 10 cm in diameter target was used in this sputtering device. In general, the metal and alloy targets are fabricated by melting either in vacuum or under protective atmospheres, followed by thermo-mechanical processing involving some combination of forging, extrusion, rolling and annealing, and ending with machining to final dimensions. The targets must be bonded to a cooled backing plate to avoid thermal cracking during sputtering. The fabrication of the transparent conducting oxides targets used in this study was described in detail in Chapter 5.

The main thinking of using sputtering method substitute for electron beam evaporation method is explained: in contrast to the fractionation of alloy melts during evaporation, with subsequent loss of deposit stoichiometry, sputtering allows for the deposition of films having the same composition as the target source [16]. This is a primary reason for the widespread use of sputtering to deposit metal alloy films. And this is why film composition is maintained during sputtering and not during evaporation. One reason is that there is generally much greater disparity in vapor pressures compared to the difference in sputter yields under comparable deposition conditions. Secondly, and more significantly, the melting homogenizes readily because of rapid atomic diffusion and convection effects in the liquid phase; during sputtering, however, minimal solid state diffusion enables the maintenance of the required altered target surface composition.

The deposition of ITO thin film using magnetron sputtering method was considered as the alternative to the previous electron beam evaporation method. The oxygen composition of the ITO

target was at the medium class with green color. In the ITO sputtering deposition, the argon gas was used as the sputtering gas introduced from the gas tube to the target. The argon gas became the plasma after high potential discharged enclosed by the magnetic field, then collided with the target. The substrate was put on the lower part of the chamber. The distance between the target and the substrate was 260 mm. Moreover, the heater for the heating substrate was set up under the substrate holder, and the substrate temperature was measured by the thermo-couple between the heater and the substrate. When the chamber was pumped to 8.0×10^{-4} Pa by the rotary and turbo-molecular pumps, the sputtering processing was started by RF power output in 300 W and argon gas flow in 10.4 ccm. The sputtering time is about 20 minutes in 150 nm thickness, and the processing temperature was at room temperature. The deposited ITO thin film had the optical property of light transmittance near 90 %, and the electrical property of the surface resistivity at 23 Ω / cm^2. Its RBS spectrum detected was shown in Figure 3-13, and the peak fitting was simulated by RUMP. The indium, tin and oxygen ration was approximate 39 %, 1 % and 60 %, respectively. It was very close to the ceramic sputtering target used in this experiment.

In addition to RBS, we used the X-ray photoelectron spectroscopy (XPS) to detect the surface chemical specific of ITO. Figure 3-14 upper side shows the XPS spectrum of ITO deposited by electron beam evaporation and the downside shows the deposition using the sputtering method. As described above, if the deposition proceeded at room temperature, without sample holder heating, the opaque thin film was deposited. From the XPS spectrum, it indeed included the indium, tin and oxide element. Compared to the transparent thin films deposited by sputtering method shown in Figure 3-14 downside, the necessary elements included were all detected. While the peak intensities varied, the concentration was the main reason that resulted in the better light transmission. Here, we selected the In $3d_{5/2}$ and O 1s peaks to do the quantitative analysis, and used the atomic sensitivity factor of In $3d_{5/2}$ and O 1s as 3.777 and 0.711, respectively. The use of atomic sensitivity factors in the manner described normally yields semi-quantitative results (within 10 to 20 %). So it cannot be regarded as the exact atomic concentration in thin films and compared to the previous results measured by RBS. However, the concentration calculated using XPS atomic sensitivity factor provided a way to compare two elements and their variations and modifications during the different conditions. In the O 1s peak, it was thought the spectrum include the various peaks with different bonding energy more than two. The first and the second one were considered as the oxygen in metal oxides in the range of 530 eV to 531 eV. They are oxygen bonded to indium and tin. The third one was considered as the C-O contamination peak, according to the C 1s peak shown in Figure 3-14. Figure 3-15(a) shows the O 1s peak fitting of the opaque thin film in Figure 3-14 upside, and Figure 3-15(b) shows the O 1s relative one in Figure 3-14 downside. There was little difference in comparing these two figures. This was determined when we calculated the concentration of In $3d_{5/2}$ and peak 1 of O1s spectrum by using sensitivity factor and peak area subtracting background line.

The results indicated the In $3d_{5/2}$ to peak 1 of O 1s ratio improved from 1.39 to 1.23; the indium concentration decreased in these two different deposition conditions. XPS analysis of the ITO thin films deposited presented the similar phenomenon of the metal rich discolored effect with the RBS result during the electron beam evaporation process. The experiments indicated that the magnetron sputtering method was suitable and it could achieve the high quality ITO thin films at room temperature.

3.4 Mechanical Limitations on Flexible Substrate

Flexibility of displays is an appealing feature which will change the look and feel of a display altogether from a heavy, expensive and fragile piece of equipment to a thin lightweight and rugged device that can be used in many new surroundings. Besides, flexibility (lack of rigidity), also indicates improved ruggedness. For a number of display principles that intrinsically thin, like liquid crystal displays and organic light emitting diode displays, flexibility can be obtained by reducing the thickness of the substrates, while the choice for plastic substrates improves the ruggedness [17-19]. Although advantageous for flexibility, the properties of polymeric materials seldom match with all requirements set by display processing or display usage, either mechanically like scratch resistance, chemically like chemical resistance or physically like water permeability [20-23]. To compensate for this, a plastic display substrate needs to be engineered, for example, coated with several layers to improve the properties of the total film. A gas or moisture barrier is frequently coated, and it was described at Chapter 6. While the display side is coated with a transparent electrode material, such as indium tin oxide (ITO), and it was described prior section.

While the polymer substrate like the PET used in this study is organic material, the gas barrier and ITO are mostly inorganic materials. Since inorganic materials are commonly stiff and brittle, whereas the polymers are not, the mechanical failure of these thin brittle layers on top of a polymer base film should be considered. The base polymer and the additional layers differ significantly in their main mechanical properties: the Young's modulus. The Young's modulus indicates the rigidity of a layer, they can lead to significant strains which lead to high stress levels, particularly in thin, high modulus layers. The PET used in this study has Young's modulus of 5 GPa, and ITO thin film was reported to have about 120 GPa [24], and the SiO_2 layer as the gas and moisture barrier was about 70 GPa. It is completely different for these materials. When bending is applied in a display or a display substrate, it leads to a very well-defined deformation profile. At a given radius of curvature, the outside of the display substrate is stretched while the inside of the film is compressed, with the strain varying linearly over the thickness of the film. At a given position in the cross section of the substrate, the neutral plane, the strain does not change on bending. This location

depends on the layer structure of the film and the Young's moduli of all layers. This bending strain and the strain due to a tensile load are examples of externally applied strains.

The stresses in the multilayer inorganic and organic composite resulting from mechanical loading may cause a variety of failure mechanisms. These may lead to either cohesive failure of the inorganic layer like fracture. In this study, we deposited the inorganic layers like transparent conducting oxides and barrier layer on the PET films. One simple mechanical structure device was designed for applying the tensile loading for the testing sample shown in Figure 3-16. This mechanical structure provided the loading when the ball-screw rotate and move in 1 mm/per rotate, then the spring scale measured the tensile loading on the testing sample. This sample mechanical structure cannot detect the precious loading scale for quantitative analysis for the stress occurred on the sample, but can provide the qualitative analysis to know the defection of the inorganic layers coating on the sample. Figure 3-17 shows the cracking of 100 nm SiO_x films in axial tensile failure. The thin film cracked uniformly in one direction by a tensile strain applied. It indicated the brittle coating on the polymer based substrate face the mechanical limitation when it faced the tensile or bending on it, and easily resulted to cracking

References

1. W. A Macdonald, K. Rollins, R. Eveson, K. Rakos, A. B. Rustin, M Handa, Materials Research Society Symposium Proceedings 769, H9.3, 283-290 (2003).
2. P. J. Slikkerveer, 22nd International Display Research Conference Proceeding, 273-276 (2002).
3. P. J. Slikkerveer, Information Displays 3, 20-24 (2003).
4. http://en.wikipedia.org/wiki/Polyethylene_terephthalate
5. W. A. MacDonald, J. Mater. Chem. 14, 4-10 (2004).
6. M. Ohring, "Materials Science of Thin Films", p100-101 (2002).
7. J. R. Bellingham, W. A. Philips, J. C. Adkins, J. Phys: Condensed Matter 2(28), 6201 (1990).
8. K. Mastubara, P. Fons, K. Iwata, A. Yamada, K. Sakurai, H. Tampo, S. Niki, Thin Solid Films 431-432, 369 (2003).
9. H. Agura, A. Suziki, T. Matsushita, T. Aoki, M. Okuda, Thin Solid Films 445, 263 (2003).
10. K. Iwata, P. Fons, S. Niki, A. Yamada, K. Matsubara, K. Nakahara, T. Tanabe, H. Takasu, J. Cryst. Growth 214-215, 50 (2000).
11. Y. Chen, D. M. Bagnall, H. J. Koh, K. T. Park, K. Hiraga, Z. Zhu, T. Yao, J. Appl. Phys 84(7), 3912 (1998).
12. K. Iwata, T. Sakemi, A. Yamada, P. Fons, K. Awai, T. Yamamoto, M. Matsubara, H. Tampo, K. Sakurai, S. Ishizuka, S. Niki, Thin Solid Films 451-452, 219 (2004).

13. K. Iwata, T. Sakemi, A. Yamada, P. Fons, K. Awai, T. Yamamoto, S. Shirakata, K. Matsubara, H. Tampo, K. Sakurai, S. Ishizuka, S. Niki, Thin Solid Films 480-481, 199 (2005).
14. T. Kakeno, K, Sakai, h. Komaki, K. Yoshino, H. Sakemi, K. Awai, T. Yamamoto, T. Ikari, Mater. Sci. Eng. B118, 70 (2005).
15. T. Yamamoto, T. Sakemi, K. Awai, S. Shirakata, Thin Solid Films 451-452, 439 (2004)
16. W. D. Westwood, in Microelectronic Materials and Process. (1989).
17. M. Yanaka, et al. Mater. Res. Soc. Symp. Proc. 555, 33 (1999).
18. G. Rochat, et al., Thin Solid Films 437, 204, (2003).
19. M. Yanaka, et al, J. Mater. Sci. 33, 2111 (1998).
20. P. Servato, A. Nathan, Appl. Phys. Letters 86, 033504 (2005).
21. D. R. Cairns, et al., Appl. Phys. Letters 76, 1425 (2000).
22. M. A. Yanaka, et al. Thin Solid Films 355-356, 337 (1999).
23. Lewis J. et al, Mater. Res. Soc. Symp. Proc. 814. 18.5 (2004).
24. Y. Leterrier, L. Medico, P. C. Bouten, De Goede, IST-2001-34215-FLEXled report D17 (2003).

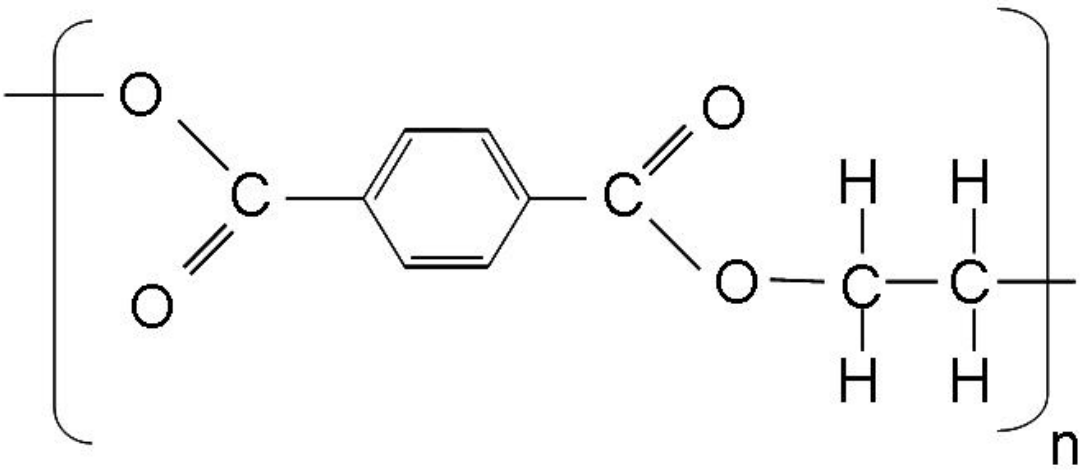

Figure 3-1. PET Chemistry structure

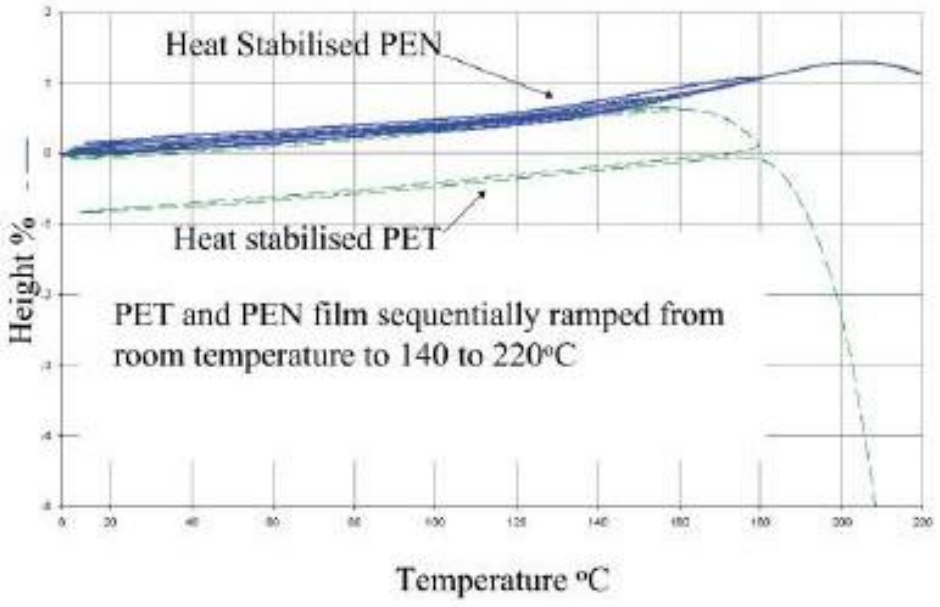

Figure 3-2. PET dimension change with temperature and time
(Reference: W. A. MacDonald, J. Mater. Chem. 14 (2004))

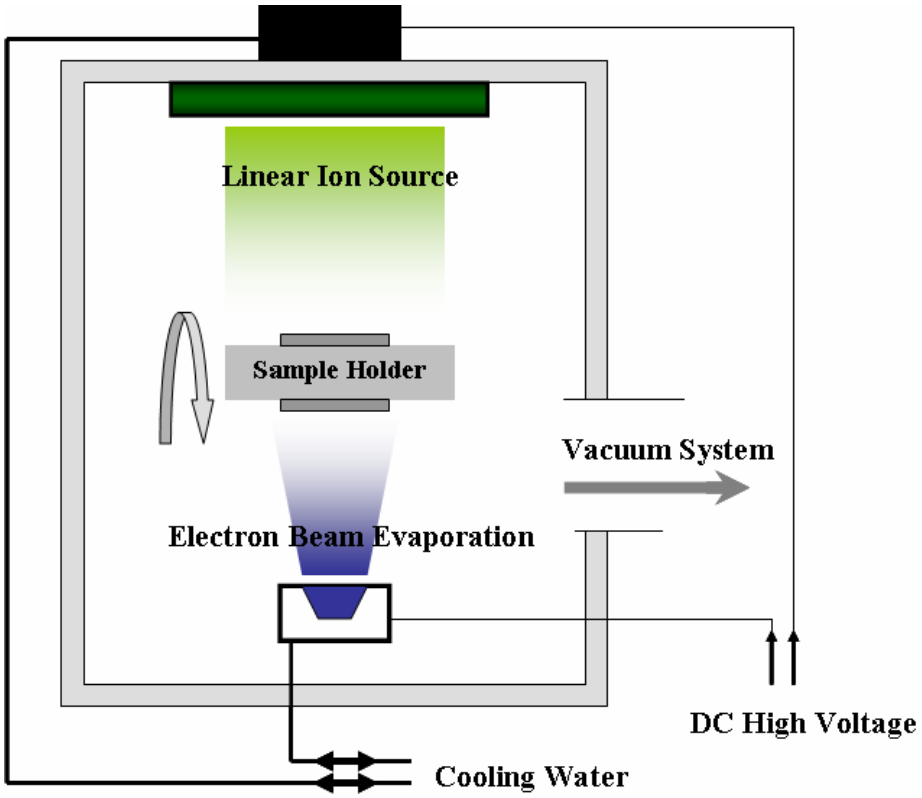

Figure 3-3. Linear ion source and electron beam evaporation system

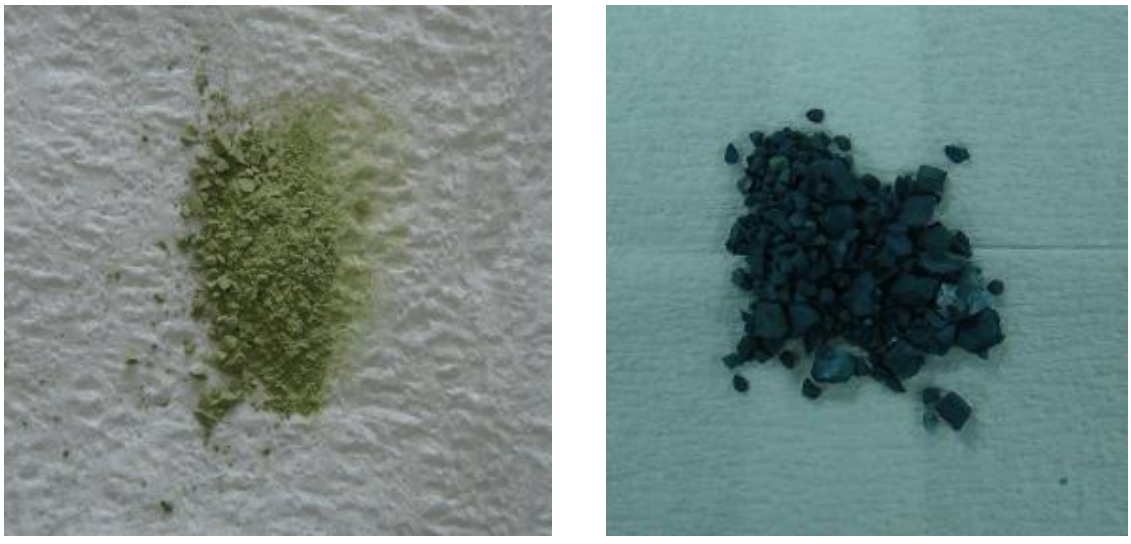

Figure 3-4. Change of ITO after electron beam evaporation

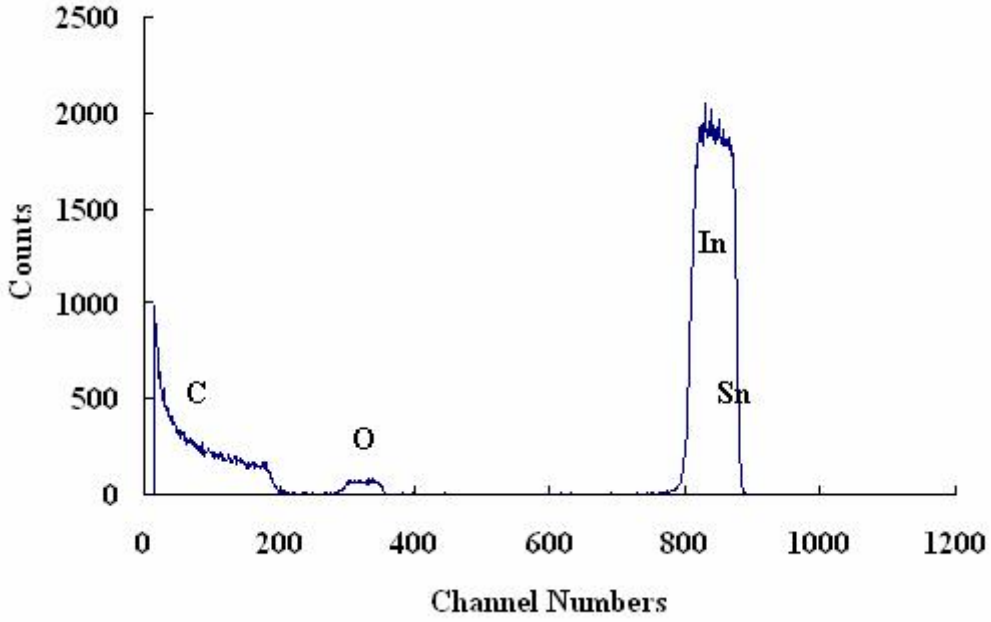

Figure 3-5. RBS spectrum of ITO deposited at RT

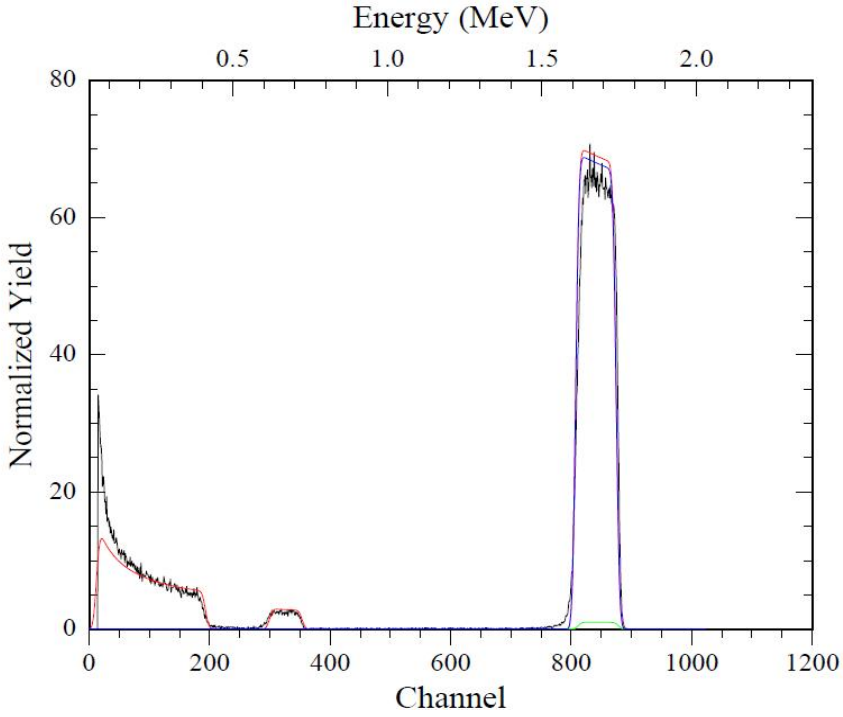

Figure 3-6. RUMP simulation fitting of Figure 3-5

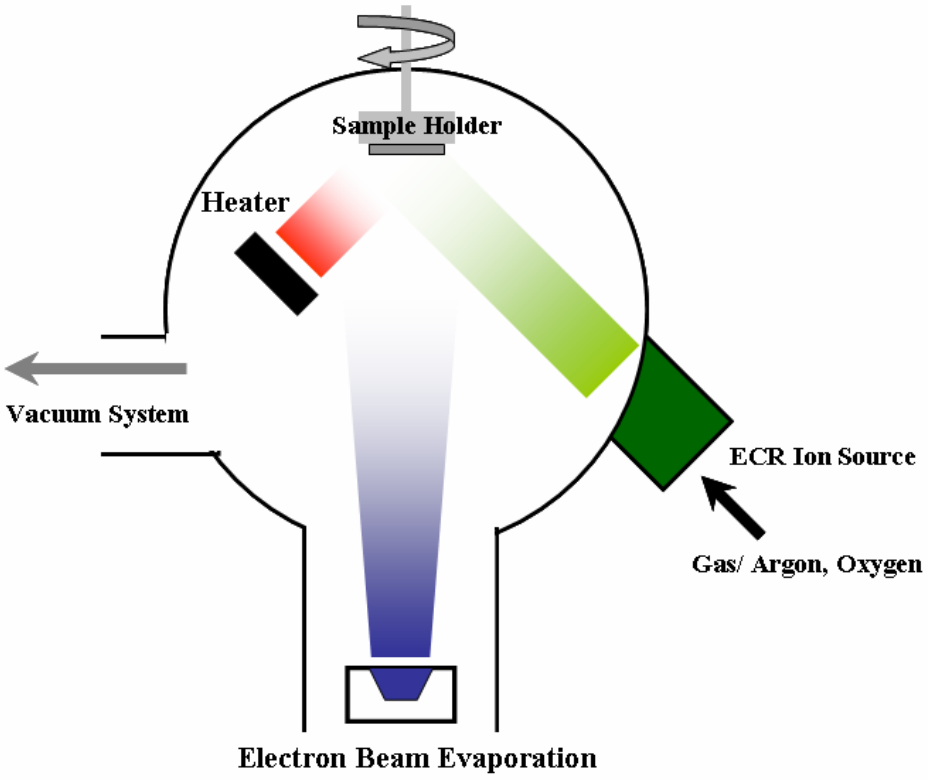

Figure 3-7. Chamber of electron beam evaporation with ECR ion source

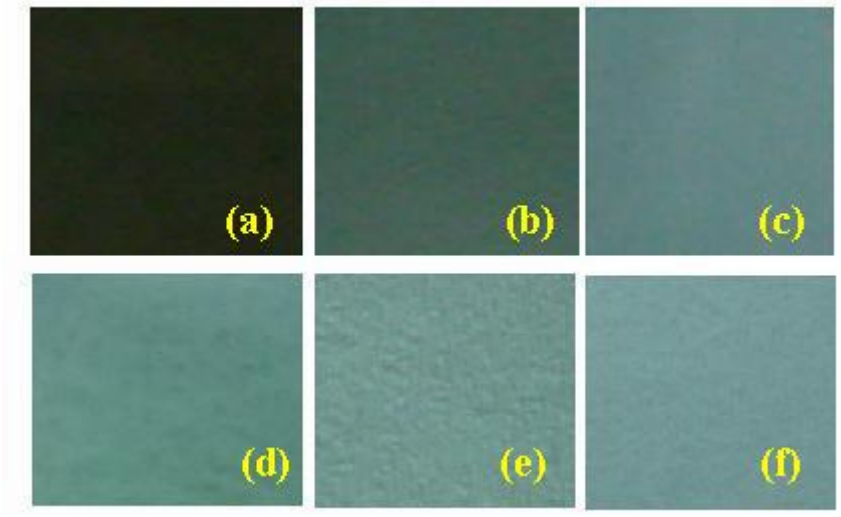

Figure 3-8. Colors of ITO thin films on glass, (a) RT, (b) 150℃, (c) 250℃, (d) 280℃, (e) Sputtering (RT), (f) No film on glass slide

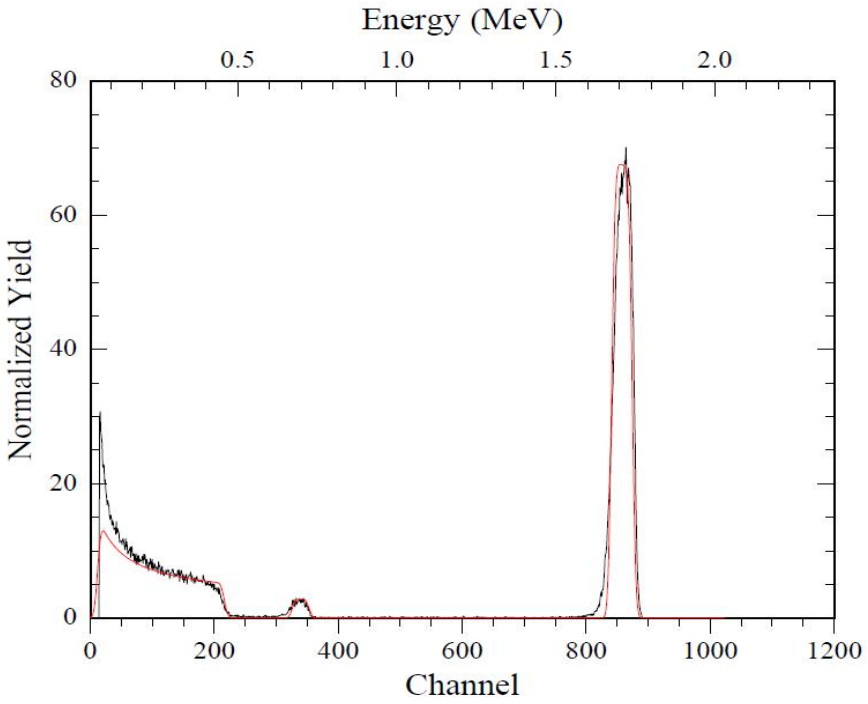

Figure 3-9. RBS spectrum of ITO deposited at substrate 150 ℃ (RUMP fitting)

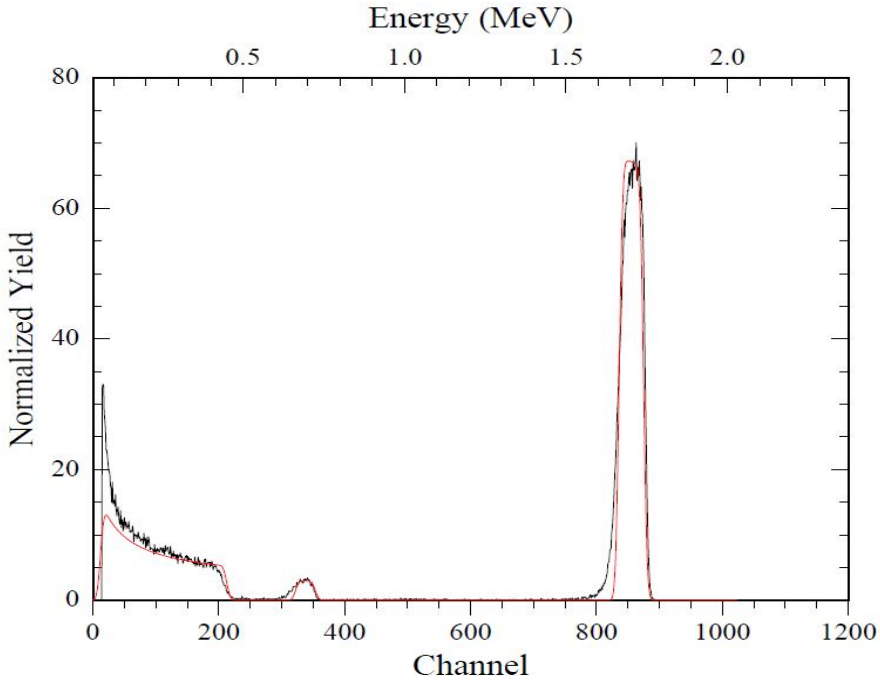

Figure 3-10. RBS spectrum of ITO deposited at substrate 250 ℃ (RUMP fitting)

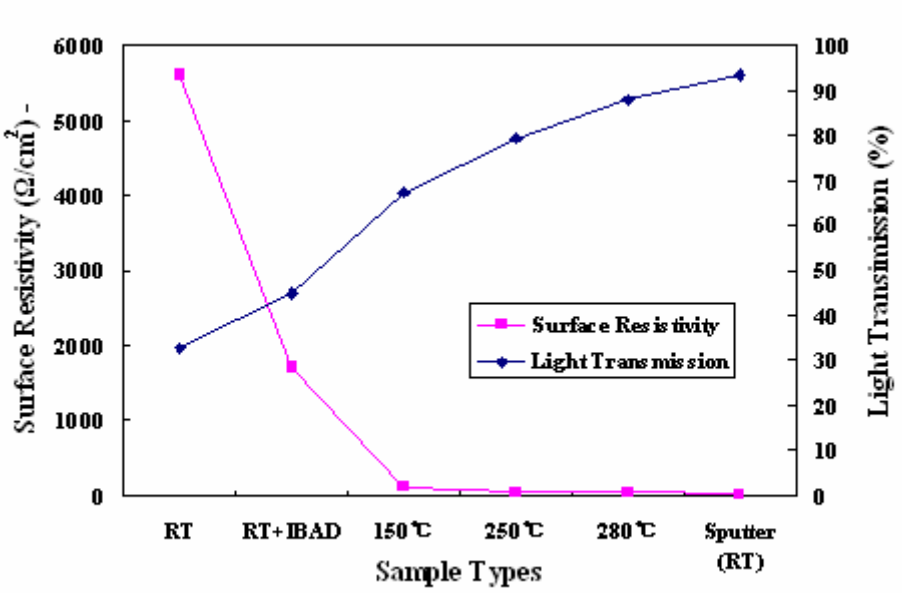

Figure 3-11. Surface resistivity and transmission of ITO deposited in various conditions

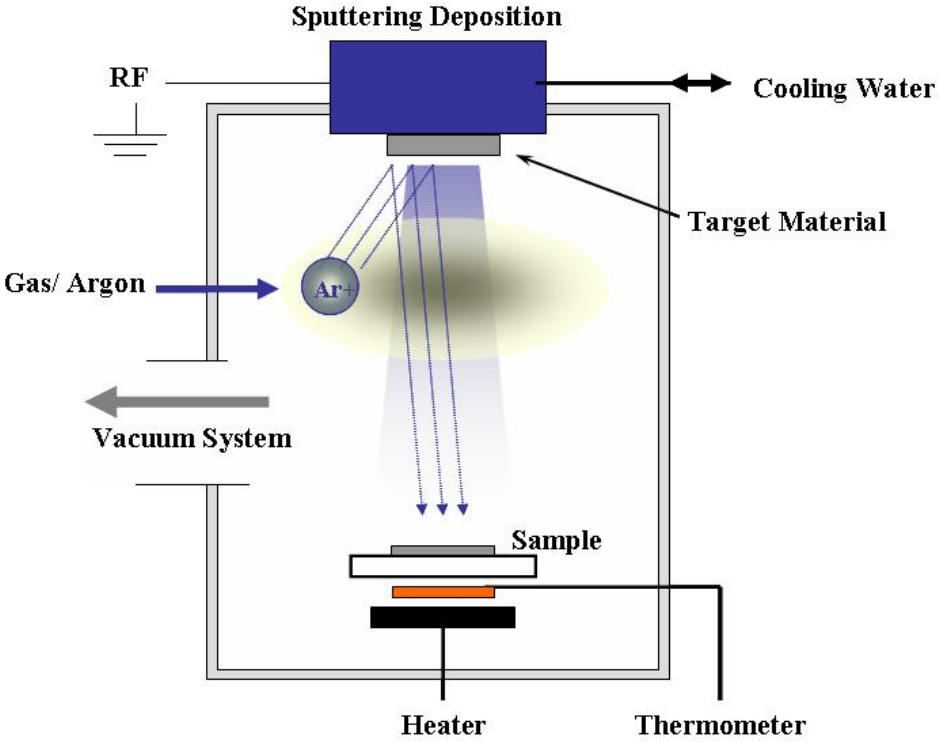

Figure 3-12. Chamber of sputtering deposition

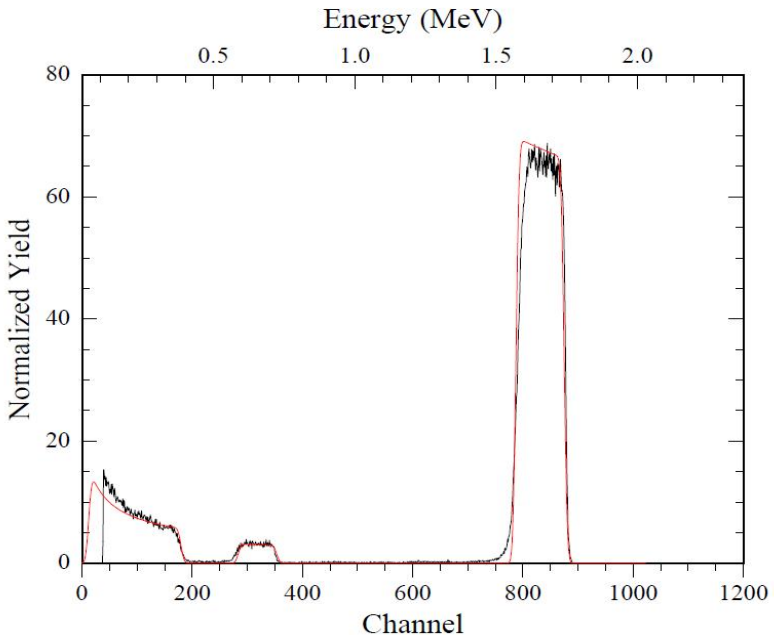

Figure 3-13. RBS spectrum of ITO deposited by sputtering at RT (RUMP fitting)

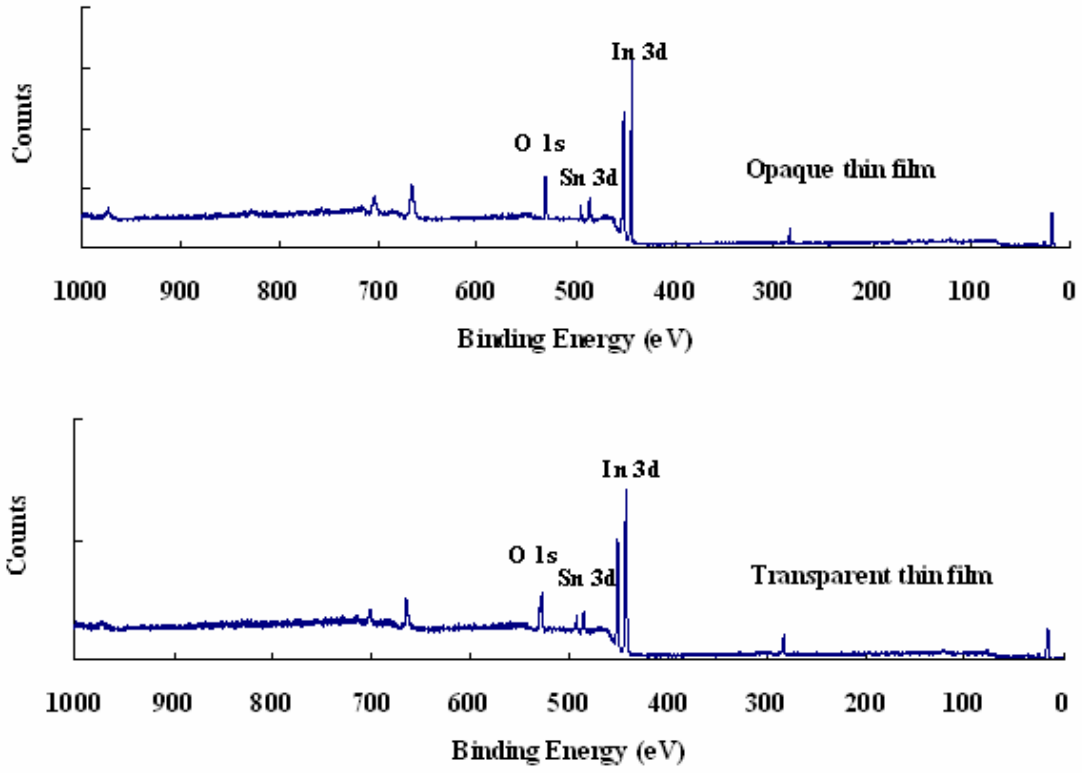

Figure 3-14. XPS spectrums of ITO deposited by electron beam evaporation (upside) and sputtering method at RT (downside)

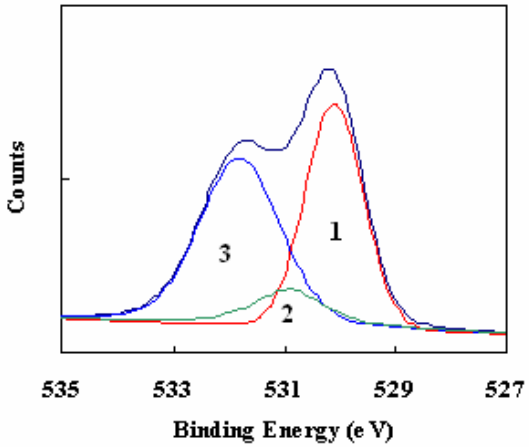

Figure 3-15(a). XPS O 1s spectrum of Figure 3-14 (upside)

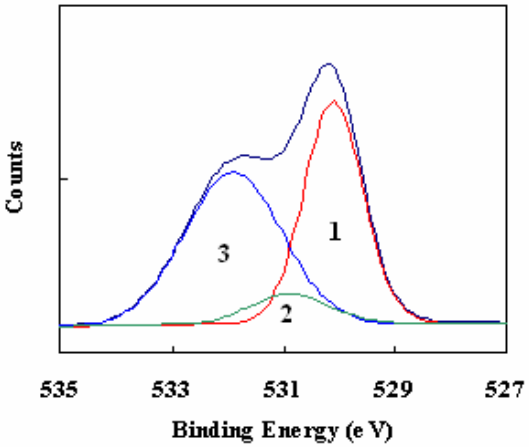

Figure 3-15(b). XPS O 1s spectrum of Figure 3-14 (downside)

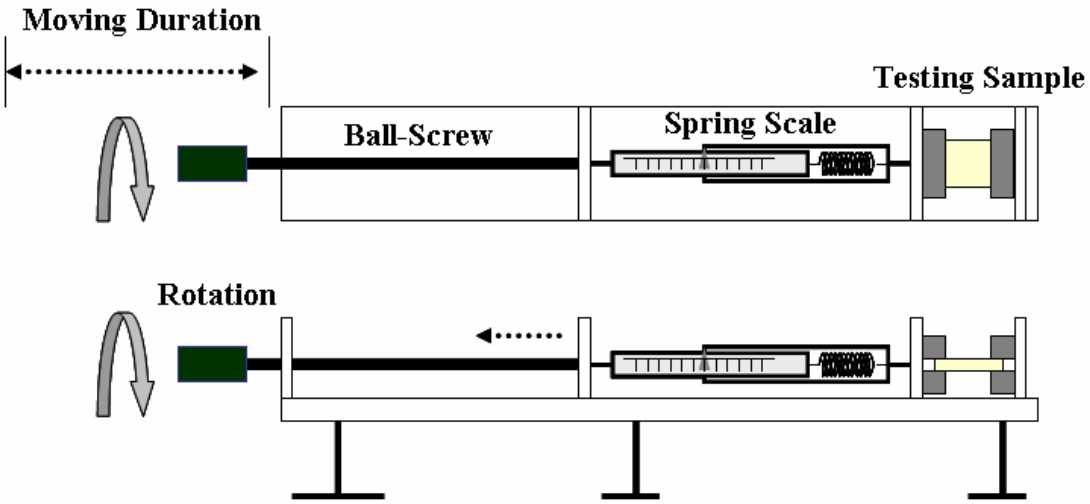

Figure 3-16. A simple mechanical structure designed for tensile loading

Figure 3-17. Cracking of brittle thin film in axial tensile failure

Chapter 4

Ion Beam Surface Treatments and Adhesion Properties

4.1 Introduction

Ion beam can be used for surface treatment with different purposes. The ions that bombard surfaces can arise from both plasmas and ion beams. Upon bombardment, a surface ions may be reflected back, stick or adsorb, scatter, eject or sputter surface atoms, or get buried in subsurface layers or called ion implantation. Surface heating, chemical reaction, atoms mixing, and alteration of surface topography are other manifestations of ion bombardment.

Ion beam energy is critical in defining the nature of the interaction with surfaces by changing the probability of surface sticking and reaction [1]. Thus at kinetic energies less than 10^{-2} eV, the sticking probability, defined as the ratio of the number of deposited atoms to the number of impinging ions, is usually unity; therefore, condensation as well as chemisorption occurs readily. From 10^{-2} to 10^{4} eV, the ion sticking probability decreases, reaching a minimum roughly at 20eV, but thereafter it rises with increasing energy. This is the important sputtering processes occur in this ion energy range. The type of ion implantation is from roughly 10^{4} eV and above to 10^{6} eV, and the sticking probability again increases to near unity as ions are buried beneath the surface. In this range of energies the sputtering probability is small. In addition to ion energy, other important variable include type of ion, the nature of surface as well underlying atoms, and the film or substrate crystallography and texture [2-4].

As a result of ion bombardment, assorted charged particles like electrons, ions, neutrals and photons of varying energies and abundances are emitted from the surface. Contained with them is a rich source of compositional and structural information on surface properties. Therefore, films can be characterized by detecting and analyzing these emitted signals. Several ion beam techniques for achieving these ends like Rutherford backscattering spectroscopy (RBS) was used in this experiment. In this chapter, we focus on the ion beam energy ranged below 2000 eV, and it was regarded as the sputtering process. It was used for surface modification for polymer substrate. It was also used for ion beam assisted deposition used for indium tin oxide deposition by electron beam evaporation and barrier layer deposition at Chapter 6. .

For the ion beam source, when generated within typical glow discharges, ion energies range from a few to a hundred electrons volts. On the other hand, ion beams possessing well-defined, generally higher energies are usually intended for processing in vacuum. For low ion energies (below 1000

eV) specially designed broad beam ion guns are employed. While ion accelerators generate high energy beams. In general, plasmas and low energy ion beams are utilized during film deposition and etching processes. However, high energy ion beams are primarily used for ion implantation, and to a lesser extent for the surface modification.

Ion beam sources have found increasing applications in the past two decades. Initially developed for space propulsion, their value for surface cleaning, etching and thin film deposition was quickly realized. Surface treatment of polymers is important to adhesion improvement and retention of mechanical properties on environment exposure. Chemical and physical treatments, in the form of traditional wet chemical methods or more frequently in the form of a gas phase treatment, can render polymers more compatible with standard adhesives and improve the adhesion of deposited films. Implantation of chemical functional groups, cross linking, thin film deposition, and chain scission can promote chemical compatibility of a polymer surface to an over-layer. Physical roughening can also promote adhesion of both chemical adhesives by increasing surface areas of physically deposited films [5-9].

Techniques used for the cleaning and pretreatment of surfaces have long been recognized as important components of a successful vacuum coating process. Cleaning process is commonly used to increase surface energy of a substrate material, thus improving wetting and adhesion of a deposited film. A variety of pretreatment process exist which can improve adhesion between films and substrate. These techniques are applicable to a wide range of coating applications. Virtually all vacuum deposition process use plasma technologies to achieve beneficial surface effects. The mechanism in which the plasma is generated is different but the effect on surface wet ability is similar. One plasma technique that has shown great promise in the application of surface cleaning and pretreatment is ion beam technology.

Ion beam technology has been successfully applied to the pre-cleaning of a variety of substrates, including glass, metals, and polymers. Numerous literature references relate how pre-cleaning can enhance the adhesion of a deposited film to a substrate, improve wear characteristics, and render a substrate more receptive to a coating [10-12]. These benefits arise from three surface phenomena associated with ion beam treatment. The first one is the removal of residual surface contaminants. Substrate are given mechanical or chemical cleaning treatments prior to vacuum processing. While effective at removing a large portion of possible contaminants, pre-cleaning substrates in vacuum produces a more pristine surface. In vacuum, a cleaned substrate will remain clean for a much longer period of time. Argon and oxygen are commonly used to remove residual surface organics and can be especially useful when applied to polymer substrates. The second effect of ion beam pre-cleaning of substrates is surface roughening. This effect happens most often on polymeric substrate and can be well controlled. Surface roughening increases the surface area of the interface between a coating and substrate, thus yielding better adhesion. The third effect is the chemical

modification of a surface. Ion beam treatment of a surface in vacuum can modify the chemical structure of the surface layers to enhance adhesion. The energy of bombarding species can leave bonds in this surface layer of polymeric material, producing a more reactive surface. The use of reactive gases can functionalize the surface of many materials to increase adhesion to subsequent layers.

In this study, the linear ion source developed and typical ECR ion source were used for surface treatment. The linear ion linear source is kind of gridless ion source technology compared to other ion source. Gridless ion sources can produce ion beams with a wide distribution of ion energies with easy operation and maintenance. The high throughput, broad energy distribution, and ease of operation make gridless ion source technology well-suited to the surface modification of polymers.

4.2 SRIM and TRIM Simulation

SRIM, the stopping and range of ions in solid, is a program which can calculate the stopping and range of ions (10 eV to 2 GeV) into matter using a full quantum mechanical treatment of ion-atom collisions [13]. The calculation is made by the statistical algorithms which allow the ions to make jumps between calculated collisions and then averaging the collision results over the intervening gap. During the collisions, the ion and atom have a screened Coulomb collision, including exchange and correlation interactions between the overlapping electron shells. The ion has long range interactions creating electron excitations and plasma within the target. And TRIM, the transport of ions in matters, is the comprehensive program included in SRIM. TRIM will accept complex targets made of compound materials with multi-layers, each of different materials. It will calculate the final 3D distribution of the ions and also all kinetic phenomena associated with the ion's energy loss, target damage, sputtering, ionization, and phonon production. We used the SRIM and TRIM to simulate when the oxygen and argon ions bombard to the PET surface in the various ion energy, and setup 10000 ions simulated as number. After we setup the ion type and ion energy and the depths, density and compositions of the target, the sputtering yield of each element, energy loss, ions in each direction of the longitudinal range and its collision plots, the ions number of backscattered, transmitted, vacancies were calculated.

First, we used TRIM to calculate the different ion incident angle effects. The ion source we used here has two kinds of mode for ion incident angle. The ECR ion source has been setup to emit ion beam at 45 degree with respect to the surface, and target surface are rotating at the constant speed to receive the uniform ion irradiation. Another is the linear ion source, in general, the ion beam is normal to the target substrate, but we can use the flat-plate type sample holder to adjust the irradiation angle to any degree. We simulated the argon and oxygen ion beam incident angle from 0

degree to 89 degree, and the sputtering yield to incident angle was shown in Figure 4-1. The sputtering yield S(θ) depends on the angle θ defined between the directions of ion incidence and the target normal. In Figure 4-1, the sputtering yield is enhanced relative to S(θ =0) degree that the ratio S(θ)/ S(θ =0) is found to vary as (cos θ)$^{-1}$ for values of θ up to 70 degree, and the maximum sputtering yield occurs near the angle of 70 degree. Physically, shallower collision cascades create a greater density of displaced surface atoms that can be potentially sputtered However, the (cos θ)$^{-1}$ dependence obviously fails at glancing angles approaching 90 degree because the number of ions penetrating the surface drops precipitously. This simulation got the same results with H. Oechsner (1975) [14]. The ECR ion source with 45 degree incident angle, when it compared the linear ion source setup the ion beam normal to the target surface, the sputtering effects was much clearer and it was described later.

Secondly, we used SRIM and TRIM to calculate the sputtering yield of each element. From the foregoing description, the ion energy used in this study was ranged from several hundreds to maximum 1500 eV. When the oxygen and argon ions bombs the PET surface, the sputtering and attachment phenomenon happens on the surface in this range of ion beam energy [15]. And the various ion energy irradiation results in the different sputtering rate of H, C, O and its incident distance were calculated. For the argon and oxygen ions, the sputtering rates ranked from high to low were H, O, C, and it increased corresponding to the ion energy increasing. If we compared the same energy between argon ions and oxygen ions, the sputtering rate of argon ions was bigger than oxygen ions. The third one, we calculated the energy loss of each ion energy irradiation for the calculation of the thermal effect in PET substrate, and it was described in detail later. The last one, we used SRIM to calculate the stopping energy for the density calculation of Rutherford backscattering spectroscopy (RBS) analysis. The incident ions were 2 MeV He^{+2}, and calculated the backscattering ions energy. Then using the kinematic factor for each element in the equation of Appendix RBS, the thin films density can be calculated if the film thickness is known.

4.3 Ion Beam Surface Treatment

Techniques used for the cleaning and pretreatment of surfaces were recognized as important method of a successful vacuum processing, and cleaning process is commonly used to increase surface energy of a substrate material, thus improving wetting and adhesion of a deposited film. A variety of pretreatment process exist which can improve adhesion between films and substrate. Ion beam surface treatment has shown great promise in the application of surface cleaning and pretreatment. Ion beam irradiation provided an elastic collision approximate happens between an incident ion and the substrate surface. Considerable sub- and near surface atomic shuffling may

occur by the momentum pass, this eventually leads to rearrangement of surface atoms. Thus we may expect modification of both surface structure and composition. Ion bombardment of growing films modifies the measurable characteristics of its structure, surface topography and roughness. Ion beam technology has been successfully applied to the pre-cleaning of a variety of substrates, including polymers. how pre-cleaning can enhance the adhesion of a deposited film to a substrate, render a substrate more receptive to a coating. It can remove residual surface contaminants. And roughen the surface for the better adhesion properties. Moreover, ion beam treatment also modifies the chemical structure of surface. If the adhesion can be improved by ion beam treatment between thin film and substrate, it is considerable to remove the adhesive layer usually used. That is the merit for cost effective in the production.

In this experiment, various discharge ion energy was applied in the linear ion source and ECR ion source to modify the PET substrates. Table 4-1 shows the conditions of the sample lists. Linear ion source and ECR ion source were used in this experiment. Argon and oxygen gas were introduced in ion source as the irradiation ion. In the case of the linear ion source, the chamber was pumped to approximate 4×10^{-4} Pa base pressure, then argon and ion gas was introduced in 20 ccm, the working pressure was 5.5×10^{-2} Pa for argon gas and 3.6×10^{-2} Pa for oxygen gas. For the ECR ion source, the chamber was pumped to 3×10^{-3} Pa as base pressure, and introduced argon and oxygen at 8 ccm, then the working pressure was about 2.8×10^{-2} Pa. The ion incident angles to the sample surface were 90 degree for linear ion source and 45 degree for ECR ion source. The incident angle of linear ion source can be adjusted by turning the angle of sample holder described at Chapter 2. Three types of irradiation dose value were applied, and it was 5×10^{15}, 1×10^{16}, and 5×10^{15} ions/cm^2. The ion energy and current density for dose valued and irradiated time can be referred and shown in Table 4-1. After the surface modification of ion irradiation, X-ray photoelectron spectroscopy (XPS) was used to measure the surface chemical structure. Atomic force microscopy (AFM) was used to detect the surface topography and roughness. Scanning electron microscopy (SEM) was used to measure the photography of surface in 1 um scale. At last, the temperature effect of ion beam irradiation was discussed.

4.2.1 Thermal Effects

The PET used in this study is the thermally sensitive material. In this study, either the ECR ion source or the linear ion source has no water or air cooling system for the sample holder. That is the reason why the thermal effects should be considered during the ion irradiation process for the surface modification. One dimension heat conduction equation is given by equation (4-1)

$$\rho c \frac{\partial T}{\partial t} = \lambda \frac{\partial^2 T}{\partial x^2} \quad (4\text{-}1)$$

Here, ρ is the mass density, c is the specific heat, λ is the thermal conductivity, and the heat flux was passing through a unit area in the cross section x in the time t. It was used to calculate the thermal effects diffusing in PET substrate and the stainless steel sample holder. The thermal diffusion was assumed as the homogeneous diffused in the bulk material, and the boundary condition was setup as the start point at the first layer of PET upside surface and end point at the stainless steel downside surface facing to vacuum. At first, we considered the energy passed from the ion beam to the PET surface. PET as the polymer material is the insulator lacking free electron, energy is passing and diffusing by the lattice vibration. When the ions are introduced into the target surface, one part of the energy is lost, and transferred to the lattice vibration. The energy loss of argon and oxygen ions in PET films were simulated by SRIM and TRIM, the energy loss of phonos column, about 39 %, results in the lattice vibration. It was considered as the energy flux for the thermal diffusion in the PET. For example, when argon ion was discharge at 1500 V, the ion energy was about 525 eV and the current density was 90 uA/cm^2 measured at Chapter 2. The ion energy irradiated on surface was about 472.5 W/m^2, and considered about 39 % energy loss as the lattice vibration. The energy flux as the thermal effects was about 184.2 W/m^2 diffusing the PET substrate, and it was the energy considered to contribute in thermal effect.

In this experiment, The PET films were attached on a 1 mm thickness stainless steel. The specific heat and density of PET and stainless steel are 1050 J/K Kg, 1400 Kg/m^3 and 500 J/K.Kg, 7900 Kg/m^3, respectively. After the calculation, the thermal effect resulted in the temperature increase is shown in Figure 4-2, When the 1500 discharge voltage and irradiated time 550 sec, the increased temperature was about 27 ℃. If the room temperature is 26 ℃, and the simulated maximum temperature is about 53 ℃. It is below the glass transition temperature (78 ℃) of the PET used in this study. We did the testing for the actual temperature by posting the 80 ℃ and 100 ℃ thermal testing sheets, the color was not changed after the irradiation process. The simulation model we used was a simple model here, so it cannot be used to expect the precise prediction of thermal process. Compared to the PET substrate and stainless steel sample holder, stainless steel has high heat conductivity. It means the stainless steel holder is like a source of cooling and acts as a heat sink that withdraws heat form the PET films.

4.2.2 Surface Chemical Analysis

X-ray photoelectron spectroscopy (XPS) was used to analyze the surface chemical condition after the ion modification. The principle and introduction of XPS was described at Appendix XPS part.

AXIS 165S (Shimadzu) was used for the XPS analysis, and the X-ray was monochromatic Al, K α (1486.6eV). X-ray anode voltage was 14 KV, and the emitting current was 10 mA. The sample was measured in two different kind of mode: wide mode at 80 eV and narrow mode at 20 eV. The wide mode was for calculating the composition of each element on the surface, and the narrow mode was used to compare the modification of each element after the peak fitting. In the narrow mode measurement, the O 1s peak was ranged from 523 eV to 543 eV and C 1s peak was from 280 eV to 300 eV. Figure 4-3 shows the XPS spectrum of PET film surface without any modification, and Figure 4-3(a) is C1s spectrum including the three fitted peaks. Figure 4-3(b) shows the spectrum of O1s with two fitting peaks. Figure 4-4 shows PET $C_{10}H_8O_4$ chemical structure composed of the benzyne, ester and methylene parts, and the different types of carbons, oxygen and hydrogen atoms. As Figure 4-4 shows, there are four kinds of carbon in PET chemical structure, it was, C1, ester bonded to benzyne, C2, carbons in benzyne without bonding to ester, C3, carbon methylene bonded to oxygen atom, and C4, carbon atom in ester. And two kinds of oxygen atoms, it were O1 carbonyl oxygen atom, and O2 ester oxygen atom. The energy shift of C1 and C2 was thought too small, so we combined it in one peak and totally fitted three peaks in C1s spectrum, and two peaks in O1s spectrum.

In the wide mode, with the relative sensitivity factors (S_n), the relative atomic concentration of any chosen element A, can be obtain from

$$C_A = \frac{I_A / S_A}{\sum_n (I_n / S_n)} \qquad (4\text{-}2)$$

C_A is the concentration of element A. Here, the software named VISION, included in the XPS controlling system, can analyze the each element composition of XPS spectrum measured in wide mode. However, we used the atomic sensitivity factors and the peaks area in equation (4-2) to calculate the composition of each element included in PET films. The atomic sensitivity factors of C 1s and O 1s are 0.296 and 0.711, respectively. Using this sensitivity factor and peak area subtract background line, the various composition of each element in the PET films can be calculated. For quantitative analysis of polymer spectra, it is better to use straight line background, and it provided some care is taken to ensure consistent application like the choice of start point and end point [16]. Figure 4-5 (a) and (b) show the experiments results of carbon and oxygen relative concentration changed in the different discharge voltage of the linear ion source, when the radiation dose value was 1 x 10^{16} ions/cm^2. From Figure 4-5, it indicated that the irradiation ion energy increased, either in argon ions or oxygen ions irradiation, the C 1s concentration went up and O 1s concentration down. In argon ions irradiation conditions, the C 1s to O1s ratio of PET without irradiation was about 70 % to 30 %, and it became to 85 % to 15 % approximately at 1500 V discharge. However, in oxygen ions irradiation condition, O 1s concentration went down slowly, and it reached to 78 %

to 22 % at the same discharge. The oxygen composition to carbon under oxygen ion was better than argon ion irradiated. The oxygen ion injection and some attachment occurred that increased the O 1s concentration was one of the reasons considered for this phenomenon [17, 18]. It will be discussed in more detail later.

Before comparing the modification effect detected from XPS spectrum for C 1s and O 1s peaks, we used the SRIM and TRIM software to simulate the conditions used in this experiment, and 10000 ions was simulated. The ion energy range in this experiment was considered as the sputtering effect for the surface modification. When the ion impact establishes a train of collision events in the target, leading to the ejection of a matrix atom, it is regarded as sputtering. Since sputtering is the result of momentum transfer it has been aptly likened to the atom pool where the ion breaks up the close packed rack of atoms, scattering some backward. The sputter yield S is defined as number of sputtered atoms divide incident particle. And it is a measure of the efficiency of sputtering. Here, we used TRIM software to simulate the sputtering yield and the longitudinal distance when the oxygen and argon are injected into the surface. Figure 4-6(a) and 4-6(b) show the sputtering yield when the argon and oxygen ion to hydrogen, carbon and oxygen atoms at the different ion energy.

For the sputtering yield by either argon ions or oxygen ions, the carbon, hydrogen and oxygen are ranked from high sputtering yield to low. It was considered that PET chemical structure composed of 10 carbon atoms, 8 hydrogen atoms and 4 oxygen atoms, and the value of atoms from high to low was the same as the sputtering yield ranking. If we compare the sputtering between argon ion and oxygen ion at the same ion energy to the same atom, the sputtering yield of oxygen ion is better than argon ion. Oxygen ion has the lighter mass quantity than argon ion. When they are speeded up to with the same energy, the oxygen ion has higher speed than argon ion. And that was reason why oxygen ion has higher sputtering yield than argon yield averagely. Figure 4-7 shows one example of simulation result as the 10000 oxygen ions of 1000 eV ion energy impinged to the PET surface, and all effects happened about 20 nm from the surface. Figure 4-8 shows simulation result of 10000 argon and oxygen ions impinged to the PET surface from 100 eV to 2000 eV ion energy, the longitudinal distance to the different ion energy. It indicated the interaction between incident ions and atoms happened in 10 nm distance from surface with the atoms. The distance also increased by the simulation ion number or the irradiation dose increased.

Figure 4-9 to Figure 4-14 show the C 1s and peaks fitting result of PET modified by the linear ion source. Figure 4-15 to Figure 4-17 show O 1s spectrum and two peaks fitting. It was clearly observed, for the C 1s spectrum, the peak 2 and peak 3 in C 1s spectrum decreased depending on the discharge voltage increased. And for the O 1s spectrum, two peaks in O 1s spectrum decreased when the irradiated ion energy increased. Moreover, the peak 2 of O 1s decrease sharply relative to peak 1. For the irradiation time effects, either C 1s or O 1s, for the peaks relatively ratio, it seemed difficult to recognize the apparent change when the irradiation dose increased. When we did the

quantitative analysis to compare the ratios of each peaks area, Figure 4-18(a) shows the three carbon peaks relative modification, and Figure 4-19(b) the change of two oxygen peaks. In Figure 4-18, peak 2 and peak 3 areas were calculated and normalized as the peak 1 was 1. The associative value to the discharge voltage of linear ion source should be carefully to evaluate, according to the real irradiated ion energy which was approximately 35 % of discharge voltage. In other words, when the discharge voltage was 1500 KV, the irradiated ion energy was about 525 eV. Firstly, we compared three peaks in C 1s spectrum, relative to peak 1, the peak 2 ratio went stable in oxygen ions and decreased a little in argon ions, and peak 3 went down then stabilized in both oxygen ions and argon ions. Then we compared two peaks in O 1s spectrum, the peak 2 went down first, then became unstable for argon ion and seemed to go up in oxygen ions. In conclusion these peaks displayed a trend and their chemical bonding associated with peak 3 of C 1s was carbon in easter, and it bonded to two oxygen affecting the two peaks in O 1s spectrum.

When the ion irradiation started and at the low energy, it was thought as the cleaning effect for surface. After the impurity attached on the surface was sputtered out, the atoms included in PET surface was bombarded and sputtered. From the sputtering yield point of view, carbon and hydrogen has high sputtering rate, it was considered that the methylene bonded to oxygen moved out earlier, it affected the peak 2 of C 1s and O 1s decreased, specially have in O 1s case. At the same time, the benzyne also composed of carbon and hydrogen also high sputtering yield that was the reason considered why peak 2 of C 1s went down, but the slope was smaller than the peak 2 in O 1s. Depending on the irradiated ion energy increase, the bonding cut-off, and benzyne, ester and methylene parts split out more. However, in the meantime, the dissociated parts re-bonded. That was considered as the reason why the second 2 of O 1s become unstable in argon ion, but increased in oxygen ion. It was much cleaner when we used the ECR ion source with much higher ion energy.

The ECR ion source irradiation was compared to the linear ion source, and the accelerated voltage was set at 500 V, 1000 V and 1500 V. The ion energy was bigger than the linear ion source. Figure 4-19 shows the C 1s spectrum modification by ECR ion source, it was obvious to find the peaks become small, and the second, peak 3 was apparent, especially for peak 2. Figure 4-20 shows the O 1s spectrum changed under the irradiation by ECR ion source, the peak became smaller, and peak 2 also decreased more than peak 1. Figure 4-21(a) and 4-21(b) show the carbon to oxygen ratio comparison when ion energy increased from 500 eV to 1500 eV. It was the same as the linear ion source, following the ion energy increasing, the carbon concentration went up and oxygen ratio went down. The ratio of 500 eV ECR ion source argon ion was 81 % (carbon) to 19 % (oxygen), and 1500 V (about 525 eV) linear ion source argon ion was 84 % (carbon) to 16 % (oxygen). In oxygen ion case, the 500 eV ECR ion source ions had 75 % (carbon) to 25 % (oxygen) results, and 525 eV linear ion source had 78 % (carbon) to 22 % (oxygen). It showed that these two ion sources had the same results and relative. When the irradiation ion energy increased, the carbon

concentration compared to oxygen increased It was considered that when the surface structure was modified by ion and sputtering, the disconnected bonded and re-bonded occurred as the breakage –reunion reaction. When the bonding with oxygen is disconnected, oxygen atoms become ions, it re-bonded with other parts or become oxygen from surface to vacuum, but carbon ions or atoms kept on dissociating on the surface. It may be the reason why the carbon concentration increased and oxygen decreased. The average of oxygen to carbon ratio was higher when we compare the oxygen ion irradiation and argon ion. It is thought that the oxygen ion injected has much higher possibility to re-bond in ester or with methylene, and become the part stable structure of PET.

The Figure 4-22 shows the peaks ratio changes in C 1s and O 1s spectrum under ECR ion source. Figure 4-23 shows the three peaks in C 1s and two peaks in O 1s modified effects that we mapped from the results of linear ion source compared with ECR ion source. In C 1s spectrum, the ratio of peak 2 to peak 1 was roughly stable, and the peak 3 went down and became stable. The peak 3 ratio increased when 1000 eV and 1500 eV oxygen ion was irradiated, it was regarded as the re-bonded effect of oxygen in ester. The same situation also happened at O 1s, the peak 2 of O 1s increased at 1000 eV and 1500 eV, and this trend seemed to indicate the ratio of peak 1 and peak 2 approached to equal and stable. It means that the much higher energy oxygen ion irradiation contribution the oxygen re-bonded and formed the more stable ester structure. However, it cannot be clearly observed at argon ion irradiation. When the argon ion energy was increasing, the sputtering effect became more active, and the disconnected and re-bonded reaction happened much frequently and random. That was the reason considered why peak 2 of O 1s was unstable and went up and down.

Finally, we did not find the significant difference when we extend the irradiation time. Figure 4-24 shows four TRIM simulations at 1 KeV argon ions and oxygen ions at 10000 and 100000 counts. It showed the effective area become larger and deeper when the ions number increased to 10 times, but the difference was not so obvious. The XPS spectrum has detected the chemical structure modification 4 nm on surface. Therefore, it is probable that the chemical structure change and modification were not so different when the same ion energy irradiation applied.

4.2.2 Surface Topography Analysis

Atomic force Microscopy (AFM) and scanning electron microscopy (SEM) was used to detect the surface topography condition in nm scale and um scale after the ion modification. The principle and introduction of AFM was described in detail at Appendix. The AFM used in this experiment is NanoScope Ⅲ (Digital Instruments), and SEM is S-4500 type with the resolution from 1.5 nm at 15 KV accelerated voltage and 40 nm at 1 KV accelerated voltage. PET film is a soft substrate. We attached it on the silicon substrate by the instant adhesive before measured by AFM. Figure 4-25 to

Figure 4-32 show the 3-D AFM image of the surface modified by the argon ions and oxygen in the various ion irradiation conditions. From the AFM measured data, we can calculate the root mean square (RMS) roughness of each measured surface. Figure 4-35 shows the RMS roughness change depending on the various argon ions and oxygen ion dose irradiations. In the case of oxygen irradiation, the surface became rougher after the oxygen ion irradiation, and the RMS roughness increased before 1000 V discharge, then the surface went much rougher with increasing ion irradiation time and discharge. For the samples modified by argon ions, the RMS roughness increase when the ion dose value and discharge is below 1000 V. When the irradiation time is extended, the RMS roughness become smaller, and the surface become flat. In addition to AFM detecting the nm scale of the topography on surface, we also used the SEM to detect the um to nm scale of the surface topographical image after the ion irradiation. Figure 4-33 and Figure 4-34 show the SEM photo of PET before and after the 1500 KeV irradiated by ECR ion source. It indicated the surface became rougher totally [19].

The range of ion beam energy used was considered have the sputtering effects to the surface, in either oxygen ion or argon ion. At the initial stage of the ion irradiation, the impurity attached on the surface like the carbide, was sputtered out, and it was regarded as a cleaning effect on the surface. Accordingly, the removal of impurity originally attached on the surface make the surface become rougher at AFM detecting photo. After the impurity attached was moved out, the sputtering effect was occurred the higher part of the surface topography, the numerous hills on the surface was shoveled, and the surface became flatter. However, by increasing the ion irradiation time, the sputtering effects start to roughen the surface gradually. And it was obviously observed at the oxygen ion irradiation.

4.3 Adhesion testing

The use of thin films have been in a variety of electronic, engineering, optical, biomedical, nuclear, space, and other applications. Whatever the use maybe be, the properties, structure, functional characteristics, and performance are all related to the adhesion between the coating and the substrate. Adhesion determines the durability of thin film devices, for example, in electronic circuits, and it affects the durability and longevity of thin films. They are largely dependent on their adhesion to the substrate since this determines the ease of removal. Moreover, adhesion is also a fundamental parameter in surface chemistry and physics because it depends directly on intermolecular forces. After the ion irradiated modification of PET, the surface chemical and physical roughness was measured, and the adhesion was tested in this section. A comprehensive review of the various methods for the measurement of adhesion of thin film is presented. Most of

the methods catalogued in this review have been harnessed in measuring the adhesion of thin evaporated or sputtered thin films on an assortment of substrates [20]. The methods of determination of adhesion are discussed under three headings: Nucleation methods, mechanical methods and miscellaneous techniques. Furthermore, the mechanical methods are categorized depending on the mode of application of the force to disrupt the interface [21]. The principle, merit, potentiality, and limitation of each technique are outlined, and the difficulty associated with measuring adhesion strengths and their relationship to basic adhesion is different.

The adhesion is related to the nature and strength of the binding forces between two materials in contact with each other. The forces could be either primary valence type or pseudo primary valence type. But this basic definition of adhesion is not very helpful as it is not possible either to calculate the magnitude or to measure such adhesion forces in practical system. More common terms for this are “bonding strength” or “adhesion strength”. Experimentally, adhesion can be measured in two ways: (a). in terms of the forces, defining the force of adhesion as the maximum force per unit area exerted when two materials are separated, and (b). alternatively, in terms of work or energy, defining the work of adhesion as the work done in separating or detaching two materials from one another. When we considered the measurement of adhesion, the mechanical method was selected from the three main method described. For the mechanical method, all mechanical method use some means of removing the film from the substrate. It also has some different way to approach, and can be broadly classified into two categories depending on the mode of detachment of the film. First is the method involving detachment normal to the interface, and the second one is involving the lateral detachment of the film from the interface. The methods involving detachment normal to the interface include direct pull-off method, moment or topple method, ultrasonic method. The methods based on the application of lateral stresses for detachment comprise scotch tape method, peel test, tangential shear or lap shear method, scratch or stylus method and blister method. The scratch or stylus method was used in this study to measure the adhesion between the PET and thin films [22].

The scratch testing is frequently used to assess the behavior of thin films under the influence of an applied load. In particular, scratch testing can be used to assess coating adhesion when this is the failure mode occurring. Essentially, in this test, a diamond tip is drawn across the film surface, and a vertical load, applied to the point, is gradually increased until the film is completely removed resulting in a clear marking. The critical load at which the clear track is formed is taken as a measure of adhesion. The onset of adhesion failure is normally identified through subsequent examination of the surface by optical microscopy, or by continuously monitoring the frictional force or acoustic emission. Heavens and Collins were the first to use this test to study quantitatively the adhesion of thin evaporated metallic films on glass and the effect of chromium inter-layers. Weaver and Hill studied the increase in adhesion of aluminum films to glass by pre-deposition of films of chromium. They also used the load necessary to strip the film completely as measure of adhesion.

Benjamin and Weaver (1960) analyzed the scratch test in detail and derived some simple equations to convert the critical load into numerical values for adhesion [23, 24]. A capsule description of their analysis and findings is given below. A detailed analysis showed that action of the point always involved plastic deformation of the substrate and this deformation produces a shearing force at the film substrate interface around the rim of the indentation produced by the point, and a simple relationship between the applied load and the shearing force was developed, so that adhesion could be calculated as a shearing force. Referring to Figure 4-36, it showed the forces acting on the spherical point. W is the load on the point of radius r, F is the shearing force per unit area due to the deformation of the surface and a is the radius of the circle of contact. P is similar to a uniform hydrostatic pressure acting normal to the surface of the indentation and can therefore be taken as the indentation hardness of the substrate material. From the triangle of forces, ABC, shown in the Figure 4-36:

$$F = P\tan\theta = \frac{aP}{\sqrt{r^2 - a^2}} \tag{4-3}$$

Where $a = \sqrt{\frac{W}{\pi P}}$ (4-4)

Where W is the critical load, r is the radius of the tip, and F is the shearing force per unit area due to the deformation of the surface, a is the radius of the circle of contact, and P is the indentation hardness of the substrate material. Benjamin and Weaver found (1) the measured load became constant for film thicknesses exceeding a certain value; this value was close to 80 nm. For thinner films a slightly smaller load was required and thy surmised that this could be attributable to film structure and it was no innate weakness of the method. The measured thin films were over 80 nm in this study. (2) The load did not depend directly on the mechanical properties, hardness, elasticity or tensile strength of the film as the load did not vary with the thickness of the film. (3) The load depended on the nature of both the film and substrate, without being directly attributable to the mechanical properties of either. From these observations they concluded that the load is determined essentially by the properties of the interface.

The micro scratch tester is the instrument used for characterizing the adhesive properties [25-27]. The technique involves generating a controlled scratch, with a diamond tip, on the sample under test. The tip, either a Rockwell C diamond or a sharp metal tip, is drawn across the coated surface with a constant or progressive load. At a certain critical load, the coating will start to fail. In this research, SST-101 (Shimadzu) was used and its schematic was shown in Figure 4-37. A ball-type of the diamond stylus is installed on a cantilever, and it contacted the target sample during the detection. The cartridge body was started by the forced vibration as the constant amplitude. When the diamond stylus doesn’t contact the surface yet, there is no relative movement between the stylus

and cartridge body. While the diamond stylus starts to contact the surface, the relative motion occurs between the stylus and the cartridge body. Once the relative motion occurs, the magnet sensors located in the cartridge works, and results in the potential difference of the coil. This voltage difference was used to detect the movement between diamond stylus and cartridge body. During the measurement, the cartridge body keeps on moving downward to the target surface gradually, and the normal loading of the diamond stylus on the target become bigger. The adhesion increases, when the normal direction to the surface loading is increased. Finally, the vibration of the stylus stops and the thin film on the surface was scratched off. The critical loads are detected precisely by means of the sensors attached to the indenter holder.

In this experiment, 15um diamond stylus was used, cantilever and stylus loading speed was 1um/sec, forced vibration amplitude was 100um and stage feeding speed was 20um/s. Figure 4-38 shows a microscopic image of scratching mark of the ITO thin film on PET substrate after scratch test, and Figure 4-39 and 4-40 show the graph of cartridge output to output loading and the distance. The detaching point loading shown in Figure 4-39 was thought as the point when the film started to detach. After the line of detachment, the slope of output voltage to loading changed abruptly, and the marking in Figure 4-38 varied suddenly when the thin film was peeled off after the detaching points. Then we can use the output loading to compare the adhesion of each sample. However, they cannot be applied to compare directly the output loading of thin films on the different kinds of substrates, according to the hardness of substrates are totally different referring to equation (4-2). Glass and silicon has the high value of hardness compared to polymer PET films. The Vickers hardness (HV) of glass, silicon and PET film were measured by micro-hardness tester. The HV values of silicon, glass, and PET film were 860, 626 and 31.

Figure 4-41 shows the scratch testing output loading of the various modification samples used in this experiment. The deposited thin film was ITO layer with 150 nm thickness. The result indicated when linear ion source discharge at 1000 V discharge and the oxygen ions of 5×10^{16} ions/cm^2 dose irradiation had the largest adhesion measured among all samples, and this adhesion was nearly 1.8 times compared to the sample without any ion irradiation. From AFM image, it was inferable this topography of surface was modified to be the numerous and sharp mountains, and totally deposited area extended. It was considerable for the enhancement of adhesion. According to mechanical theory, adhesion occurs by the penetration of adhesives into pores, cavities, and other surface irregularities of the surface of the substrate. A positive contribution to the adhesive bond strength results from the mechanical interlocking of the adhesive and the surface. While the surface does become rougher by mechanical interlocking, it is believed that changes in physical and chemical properties of the surface increase an adhesive strength.

4.4 Conclusions

For the ion beam treatment, ion beams can be used for two different purposes, directly alter the surface composition of the material [28], or to sputter off target species which are then deposited on the surface. The latter one was not dealt with in this chapter. Ions are energetic species with a high momentum and relatively low mean free path, due to their mass. Therefore they strongly affect surface composition, leading to extensive chemical modification and surface topography.

In this chapter, the linear ion source was used to modify the PET surface by discharge voltage from 500 V to 1500 V, and ECR ion source was used as a comparison. At the range of ion energy used was regarded as the cleaning and sputtering mainly. The sputtering yield and the different incident angle of argon and oxygen ion in the various conditions were simulated by SRIM and TRIM software. The XPS analysis indicated the chemical structure of the PET was modified, the carbon to oxygen concentration increased depending on the ion energy increasing. It indicates that the bonding was cut off by irradiated ion, the carbon remained on surface, but the oxygen went into the vacuum. For the ester, benzyne, methylene structure in PET chemical structure, the ester bonding was disconnected and re-bonded when we increased the irradiated oxygen ion energy, and it was detected both at XPS spectrum of C 1s and O 1s.

For the modification of surface topography by ion irradiation, the AFM and SEM were used to detect the surface graphitization and RMS roughness. The surface became flatter and rougher depending on its energy and irradiation time. The average RMS roughness was located in the range of 1.5 nm to 3.5 nm. The oxygen ions irradiation achieved rougher surface than argon ions. Finally the adhesion between the ITO thin films and PET surface was measured by the micro-scratch testing. In all samples, the maximum adhesion occurred at the sample after the oxygen at 5 x 10^{16} ions/cm^2 dose irradiation, and the loading in scratch testing measured had 1.8 times value when it compared to the surface without ion irradiation.

References

1. J. W. Mayer, E. Rimini, "Ion Beam Handbook for Material Analysis" (1977)
2. J. R. Tesmer, M. Nastasi, "Handbook of Modern Ion Beam Materials Analysis", 37 (1995).
3. P. Mazzoldi, G. W. Arnold, "Beam Modification of Materials, 2”, (1987).
4. L. C. Feldman, J. W. Mayer, "Fandamentals of Surface and Thin film Analysis" (1986).
5. J. Ge, J. K. Kivilahti, J. Appl. Phys. 92 (6), 3007-3015 (2002)
6. S. Kim, K. J. Lee, Y. Seo, Lamgmuir 20, 157-163 (2004)
7. J. M. Burkstrand, J. Appli. Phys. 52 (7), 4795-4799 (1981)

8. D. Y. Shih, N. Klymko, R. Flitsch, J. Parazczak, S. Nuces, J. Vac. Sci. Technol. A9 (6), 2963-2974 (1991)
9. K. L. Mittal, J. Vac. Sci. Technol 12 (1), 19-25 (1976)
10. J. N. Shou, A. Rar, D. Otte, J. A. Barmard, J. Appl. Phys. 88 (4), 1880-1885 (2000)
11. S. H. Kim, S. W. Na, N. E. Lee, Y. W. Nam, Y. H. Kim, Surf. Coat. Technol. 200, 2072-2079 (2005)
12. K. W. Park, A. Ruoef, J. Adhesion Sci. Technol. 4 (6), 465-474 (1990)
13. http://www.srim.org/.
14. H. Oechsner, Appl. Phys. 8, 195 (1975)
15. J. B. Malherbe, Crit. Rev. Solid State Mat. Sci. 19 (2), 55, (1994)
16. D. Briggs, “Surface Analysis of Polymers by XPS and static SIMS”, Cambridge Uinversity (1998)
17. B. D. Silverman, J. W. Bartha, J. G. Clabes, P. S.Ho, J. Poly. Sci. A 24, 3325-3333 (1986)
18. J. S. Gwang, C. G. Jhun, J. C. Kim, T. H. Yoon, J. Appl. Phys. 96 (1), 257-260 (2004)
19. S. Kim, K. J. Lee, Y. Seo, Langumir 20, 157-163 (2004)
20. C. Weaver, J. Vac. Sci. Technol. 12, 1, 18-25 (1975)
21. K. L. Mittal, Electrocomponent Science and Technology, 3, 21-42 (1976)
22. Tribology International 39, 61 (2006)
23. P. Benjamin, C. Weaver, Proc. Roy. Soc. A, 254, 163-176 ((1960)
24. P. Benjamin, C. Weaver, Proc. Roy. Soc. A, 254, 177-183 ((1960)
25. S. Benayoun, J. J. Hantzpergue, A. Bouteville, Thin Solid Films 389, 187-193 (2001)
26. J. Ye, N. Kojuma, K. Ueoka, J. Shimanuki, J. Appl. Phys. 95, 7, 3704-3710 (2004)
27. J. Qi, C. Y. Chan, I. Bello, C. S. Lee, S. T. Lee, J. B. Luo, S. Z. Wen, Surface and Coatings Technol. 145, 38-43 (2001)
28. P. Siohansi, Thin Solid Films, 118, 61(1984)

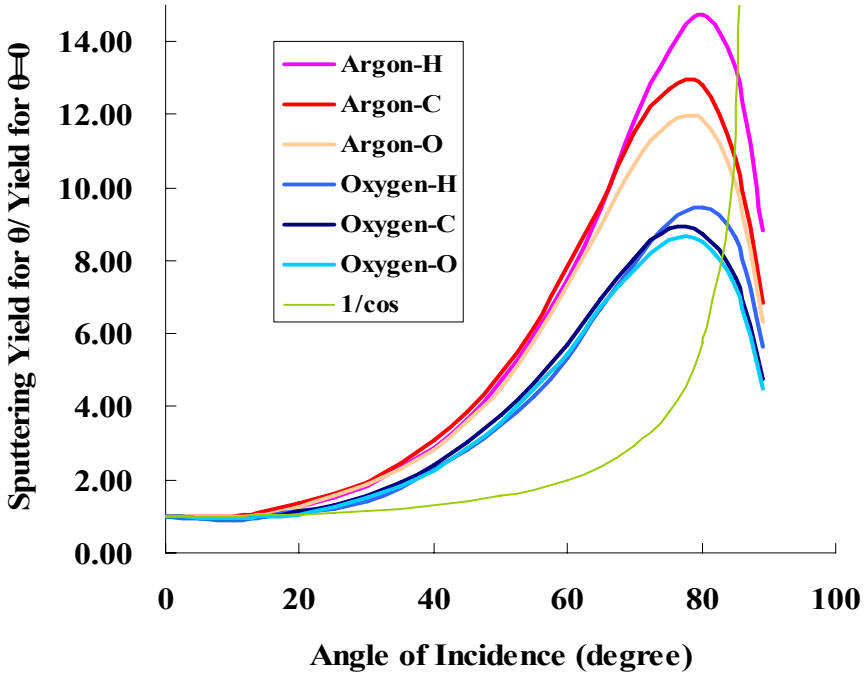

Figure 4-1. Sputtering yield depending on different ion incidence

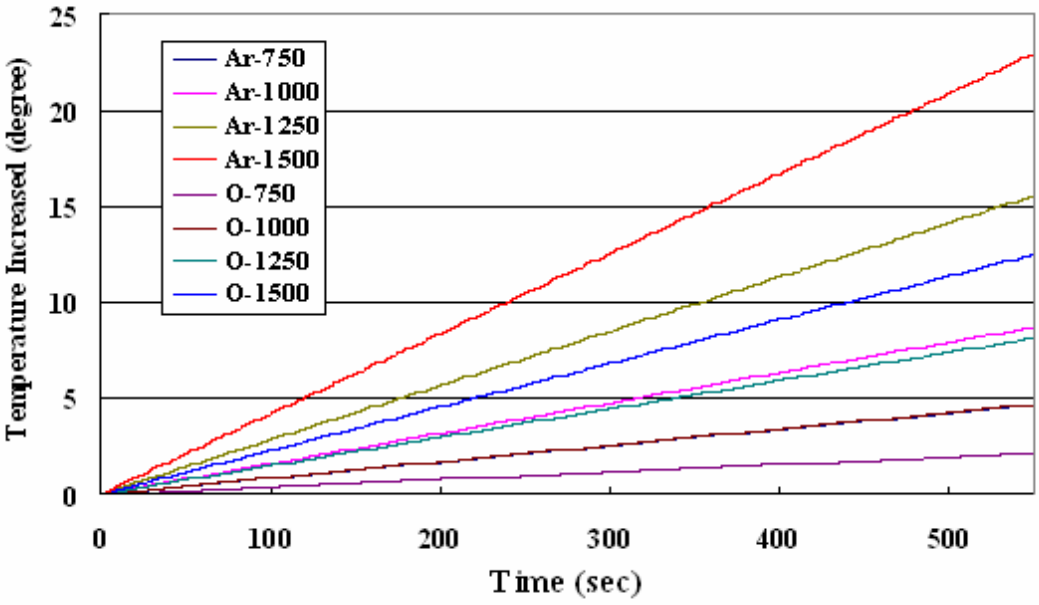

Figure 4-2. Temperature increase calculated by irradiated time

Table 4-1.

Samples list and its various irradiation conditions

Sample No.	Ion Source	Ion Gas	Discharge Voltage (V)	Incident Angle (°)	Ion Energy (eV)	Current Density (uA/cm^2)	Irradiation Dose ($Ions/cm^2$) and Time (sec)		
							5×10^{15}	1×10^{16}	5×10^{16}
1	LIS	Argon	750	90	263	32.3	25	50	248
2	LIS	Argon	1000	90	350	45	18	36	178
3	LIS	Argon	1250	90	438	64.2	13	25	125
4	LIS	Argon	1500	90	525	79	10	20	101
5	LIS	Oxygen	750	90	263	15.3	52	105	524
6	LIS	Oxygen	1000	90	350	25.2	32	64	318
7	LIS	Oxygen	1250	90	438	35.2	23	46	228
8	LIS	Oxygen	1500	90	525	45.2	18	35	177
9	ECR	Argon	500	45	500	6.4	125	250	1252
10	ECR	Argon	1000	45	1000	9.3	86	172	861
11	ECR	Argon	1500	45	1500	10	80	160	801
12	ECR	Oxygen	500	45	500	6.5	123	246	1232
13	ECR	Oxygen	1000	45	1000	10	80	160	801
14	ECR	Oxygen	1500	45	1500	11	73	146	728

LIS: Linear Ion Source

ECR: Electron Cyclotron Resonance Ion Source

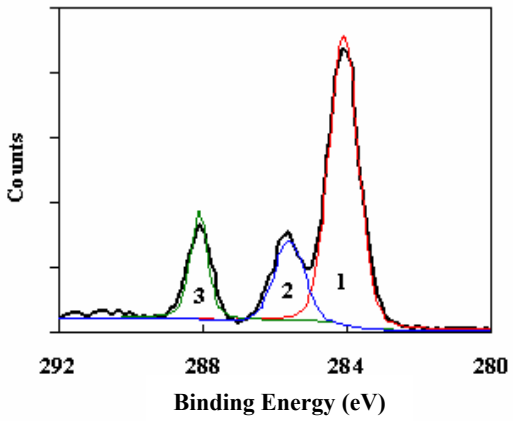

Figure 4-3(a). XPS C 1s spectrum of PET (Without ions treatment)

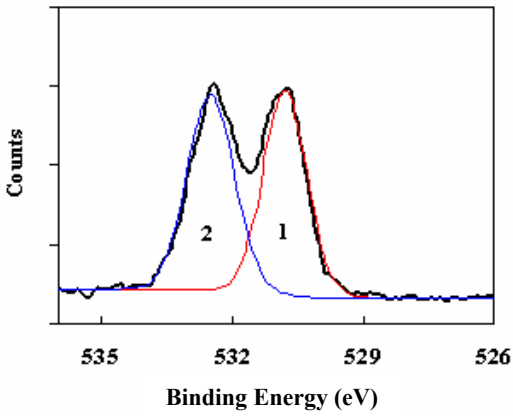

Figure 4-3(b). XPS O 1s spectrum of PET (Without ions treatment)

C1 - Ester bonding to Benzyne
C2 - Carbons in Benzyne, not bonding to Ester
C3 - Carbon in Methylene bonding Oxygen
C4 - Carbon in Easter

O1 - Carbonyl Oxygen atom
O2 - Ester Oxygen atom

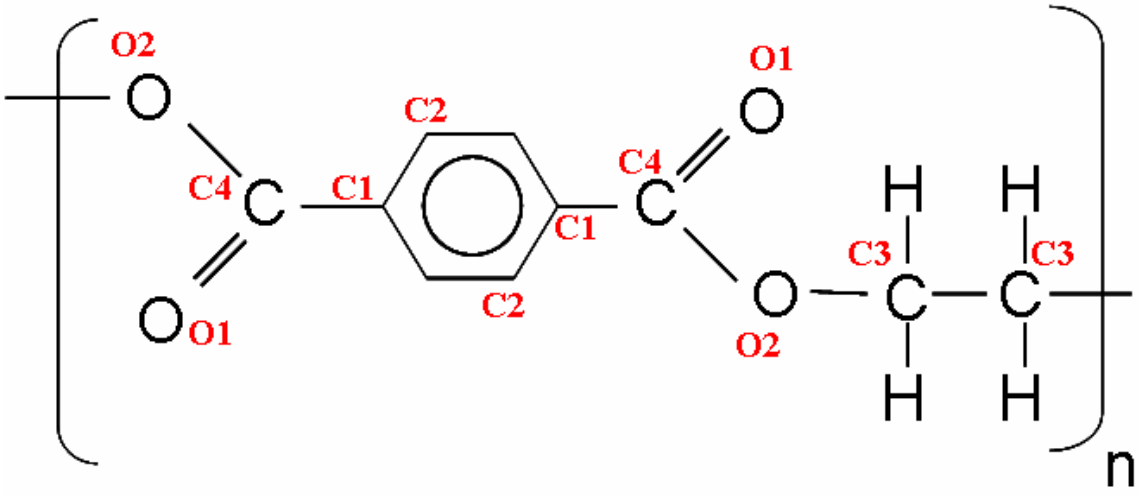

Figure 4-4. PET chemical structure and different bonding

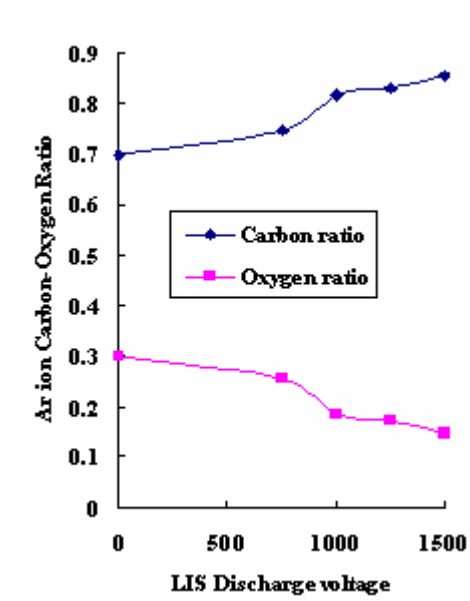

Figure 4-5(a). C 1s to O 1s ratio (Ar ions)

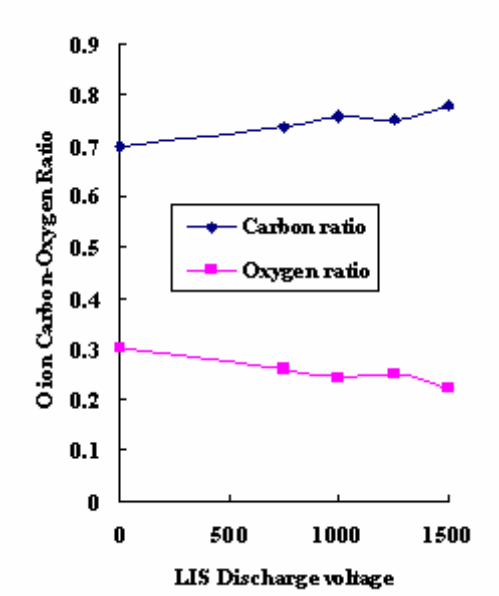

Figure 4-5(b). C 1s to O 1s ratio (O ions)

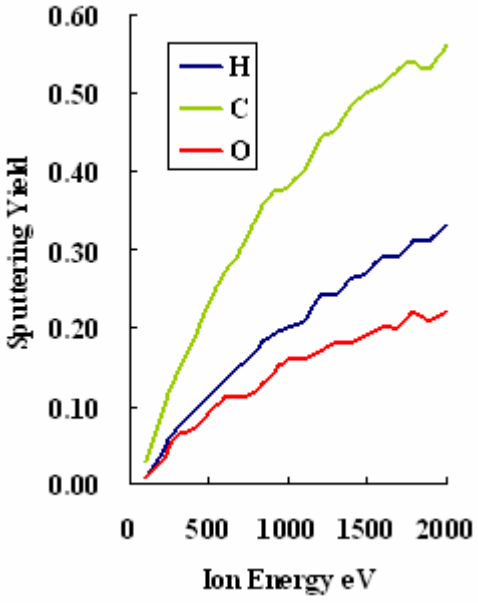

Figure 4-6(a). SRIM simulation of sputtering yield. (Ar ions)

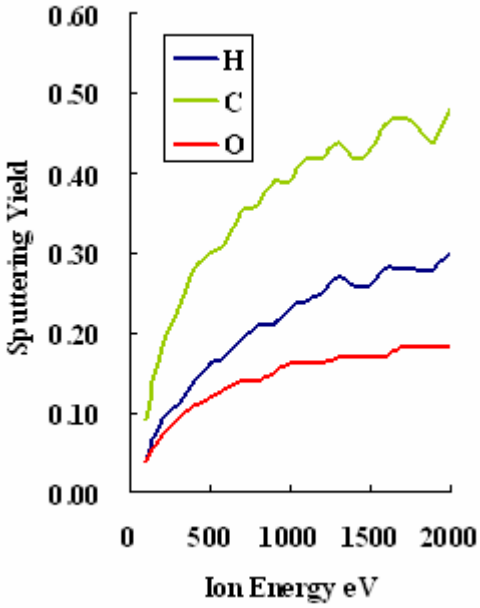

Figure 4-6(b). SRIM simulation of sputtering yield. (Oxygen ions)

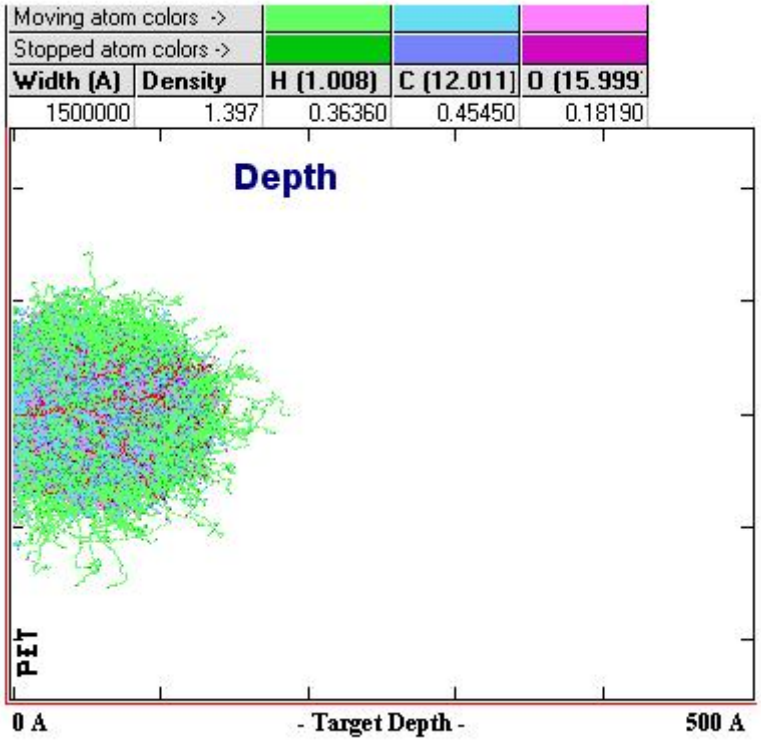

Figure 4-7. TRIM simulation of 10000 oxygen ions (1000 eV) impinged to PET films

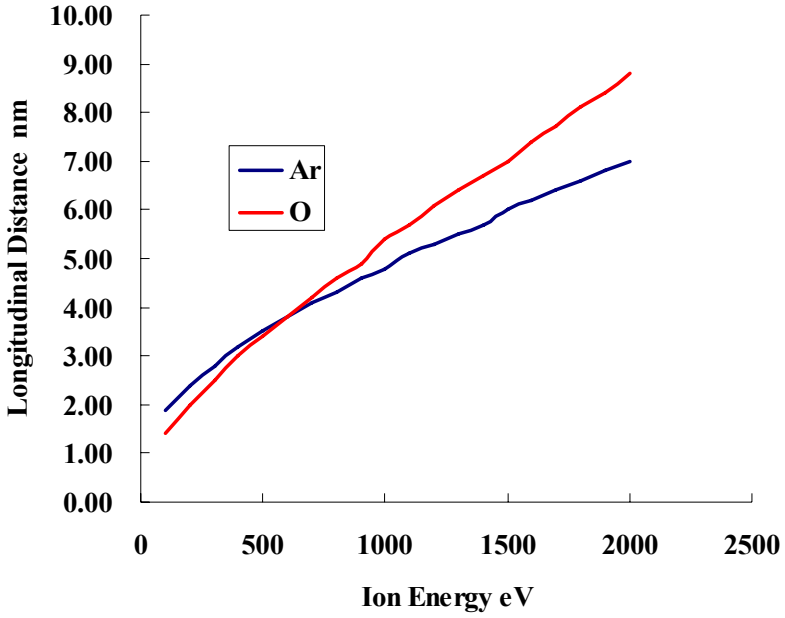

Figure 4-8. Longitudinal distance of 10000 Ar and O ions at different ion energy. (TRIM)

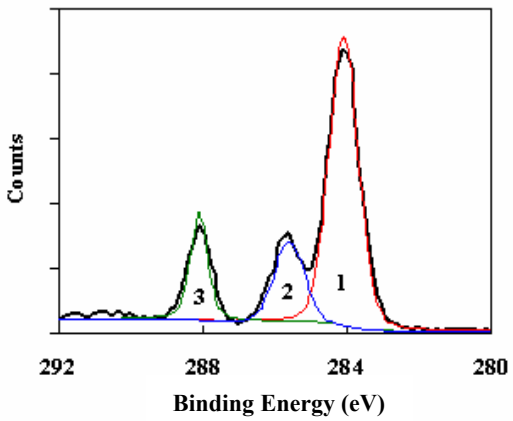

Figure 4-9(a). C 1s (Without treatment)

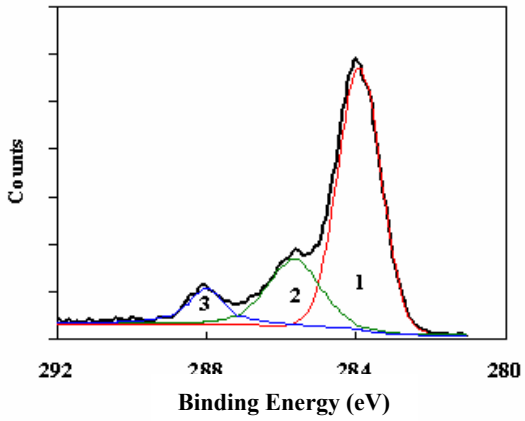

Figure 4-9(b). C1s (Ar 750V, 5 x 10^{15} ions)

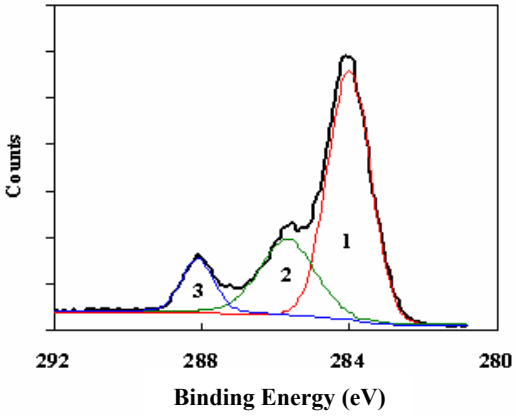

Figure 4-10(a). C1s (Ar 1000V, 5 x 10^{15} ions)

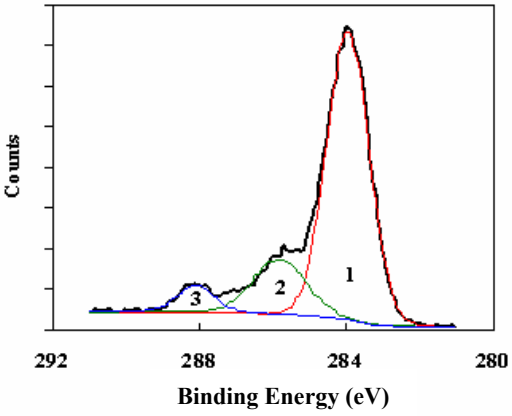

Figure 4-10(b). C1s (Ar 1250V, 5 x 10^{15} ions)

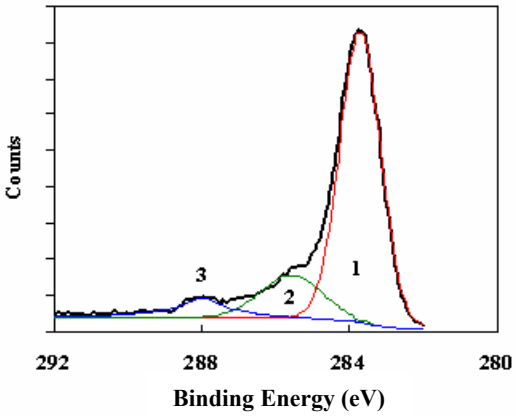

Figure 4-11(a). C1s (Ar 1500V, 5 x 10^{15} ions)

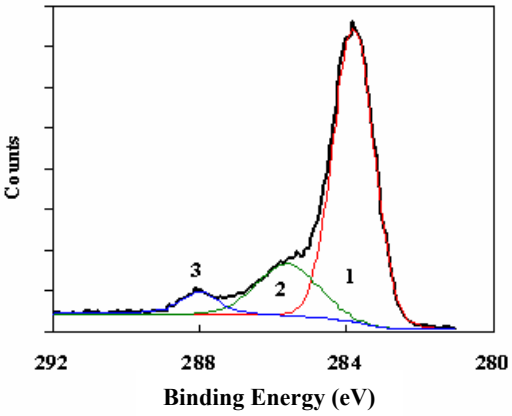

Figure 4-11(b). C1s (Ar 1500V, 5 x 10^{16} ions)

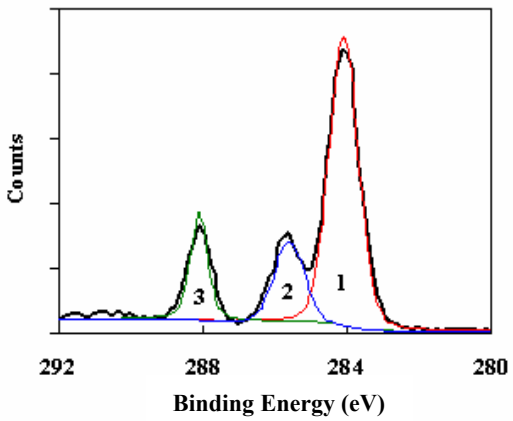

Figure 4-12(a). C 1s (Without treatment)

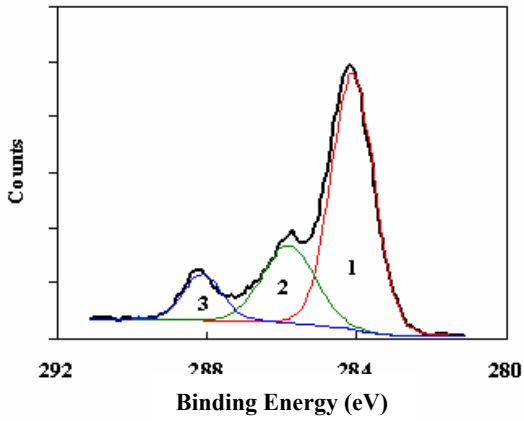

Figure 4-12(b). C 1s (O 750V, 5 x 10^{15} ions)

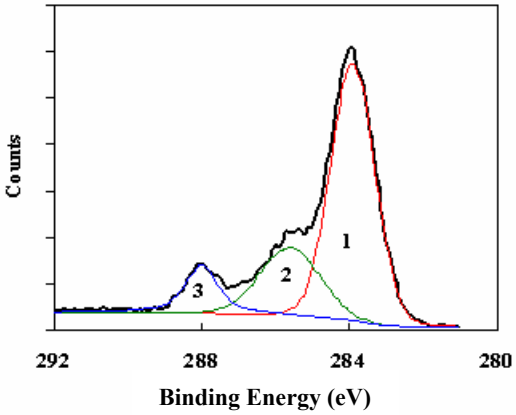

Figure 4-13(a). C 1s (O 1000V, 5 x 10^{15} ions)

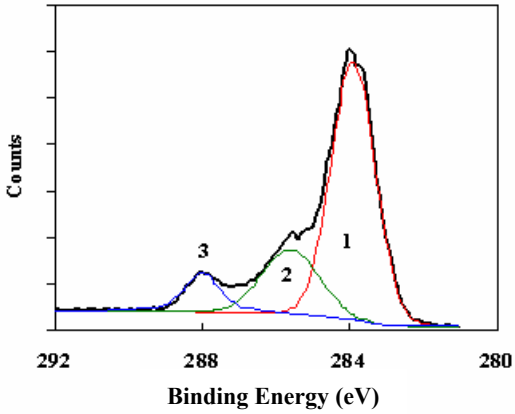

Figure 4-13(b). C 1s (O 1250V, 5 x 10^{15} ions)

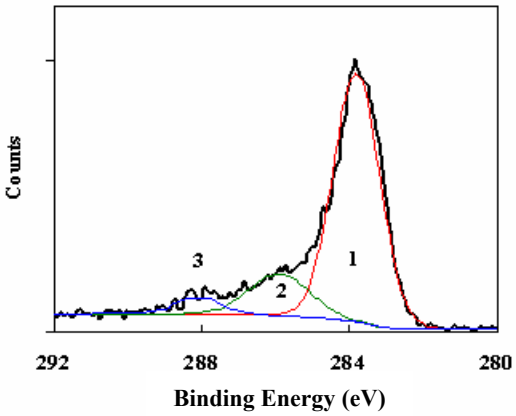

Figure 4-14(a). C 1s (O 1500V, 5 x 10^{15} ions)

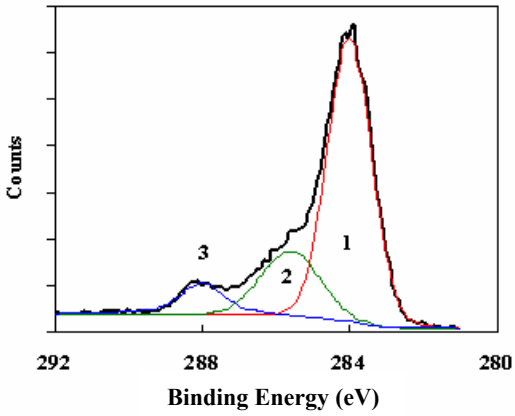

Figure 4-14(b). C 1s (O 1500V, 5 x 10^{16} ions)

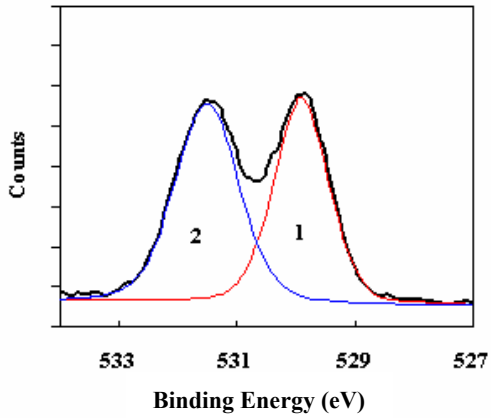

Figure 4-15(a). O 1s (Without treatment)

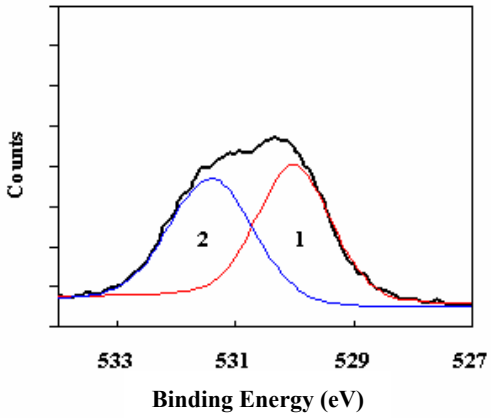

Figure 4-15(b). O 1s (O 750V, 5 x 10^{15} ions)

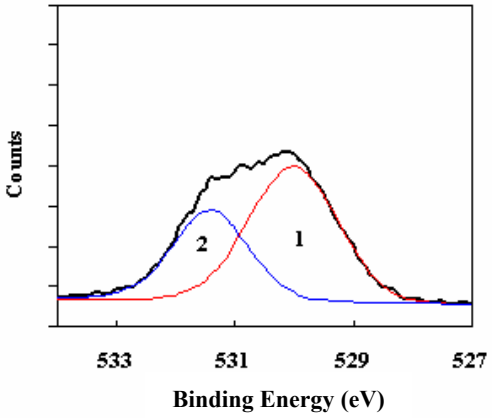

Figure 4-16(a). O 1s (Ar 750V, 5 x 10^{15} ions)

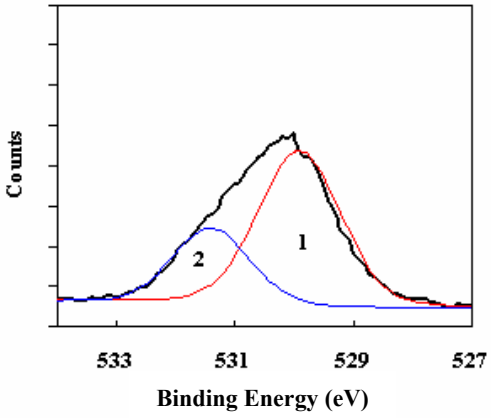

Figure 4-16(b). O 1s (O 1000V, 5 x 10^{15} ions)

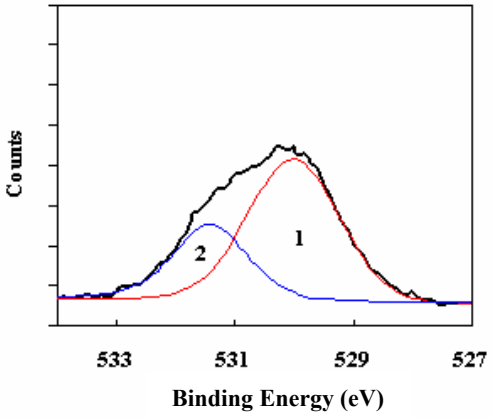

Figure 4-17(a).O 1s (Ar 1000V, 5 x 10^{15} ions)

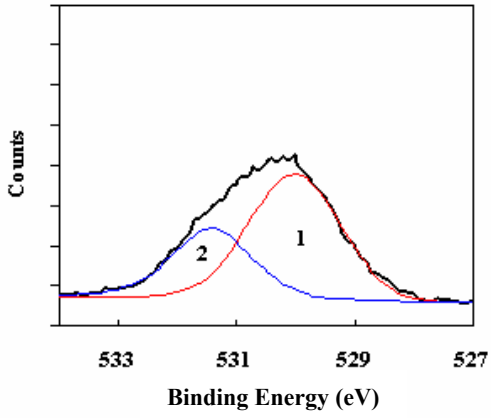

Figure 4-17(b). O 1s (O 1500V, 5 x 10^{15} ions)

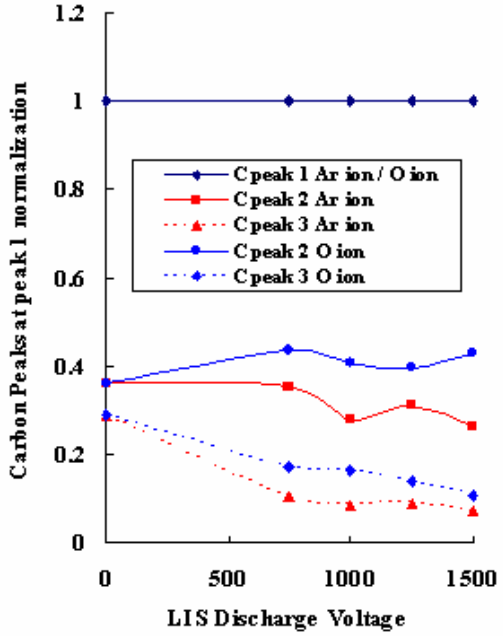

Figure 4-18(a). Peaks in C 1s comparison

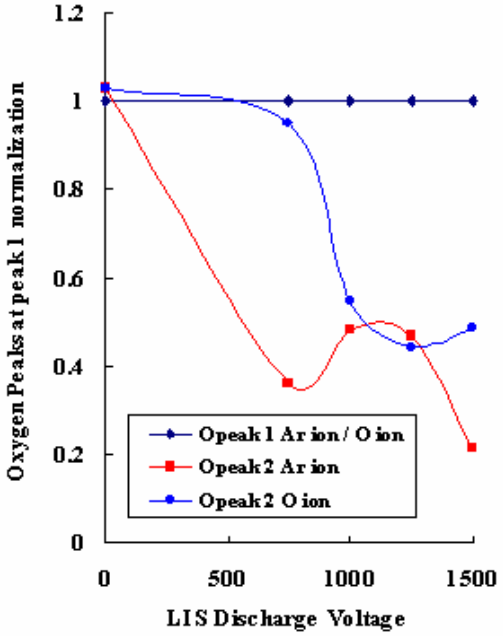

Figure 4-18(b). Peaks in O 1s comparison

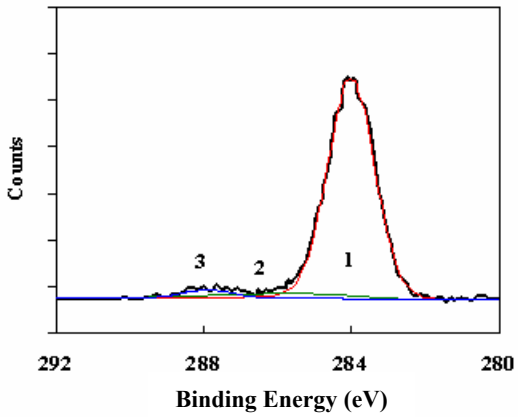

Figure 4-19(a).C 1s (Ar 1000V, 5 x 10^{15} ions) – ECR ion source

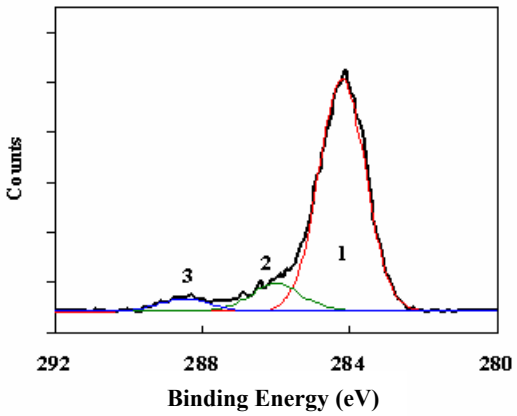

Figure 4-19(b). C 1s (O 1000V, 5 x 10^{15} ions) – ECR ion source

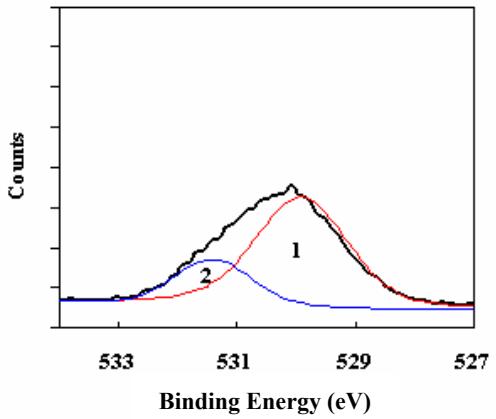

Figure 4-20(a).O 1s (Ar 1000V, 5 x 10^{15} ions) – ECR ion source

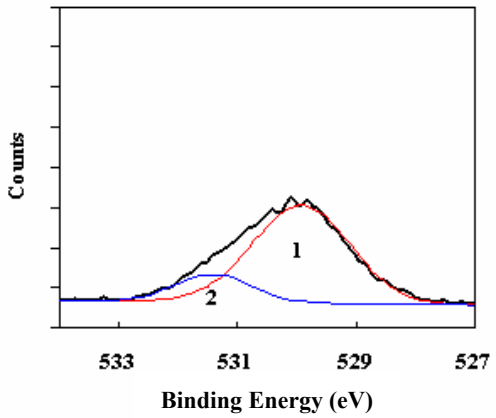

Figure 4-20(b). O 1s (O 1000V, 5 x 10^{15} ions) – ECR ion source

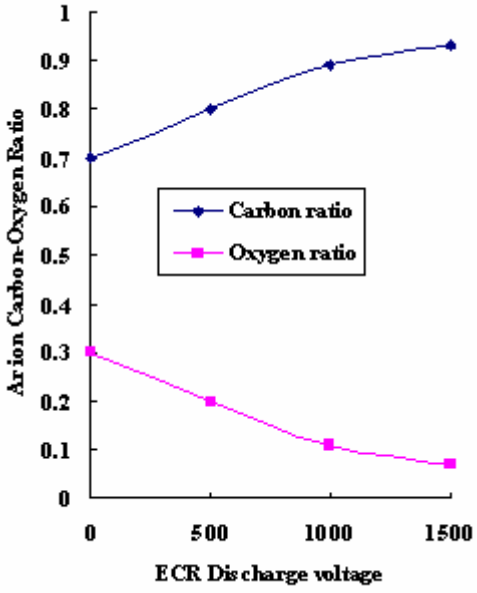

Figure 4-21(a). C 1s to O 1s ratio (Ar ions) - ECR ion source

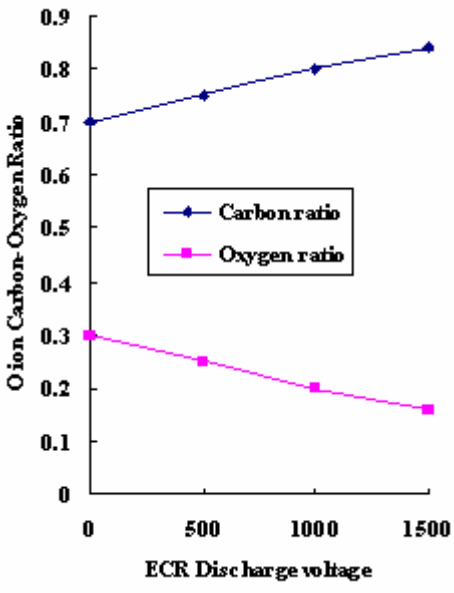

Figure 4-21(b). C 1s to O 1s ratio (O ions) - ECR ion source

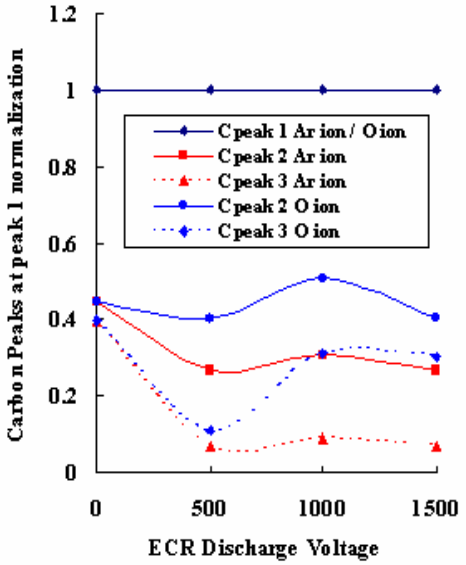

Figure 4-22(a). Peaks in C 1s comparison - ECR ion source

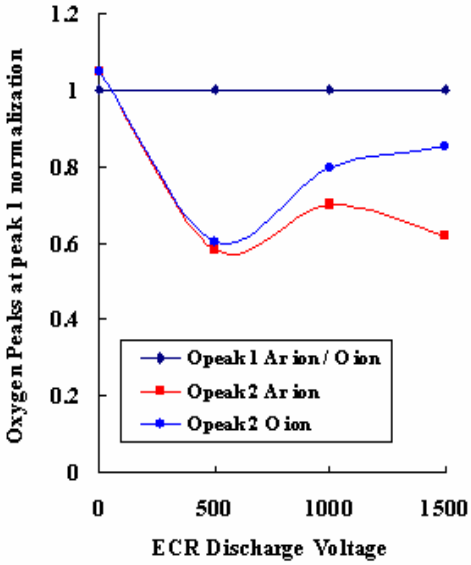

Figure 4-22(b). Peaks in O 1s comparison - ECR ion source

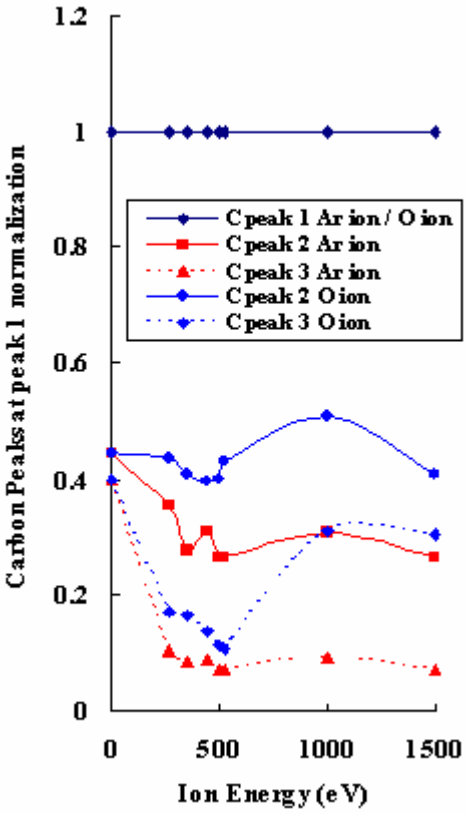

Figure 4-23(a). Peaks in C 1s comparison

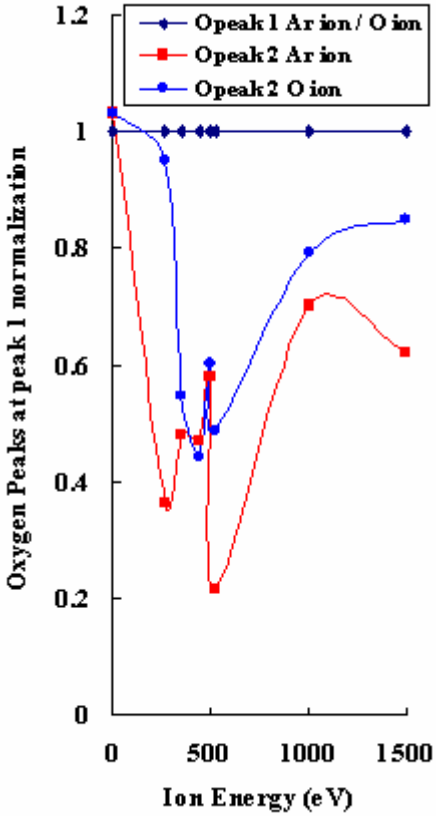

Figure 4-23(b). Peaks in O 1s comparison

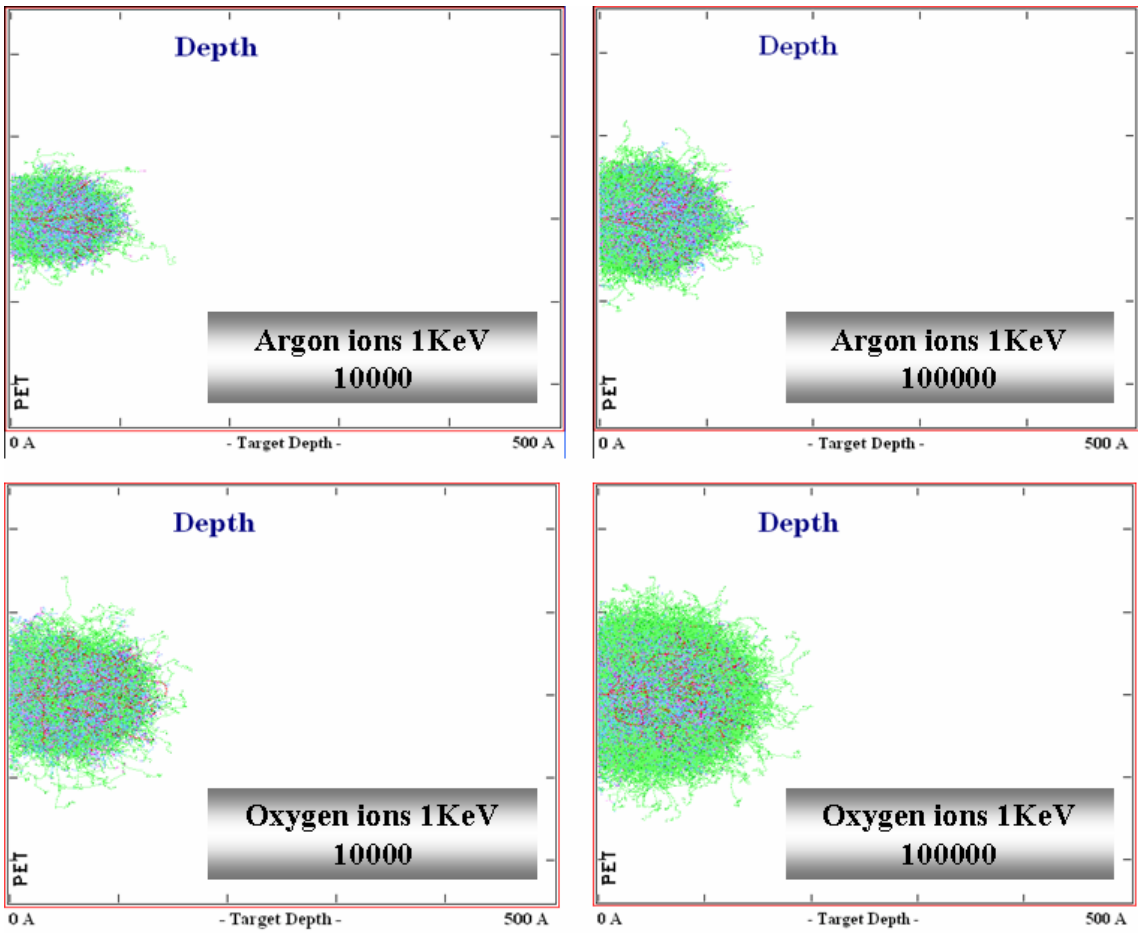

Figure 4-24. TRIM simulation of 10000 and 100000 Ar, and O ions (1 KeV)

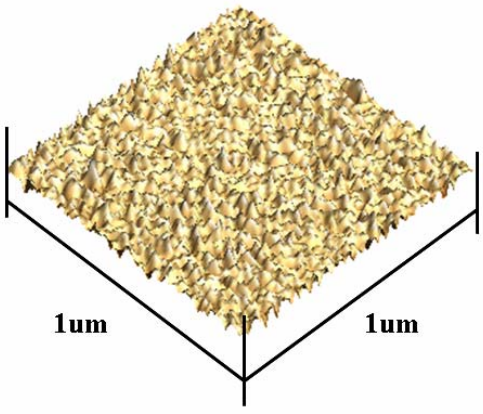

Figure 4-25(a). Without treatment

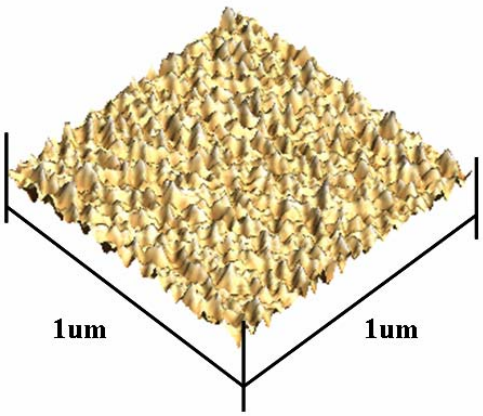

Figure 4-25(b). Ar 750 V, 5 x 10^{15} ions

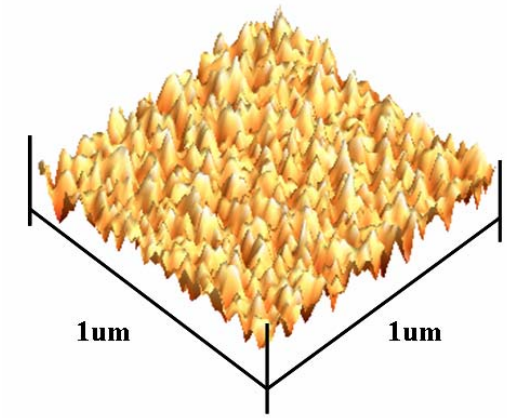

Figure 4-26(a). Ar 1000 V, 5 x 10^{15} ions

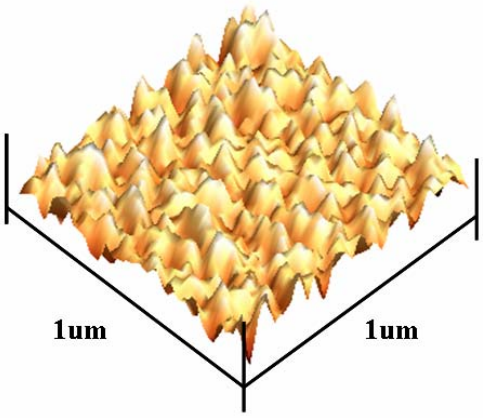

Figure 4-26(b). Ar 1250 V, 5 x 10^{15} ions

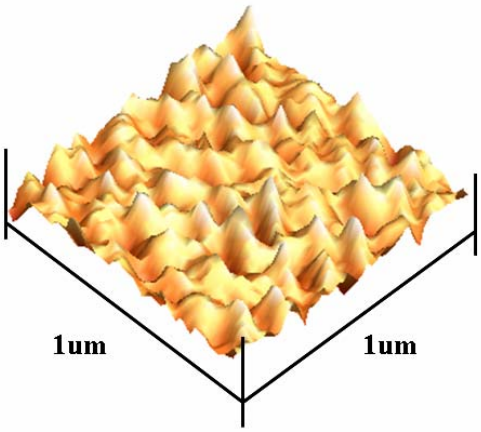

Figure 4-27(a). Ar 1500 V, 5 x 10^{15} ions

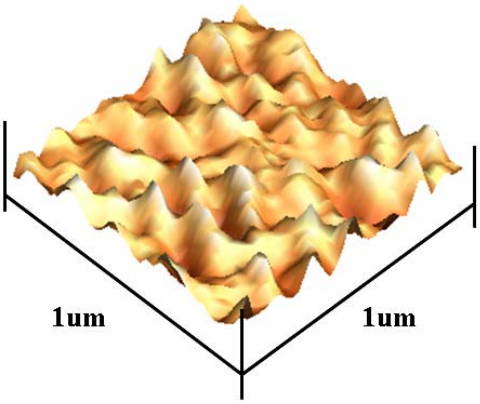

Figure 4-27(b). Ar 1500 V, 5 x 10^{16} ions

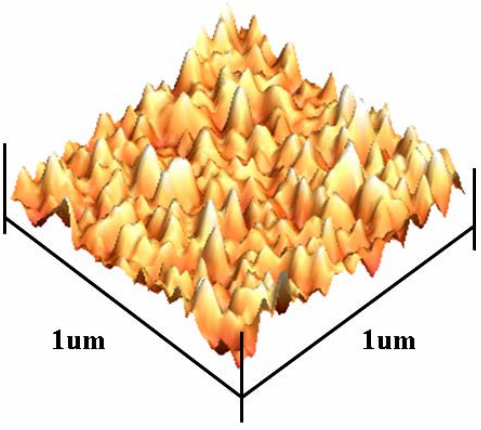

Figure 4-29(a). O 750 V, 5 x 10^{15} ions

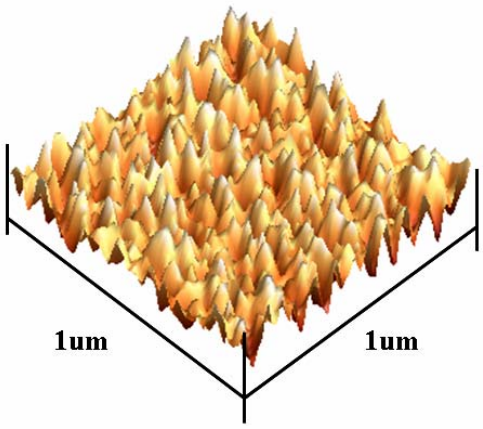

Figure 4-29(b). O 1000 V, 5 x 10^{15} ions

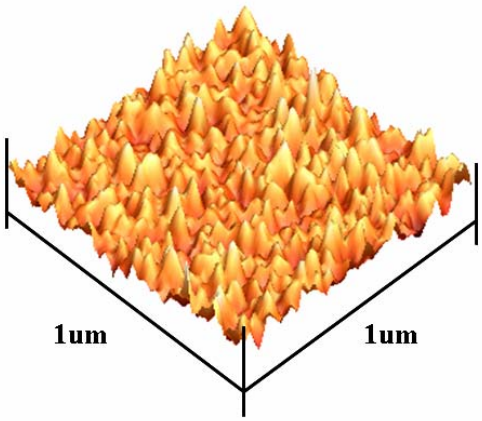

Figure 4-28(a). O 1250 V, 5 x 10^{15} ions

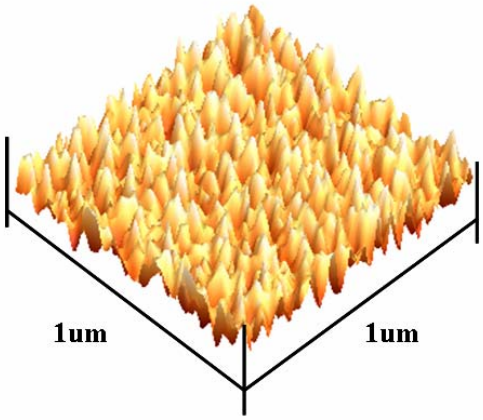

Figure 4-28(b). O 1500 V, 5 x 10^{15} ions

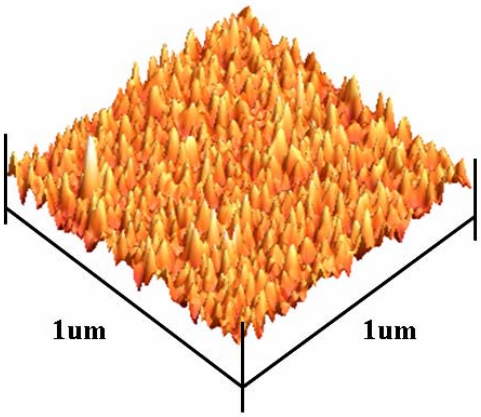

Figure 4-30(a). O 1500 V, 1 x 10^{16} ions

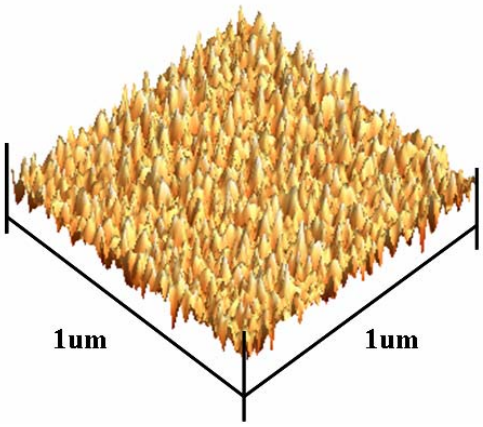

Figure 4-30(b). O 1500 V, 5 x 10^{16} ions)

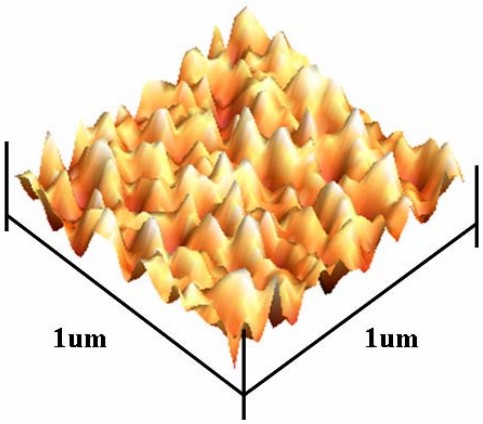

Figure 4-31(a). Ar 750V, 5 x 10^{16} ions

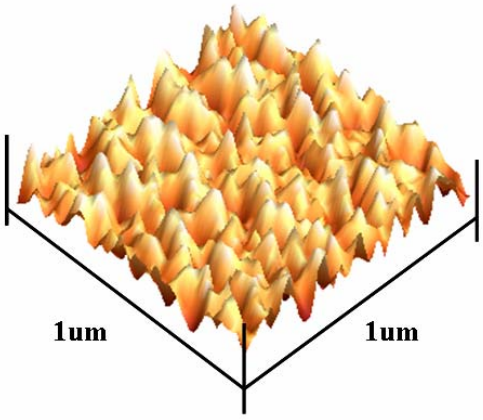

Figure 4-31(b). Ar 1000V, 1 x 10^{16} ions

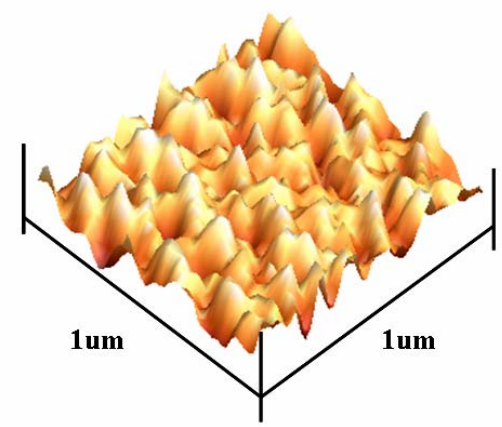

Figure 4-32(a). Ar 1000 V, 5 x 10^{16} ions

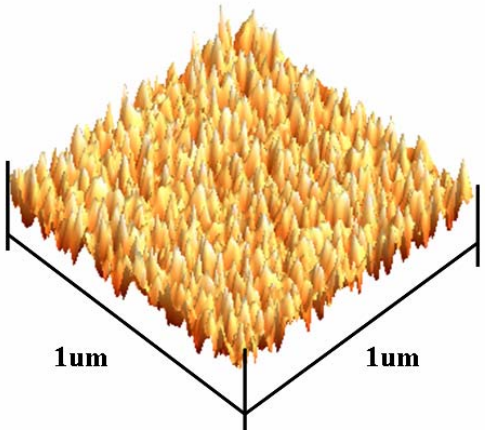

Figure 4-32(b). O 1000 V, 5 x 10^{16} ions

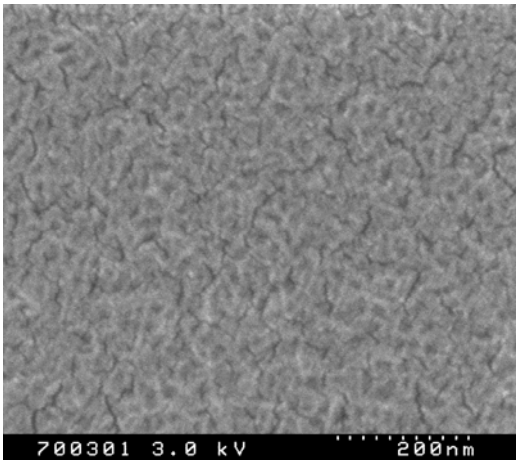

Figure 4-33(a). Without treatment

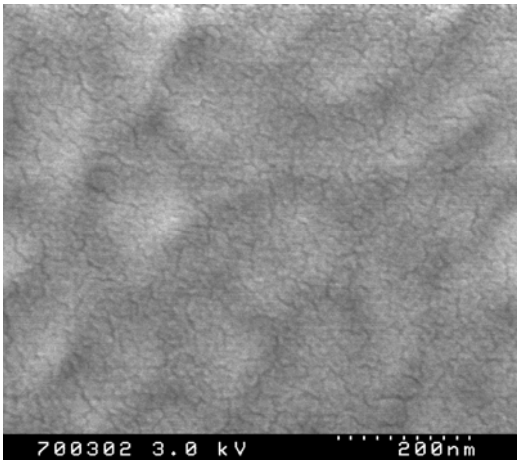

Figure 4-33(b). Ar 1000 V, 5 x 10^{15} ions

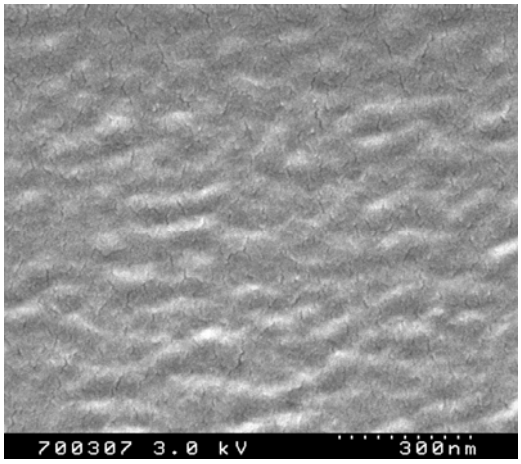

Figure 4-34(a). O 1000 V, 5 x 10^{15} ions

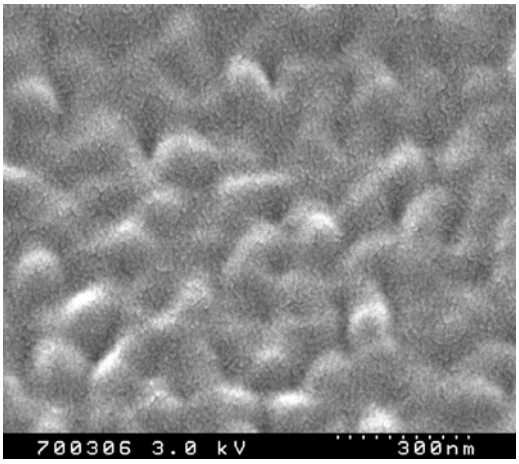

Figure 4-34(b). O 1000V, 5 x 10^{16} ions)

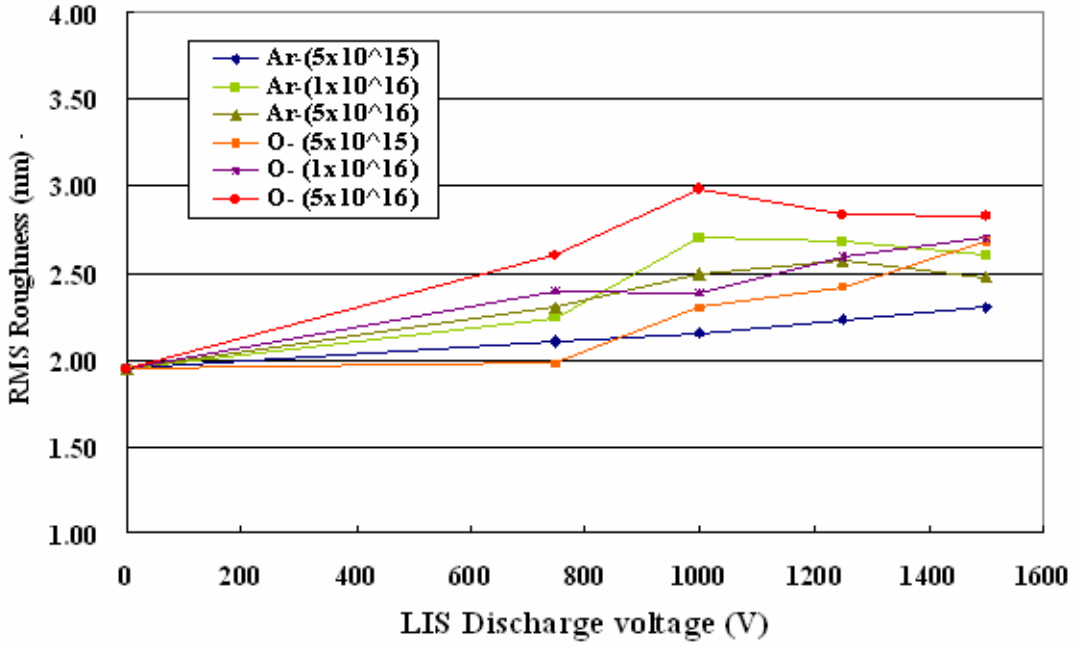

Figure 4-35. RMS roughness modification of various ions conditions

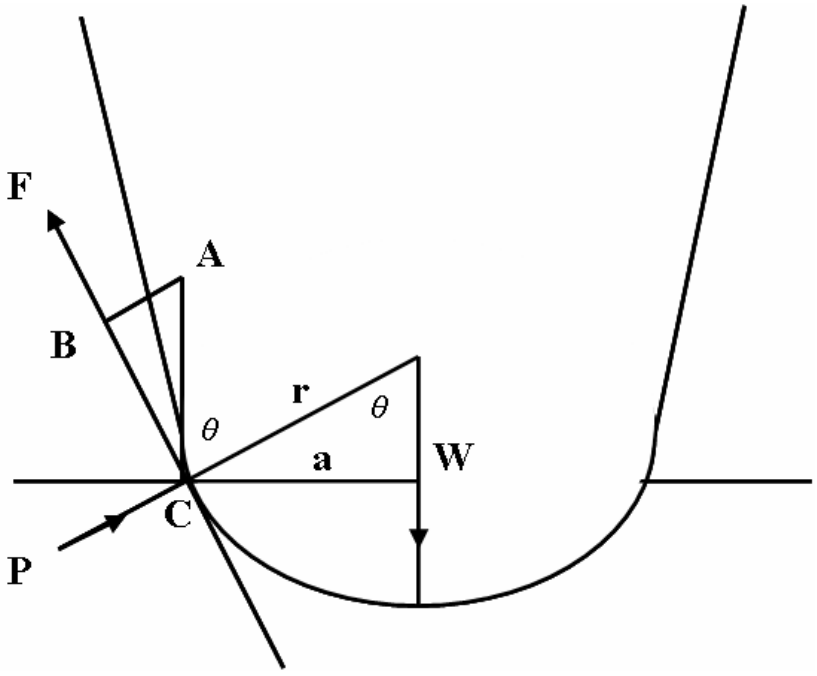

Figure 4-36. Forces acting on the spherical point (The stylus)

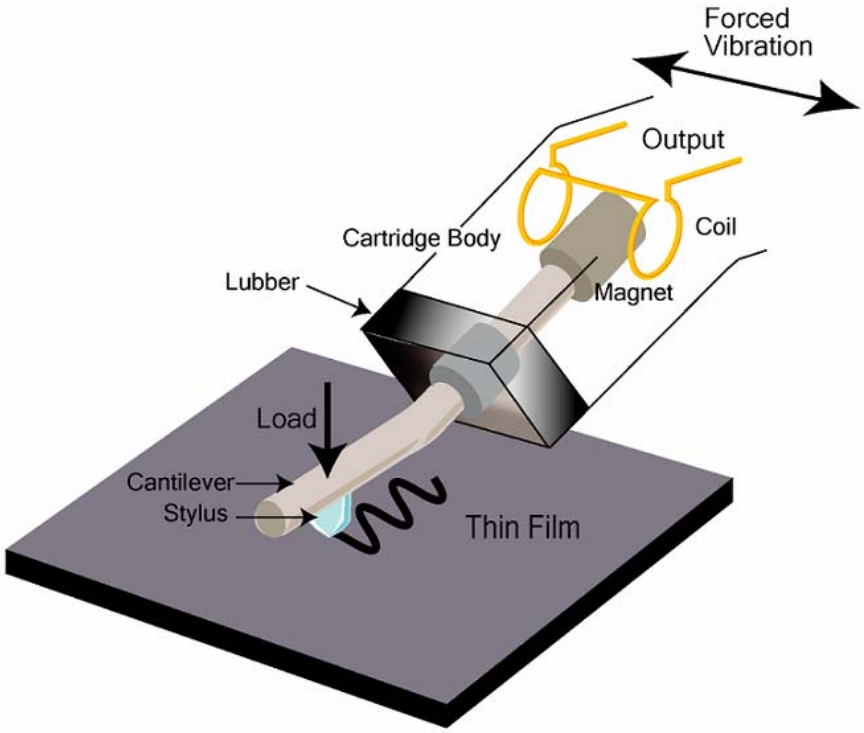

Figure 4-37. Schematic of scratching testing

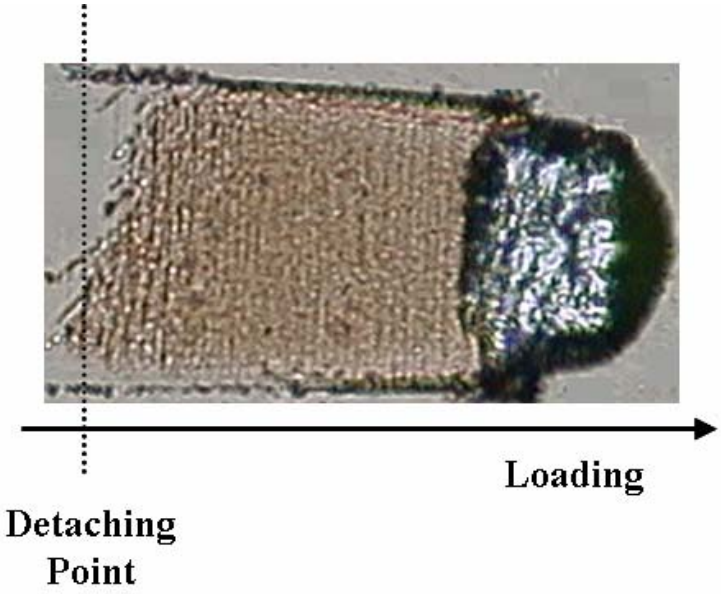

Figure 4-38. Microscopic image of scratching mark

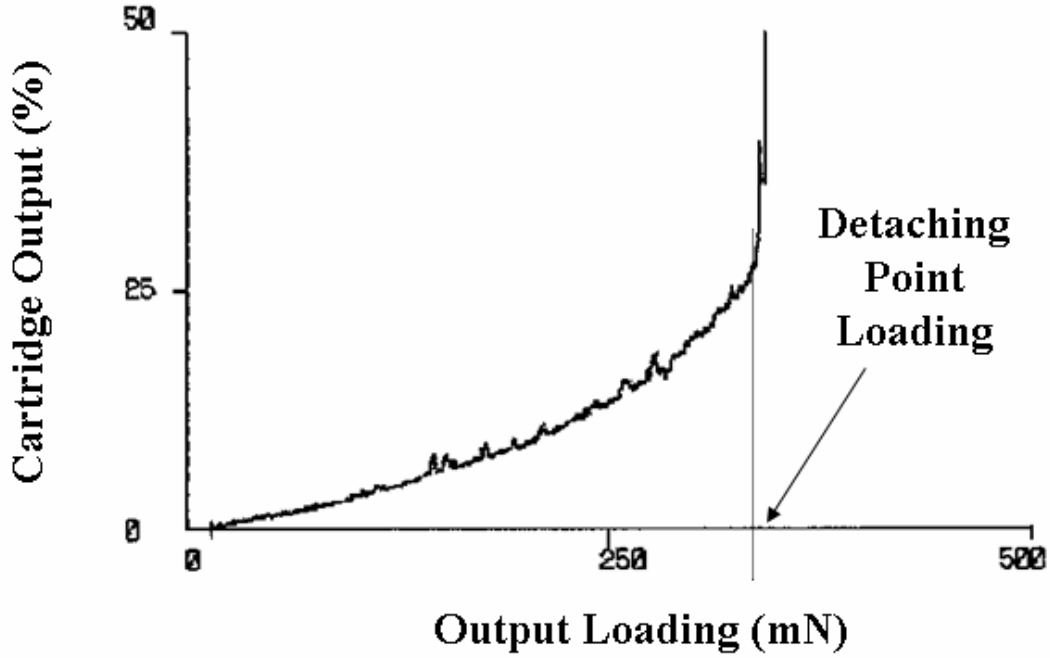

Figure 4-39. Cartridge output to out loading during scratch testing

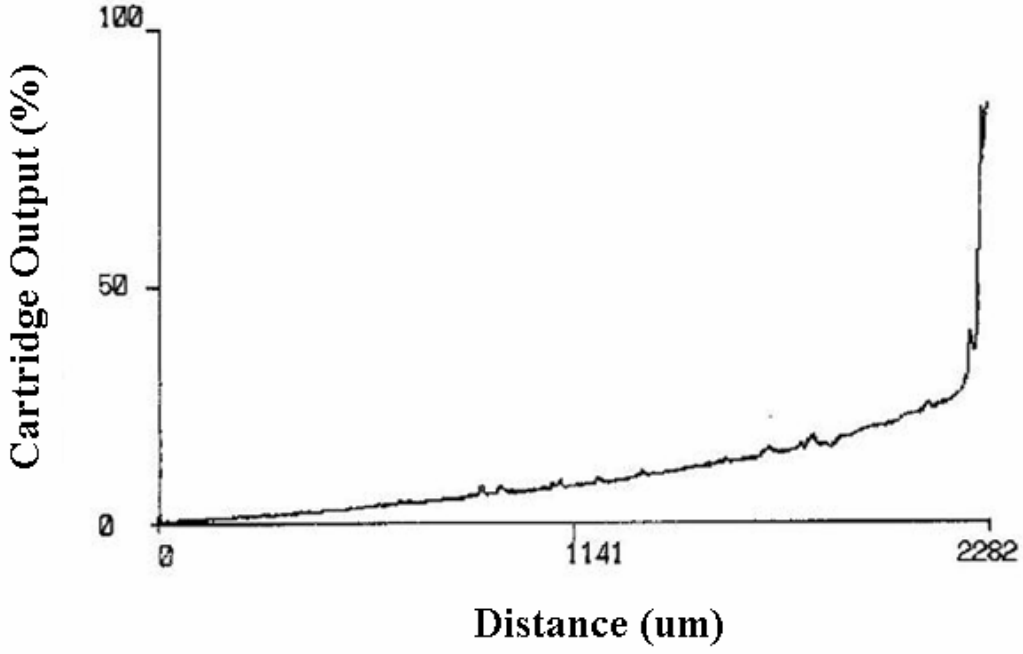

Figure 4-40. Cartridge output to distance (Corresponding to Figure 4-39.)

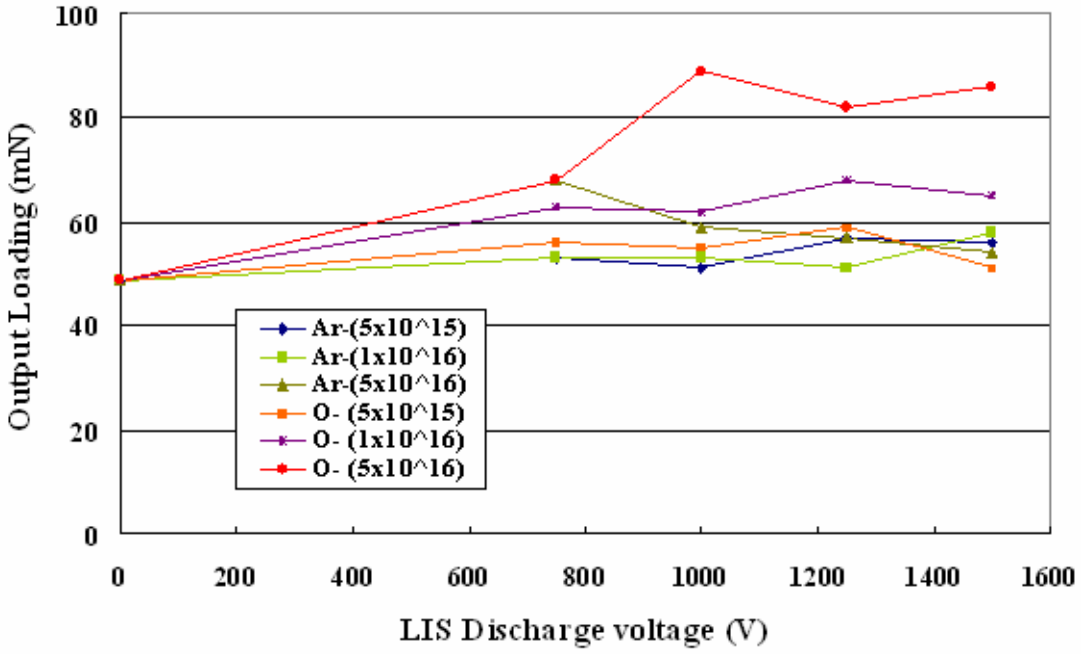

Figure 4-41. Scratch testing output loading of the various conditions

Chapter 5

Transparent Conductive Oxides of ITO and ZnO with Dopants

5.1 Introduction

The first transparent conducting oxide (TCO) was reported in 1907 by Baedeker, who used a primitive vapor deposition system to deposit thin film CdO that was both optically transparent and electrically conducting [1]. The first Indium tin oxide (ITO) was reported by Rupperecht in 1954, transparent conducting indium oxide doped with tin was developed for window coatings in the mid 1950s and in the subsequent half-century it has become the material of choice for a variety of high-performance applications [2]. The applications of transparent conductors include electrodes for most flat panel display technologies, collector electrodes in solar cells, deicing electrodes on airplane cockpit windows, static dissipation, and electromagnetic shielding. In the flat panel display industry, TCOs are widely used as transparent electrodes in optoelectronic devices such as liquid crystal display, organic light-emitting diode.

For the transparent electrodes used in flexible flat panel displays, although organic polymer like polyethylene dioxythiophene (PEDOT) was considered to be the alternative material studied and it has the property of over 10 % strain resistance compared to ITO widely used as TCO under 2 %. However, the great properties of ITO conclude the resistivity of 50 Ω/cm^2 and light transmittance nearly 90 %, and compared to 1000 Ω/cm^2 and lower than 85 % transmittance for PEDOT [3]. Indium tin oxide (ITO) was the typical conducting layer widely used.

TCOs need the combined properties of high electrical conductivity and high optical transparency in the visible region. Review for the selection of TCOs materials at present for display application shows that ITO is entirely used in the majority of high-performance display application due to its superior combination of environmental stability, relatively low electrical resisitivity and high light transmittance. However, in ITO, indium is the principal ingredient, and it is a scarce metal and expensive, the alternative TCOs materials based on mixed binary and ternary oxides of the Cd^{+2}, Zn^{+2}, In^{+3}, and Sn^{+4} were under development, and numerous studies on binary, ternary compound oxides composed of combination of In, Zn, Cd, Sn and Ga have been reported [2]. Recently, indium zinc oxide, zinc oxide was known to be transparent in the visible region of about 400 nm to 700 nm and exhibit a high conductivity [4]. Moreover, the suitable impurity doped ZnO has gained much attention as an alternative material for ITO. In general, it is believed that high optical transparency is incompatible with high electronic conduction. ZnO has a band-gap of 3.3eV, and it can meet the

needs of the optical transparency requires band gaps larger than 3.3 eV.

For flexible displays, polymer based substrates impose additional restrictions on their sensitivity to heat treatment and they suffer from dimensional and structural instability when it exposed to heat. Even at modest substrate temperatures of 100 ℃ to 150 ℃, the dimensional stability of many polymers are poor and may lead to increased film stress and failure by cracking. The primary consideration in the selection of a transparent conductor and the processing methods for use is the ability to deposit material with adequate optical and electrical properties, according the polymers substrates with an additional set of restrictions. As such, the deposition of transparent conductive oxides onto polymeric substrates requires a process that uses minimal exposure to energetic radiation and negligible substrate heating.

In this experiments, polyethylene terephthalate (PET) and glass were used as the substrates, and TCOs materials were deposited at the different temperature and annealing process. The ITO, ZnO and MgO, Al_2O_3, Ga_2O_3, In_2O_3 doped ZnO were used as the ceramics targets for sputtering deposition [5, 6]. Then, each TCO thin film property and the optical and electronic properties were measured and discussed in this chapter.

5.2 ITO and ZnO Doping In-, Mg-, Al-, Ga- Oxides

Indium tin oxide (ITO) electrodes are the most common transparent electrodes used as TCOs. Besides ITO, zinc oxide (ZnO), In-doped ZnO (IZO), Mg-doped ZnO (MZO), Al-doped ZnO (AZO), Ga-doped ZnO (GZO), Al-doped MZO (AMZO), Ga-doped MZO (GMZO) were used as TCOs materials in this experiment. They were deposited by RF sputtering method [7-9]. In this experiment, we made the sputtering targets by ourselves. The eight types of these ceramics targets were produced, and its production process involved the following seven main stages:

1. The first stage: Sintering stage for each material powder

At first, we prepared each oxide compound like indium oxide, tin oxide, zinc oxide, magnesium oxide with 99.9 % in purity. Sintered them at 800 ℃ in an oven, and then made each material in the condition of powders with the similar grain size similar to the next process.

2. The second stage: Well-mixing and Drying

There are eight types of mixed oxides used as the ceramic target. In order to keep its mixed ratio accurate and uniformity, first we put the proper calculated weight of each material ratio together with pure water in the ball-mill, and mixed well. Then placed them in the stirrer with the ceramic container and ceramic ball, and rotated them at the constant speed for one hour to be well-mixed.

Then put these pulverization and entire mixing into 80℃ oven for drying.

3. The third stage: Granulation

The powder collected from the second stage was pulverized again in ball-mill for about 30 min, and the uniform grain size of the powder was formed at this stage. In order to increase the strength in the next forming stage, we added 5 % water in the material and sealed them up for one hour. It made the moisture to spread uniformly in the mixed material.

4. The fourth stage: Simulated formation by press machine

In order to know the exact quantity required in the die-mould at final forming, we did the simulated formation process by using the smaller die-mould with 38 mm in diameter. The target material was filled in 38 mm die-mould in diameter, and pressed them with roughly 35 Mpa pressure. The thin disk type of ceramic target was made, and then we measured the thickness to simulate what is the proper quantity required for final forming in 130 mm die-mould with 5 mm in thickness. Then pulverize them for re-use.

5. The fifth stage: Finished forming

Put the proper quantity of powder in the 130 mm die-mould in diameter and press with 35 Mpa pressure. It can be formed as 130 mm in diameter and 5 mm in thickness shown in Figure 5-1(a). And this is the finished forming for the ceramic targets.

6. The sixth stage: Final Sintering

Put the pressed material at stage fourth in calciner at 1400℃. Through this process, the diameter shrunk to about 110 mm and do the final well-polished to adjust size about 101.6 mm for sputtering target shown in Figure 5-1(b). Up to this stage, the fabrication of sputtering target is finished.

7. The seventh stage: Bonding

In order to install the target in the sputtering device, the target will be mounted on the copper circle plate shown in Figure 5-1(c). According to the wholly different between copper and all transparent conducting oxide material, it can easily result to cracking when it is cooled after the bonding. The metal Indium is used the bonding material between target material and cooper plate. Its low melting temperature 156 ℃ and good plastic deformation characteristics can reduce the difference of thermal expansion coefficient effect from TCOs material and copper.

The Figure 5-1(d) shows the SEM photo of the target produced, it achieved the uniform grain size. The thickness, mass, density of eight types of TCOs targets list is shown in Table 5-1, and its

concentration is listed as follows:

1. ITO (2 wt % SnO_2 doped In_2O_3)
2. ZnO
3. IZO (In_2O_3: ZnO = 40 : 60 mol ratio)
4. MZO (10 mol % MgO doped ZnO)
5. AZO (2 wt % Al_2O_3 doped ZnO)
6. GZO (5 wt % Ga_2O_3 doped ZnO)
7. AMZO (2 wt % Al_2O_3 doped MZO (MgO 2 mol %))
8. GMZO (5 wt % Ga_2O_3 doped MZO (MgO 2 mol %))

There were eight types of TCO materials used: (1), ITO was 2 wt % SnO_2 doped In_2O_3, (2). ZnO, (3). IZO was mix In_2O_3 and ZnO at 4 : 6 mol ratio, (4). MZO was 2 mol % MgO doped ZnO, (5). AZO was 2 wt% Al_2O_3 doped ZnO, (6). GZO was 5 wt% Ga_2O_3 doped ZnO, (7). AMZO was 2 wt % Al_2O_3 doped MZO at MgO 2 mol %, and (8). GMZO was 5 wt % Ga_2O_3 doped MZO at MgO 2 mol %. Table 5-2 shows the weight ratio and molecular ratio of each target.

In Chapter 3, the sputtering apparatus detail used in the experiment has been described, the thin films deposition conditions were as follows: argon gas was introduced into chamber as sputtering gas used in this experiment; the gas flow was set at 10.4 ccm and the RF power output is 300 W; the substrate temperature were heated in different levels of room temperature (RT), 100℃ and post process to heated to 150℃ after the deposition process, it is expected to modify the properties of TCOs thin films [10-12]; and the distance between targets to deposited substrate was 260 mm.

In order to analyze the different properties of TCOs thin films, the different kinds of samples were prepared. The optical commercial PET films with 125 um in thickness, glass slide, silicon wafer and carbon slice with well-polished surface were used as substrates. The TCOs deposited on 5 mm x 5mm and 20 mm x 20 mm glass and silicon substrates were used for atomic force microscopy (AFM) and X-ray diffraction (XRD) detected, and on 5 mm x 5mm carbon substrates for Rutherford backscatter spectroscopy (RBS) analysis. The deposition on 20 mm x 30mm glass substrates were used for the optical properties of transmittance and reflectivity, and electronical properties of surface resistivity measurement.

Before the deposition process, the PET, glass and silicon substrates were cleaned by the supersonic cleaner with acetone for 15 min to remove oil and dust particles from surface, and washout by pure water then drying for 20 min. The thickness of TCOs thin films were measured by Tencor Alpha-Step 500 Surface Profiler owned by Kyoto Thin-Film Materials Institute (KTM). The silicon substrates with half covered Kapton-tape were deposited on TCOs thin films and then peeled

the Kapton-tape off. The thickness of thin films can be measured by the probe detector moving cross the surface of the TCOs thin films deposited and not deposited parts. The average calculated from the three times measurement for each sample was the thickness used in this experiment.

5.3 Properties of the Transparent Conducting Oxides (TCOs) films

Indium tin oxide (ITO), ZnO, In_2O_3 doped ZnO (IZO), MgO doped ZnO (MZO), Al_2O_3 doped ZnO (AZO), Ga_2O_3 doped ZnO (GZO), Al_2O_3 doped MZO (AMZO), Ga_2O_3 doped MZO (GMZO) were deposited by sputtering method in the various conditions. Table 5-3 shows the experiment conditions and sample types. The sputtering chamber was pumped to 8 x 10^{-4} Pa by the rotary pump and the turbo-molecular pump about one hour, and The PET and glass substrate were deposited on eight types of TCO thin films in different thermal conditions. It was 100 ℃ for PET substrate and 100 ℃, 200 ℃ for glass substrate. The substrate was heated to the target temperature gradually during the vacuum pumping process. The post annealing process was only applied for the sample deposited under room temperature for 30 minutes. The ambient gas was argon in 10.4 ccm, and RF was 3.7 W/cm^2. The shutter was open after 5 minute target discharge voltage is applied during the sputtering process to remove the impurity on the ceramic target surface. The sputtering time was about 20 minutes, and it achieved the roughly 150 nm thickness of thin film. The deposition rate was about 0.125 nm/sec, and it was much slower when compared to the thin films deposited by the electron beam evaporation. We used the sputtering method for the various TCO thin films deposition in this study.

In order to analyze the various properties of the deposited thin films, the following apparatuses were used. The chemical composition ratio of TCOs thin films were detected and calculated by Rutherford backscatter spectroscopy (RBS). SRIM described in chapter 4 and RUMP software was used to do simulation and peak fitting for the density and chemical composition calculated. The crystal structure of thin film was evaluated by X-ray diffraction (XRD) method by using 50 KV, 300 mA Cu X-radiation (ATX-G, Rigaku), and the remaining stress in the thin films can be calculated from XRD peak. The roughness and topography of surface was measured using atomic force microscopy (AFM), and surface chemical specific was measured by X-ray photoelectron spectroscopy (XPS).

5.3.1 Thin Films Composition

Rutherford backscatter spectroscopy (RBS) was used to analyze chemical composition and thin

film density. The sputtering allows for the deposition of films having the nearly same composition as the target source [13]. Here, we used the accelerator of Rutherford backscatter spectroscopy measurement located at Kyoto University Quantum Science and Engineering Center: QSEC. The irradiated ion is 2 MeV accelerated He^{+2} ions, and the backscatter angle was 170 ℃. In order to distinguish to the peaks overlapped much easier, we used the carbon substrate to substitute for the silicon and glass substrates, and it was deposited on the target films at the same condition. How to calculate the element calculation by peak area and density is described at the Appendix 3 RBS part. We calculated the area of each peak area subtracting background line, then compared to the cross section of every element. Accordingly, we knew the concentration of each element including in the films. Figure 5-2, 5-3, 5-4, 5-5 show the RBS spectrums of ZnO, MZO, AZO and IZO, respectively. They were easy to be recognized which peak belongs to which elements by using Au and Si peak channel calibration. The concentration was calculated with the cross section of Zn (117.56), Mg (17.95), Al (21.285), In (315.195), O (7.414) and the peak areas.

The concentrations of each thin films were ZnO with 48 % Zn and 52 % O, MZO with Mg 7 %, Zn 41 % and O 52 %, AZO with Al 3 %, Zn 45 % and O 52 %, IZO with In 25 %, Zn 15 % and O 60 %. The oxygen to metal ratio was higher than the theoretical value in these four samples. When we compared the samples deposited at room temperature without annealing and with 150 degree post annealing process, the oxygen ratio improved insignificantly. For the elements of GZO, AMZO and GMZO thin films concentration analysis, it was very difficult to define the peak overlapped in the cases of Ga to Zn and Mg to Al. The peaks cannot be precisely calculated for the composition calculation. The software used in Chapter 3, RUMP (Rutherford Universal Manipulation Program), was used. Figure 5-6 and 5-7 show the GZO and AMZO RBS spectra after simulation fitting.

From this simulation and fitting approach, we can clearly define the elements and their stoichiometry in thin films. After knowing the composition ratio of each thin film, we found the oxygen concentrations were higher than the theoretical value in all samples. The comparison between the metal to oxygen RBS measured value to the theoretical value was shown in Figure 5-8. The concentration of each element is not different between the sputtering target and the deposition films normally. This is also a primary reason for the widespread use of sputtering to deposit metal alloy films. However, we found the oxygen ratio of all samples became higher. One reason considered was the impurity like the hydroxide attached on surface after the deposition and exposed to the atmosphere when it was transferred to RBS chamber. Another reason considered was the oxygen ions were absorbed in thin film, and remained in the defection of crystalline structure.

For the thermal process, we cannot find the concentration change between the metals, even in the case of annealing process. Oxygen ratio decreased a little after annealing process, but it was still higher than the theoretical value. In the X-ray photoelectron spectroscopy (XPS) analysis, besides the oxygen that bonded to the metal, the OH and H_2O bonding were detected in the chemical

specific, even if we have removed the impurity hydroxide by sputtering the surface. The post annealing process contributed to parts of oxygen to get out from the surface, but it still cannot remove all the additional oxygen from the thin films. It was considered the remaining oxygen in this thin film resulted in the unstable ZnO crystal structure.

5.3.2 Crystal structure

The θ－2θ measurement by X-ray diffraction (XRD) analysis was used to detect the crystal structure, and the ATX-G (Rigaku) located at Kyoto University Venture Business Laboratory (VBL) was used. The X-ray source was Cu, and accelerated voltage was 50 kV. The scanning interval was 0.01 deg and speed was 2.00 degree/min [14]. In general, the crystal structure of zinc oxide is Wurtzite structure when it is deposited by sputtering method and the c axis of Wurtzite structure is normal to the substrate surface [15]. For the ZnO series thin films used in this experiment, except IZO, only a peak in (002) direction was investigated by XRD. From the spectrums intensity of XRD measurement, the Bragg angle 2θ, the lattice spacing d, the grain size and the internal stress σ can be calculated. The principle of XRD measurement and how to calculate the above values was described in Appendix XRD part. The standard lattice spacing d and the crystal orientation of ZnO were referred to Joint Committee on Powder Diffraction Standards: JCPDS.

Figure 5-9 shows the XRD peaks of ZnO deposited at room temperature. From this peak data, we can know the peak degree, peak intensity, and FWHM degree of peak. Then we can calculate the lattice spacing d, grain size t, and lattice parameter c [6, 16]. Moreover, we can calculate the stress σ in the film based on the biaxial strain model by equation (5-1). In equation (5-1), the elastic constant C_{ij} of single crystalline ZnO have been used as C_{11} =208.8, C_{33} = 213.8 and C_{13} = 104.2. They were calculated as 232.8 almost 233 in equation (5-1). Then we can calculate the stress in c-axis in thin film [17-19].

$$\sigma_{film} = \frac{2c^2{}_{13} - c_{33}(c_{11} + c_{12})}{2c_{13}} \frac{c_{film} - c_{bulk}}{c_{bulk}} = -233 \times \frac{c_{film} - c_{bulk}}{c_{bulk}} \tag{5-1}$$

The ZnO spectrum shown in Figure 5-9, the Bragg angle θ_B was 33.73 degree, FWHM was 0.7 degree from 33.44 degree to 34.14 degree. Then the calculated lattice spacing d was 2.66, grain size t was 13.66 nm, lattice parameter c was 5.32, the stress σ in c-axis was -5.12 GPa. And it was also used to calculate the value of other thin films.

Figure 5-10 shows the ZnO, MZO, AZO, GZO, AMZO and GMZO deposited at room temperature have XRD peaks near 34 degree. We cannot detect the IZO peak near 34 degree. Referring to the ZnO database from JCPDS, there is a (002) peak at Bragg angle 2θ = 34.421 degree,

and the theoretical lattice spacing d is 2.603 Å. The ZnO related sample with peak detected near 34 degree in this experiment except IZO, and it was thought as the (002) orientation. Figure 5-11 shows the lattice spacing d and the Bragg angle of various kinds of TCOs thin films deposited at room temperature compared with the theoretical one, and Figure 5-12 shows the grain size and stress of each sample. It indicated the Bragg angle of all samples were smaller than the theoretical one 34.421 degree, and the calculated lattice spacing d was bigger than the theoretical one 2.603 Å. The spacing between zinc or oxygen atoms was wider. It was thought the all sample deposited at room temperature did not form the stable organized Wurtzite structure [20, 21]. Another possibility was the doping atoms (Al, Ga, Mg, In) in the ZnO crystal structure resulted in the crystalline defection. In these sample, AZO had the most different Bragg angle from the theoretical value, and its lattice spacing d was also the biggest one, moreover, the stress σ was the largest one in these sample. Compared to the ionic radius of each element, In (0.8Å), Mg (0.72Å), Ga (0.62Å), Al (0.54Å) has the most different value from Zn 0.74Å[22]. It was considered that the Al doping in ZnO was easier to affect the stability of the ZnO crystal structure [23, 24]. However, the same situation cannot be observed at the case of AMZO. For IZO deposited at room temperature, we cannot find the clear peak from 20 to 80 degree. It was thought the IZO amorphous thin film was deposited at room temperature.

Next, when we observed the thermal effects for the crystal structure modification. It was reported the spacing d decreased and the stress released when the substrate temperature increase from M. Chen (2000) [25]. The same results were detected in some of our experiments. For ZnO, MZO, AZO, and GZO, the spacing d decreased when the substrate was pre-heated to 100 degree and underwent post annealing process. The lattice spacing d of ZnO was decreased from 2.66 to 2.63 after annealing, and AZO was decreased from 2.67 to 2.65 at the condition of 100 degree substrate temperature. The Bragg angle became much nearer to the theoretical one after the post annealing process in these four samples. However, for AMZO and GMZO, it seemed not regular when we heated up the substrate and after the post annealing process. For AMZO, the lattice spacing increased from 2.64 to 2.66 when the deposition at 100 degree substrate, but it decreased little to 2.635 after the post annealing. When we compared the correspondence between the substrate temperature and annealing process to the peak intensity, the peak intensity decreased when substrate temperature increased to 100 degree, it meant the orientation of crystal structure became weak. It cannot be considered that the crystal structure become stable when we increased the substrate temperature. However, the PET substrate is weak for thermal process, and we cannot increase the substrate to higher temperature than 150 degree, otherwise, the crystal structure may become more stable when the deposition at much higher temperature [11, 12]. The intensity increased a little after annealing process in single doping conditions like AZO, MZO and GZO, and seemed not change at AMZO and GMZO. When we compared the single doping and double doping as AZO to AMZO

and GZO to GMZO, the single doping was much easier to approach the stable structure after the thermal process during the deposition [26]. However, for the double doping of AMZO and GMZO, it was not so smooth to become the stable crystal structure when the temperature increased.

In this experiment, the annealing process was a little different from the substrate temperature increasing during the deposition. The lattice spacing d decreased and the peak intensity increased after annealing. The internal stress was released during the annealing process. The crystal structure became more stable and approached the theoretical value.

5.3.3 Surface Specific and Roughness

X-ray photoelectron spectroscopy (XPS) was used for surface chemical composition detecting and atomic force microscopy (AFM) and scanning electron microscopy (SEM) were used to measure the surface roughness and topography. The principle of XPS, AFM and SEM was described at Appendix XPS, AFM, SEM parts. We used the XPS apparatus AXIS 165S (Shimadzu) located at Kyoto University Venture Business Laboratory. X-ray was monochromatic Al, Kα (1486.6eV), and X-ray anode voltage was 14 KV, emitting current was 10 mA. The sample was measured in wide mode at 80 eV and narrow mode at 20 eV. For the narrow mode measurement, Zn $2p_{3/2}$ has the peak range from 1015 eV to 1065 eV, Mg $2p_{3/2}$ from 40 eV to 60 eV, Al $2p_{3/2}$ from 63 eV to 83 eV, Ga $2p_{3/2}$ from 1107 eV to 1127 eV, In $3d_{5/2}$ from 438 eV to 458 eV, O 1s from 523 eV to 543 eV and C 1s from 280 eV to 300 eV.

According to the ZnO and its related thin films were regarded as the semiconductor materials, we needed to neutralize the target sample before XPS measurement, and avoid the charge up effects occurred. The charge up effect results in the photoelectron spectrum peaks shift to the higher energy side. When the sample finished the deposition process, and moved to the XPS chamber. It took a period of time to expose to the atmosphere, and easily to be attached on the impurity like carbide. In Chapter 3, when we measured the ITO spectrum, besides indium, tin and oxygen elements, we also found the carbon peak in it. In order to move the carbide on the surface, sputtering was used to clean the surface before X-ray detection, since it may change the properties of surface and we cannot apply this in Chapter 4. It may result in the different treatment and hard to distinguish the effects from XPS argon ion sputtering or indicated ion source irradiation. But it is suitable to use the argon ions sputtering to clean the surface of TCOs before XPS measurement. The sputtering condition was argon ions accelerated by 3 KV and irradiation time was 90 second. Figure 5-13(a) shows the XPS C1s spectrum before the sputtering and Figure 5-13(b) shows the condition after cleaning. It is obvious the carbon was totally removed after the argon ions sputtering.

For XPS analysis of the TCO thin films, Figure 5-14, 5-15 and 5-16 show the O 1s spectrums of

ZnO, MZO, AZO, GZO, AMZO, and GMZO. As the described above, we used the argon ions sputtering and cleaned the surface before XPS measurement. From the O 1s spectrum, it seemed not to only include one O 1s peak bonding to metal. The metal oxides O 1s was roughly at 528 eV to 531 eV, so the main peak of O 1s spectrum corresponds to the oxygen bonded to zinc or other few doping elements. Where the other higher energy peaks should be assigned to OH and H_2O species, respectively [27]. It was considered the H_2O adsorbed on ZnO films was dissociated into H and OH groups. When we compared the O 1s peak between the deposition at room temperature and at 100 degree substrate, the OH or H_2O peak still existed. In the comparison to the post-annealing samples, the OH and H_2O peaks didn't vanish and decrease. The water adsorption in ZnO films cannot be removed by the thermal process used in this experiment. That is the possible reason considered why good crystal structures were not formed and detected by XRD in the pervious section. The OH- and H_2O of the oxygen bond resulted in the defection of crystalline structure. The adsorption and dissociation of water on the surface of metal oxides have been investigated by Almeida (1998) [28]. The defects such as vacancies play an important role in initiating the dissociation of water. The defects on the surface could change the physical and chemical properties and even increase dissociation energies. The water would dissociate at the sites of the defects rather than physisorption.

Figure 5-17 and 5-18 show the Zn $2p_{3/2}$ spectrums of ZnO, AZO, GZO, and AMZO. Each peak was a full peak, and it can be completely fitted by XPSPEAK software. They all presented as the symmetrical peaks, and indicated that the Zn $2p_{3/2}$ totally bonded to oxygen. When we compared the peak intensity, it was easy to find the ZnO has the higher peak than others, then AZO and GZO were higher than AMZO. The intensity decreased gradually when we doped the single, then the double metal oxides in ZnO. The quantitative analysis of XPS spectrum for the concentration of each element included was not applied in the TCOs films here, since it is less-accurate.

AFM and SEM were used to detect the surface morphology of TCO thin films. The AFM NanoScope Ⅲ (Digital Instruments) and SEM S-4500 type were used. Figure 5-19(a) shows the AFM photo of ZnO surface, and Figure 5-19(b) shows AMZO surface in 1 um square area. Figure 5-20 shows the RMS roughness of the TCOs thin films deposited at room temperature. They were located at 1.5 nm to 2.5 nm. Figure 5-21 shows the SEM photo of ZnO thin film.

5.4 Transmittance and Resistivity of the TCO films

The optical and electrical properties of TCO films were the most important issue when they are used for the display application [29-31]. In this section, we measured the light transmittance and the surface resistivity of the TCO films for their optical and electrical properties. We used the by 4-pin

probe, constant-current method using the low resistivity-meter Loresta-EP MCP-T360 (Mitsubishi Chemical) [32]. The four pin probe was put on the surface of sample, the constant current was passed from the two sides of four pins, and the middle two pins measured the voltage shown in Figure 5-22. The surface resistivity and the volume resistivity can be derived from equations (5-2) and (5-3):

Surface resistivity $\rho_S(\Omega/cm^2) = \frac{V(V)}{I(A)} \times RCF$ (5-2)

And the volume resistivity is $\rho_V(\Omega \cdot cm) = \rho_S(\Omega/cm^2) \times t$ (5-3)

Here, RCF is the Resistivity Correction Factor corresponding to the measured point and the surface area [33]. When we measured the surface resistivity in the case of the small area of sample or the measured point was from the side of target pieces. The electrical field intensity extends to outside of the measured piece and results in the higher resistivity measured. Therefore, the RCF was used to correct the electrical field intensity and calculate the exact surface resistivity or volumn resistivity. If we defined the any point of electrical field on the target sample as $\Phi(r)$, the RCF can be derived from the poisson (5-4) equation, and solve the RCF as equation (5-5) referred to the Figure 5-23.

Poisson Equation $\Delta^2\Phi(r) = 2\rho_V I[\delta(r-r_D) - \delta(r-r_A)]$ (5-4)

$$
\begin{aligned}
RCF^{-1} &= \frac{y_B - y_C}{a} \\
&+ \sum_{m=1}^{\infty} \frac{2}{a\varepsilon \sinh(b\varepsilon)} \times [\{\cos(\varepsilon x_B)\cosh[\varepsilon(y_B + \tfrac{b}{2})] - \cos(\varepsilon x_C)\cosh[\varepsilon(y_C + \tfrac{b}{2})]\} \times \\
&\cos(\varepsilon x_A)\cosh[\varepsilon(y_A - \tfrac{b}{2})] - \{\cos(\varepsilon x_B)\cosh[\varepsilon(y_B - \tfrac{b}{2})] - \cos(\varepsilon x_C)\cosh[\varepsilon(y_C - \tfrac{b}{2})]\} \times \cos(\varepsilon x_D)\cosh[\varepsilon(y_D + \tfrac{b}{2})]\} \\
&+ \sum_{n=1}^{\infty} \frac{2}{a\eta \sinh(b\eta)} \times [\{\cosh[\eta(y_B + \tfrac{b}{2})] - \cosh[\eta(y_C + \tfrac{b}{2})]\} \times \cosh[\eta(y_A - \tfrac{b}{2})] - \\
&\{\cosh[\eta(y_B - \tfrac{b}{2})] - \cosh[\eta(y_C - \tfrac{b}{2})]\} \times \cosh[\eta(y_D + \tfrac{b}{2})]\} \\
&+ \sum_{m=1}^{\infty}\sum_{n=1}^{\infty} \frac{4}{a\zeta \sinh(b\zeta)} \times [\{\cos(\varepsilon x_B)\cosh[\varepsilon(y_B + \tfrac{b}{2})] - \cos(\varepsilon x_C)\cosh[\zeta(y_C + \tfrac{b}{2})]\} \times \\
&\cos(\varepsilon x_A)\cosh[\zeta(y_A - \tfrac{b}{2})] - \{\cos(\varepsilon x_B)\cosh[\zeta(y_B - \tfrac{b}{2})] - \cos(\varepsilon x_C)\cosh[\zeta(y_C - \tfrac{b}{2})]\} \times \cos(\varepsilon x_D)\cosh[\zeta(y_D + \tfrac{b}{2})]\}
\end{aligned}
$$

(5-5)

Where,

$\varepsilon = \frac{m\pi}{a}$ (m is integer), $\eta = \frac{n\pi}{t}$ (n is integer) and $\zeta = (\varepsilon^2 + \eta^2)^{\frac{1}{2}}$

And r is the vector of any point on the measured target, (x_w, y_w) are the x and y coordinates of the pins w (A, B, C, D) in cm.unit.

For the measurement results, ITO had the surface resistivity at about 27 Ω/cm^2, and 22 Ω/cm^2 after annealing process. It was very close to the ITO thin films with 20 Ω/cm^2 used in display industry. Figure 5-24 shows the surface resistivity measured of the samples. The ZnO and MZO had high surface resistivity and it was out of the measurement range of the four pin detector. IZO had very low surface resistivity 52 Ω/cm^2 compared to other ZnO doping thin films and near to the value to ITO. The ZnO and MZO thin films had bad electrical conductivity. MgO doping was expected to enhance the light transmission by enlarging the band gap. That was the reason why we selected as few as the doping quantity for AMZO and GMZO at 2 %. Except ITO and IZO with the premium low surface resistivity below 60 Ω/cm^2 average, and ZnO, MZO with extra high surface resisitivity. AZO, GZO, AMZO, GMZO had the surface resistivity in the range of 10^3 to 10^4 Ω/cm^2.

When we doped Al_2O_3 and Ga_2O_3 in MZO as AMZO and GMZO, the surface resistivity decreased compared to MZO. It was considered that Al_2O_3 and Ga_2O_3 doping contributed in the electrical property improvement. When we compared the Al_2O_3 doping and Ga_2O_3 doping, we found the Ga_2O_3 doping had the lower resistivity. But it is difficult to conclude that the Ga_2O_3 doping was better than Al_2O_3 doped, since the doping quantity was different [34-36]. For the thermal effect, we found the surface resistivity of AZO and GZO decreased a lot in the case of 100 ℃ substrate, and improved a little for AMZO and GMZO. The annealing process also improved the surface resistivity, and better than heated substrate in AZO and GZO, but worse in AMZO and GMZO.

Besides the surface resistivity of electrical property, the light transmittance is an important property for TCOs films. The spectral transmittance and reflectance of TCOs layers were measured from 900 nm to 200 nm in wavelength by the spectrophotometer V-560 by JASCO, and the visible spectrum wavelength was regarded from 380 nm to 780 nm. Because the TCOs thin films did not have the same thickness, after we measured the light transmission of each sample, we transformed the measured light transmission to the one with same thickness of 150 nm standard. If we assumed the light intensity I(t) at t thickness position. The difference of intensity varied when light pass through dt is as:

$$\frac{dI(t)}{dt} = \alpha \times I(t) \tag{5-6}$$

The above differential equation can be solved as:

$$I(t) = I_0 e^{-\alpha t} \tag{5-7}$$

And transmittance $T = \frac{I}{I_0} = e^{-\alpha t}$ (5-8)

So the different thickness of transmittance can be transformed and calculated by the following equation (5-9), here, we set x was 150 nm in thickness.

$$T_x = e^{\frac{x}{y} InT_y} \tag{5-9}$$

Figure 5-25 and 5-26 show the transmittance and reflectivity spectrum of ZnO and IZO. Figure 5-27 shows the transmittance of ZnO, MZO, and ITO, and it is clearly observed that MgO doped can improve the transmittance spectrum in low wavelength side. The transmittance at 380 nm of ZnO was 37.3 %, it was obviously lower than MZO at 72 %. Moreover, the average transmittance of the visible wavelength from 380 nm to 780 nm, MZO was 92.3 % in average which is better than ZnO 89.4 %. The MgO doping indeed improved the light transmittance for optical property, however, it degraded the electrical property of ZnO thin film [37-39]. That was the reason why the doping ratio was considered as few as possible. Figure 5-28 shows the transmittance of ZnO, IZO, AZO and GZO, the doping of In_2O_3, Al_2O_3 and Ga_2O_3 all improved the transmittance of ZnO at low wavelength, but less effective than MgO doping. ZnO, AZO and GZO had similar shape of spectrum except GZO. Figure 5-29 shows the transmittance spectrum of AZO, GZO, AMZO and GMZO, GZO and GMZO had very similar spectrum, and AMZO had a little better transmittance at low wavelength. That was considered as the MgO doping effects. For the thermal effect for the light transmission, either substrate temperature increase or annealing process improved the average light transmittance during the visible wavelength 380 nm to 780 nm.

The absorption coefficient α of thin films can be calculated from the transmittance T and the reflectivity R of thin films from.

$$\alpha = \frac{1}{t} \times \ln(\frac{T}{1-R}) \tag{5-10}$$

The light absorption happened when the electron in the valance band was excited over the band gap. For the direct transition semiconductor material like ZnO or its related doping materials, the absorption is proportional to the transition probability. When transition probability is not zero, the absorption coefficient to energy is as:

$$\alpha(h\nu) = C \times \frac{(h\nu - E_g)^{\frac{1}{2}}}{h\nu} \tag{5-11}$$

Here, h is Planck constant (6.626 x 10^{-34}Js), v is frequency of vibration. In the equation (5-11), if we plotted ($\alpha h\nu$)^2 as y-axis, and ($h\nu$) as x-axis. The straight line cross the x axis is the point of the band gap value [40]. Figure 5-30 shows the straight line cross the x axis at 3.26 eV for the band gap

of ZnO. Figure 5-31 shows the plotting of ZnO, MZO, IZO and ITO. Figure 5-32 shows AZO, GZO, AMZO and GMZO. The ZnO, MZO, IZO, ITO had the cross points as the band gap of 3.26 eV, 3.54 eV, 3.58 eV and 3.65 eV, respectively. And AZO, GZO, AMZO and GMZO had band gap of 3.38 eV, 3.37 eV, 3.44 eV and 3.39 eV correspondingly. The band gap of ZnO was increased from 3.26 eV to 3.54 eV by doping MgO, it is also effective for AZO and AMZO from 3.38 to 3.44. Not only the MgO doping, Al_2O_3, Ga_2O_3 and In_2O_3 single doping or Al_2O_3, Ga_2O_3 and MgO double doping also enlarged the band gap of ZnO, and In_2O_3 doping achieved the biggest value. When the band gap increased more, the light transmission of the lower wavelength increased. IZO had the biggest band gap in the ZnO doping materials, and corresponding to its 3.58 eV band gap, the wavelength is about 346 nm. It was located out of the visible wavelength between 380 nm to 780 nm.

5.5 Figure of Merit for TCO Films

When we evaluated the TCOs films, the light transmission of optical property and the surface resistivity of electrical property are both important factors and we cannot trade each of them for another of more or less equal value as the TCOs layers. We tried to find the maximum light transmittance and the lowest surface resistivity material for the TCOs applications. However, in most of the case, these two properties were relatively opposite. Common to all transparent conductive layers are the need for optimizing the electrical and optical coating parameters. Ideally, both parameters should be as large as possible. Their interrelationship, however, excludes, in most cases, the simultaneous achievement of maximum transmission and conduction. The screening of the available transparent conducting materials can be performed using a figure of merit that consider the ratio of the optical transmittance (often cited at 550 nm and scaled by the tenth power) of a material to its sheet resistance from Haacke (1976) [41].

$$\phi = \frac{T^{10}}{R_s} \tag{5-12}$$

T is the transmittance, and R_s is the surface resistivity. Fraser and Cook (1972) has proposed and defined a figure of merit F_{tc} as

$$F_{TC} = \frac{T}{R_s} \tag{5-13}$$

And it can be derived as

$$F_{TC} = \sigma t \times e^{-\alpha t} \tag{5-14}$$

When combined the equation (5-13) and $R_s = \frac{1}{\sigma t}$ [42].

Where σ is the electrical conductivity, and t is the thickness.

In equation (5-14), F_{TC} is the is a function of the thickness *t*, and it can achieve a maximum value at t_{max} from:

$$\frac{\partial F_{TC}}{\partial t} = \frac{\sigma e^{\alpha t} - \sigma t \alpha e^{\alpha t}}{e^{2\alpha t}} = 0 \text{ , and } \quad t_{\max} = \frac{1}{\alpha}$$

And when we substitute t_{max} into equation (5-13), it yields the transmission at maximum F_{TC} at T = e^{-1} = 0.37, And this result demonstrated the maximum F_{TC} occurs at the thickness which reduces the light transmittance to only 37 %. It is too low for the most TCO thin films and useless. Haacke refined the new figure of merit for a transparent conductor [41]. The definition in equation (5-13) weighs F_{TC} too much in the surface resisitivity, thus resulting in a maximum F_{TC} at a comparatively large thickness. A better balance between transmission and resistivity was achieved when Haacke refined the figure of merit by equation (5-12). It offered a simplified numerical calculation of practical figure of merits. In addition, few transparent layers require more than 90 % transmission. The difference between F_{TC} and Haache's rose from the added stipulation that the maximum occurs at 90 %, not at 37 %. It is

$$\phi = \frac{T^{10}}{R_s} = \sigma t e^{-10\alpha t} \text{ , and } \quad t_{\max} = \frac{1}{10\alpha}$$

So the figure of merit φ defined by Haacke provides a useful tool for comparing the performance of transparent conductive layer when their electrical surface resistivity and optical transmission are known. Figure 5-33 shows the transmission and 10 power of transmission of the samples at wavelength 550 nm and including the substrate absorption. Figure 5-34 shows the figure of merits calculated by the foregoing surface resistivity and light transmittance. Because we cannot detect the surface resistivity of ZnO and MZO, so we assume they are 10^5, according to that is out of the measurement range. From the figure of merit for each TCO material used in this study, ITO and IZO had good value of 5 x 10^{-3} and 6 x 10^{-3}, and the next better two were GMZO and GZO had 1 x 10^{-4}, and 2 x 10^{-4}. Then AZO, AMZO, MZO and ZnO were located at range of 10^{-5} to 10^{-6}. The values were much worse than ITO and IZO. ITO is the general TCO material used in current display industry, and IZO is expected to be next good material. For GZO and GMZO, the experiments applied in this study were almost at room temperature and at low temperature thermal process. And the main reason is the PET used as the flexible substrate is weak to the thermal proceeding. If the thermal properties of the new material substrate can be improved more, the deposition can be more flexible and enhance the properties of TCO thin films. Then either GZO to GMZO or AZO to AMZO thin films can achieve much better figure of merit by changing the various deposition

conditions.

5.6 Conclusions

In this chapter, we tried to deposit the different kinds of TCO layers including the MgO, Al_2O_3, Ga_2O_3, In_2O_3 doping ZnO, ZnO, and ITO by sputtering method. They were deposited at room temperature and with low temperature thermal process of 100 ℃ substrate and 150 ℃ post annealing. RBS, XRD, XPS, AFM and SEM were used to investigate the basic properties of the thin films and compared its properties to its optical and electrical properties. As the result, ITO and IZO with the best figure of merit, and next was GZO and GMZO. ZnO and MZO had the worst surface resistivity and out of the measurement range. However, MgO doping degraded the conductivity of ZnO films, but it had a great effect on increasing the band gap of ZnO, either in ZnO, AZO and GZO. The band gap extension increases the light transmission at low wavelength referred to the Figure 5-35 from H.K. Pulker (1971) [43]. The transmittance at area A is affected by the absorption due to energy gap.

The TCOs thin films used in this study were not deposited in the stable crystal structure. The deposition at room temperature was the main reason considered, and it improved a little when we added the thermal process. Another problem was the additional oxygen detected either in RBS analysis or XPS analysis. Even, after removing the impurity on surface by argon ions sputtering, the oxygen bonding was detected in XPS spectrum. That was considered as the OH or H_2O remained in the defection of crystalline structure, and that the ZnO crystal structure cannot become stable and achieve the lattice spacing much close to the theoretical value. IZO had the premium surface resistivity and light transmission, but no peak detected at XRD spectrum. Minami et al. [44] reported that crystalline In_2O_3 peaks were observed for films deposited with targets having a Zn content of 0 – 7.6 %, and that the films with targets having a Zn content of 9 -34 % were amorphous. Jae-Soung Park et al. [45] reported the films deposited at room temperature were amorphous when targets of 50 % In_2O_3 doping 50 % ZnO. In this study, we had the amorphous IZO deposited at 40 % In_2O_3 to 60 % ZnO. For the XRD spectrum of ITO deposited at room temperature, we cannot find any peaks. At low substrate temperatures, ITO is deposited as an amorphous film over a wide range of processing conditions and techniques. The optoelectronic properties of these amorphous materials are usually inferior to those of the crystalline state. Fortunately, amorphous thin films of doped and undoped indium oxide deposited at room temperature have an optical transmittance and electrical conductivity that is adequate for present display technologies

References

1. K. Baedeker, Annals of Physics 22, 749-766 (1907).
2. H. Hosono, Thin Solid Films, 515, 15, 6000-6014 (2007).
3. D. R. Cairns, G. P. Crawford, Proceeding of the IEEE, 93, 8 (2005).
4. S. Shirakata, T. Sakemi, K. Awai, T. Yamamoto, thin Solid Films 451-452, 212 (2004).
5. M. Chen, X. Wang, Y. H. Yu, Z. L. Pei, X. D. Bai, C. Sun, R. F. Huang, L. S. Wen, Appl. Surf. Sci. , 158, 134 (2000).
6. M. Chen, Z. L. Pei, X. Wang, C. Sun, L. S. Wen, J. Vac. Sci. Technol., A19(3), 963 (2001).
7. Z. C. Jin, I. Hamberg, C. G. Branqvist, J. Appl. Phys. 64(10), 5117 (1988).
8. M. Chen, Z. L. Pei, C. Sun, J. Gong, R. F. Huang, L. S. Wen, Mater. Sci. Eng. B85, 212 (2001).
9. M. Chen, Z. L. Pei, C. Sun, L. S. Wen, X. Wang, J. Cryst. Growth 220, 254 (2000).
10. T. Minami, S. Ida, T. Miyata, Thin Solid Films, 416, 92 (2002).
11. E. G. Fu, D. M. Zhang, G. Zhang, W. F. Yang, M. Zhan, Appl. Surf. Sci. 217, 88 (2003).
12. Y. Igasaki, H. Saito, J. Appl. Phys. 69(4), 2190 (1991).
13. W. D. Westwood, “in Microelectronic Materials and Processes” (1989).
14. Rigaku, “X-ray Diffraction” (2002).
15. http://en.wikipedia.org/wiki/Zinc_oxide
16. K. H. Kim, K. C. Park, D. Y. Ma, J. Appl. Phys., 81(12), 7764 (1997).
17. J. Mass, P. Bhattacharya, R. S. Katiyar, Mater. Sci. Eng. B103, 9-15 (2003).
18. V. Gupta, A. Mansingh, J. Appl. Phys., 80(2), 1063 (1996).
19. R. Cebulla, R. Wendt, K. Ellmer, J. Appl. Phys. 1087 (1998).
20. E. G. Fu, D. M. Zhuang, G. Zhang, W. F. Yang, M. Zhao, Appl. Surf. Sci. 217, 88 (2003).
21. M. Chen, Z. L. Pei, C. Sun, J. Gong, R. F. Huang, L. S. Wen, Mater. Sci. Eng. B85, 212 (2001).
22. http://en.wikipedia.org/wiki/Ionic_radius
23. P. Bhattacharya, R. R. Das, R. S. Katiyar, Thin Solid Films 447-448, 564 (2004).
24. David R, Lide, Handbook of Chemistry and Physics, 12-8 (1992).
25. M. Chen, Z. L. Pei, C. Sun, L. S. Wen, X. Wang, J. Cryst. Growth, 220, 254 (2000).
26. S. Fujita, T. Takagi, H. Tanaka, S. Fujita, phys. stat. sol. (b), 599 (2004).
27. Y. F. Lu, H. Q. Ni, Z. H. Mai, Z. M. Ren, J. Appl. Phys. 88, 498 (2000).
28. A. L. Almeida, J. B. L. Martins, C. A. Taft, E. Longo, W. A. Lester, Jr., J. Chem. Phys. 109(9), 3671 (1998).
29. T. Minami, S. Suzuki, T. Miyata, Thin Solid Films, 398-399, 53 (2001).
30. S. Suzuki, T. Miyata, M. Ishii, T. Minami, Thin Solid Films 434, 14 (2003).
31. T. Minami, T. Miyata, T. Yamamoto, J. Vac. Sci. Technol. A17(4), 1822 (1999).
32. Tabata, CMC, “Transparent Conductive films” (2002).

33. Mitsubishi Chemistry, ”The Manual of Lorestra-EP MCP-T360”
34. K. H. Kim, K. C. Park, D. Y. Ma, J. Appl. Phys. 81(12), 7764 (1997).
35. M. Chen, Z. L. Pei, X. Wang, C. Sun, L. S. Wen, J. Vac. Sci. Technol. A19(3), 963 (2001).
36. J. Mass, P. Bhattacharya, R. S. Katiyar, Mater. Sci. Eng. B103, 9-15 (2003).
37. T. Minemoto, T. Negami, S. Nishiwaki, H. Takakura, Y. Hamakawa, Thin Solid films 372, 173 (2000).
38. K. Matsubara, H. Tampo. H. Shibata, A. Yamada, P. Fons, K. Iwata, S. Niki, Appl. Phys. Letters 85, 1374, (2004).
39. F. K. Shan, B. I. Kim, G. X. Liu, Z. F. Liu, J. Y. Sohn, W. J. Lee, B. C. Shin, Y. S. Yu, J. Appl. Phys. 95(9), 4772 (2004).
40. T. Minemoto, T. Negami, S. Nishiwaki, H. Takakura, Y. Hamakawa, Thin Solid Films 372, 173 (2000).
41. G.. Haacke, Journal of Applied Physics 47, 9, 4086-4089 (1976).
42. D. B. Fraser, H. D. Cook, J. Elestrochem. Soc. 119, 1368 (1972).
43. H.K. Pulker, Applied optics, 18,12, 1969 (1979).
44. T. Minami, T. Yamamoto, Y. Toda, T. Miyata, Thin Solid Films, 373, 189 (2000).
45. Jae-Soung Park, Ju-ll Song, Young-Woo Heo, Joon-Hyung Lee and Jeong-Joo Kim, J. Vac. Sci. Technol. B 24(6), (2006).

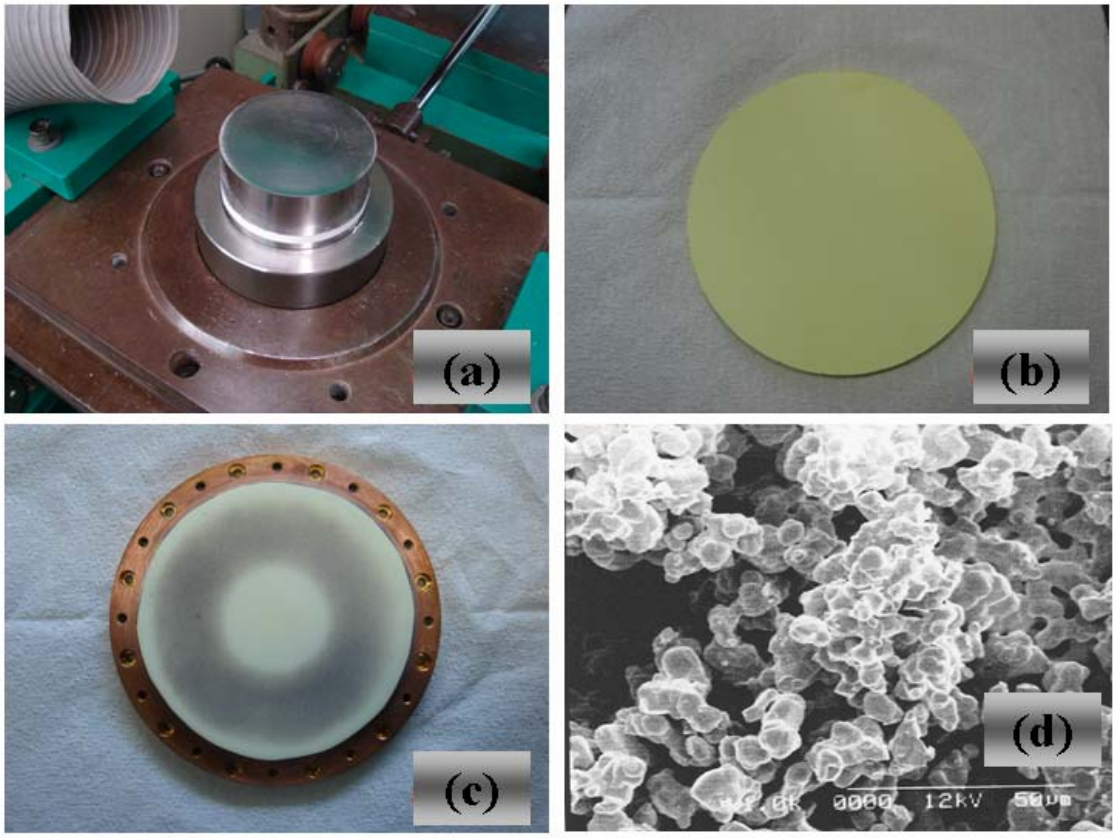

Figure 5-1. Target production (a) Pressing, (b) finished forming, (c) bonding to Cu plate, (d) SEM photo of target

Table 5-1.

The thickness, mass, density of targets list

No	Target	Mass (g)	Thickness (mm)	Diameter (mm)	Density (g/cm^3)	Cu Plate (g)	Total Mass (g)
1	ITO	217.0	6.7	99.2	4.19	337	554.0
2	ZnO	173.6	4.37	101.2	4.94	337	510.6
3	IZO	196.7	5.5	101.5	4.42	337	533.7
4	MZO	165.2	4.7	101.3	4.36	337	502.2
5	AZO	166.0	4.9	101.1	4.22	337	503.0
6	GZO	150.0	4.67	101	4.01	337	487.0
7	AMZO	138.9	4.19	102.2	4.04	337	475.9
8	GMZO	137.5	4.53	101.1	3.78	337	474.5

Table 5-2

Weight ratio and molecular ratio of each target

No.	Symbol Name	Composition	Mol. Weight	Mol. Ratio	Weight Ratio
1	ITO	In_2O_3	277.6382	96.4%	98.0%
		SnO_2	150.7088	3.6%	2.0%
2	ZnO	ZnO	81.3894	100.0%	100.0%
3	IZO	In_2O_3	277.6382	40.0%	69.5%
		ZnO	81.3894	60.0%	30.5%
4	MZO	MgO	40.3044	10.0%	5.2%
		ZnO	81.3894	90.0%	94.8%
5	AZO	Al_2O_3	101.96128	1.6%	2.0%
		ZnO	81.3894	98.4%	98.0%
6	GZO	Ga_2O_3	187.4442	2.2%	5.0%
		ZnO	81.3894	97.8%	95.0%
7	AMZO	Al_2O_3	101.96128	1.6%	2.0%
		MgO	40.3044	2.0%	1.0%
		ZnO	81.3894	96.4%	97.0%
8	GMZO	Ga_2O_3	187.4442	2.2%	5.0%
		MgO	40.3044	2.0%	1.0%
		ZnO	81.3894	95.8%	94.0%

Table 5-3.

Experiment conditions and sample types of TCOs thin films

No	Target	Substrate	Deposition Temp. (℃)	Annealing (℃)	Ambient Gas (ccm)	RF Power
1	ITO	PET	RT / 100	Not / 150	Ar (10.4)	3.7
		Glass	RT/ 100, 200			
2	ZnO	PET	RT / 100	Not / 150	Ar (10.4)	3.7
		Glass	RT/ 100, 200			
3	IZO	PET	RT / 100	Not / 150	Ar (10.4)	3.7
		Glass	RT/ 100, 200			
4	MZO	PET	RT / 100	Not / 150	Ar (10.4)	3.7
		Glass	RT/ 100, 200			
5	AZO	PET	RT / 100	Not / 150	Ar (10.4)	3.7
		Glass	RT/ 100, 200			
6	GZO	PET	RT / 100	Not / 150	Ar (10.4)	3.7
		Glass	RT/ 100, 200			
7	AMZO	PET	RT / 100	Not / 150	Ar (10.4)	3.7
		Glass	RT/ 100, 200			
8	GMZO	PET	RT / 100	Not / 150	Ar (10.4)	3.7
		Glass	RT/ 100, 200			

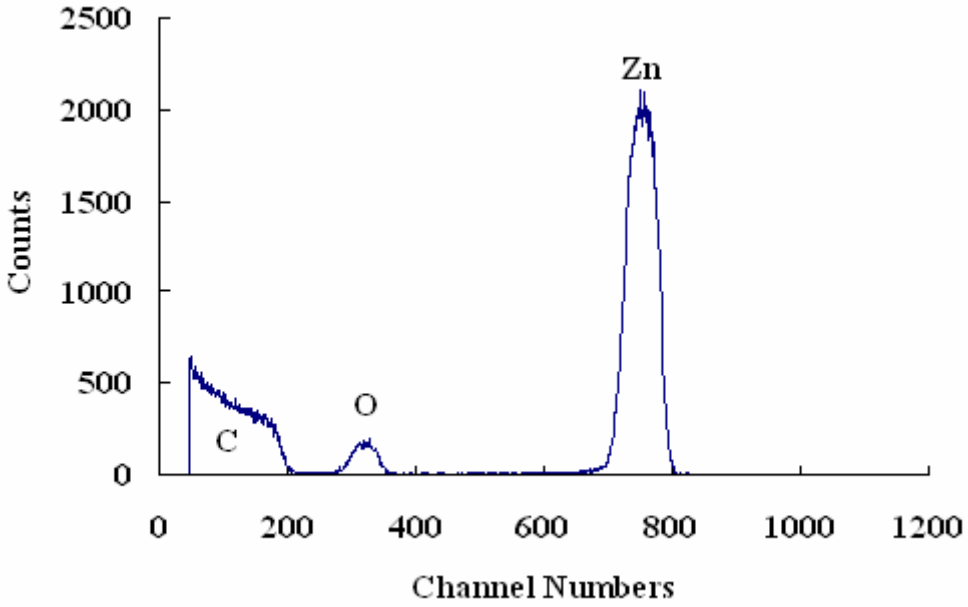

Figure 5-2. RBS spectrum of ZnO

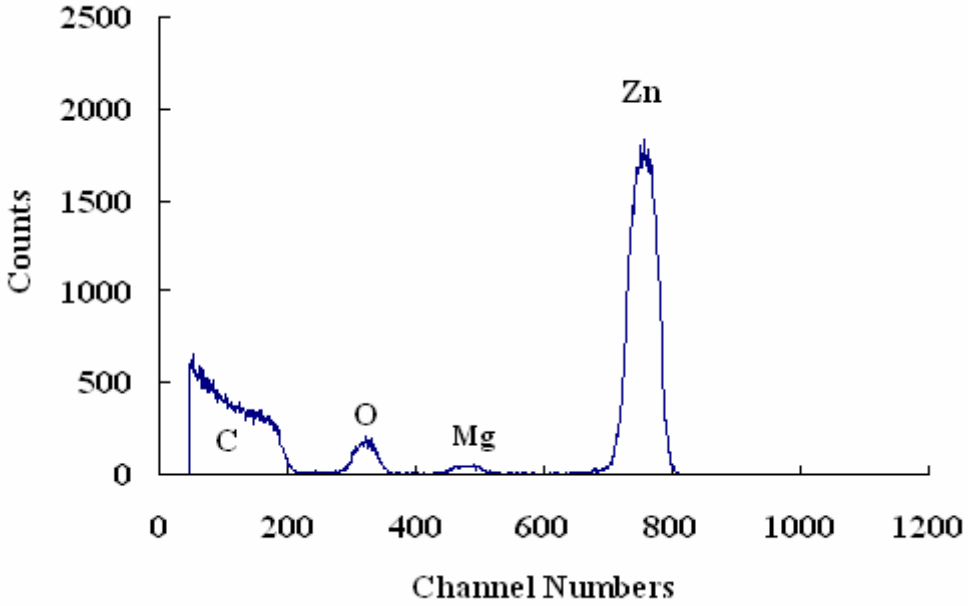

Figure 5-3. RBS spectrum of MZO

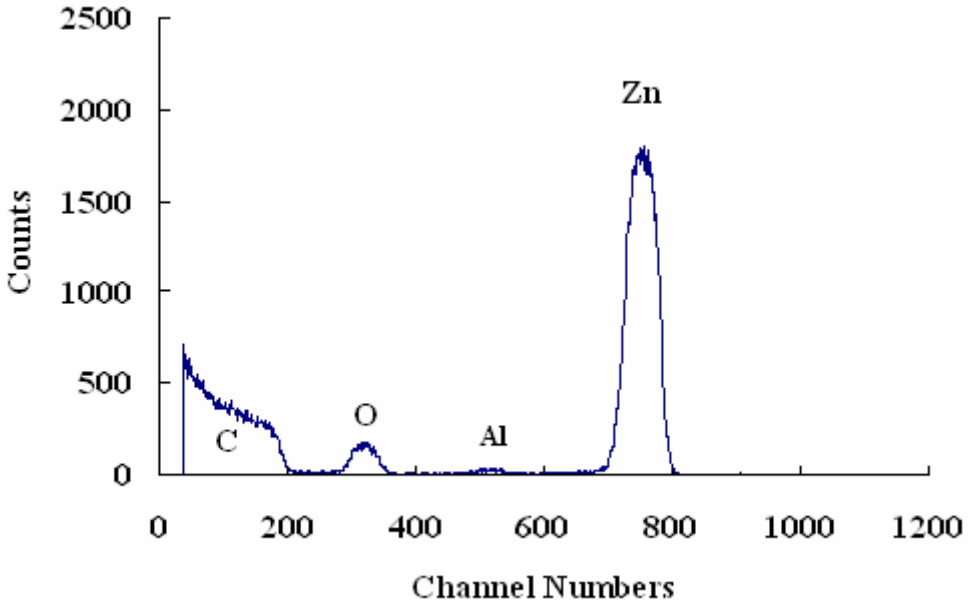

Figure 5-4. RBS spectrum of AZO

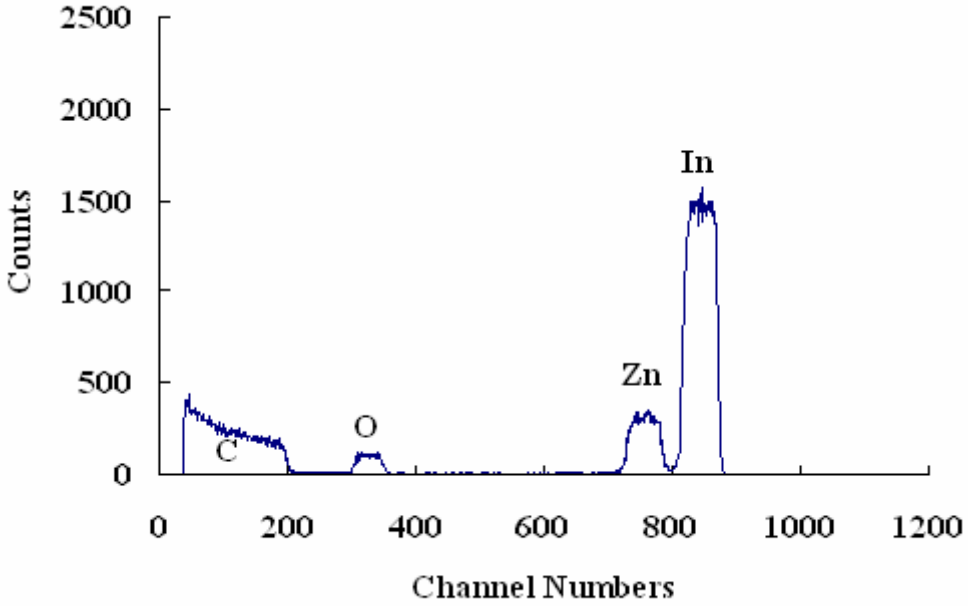

Figure 5-5. RBS spectrum of IZO

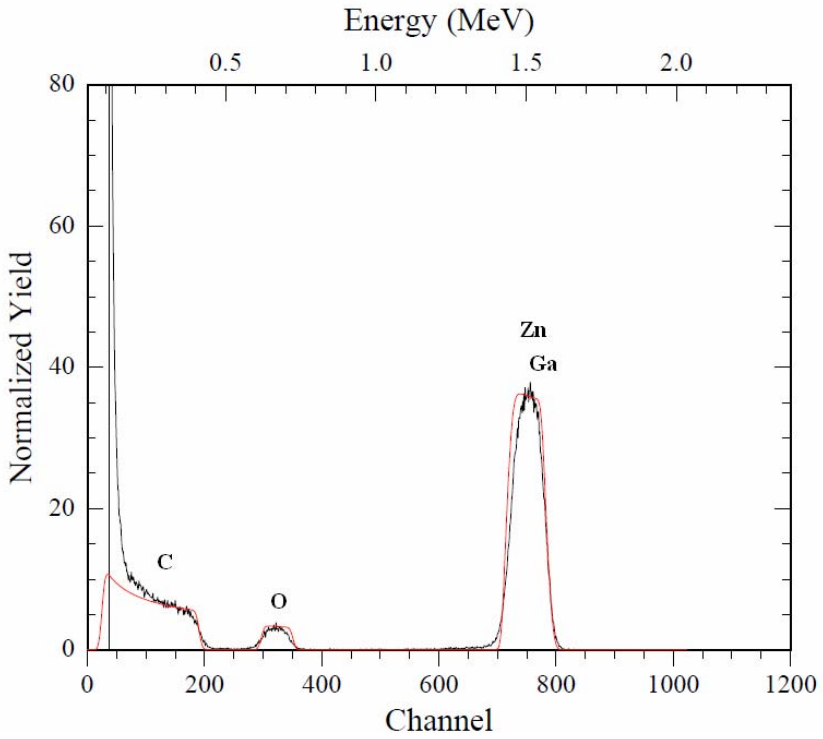

Figure 5-6. RUMP simulation fitting of GZO RBS spectrum

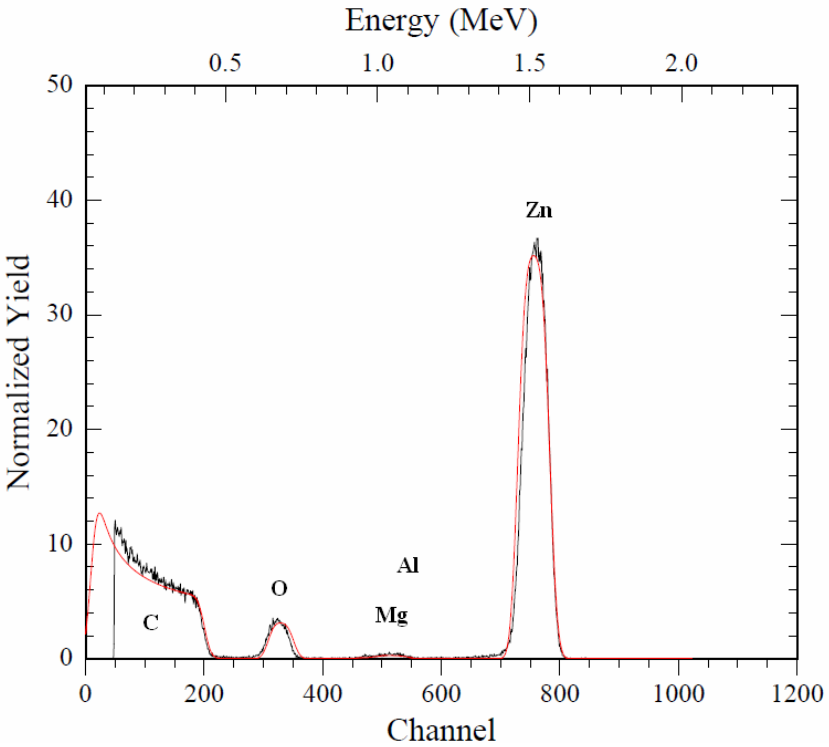

Figure 5-7. RUMP simulation fitting of AMZO RBS spectrum

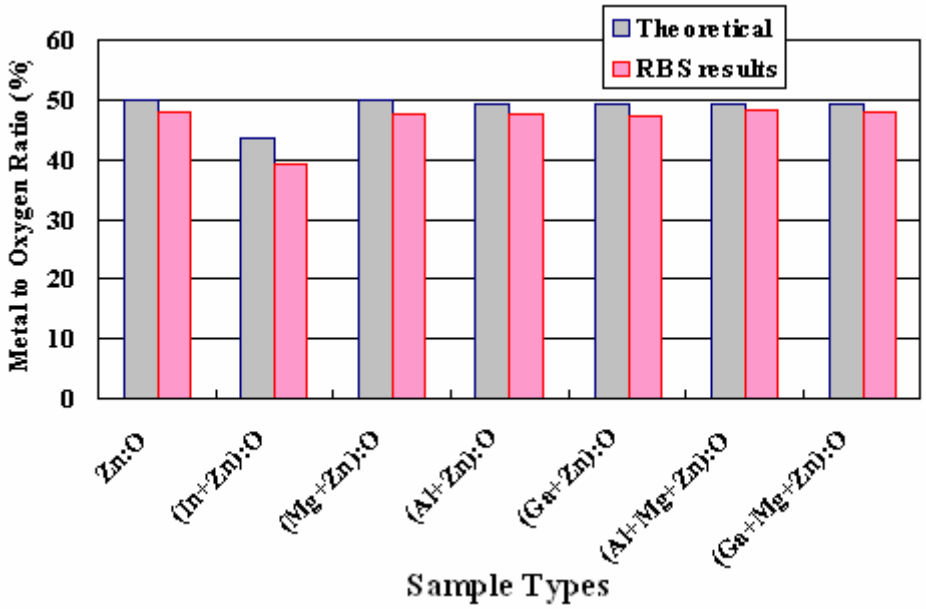

Figure 5-8. Metal to oxygen ratio of the TCOs thin films (RBS analysis)

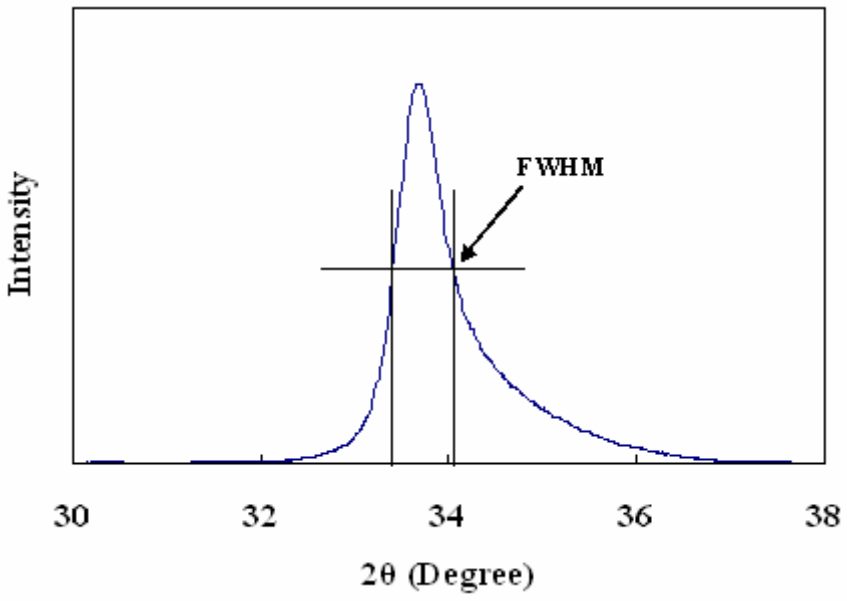

Figure 5-9. XRD spectrum of ZnO

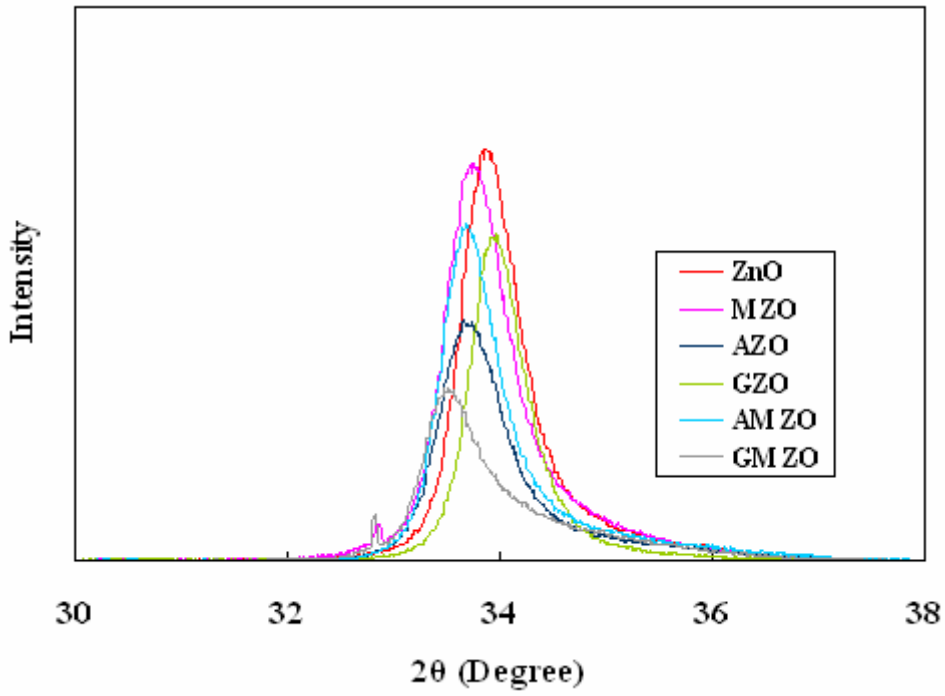

Figure 5-10. XRD spectrums of ZnO, MZO, AZO, GZO, AMZO, GMZO

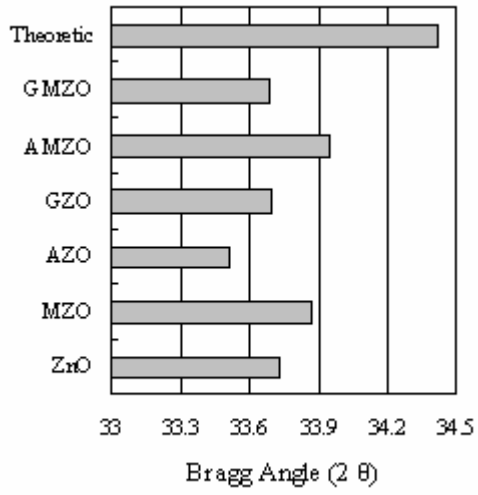

Figure 5-11(a). Bragg angle of TCOs

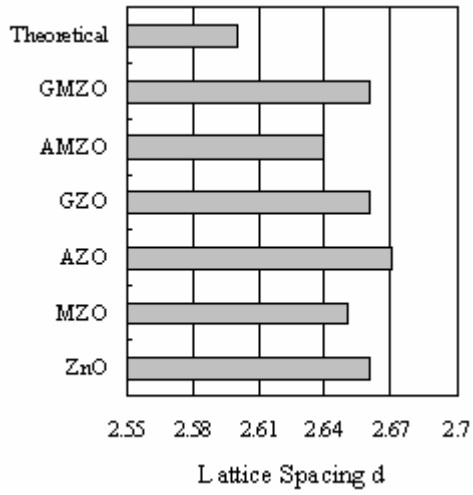

Figure 5-11(b). Lattice spacing d of TCOs

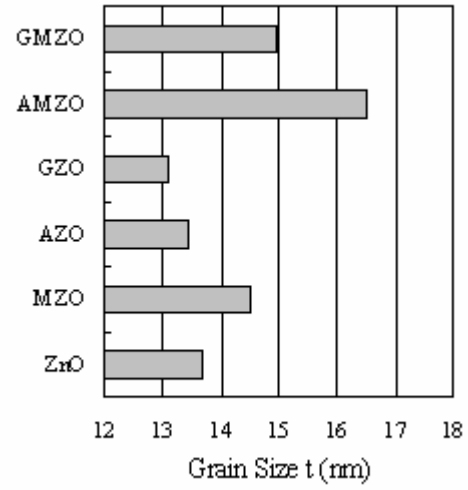

Figure 5-12(a). Grain size t of TCOs

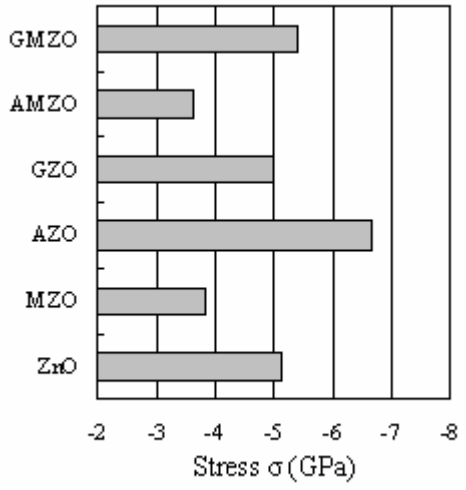

Figure 5-12 (b). Stress σ of TCOs

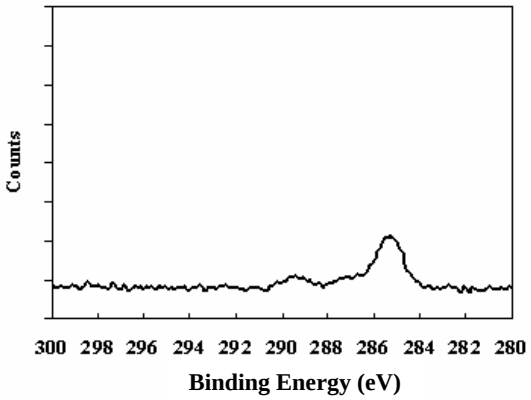

Figure 5-13(a). XPS C 1s before sputtering

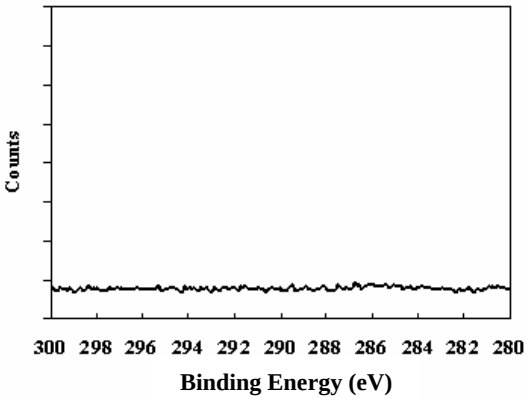

Figure 5-13(b). XPS C 1s after sputtering

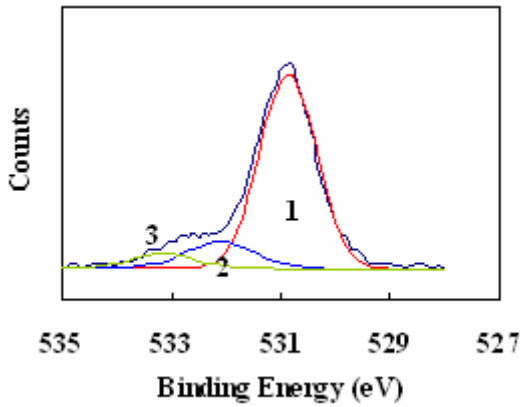

Figure 5-14(a). XPS O 1s of ZnO

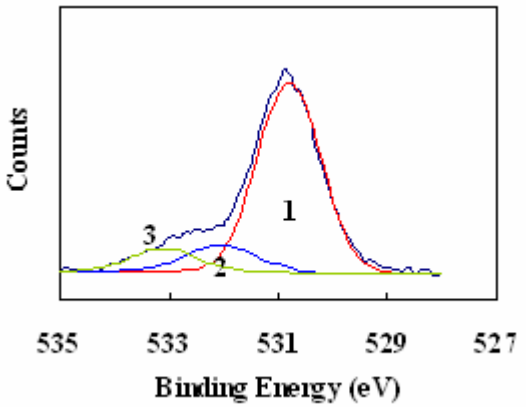

Figure 5-14(b). XPS O 1s of MZO

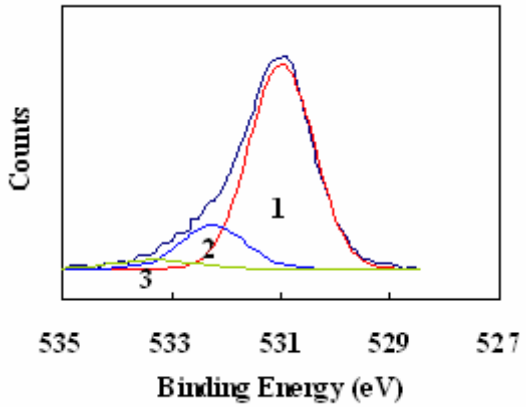

Figure 5-15(a). XPS O 1s of AZO

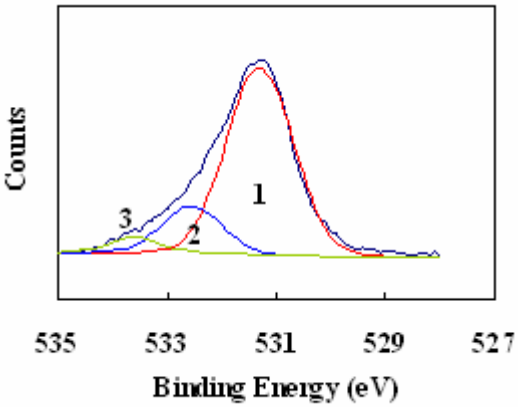

Figure 5-15(b). XPS O 1s of GZO

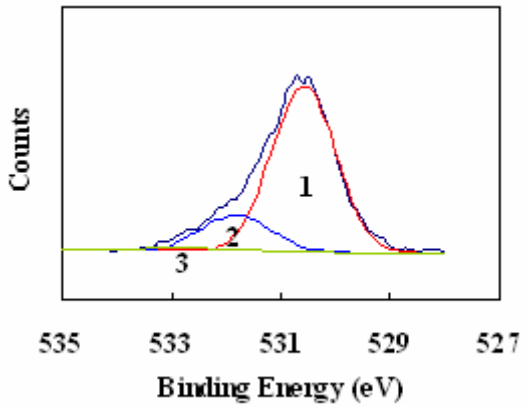

Figure 5-16(a). XPS O 1s of AMZO

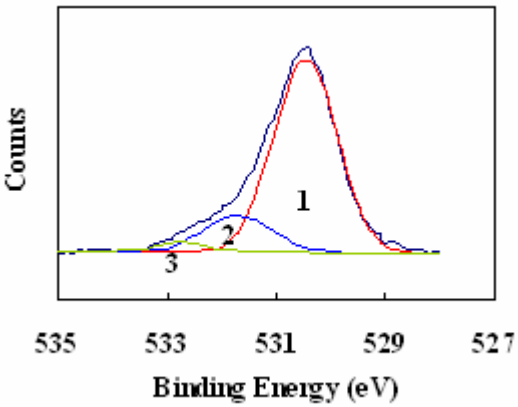

Figure 5-16(b). XPS O 1s of GMZO

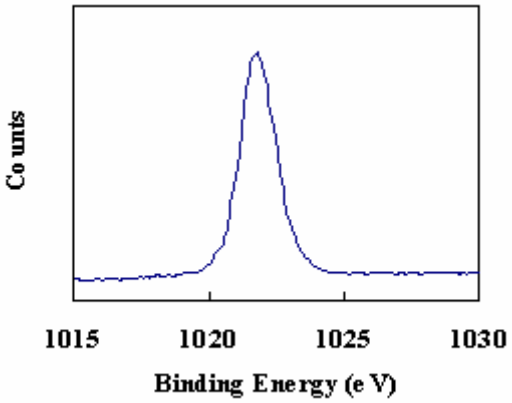

Figure 5-17(a). XPS Zn $2p_{3/2}$ of ZnO

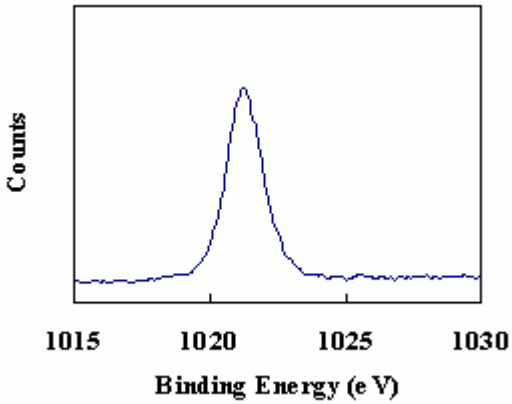

Figure 5-17(b). XPS Zn $2p_{3/2}$ of AZO

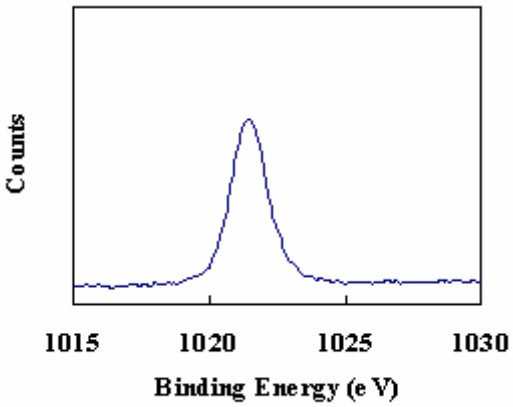

Figure 5-18(a). XPS Zn $2p_{3/2}$ of GZO

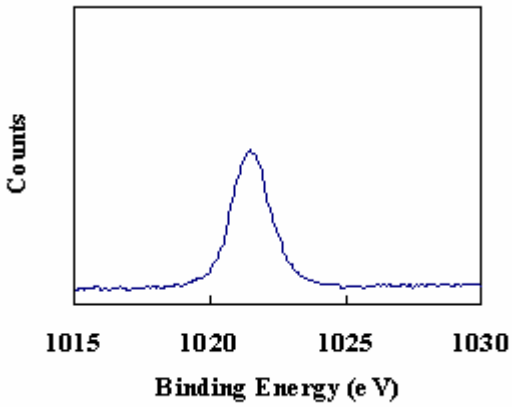

Figure 5-18(b). XPS Zn $2p_{3/2}$ of AMZO

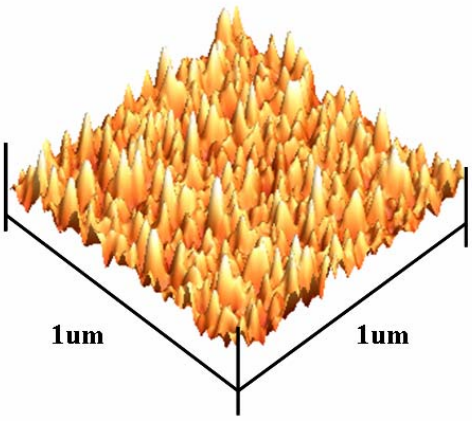

Figure 5-19(a). AFM photo of ZnO

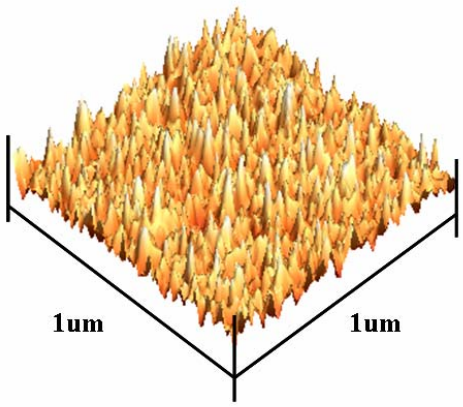

Figure 5-19(b). AFM photo of AMZO

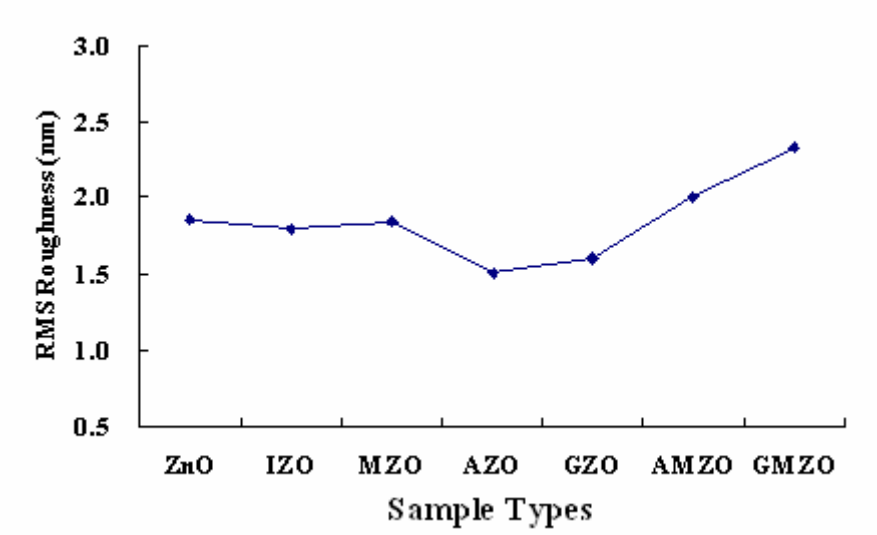

Figure 5-20. RMS roughness of the TCOs films deposited at room temperature

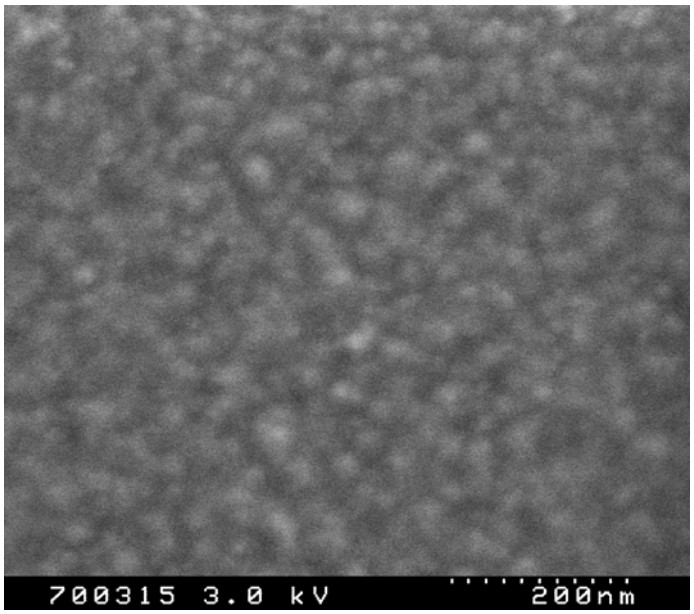

Figure 5-21. SEM photo of ZnO

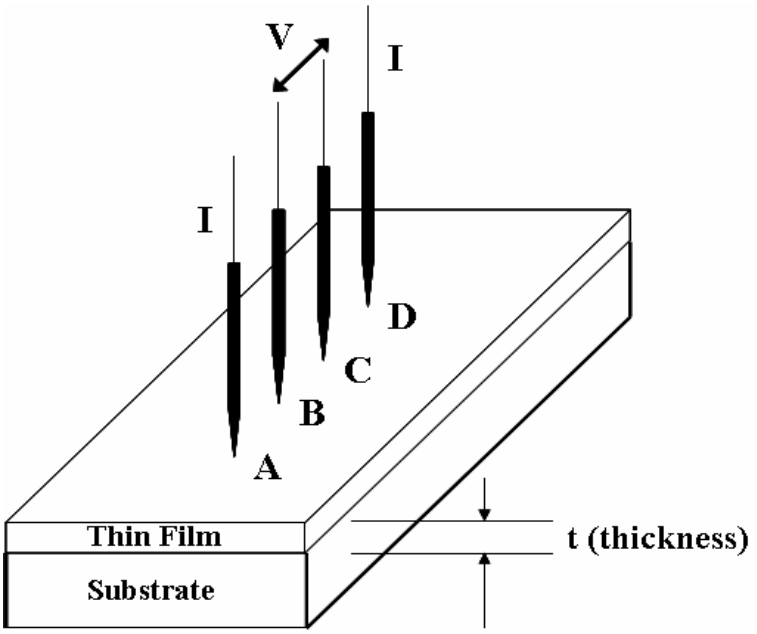

Figure 5-22. Four pin probe for surface resistivity measurement

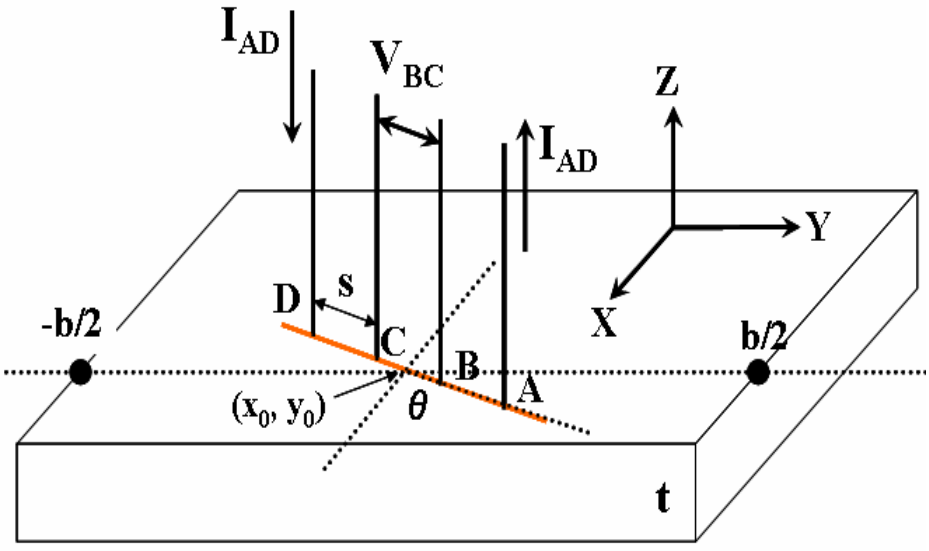

Figure 5-23. Resistivity correction factor (RCF) calculation referring coordinates

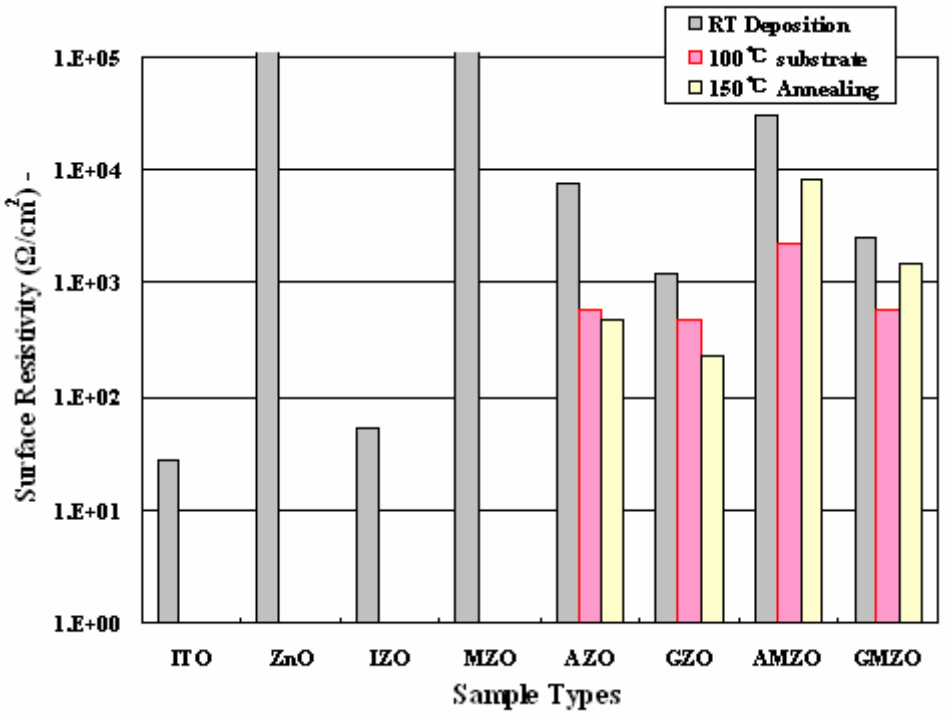

Figure 5-24. Surface resistivity of TCOs thin films

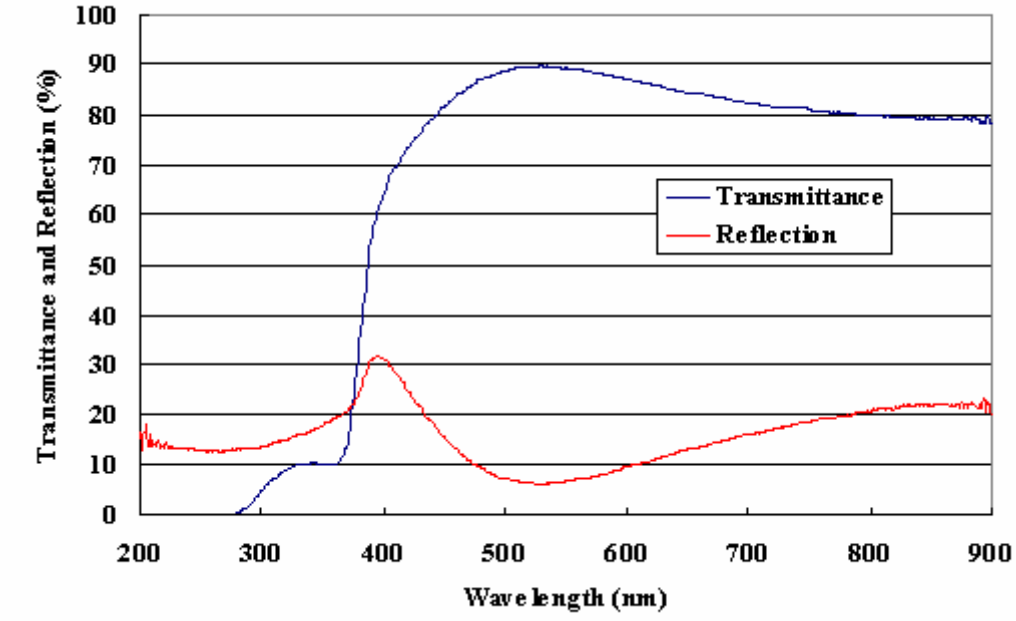

Figure 5-25. Transmittance and reflectivity of ZnO thin film

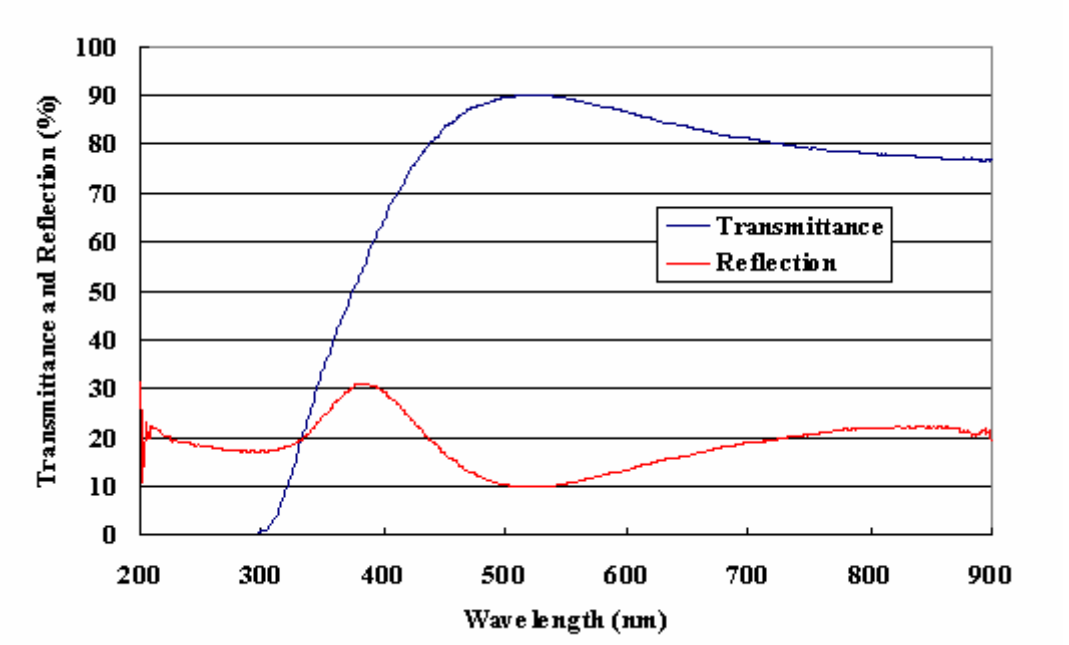

Figure 5-26. Transmittance and reflectivity of IZO thin film

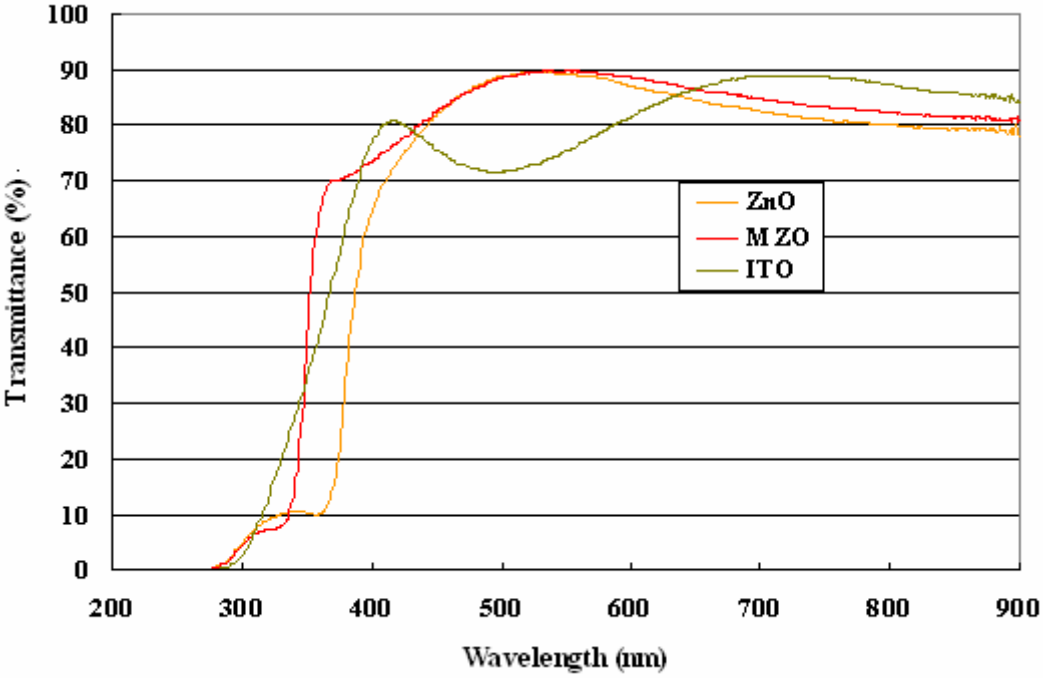

Figure 5-27. Light transmittance of ZnO, MZO and ITO thin films

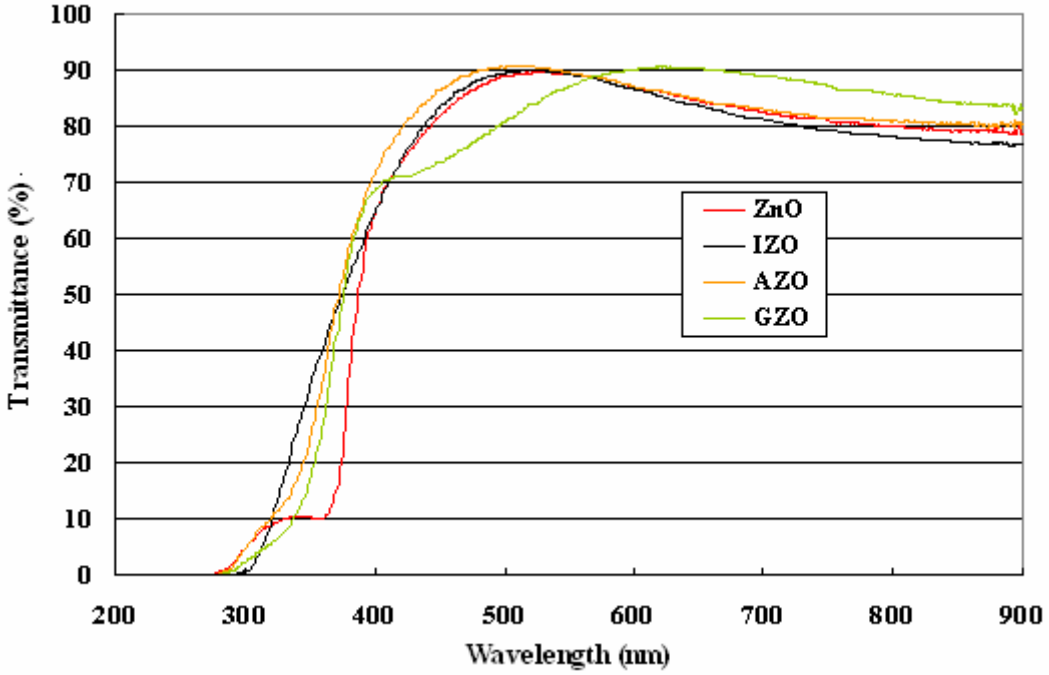

Figure 5-28. Light transmittance of ZnO, IZO, AZO and GZO thin films

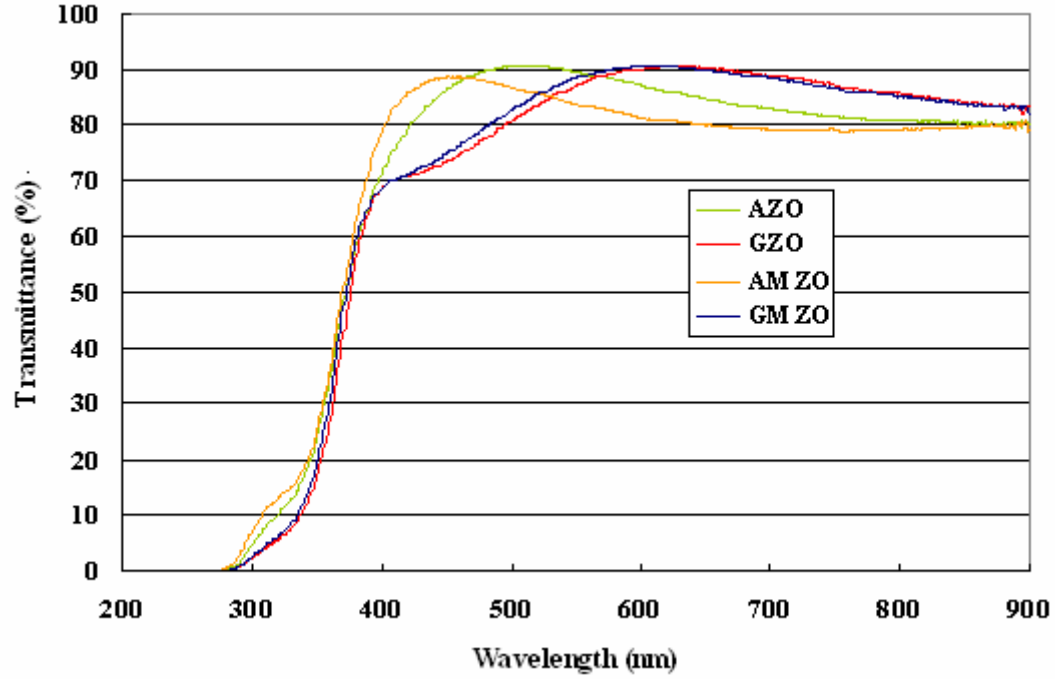

Figure 5-29. Light transmittance of AZO, GZO, AMZO and GMZO thin films

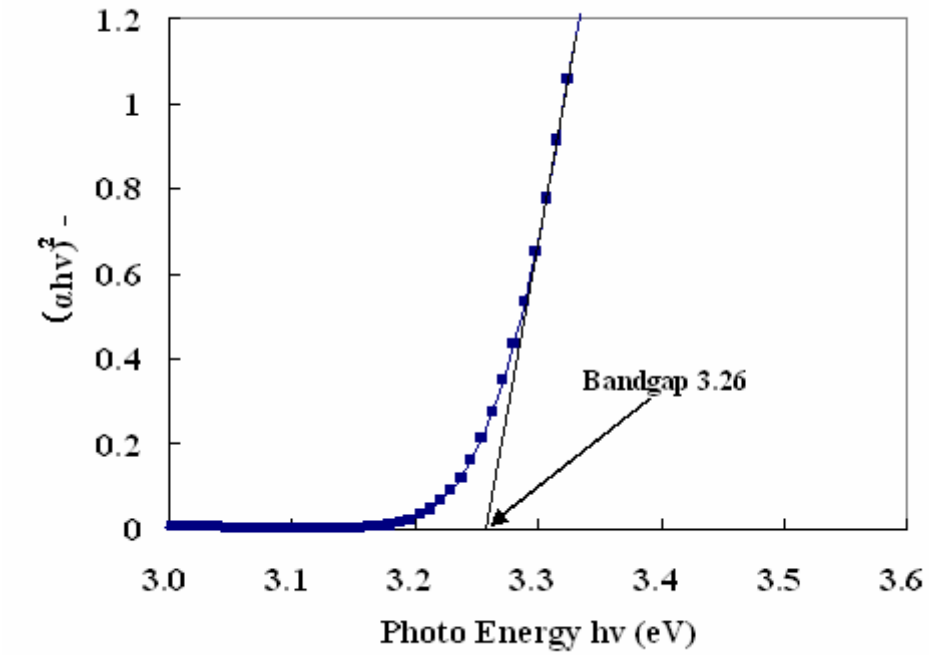

Figure 5-30. Band gap calculation of ZnO

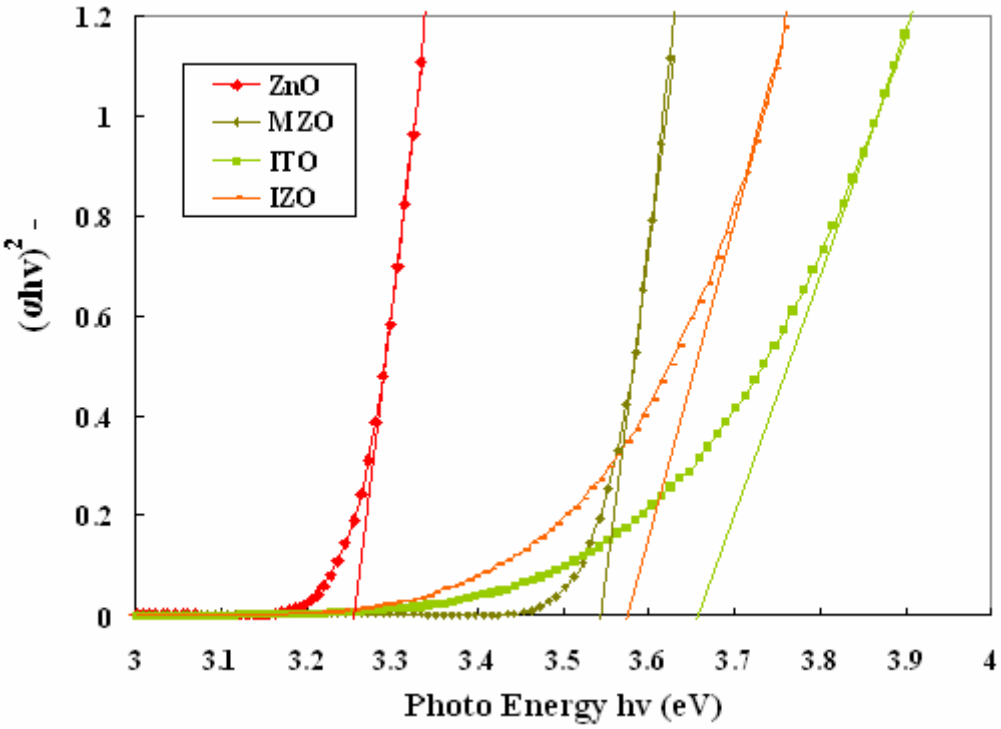

Figure 5-31. Band gap calculation of ZnO, MZO, ITO, IZO

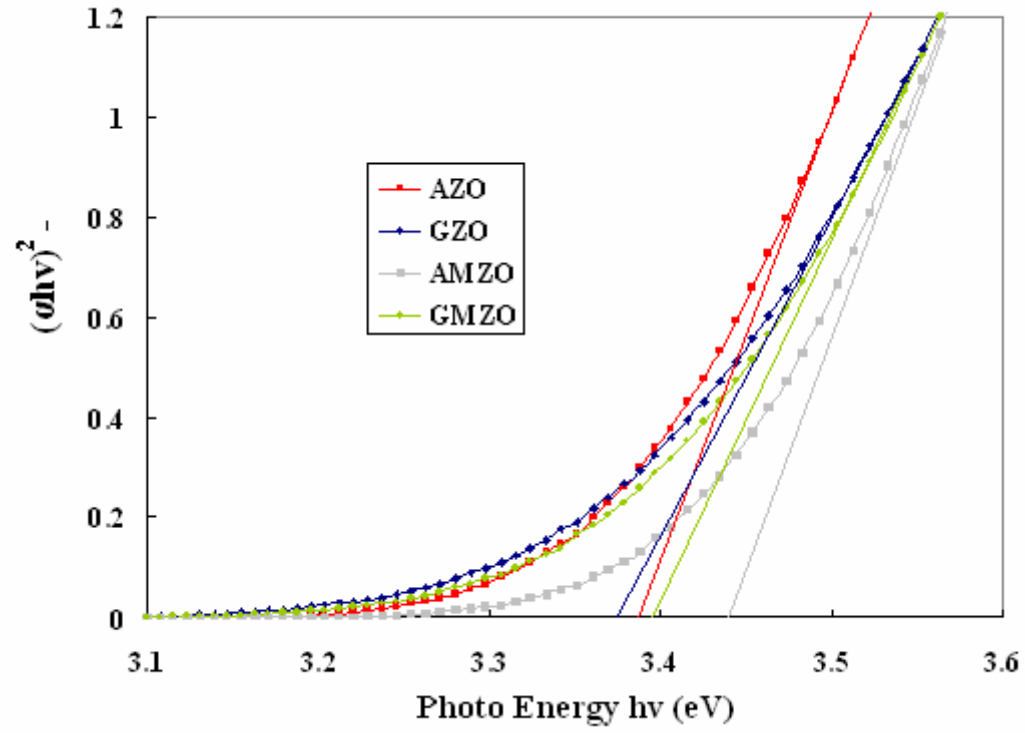

Figure 5-32. Band gap calculation of AZO, GZO, AMZO and GMZO

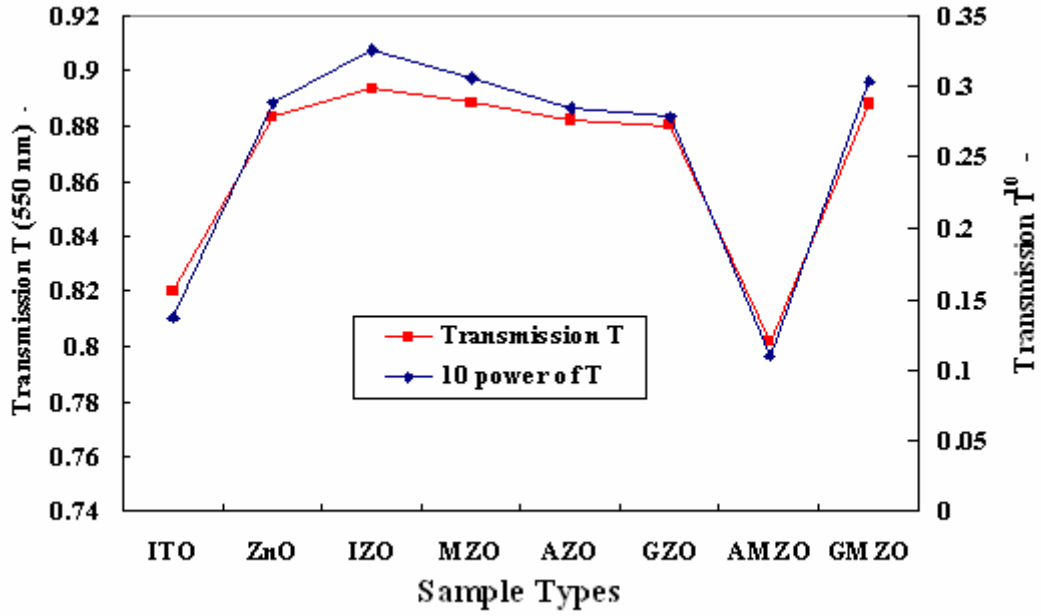

Figure 5-33. Light transmission and its 10 power of TCOs thin films

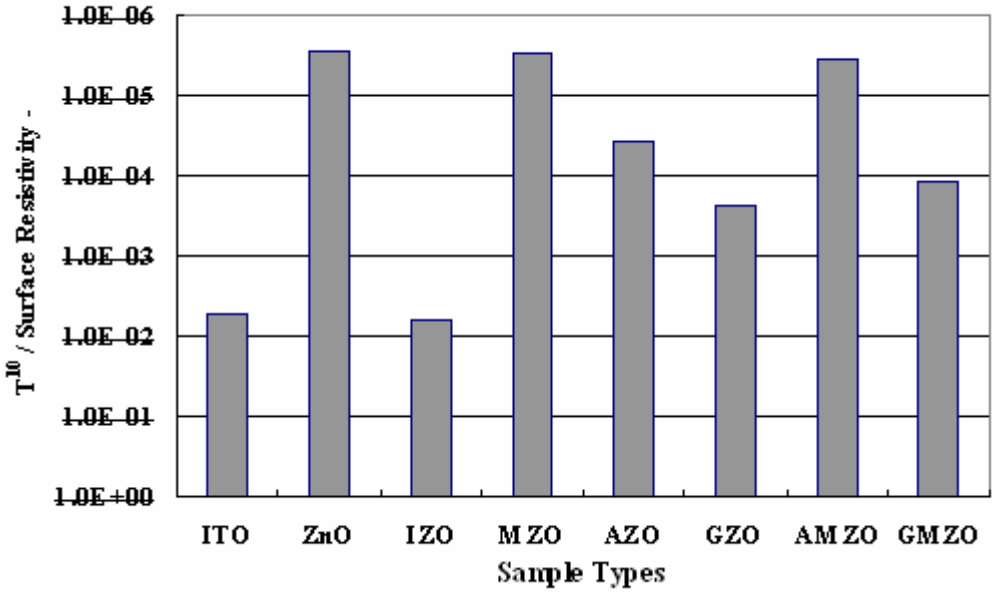

Figure 5-34. Figure of merit of TCOs thin films

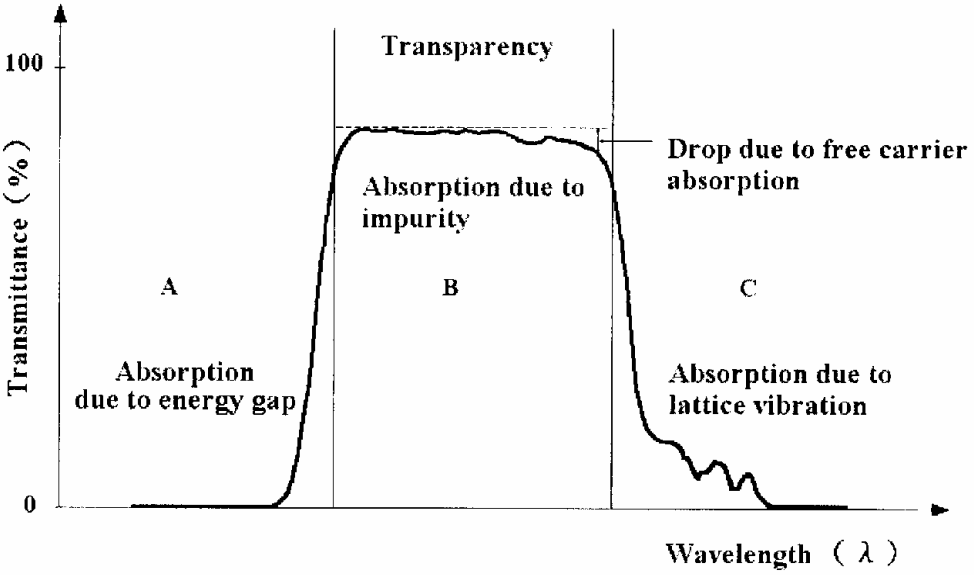

Figure 5-35. Light transmittance at each wavelength area.

(Reference: H. K. Pulker, Applied optics, 18,12 (1971))

Chapter 6

Barrier Layer to Water Vapor Permeation

6.1 Introduction

When polymeric substrates are employed in flexible display applications, a barrier layer is required to protect the enclosed functional materials and layers from oxygen and water permeation. The organic light emitting diode (OLED) materials deposited on PET substrates survive only a few hours when exposed to atmospheric conditions due to the high diffusion of oxygen and water vapor through the native polymeric substrate [1, 2]. The extreme sensitivity of OLEDs to water vapor induced degradation places severe demands on the barrier performance of flexible, thin film coating. Consequently, the major challenge in the development of plastic substrate base OLED displays has been the oxygen and moisture permeability of standard plastic films and the corrosive effect of moisture on the active components in the display. Without good barriers, the flexible OLED industry just isn't going to happen.

The micro-structural and gas barrier properties of transparent metal oxide layers deposited on plastic substrates are of great importance to the food packaging and the flat panel display industries. In the past ten years, an increasing need has risen for transparent flexible packaging with gas barrier properties. Transparent barrier packaging enables viewing of the product, microwave ability and fewer environmental concerns for better cyclability [3]. For these applications, metal oxides and nitrides, such as SiO_x, Si_3N_4, AlO_x, TiO_x have been extensively investigated. Due to the high melting temperatures and dielectric nature of these materials, high rate vacuum deposition presents a substantial challenge. In addition, thermal limitations of the polymeric substrate typically require inorganic film deposition with substrate temperature at room temperature or below 100 ℃. There are a lot of methods experimented for the deposition of the transparent barrier films using thermal and electron beam evaporation, DC, AC, RF and microwave sputtering etc., and many factors affect the final properties of vacuum deposited thin films. It all aims to the process providing the highest density, lowest defect number and smallest defect size produces the best barrier film. In this study, the transparent barrier films were deposited by the electron beam evaporation, and also used the ion beam assisted deposition to enhance the properties of transparent barrier thin films. Compared to sputtering deposition, electron beam evaporation has high deposition rate, and the thin films deposited have high purity.

Transparent silicon oxide and aluminum oxide thin films are extensively used to improve the

barrier properties for flat panel display technologies, and it is can be utilized on polymer-based substrates [4, 5]. The lightweight polymeric substrates are used in flexible display, and are demanded as protection of the enclosed functional materials from water vapor permeation. The degradation place induced by water vapor permeation through a flexible substrate is a damaging consequence to the extreme sensitivity of OLED materials. It is apparent that the water vapor barrier properties of these oxide films are currently limited by defects such as nano-scale pores and more seriously by micro-scale pinhole defects [6]. The silicon oxide coatings on PET have been the most prominently studied gas barrier system. A recent study has indicated that sputtered indium tin oxide thin films can demonstrate very low oxygen and water vapor transmission rates [7]. The silicon oxide used as the barrier layer deposited in this study was expected to have much better thin films property for the low water vapor permeation and higher optical transmission by adding the ion beam assisted deposition process [8, 9].

6.2 Properties of Barrier Thin Film Deposition

In this study, SiO_2 was used as the evaporated target placed in a crucible evaporated by electronic beam for the barrier layer. Electronic beam evaporation method was used generally in vacuum-deposited barrier layers. Figure 3-7 shows the whole system including the electronic beam evaporation device, the electron cyclotron resonance (ECR) ion source, and a heater. The incident angle of ion beams from ECR ion source is 45° to the target surface. The sample holder was rotated at the constant speed to achieve the uniform deposition and irradiation. ECR ion source for ion beam assisted evaporation was used in the next section and described later. During the deposition process, an oil diffusion pump and a rotary pump evacuated to 3×10^{-3} Pa as the base pressure. The working pressure became 3×10^{-2} Pa during the deposition process, when oxygen gas was introduced in 8 ccm. During the barrier thin films deposition, the thickness and the deposition rate were monitored by the quartz thickness monitor located close to the samples. After deposition, the thickness was re-measured by the method described at chapter 5 using Tencor Alpha-Step 500 Surface Profiler. The deposition rates were approximately 1 nm / sec, and the target thickness was 100 nm. SiO_2 is a brittle material, and it cannot be deposited too thickly to avoid the crack when the substrates are bent to a curvature [10]. Figure 6-1 shows one example of the SiO_x films crack and defect observed by the SEM. The SiO_x thin films were deposited on different kinds of substrates including PET, glass, silicon and carbon for the various analysis of the thin film properties. After the deposition process, the SiO_x thin films should be handled with care, since SiO_x is a brittle material and easily cracked.

Rutherford backscattering spectroscopy (RBS) was used for analysis of the chemical composition

of the barrier thin film. During the electron beam evaporation deposition, the composition of thin films was a little different from the evaporated target SiO_2. Figure 6-2 shows the RBS spectrum of SiO_x deposited on carbon substrate. The cross section of silicon and oxygen when incident He^{+2} at 2MeV are 24.77 and 7.414 respectively. The concentration of silicon to oxygen was calculated from the peak area subtracting background and the cross section. It was 31 % for silicon and 69 % for oxygen. Compared to the evaporated target SiO_2, the concentration ratio of oxygen increased when it was deposited as thin film by the electron beam evaporation at room temperature. Figure 6-3 shows the RUMP simulation and fitting of the measured RBS spectrum. The measured spectrum was fully fitted to the simulation data by using the calculated ratio above as the parameters.

The density of the SiO_x thin film was evaluated using the measured RBS spectrum and the thickness. Referring to Appendix in RBS part, the film thickness can be calculated if we know the stopping power of elements and the loss energy in the thin film. ΔE is the loss energy between scattered particle and incident particle and can be calculated from the width of the peak of the RBS spectrum. And the stopping power can be calculated by SRIM. Depending on the different density setup in SRIM, the stopping power is varied. We tried to adjust the density value input, and used the SRIM output stopping power with ΔE detected from RBS spectrum. The calculated thickness was close to the thickness measured by the Surface Profiler. After this loop calculation, the proper density was known when the calculated thickness was nearly equal to the measured thickness. This proper density was regarded as the density of the thin film deposited. The calculated density of SiO_x was 2.19 g /cm^3.

For the surface chemical composition, X-ray photoelectron spectroscopy (XPS) was used to analyze the thin films. The detail of principle of XPS is described in Appendix. The X-ray used was a monochromatic Al, Kα (1486.6eV), and X-ray anode voltage was 14 KV, emitting current was 10 mA. The sample was measured 80 eV for wide mode and 20 eV for narrow mode. The peaks of oxygen and silicon are located at O 1s 523 eV to 543 eV, Si 2p 89 eV to 109 eV, and Si 2s 143 eV to 163 eV, respectively. Figure 6-4 shows the SiO_x XPS spectrum, and the peaks were measured. Before the measurement, we used the argon ion sputtering to clean the impurity from the surface, it was obviously observe that the C 1s peak was removed. XPS detected the surface chemical structure about 2 nm to 4 nm depth. After the thin films deposition and transferred to the analysis, the exposed samples easily attach to the impurities. It affected the XPS measured results. In this case, we used the argon ion etching. Figure 6-5(a) shows the XPS O1s spectrum and Figure 6-5(b) shows Si 2p spectrum, and they can be completely fitted in one peak. It indicated the Si was bonded to oxygen totally.

For the optical properties of SiOx thin films, Figure 6-6 shows the transmittance and reflectivity of SiO_x thin film with glass substrate. The average transmission of glass measured was over 92 %, and the SiO_x layer with glass had the average transmittance almost over 90 %.

6.3 Ion Beam Assisted Deposition Improvement

The ion beam assisted deposition (IBAD) technique is used during the growth of thin films deposited by conventional methods, such as electron beam evaporation [11]. The Ion bombardment of films during the deposition is particularly effective in modifying film properties due to the effects of ion mixing and ion sputtering [12]. IBAD processes were invented to provide independent control of the deposition parameters, the ion beams are not derived from elevated pressure plasmas but rather stream from an ion source through a high vacuum ambient. At IBAD deposition, ion sources are generally employed in two distinct modes. The first uses an inert gas ion beam to control sputter atoms from a target: here the function of the beam is to promote the supply of target atoms for deposition. In the second mode, the beam is composed of inert argon or oxygen reactive gas ions. It is directly aimed at the substrate: here the purpose of the beam is to modify the properties of the growing film by some combination of bombardment, reaction or burial within. The second mode of IBAD was used in this experiment. IBAD combined two distinct physical operations: a physical vapor deposition and a simultaneous bombardment of the surface with ion beam. The ion bombardment provides the main benefits as followings: enhancement of adatom surface mobility, stimulation of the early stages of film formation, for example the nucleation, growth and coalescence, crystallization of amorphous films and amorphization of crystalline films, increasing adhesion between film and substrate, modification of film stress, and simulation of film sorption effects and film surface reactivity.

During the ion beam irradiation, the following physical processes occurred: sputtering of impurities from substrate surface by ion impact, and the penetration and entrapment of coating and support gas in the growing film. K.H. Muller (1986) developed the model about IBAD to explain the densification of thin films by ion assistance [13-15]. The model was shown in Figure 6-7(a), when the incident ion interacts with the target particles and produces a number of knock-on atoms which in turn produce more knock-on atoms, and a collision cascade evolved in. The collision cascade and penetration of ions occurs under a few inter-atomic spaces, and some knock-on atoms overcome the surface potential and leave the films as sputtered particles. If the transferred kinetic energy is not sufficient to knock a target atom out of its site, the transferred energy is absorbed in the form of lattice vibrations. He studied the atomic rearrangement processes occurring when the thin films are bombarded by ions during growth shown in Figure 6-7(b). The surface depletion and density enhancement by ion bombardment and the surface refilling by vapor atoms. Vacancies near the surface which are caused by bombarding ions are partially refilled by the newly arriving vapor atoms. This process results in downward packing of material, such that it no longer grow in porous structure but instead grow in densely packed structure. Moreover, he refined the process further employing a molecular dynamics approach, and concluded that the most important ion surface

interaction processes which lead to microstructure modifications are (1) atoms accumulated to form a void structure are dislodged and forward sputtered by incoming ions causing the void region to remain open until filled by new depositing atoms; (2) ion induced surface diffusion, local heating, collapse of voids and re-crystallization are the major mechanisms causing improved layer growth in IBAD process.

For the original deposition of the barrier thin films used in this experiment, most vapor deposited films have loosely packed structures resulting from low atom mobility which, in turn, results in high internal stress, extended defects, moisture adsorption, and so on [16]. IBAD during the evaporation offers a number of variables to improve the film properties. An ion source and an evaporation source which are operated independently makes IBAD processes are controllable, reproducible, and flexible for the ion flux, energy, and the incident angle. Hence, IBAD process was considered as an active technique to improve the performance of the barrier layer.

Figure 3-7 shows the electron cyclotron resonance (ECR) ion source and the electron beam evaporation included in the system for the IBAD processes. Here, the electron beam evaporation used to deposit the thin film simultaneously to the target sample was irradiated ion beam emitted from the ECR ion source. The chamber was evacuated to a base pressure of 3.0×10^{-3} Pa. During the ion beam injection, oxygen gas introduced in 8 ccm as the ion source, was generated by the ECR ion source, and the working pressure was about 3 to 2×10^{-2} Pa. The accelerated voltage was setup at 0.5 KV, 1 KV, and 1.5 KV for the various sample. After the ion source stabilization, the electron beam evaporation worked to deposit the SiO_x thin films. The process temperature was at room temperature and the sample holder rotated at the constant speed to achieve the uniform ion irradiation and thin films deposition. The ECR ion source ion current density was measured and described in Chapter 2, and the different kinds of substrates were deposited on for the various analysis. From the RBS spectrum of SiO_x thin film deposited in 100 nm and 1KeV ion energy for IBAD process. The concentration of silicon to oxygen was 31 % to 69 %, respectively. It was similar to the SiO_x thin film deposited without IBAD process. When we compared the thin film composition at 0.5 KeV, 1KeV, 1.5KeV IBAD and without IBAD, it demonstrated nearly no difference when the IBAD process was applied during the deposition.

The density of SiO_x thin film was calculated by the method introduced in foregoing section. The loop calculation of density input in SRIM and used its stopping power to let the calculated thickness approach the one measured by the profiler. The density of SiO_x deposition varied in the different conditions is shown in Figure 6-8. It indicated the IBAD indeed work to densification. The bulk density of SiO_2 is 2.65 g/cm^3, and the SiO_x thin film deposited without IBAD process was 2.19 g/cm^3, and it increased to 2.24 g/cm^3 at the 0.5 KeV oxygen ion beam assisted. Then, it was improved to 2.35 g/cm^3 at 1 KeV and 2.36 g/cm^3 at 1.5 KeV. The density increased by adding IBAD process during the deposition, and it increased much more when the accelerated voltage increased.

Then go to stabilization after 1 KeV accelerated voltage. The density of SiO_x films improved after the IBAD process, and it was expected that the higher density of barrier layers contribute to the lower water vapor permeation.

The oxygen IBAD process not only enhanced the thin films density, it also improved the light transmittance during the visible wavelength of 420 nm to 760 nm shown in Figure 6-9. The average light transmission of the SiO_x layer with glass after the oxygen IBAD process during the visible wavelength was over 91 %. It was better than the sample without IBAD had light transmission almost near 90 %.

6.4 Water Vapor Permeation Testing

After the SiO_x thin films were deposited with and without IBAD in 500 V, 1000 V and 1500V on PET and glass, the water vapor permeation testing was applied for the barrier property. We used calcium oxide as the testing material for water vapor transmission. Calcium oxide (CaO), commonly known as burnt lime, is a widely used chemical compound. It is a white, caustic and alkaline crystalline solid. Calcium oxide has the white solid appearance, and has a density of 3.35 g/cm^3. It is easy to have a chemical action with H_2O and produces heat energy by the formation of the hydrate, as in the following equation:

$$CaO + H_2O \rightarrow Ca(OH)_2 + 878\,Kcal\,/\,Kg \qquad (6\text{-}1)$$

It was considered to make a calcium oxide thin film between glass and silicon oxide thin film [17]. Then put the sample into the environment testing equipment. When water vapor transmitted across the layer of SiO_x as a barrier layer, it has a chemical action with calcium oxide layer. Then the part of CaO becomes to $Ca(OH)_2$, and the properties of thin films will change. G. Nisato et al. used reactive metals calcium as test probes for water vapor ingress and the subsequent development of the “calcium test” [18]. The test optically monitors the degradation of thin, vacuum deposited, calcium layers (<100nm thickness) on test substrates. The chemical reaction of water vapor with the thin Ca layer produces a transparent oxide or hydroxide resulting in increased light transmission. The advantage of this test is the ability to visualize coating defect sizes and number densities. This is particularly important in OLED displays, where the existence of large flaws will generate unacceptable dark spots. The Ca test has widespread adoption in the OLED community largely due to its direct correlation with OLED device life time. In this experiment, calcium coating has been considered, but we didn’t use it, since calcium is a very active material and the thin film coating cannot be smoothly applied in our current equipment. We used the near infrared (NIR) radiation to

detect the OH bonding of $Ca(OH)_2$, and JIS Z0208 testing methods for determination of the water vapor transmission.

For the NIR analysis, the part of the electromagnetic spectrum visible to the human eye extends from about 400 nm to 700 nm while the infra-red (IR) extends from 2500 nm to 15000 nm. The intermediate region between the IR and the visible is termed the near infra-red (NIR) shown in Figure 6-10. Early this century Coblentz observed that compounds with similar chemical grouping have characteristic absorption bands in the IR [19]. Chemical bonds in molecules are natural oscillators which are vibrating all the time. Thus, the molecule will absorb radiation when the vibrations occur at the frequency of the radiation wave. For anything as small as a molecule, vibration can only occur at fixed frequencies so that radiation is absorbed in discrete packets. Thus, the molecule can only have characteristic absorption bands corresponding to these fixed frequencies and the amount of radiation absorbed at each frequency is proportional to the number of similar chemical bonds which are vibrating [20, 21]. Despite the success of IR, 1964 Norris developed a new method of measurement of moisture in grain using NIR [22]. The NIR region of the spectrum had been rather neglected because measurement was not possible until photoelectric detectors had been invented. Like any simple harmonic motion, the vibrations which give rise to fundamental IR absorption bands have corresponding overtones at twice and three times the frequency which occurs in the NIR. NIR has the ability to analyze the molecular composition of compounds by measuring its unique spectral. It has the advantage of rapid, non-contact, non-destructive sampling.

The NIR instrument used in this study is InfraAlyzer 500 (BRAN+LUEBBE). The measured wavelength was from 1100 nm to 2500 nm. The initial experiment was to test the NIR spectrum measurement for the chemical reaction of calcium oxide to water and become hydrate [23]. The calcium oxide was put in the environment testing equipment for one hour and three hours. The environment was setup at 50 ℃ and 90 % RH. The appearance of testing sample changed from the white solid shape to part white solid and part white powder after one hour, and became a white powder totally after three hours. It was evident that calcium oxide absorbed water and become the calcium hydrate. For the environment of water vapor condition, the bench-top type temperature and humidity chamber SH-241 (ESPEC Corp.) was used for the environmental testing. It can be operated at the temperature from -40 ℃ to 150 ℃, and humidity ranged from 30 to 95 % RH. Figure 6-11 shows the second differential of NIR spectrum of these three samples, and the second differential spectrum is commonly used in NIR analysis [24]. It is much easier to compare the peak curve difference between the samples. In Figure 6-11, three samples has apparent difference at the wavelength ranged at 1400 nm and 2500 approximately. Figure 6-12 shows the peaks zoom out at the range of 1360 nm to 1440 nm. It is much clear to compare the calcium oxide change by the chemical reaction with water. Referring to the wavelength bond vibration and structure database of NIR, the O-H str. first overtone is at 1410 nm and O-H def. second overtone at 2380 nm [25]. It was

considered the spectrum different from the calcium hydrate with O-H compared to calcium oxide. And the peak intensity increased depending on the amount of H_2O increase.

At the next stage of experiments, we tried to make the thin films in the different conditions of with and without IBAD process. The multi-layers thin films were deposited in one vacuum. On the glass substrate, we deposited 200 nm calcium oxide thin film first, consequently, stack on 100 nm SiO_x thin film deposition. It was thought when the water vapor permeation pass through the layer of SiO_x thin film, it reacted with calcium oxide, then part of calcium oxide film change to calcium hydrate. It was expected to detect it by NIR spectrum. Figure 6-13 shows the second differential of absorbance of the sample in environment testing chamber with 50 degree and 90 % RH and the other one not in it. When we compared the original NIR spectrum, it was not easy to recognize the difference between them. The second derivative was used to distinguish the slight difference between these two spectra. From the wavelength of 1100 nm to 2500nm, these two spectra are almost overlapping, except the region from 1400 nm to 1460 nm. When we zoom out this region, we found the different peaks at the point of 1410 nm and 1440 nm. It was considered that the full O-H bonding made the difference between these spectra, and the results were similar when we compared it with other samples. However, the quantity of CaO changed to $Ca(OH)_2$ in thin film was much fewer when compared to the compounds. Therefore, it is difficult to use it for quantitative analysis, but it can be used for the qualitative analysis.

JIS Z0208 testing method for determination of the water vapor transmission was used for the quantitative analysis of water vapor transmission [26]. The schematic of the dish is shown in Figure 6-14. The testing sample with the circle dimension of 6 mm in diameter was put on the dish, and clipped solidly by a rubber ring to avoid the moisture in, except the center-circle part on the top of dish. Figure 6-15 shows the photograph of this dish with testing sample. The detector material calcium oxide was put in the dish before the testing sample clipped on it. Then the dish was placed in the environment testing chamber for 24 hours, then measured the weight increase from the calcium oxide absorbed moisture to calcium hydrate. According to the weight increase measurement and control should be properly observed. The microbalance (Sartorius CP225D) with 0.01 mg readability located in the independent environment box with the moisture controller was used to measure the weight increase of the samples. The influence from the surrounding can be reduced to minimum.

The environment testing conditions was set at 50 ℃ and 90 % RH, and the samples was exposed to this condition for 24 hours, and measured it as the first value. Then the sample was placed in 50 ℃ and 10 % RH for 30 minutes to dried out the moisture attached or absorbed on the dish surface, and measured it as the second value. From the experiment result, there is about 0.007 g decrease in average during this drying for 30 minutes, and its reproducible error was very low. Figure 6-16 shows the increasing weight to time curve of PET sample without any coating, and it

was observed that the weight increase linearly with time. This reproducible result demonstrated the dish method can be used for the quantitative analysis of water vapor permeation testing.

The area of testing sample with 6 mm diameter circle is 0.002827 m^2. We can calculate the water vapor permeation rate of PET with 125 um from the data of Figure 6-16, it was 8.9 g/m^2 per day on the average at 50 ℃ and 90 % RH condition. The same experiments were repeated and applied to the other samples with 100 nm SiO_x thin films deposited with and without IBAD process at 500 V, 1000 V and 1500 V ions accelerated voltage. Figure 6-17 shows the average water vapor transmission of each sample. Firstly, the PET with 100 nm SiO_x thin films had the water vapor permeation rate of 1.4 g/m^2 per day. It is apparent that the barrier layer coating was effective, and the water vapor permeation decreased a lot from 8.9 to 1.4 g/m^2. When we compared the sample with and without IBAD, the water vapor permeation improved a little. This implies that the density of thin films increased resulted in the less water vapor transmission. The thin films with 1 KV and 1.5 KV accelerated voltage IBAD process had the water vapor transmission rate below 1 g/m^2 per day. And it was almost the ninth part of the PET film without the barrier coating.

In the water vapor permeation testing, the 100 nm SiO_x thin filmed deposited was experimented and obviously had advantageous effect to water vapor transmission. Moreover, the additional IBAD process during the deposition enhanced the waterproof property more effectively.

6.5 Conclusions

Barrier layers are critical for all types of displays based on a polymeric substrate. Compared to glass commonly used in the flat panel display industry, the polymer substrate is much more permeable to water vapor. And it is considered the main defect of liquid crystals and organic light emitting diode materials damage coming from the moisture and oxygen permeation. In this chapter, SiO_x thin film was applied as the barrier thin film and ion beam assisted deposition was used to improve the property of barrier layers.

From the RBS analysis for the thin film spectrum, the thin composition and density was calculated. The ion beam assisted deposition not only improved the density of thin films from 2.19 g/cm^3 to 2.36 g/cm^3, and it also made progress in light transmission with glass from 90 % to 91 % in visible wavelength. The ion beam was effective for improving the properties of thin film deposited.

Finally, the water vapor permeation was tested by NIR spectrum measurement for qualitative analysis, and the dish method for quantitative analysis. The PET films with 100 nm SiO_x deposited with ion beam assisted had the premium water vapor transmission rate below 1 g/m^2 per day when compared to the PET without barrier layer which had 8.9 g/m^2 per days.

References

1. J. S. Lewis, Michael, S. Weaver, IEEE J. Selected Topics in Quantum Electronics, 10, 1 (2004).
2. Y. F. Liew, Hany Aziz, Gu Xu, Zoran Popovic, Applied Pkysics Letters 77, 17 (2000).
3. T. Krug, Ludwig, R. Steiniger, 36th annual Technical Conference Proceedings, Society of Vacuum Coaters, 302 (1993).
4. B.M Henry, A. G. Erlat, A. McGiogam, C.R.M Grovenor, G. A. D. Briggs, Y. Tsukahara, T. Miyamoto, N. Noguchi, T. Niijima, Thin Solid Films 382, 194-201 (2001).
5. B. Singh, J. Bouchet, G. Rochat, Y. Leterrier, J. A.E. Manson, P. Fayet, Surfae and Coatings Technology 201, 7107-7114 (2007).
6. B. M. Henry, F. Dinelli, K. Y. Zhao, C. R. M. Grovenor, O. V. Kolosov, G. A. D. Briggs, A. P. Roberts, R. S. Kumar, R. P. Howson, Thin Solid Films 355-356, 500-506 (1999).
7. C. I. Bright, M.A. Roehrig, in: R. Bakish (Ed.), Proc. Of the Thirteenth Int. Con. On Vac Web Coat., Tucson USA, 247 (1999).
8. A. G. Erlat, R. J. Spontak, J. Phys. Chem. B 103, 6047-6055 (1999).
9. Y. G. Tropsha, N. G. Harvey, J. Phys. Chem. B 101, 2259-2266 (1997).
10. M. Yanaka, B. M. Henry, A. P. Robers, C. R. M. Grovenor, G. A. D. Briggs, A. P. Sutton, T. Miyamoto, Y. Tsukahara, N. Takeda, R. J. Chater, Thin Solid Films 397, 176-185 (2001).
11. J. M. E. Harper, J. J. Cuomo, H. R. Kaufman, Ann. Rev. Mater. Sci. 13, 413-439 (1983).
12. S. Mohan, M. Ghanashyam, Vacuum 46, 7, 645-659 (1995).
13. K. H. Muller, J. Appl. Phys. 59(8), 2803-2807 (1986).
14. K. H. Muller, R. P. Netterfield, and P. J. Martin, Phys. Rev. B35, 2934 (1987).
15. K. H. Muller, Phys. Rev. B35, 7906 (1987).
16. S. Mohan, M. G.. Kirishna, Vacuum 44, 213 (1995).
17. Nilsson, P.O and G. Forssell, Phys. Rev. B, 16, 3352-3358 (1977).
18. Nisato, G., Bouten, P. C. P., Slikkerveer, P.J., Bennett, W. D., Graff, G. L., Ritjerfprd, N. And Wiese, L. 8th International Display Workshop, Nagoya, Japan, 1435. (2001).
19. B. G. Osborne, J. Fd technol. 16, 13-19 (1981).
20. P. Lagarde, M. A. H. Nerenbery, Y. Farge, Physical Review B 8, 4 (1973).
21. W. Kim, Q. Zhang, F. Saito, J. Mater. Sci. 35, 5401-5405 (2000).
22. K. H. Norris, Agric. Engineering, St. Joseph, Mich, 45, 370 (1964).
23. T. Oohara, A. Murata, The Chemical Times, 198, 4 (2005).
24. S. Kubreti, A. Cerussi, B. Tromberg, E. Gratton, J. Biomedical Optics, 12, 2 (2007).
25. Shouta, BRAN+LUEBBE, NIR analysis 12 (1992).
26. JIS Z0208 (1976).

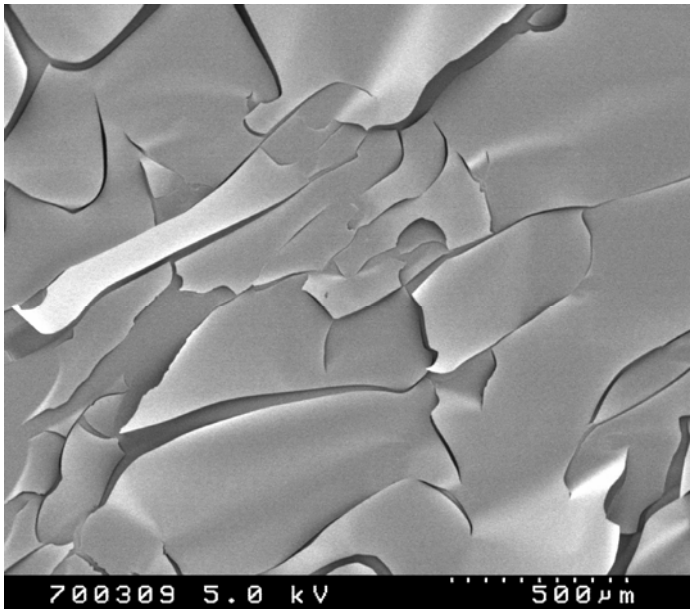

Figure 6-1. SEM photo of the cracks of SiO_x 200 nm thin film on PET

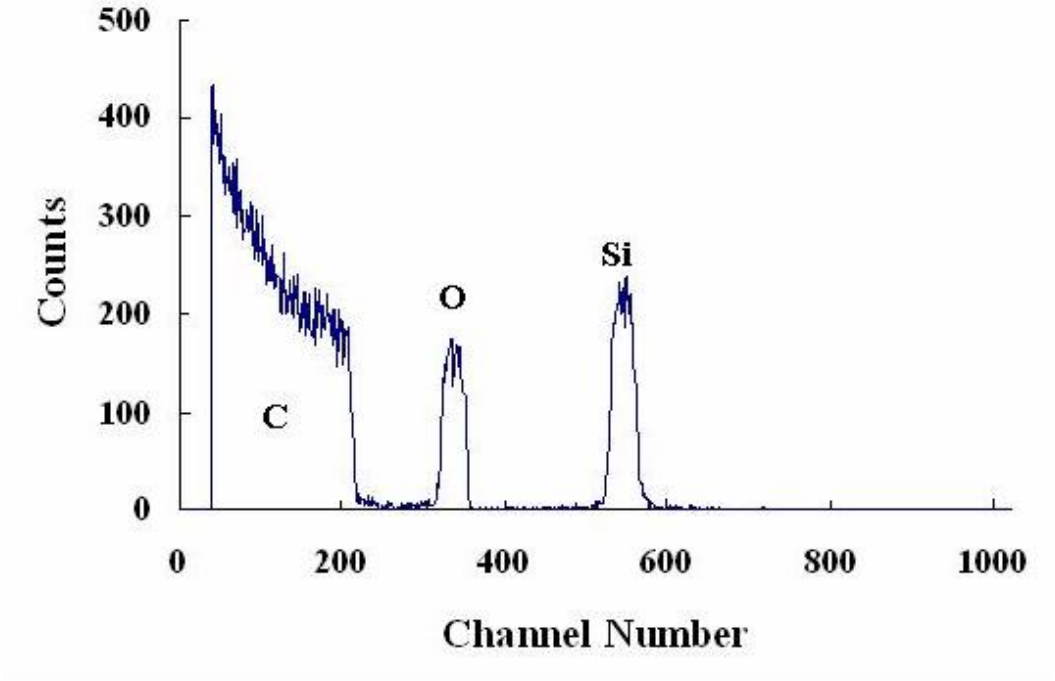

Figure 6-2. RBS spectrum of SiO_x thin film

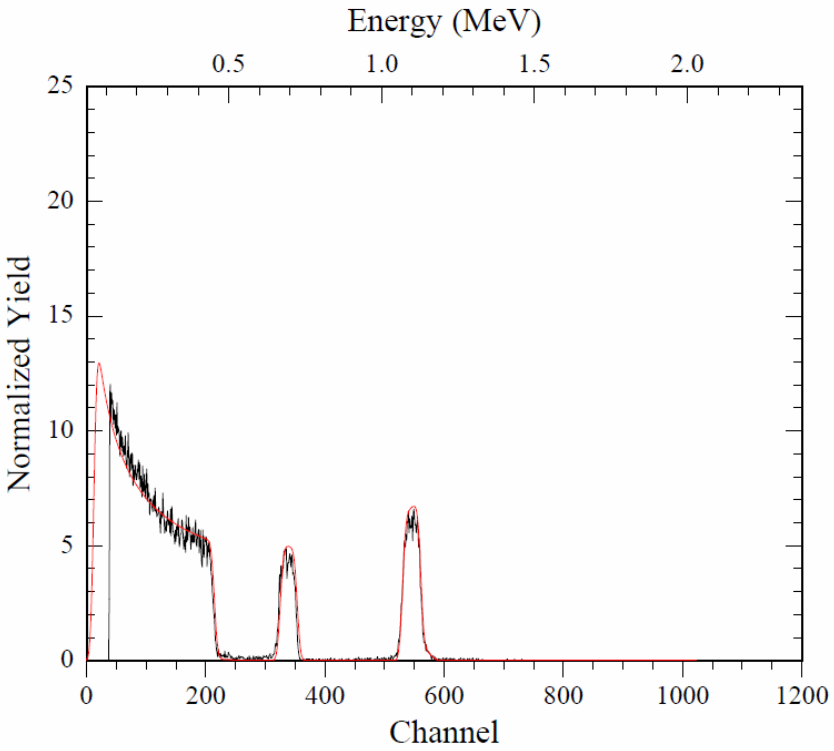

Figure 6-3. RUMP simulation to SiO_x peak fitting

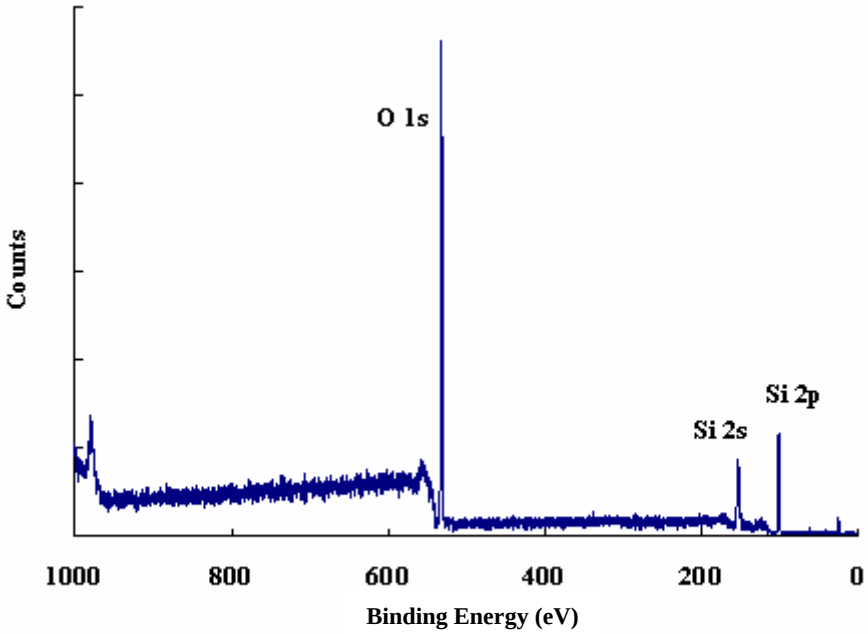

Figure 6-4. XPS spectrum of SiO_x thin film

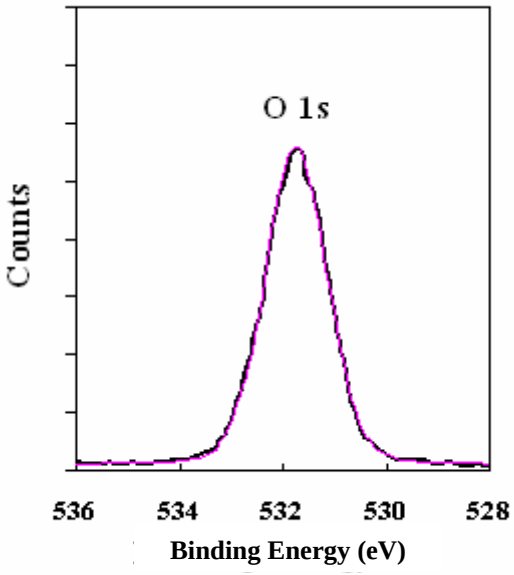

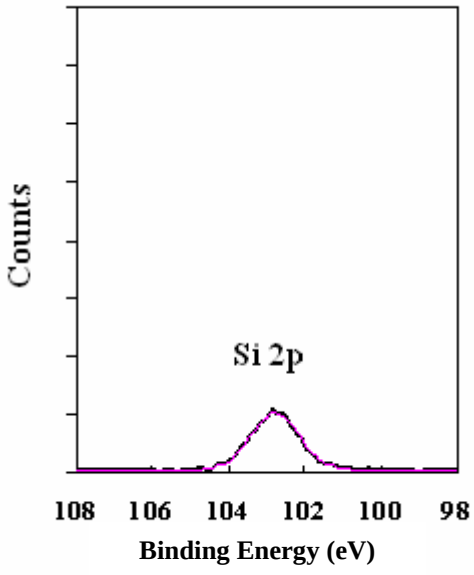

Figure 6-5(a). O 1s XPS spectrum

Figure 6-5(b). Si 2p XPS spectrum

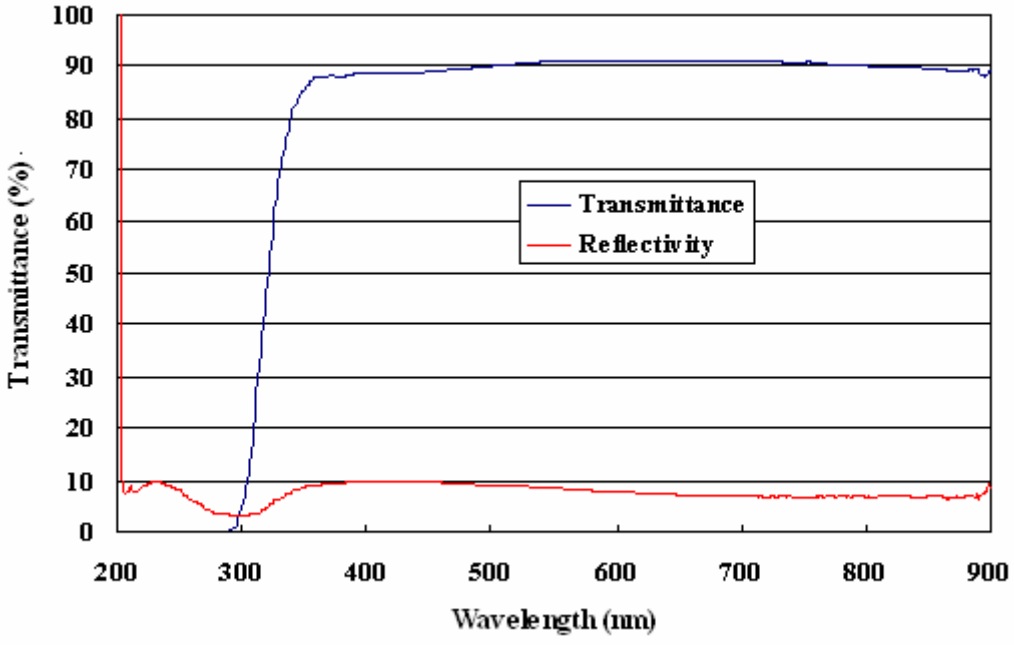

Figure 6-6. Transmittance and reflectivity of SiO_x thin film with glass substrate

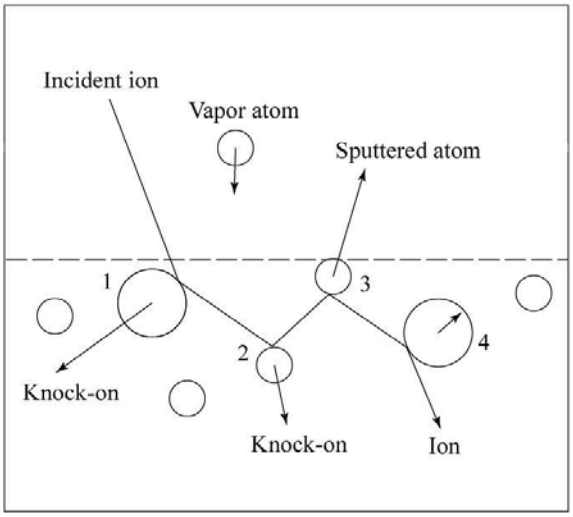

Figure 6-7(a).

Processes occurring at the surface of an ion-assisted film. While vapor condenses at the surface, incident ions strike the target atoms (1),(2) near the surface and drive them into the target. Some knock-on atoms (3) leave the surface as sputtered atoms. For atoms (4), the energy transfer too small to leave their sites. (Reference: Muller, J. Appl. Phys. 59 (1986))

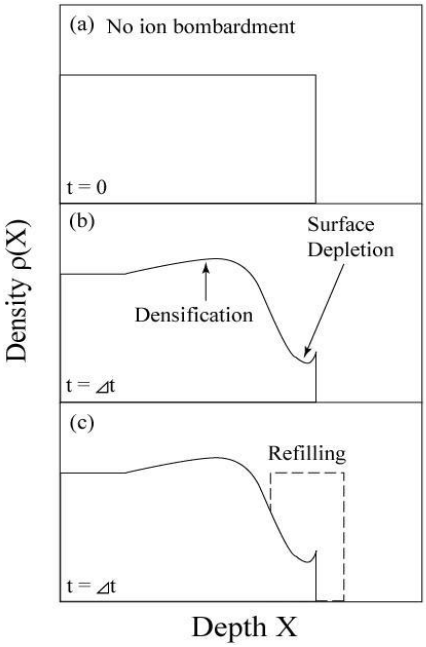

Figure 6-7(b).

(a). Film density distribution evolves without ion bombardment, assuming a sharp density decrease at the surface. (b). The density distribution caused by ion incorporation, sputtering, and recoil implantation. (c). The vapor refilling of the depleted surface region and vapor deposition.

(Reference: Muller, J. Appl. Phys. 59 (1986))

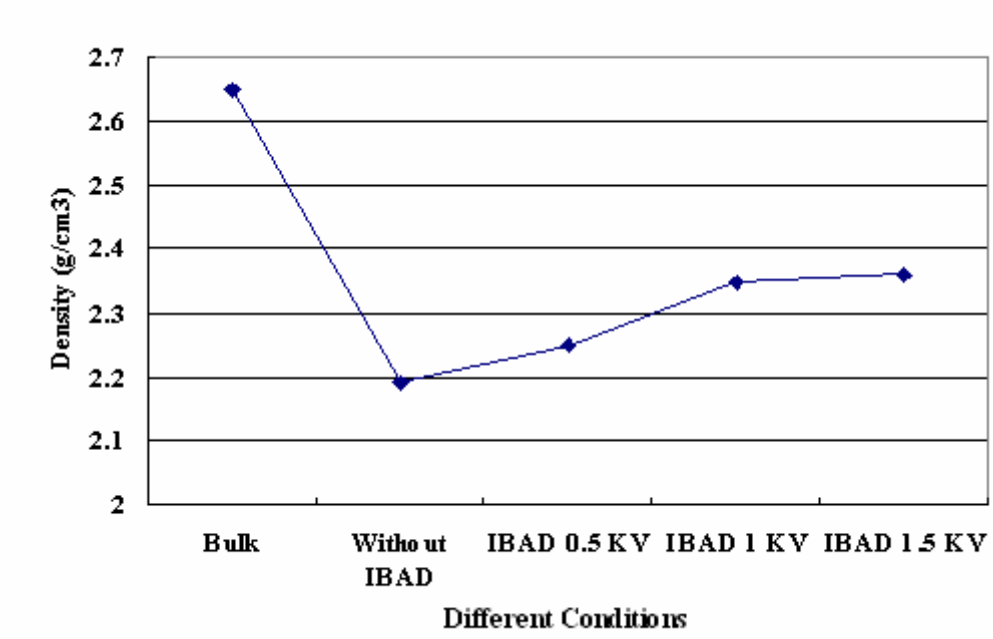

Figure 6-8. Density of SiO_x deposited at different conditions

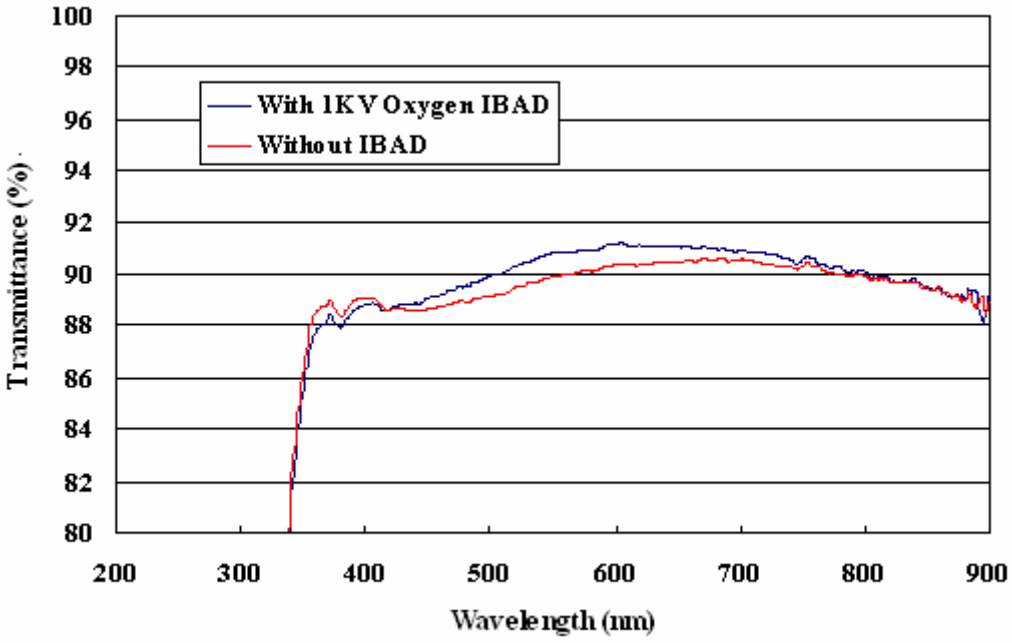

Figure 6-9. Light transmission of SiO_x with and without IBAD

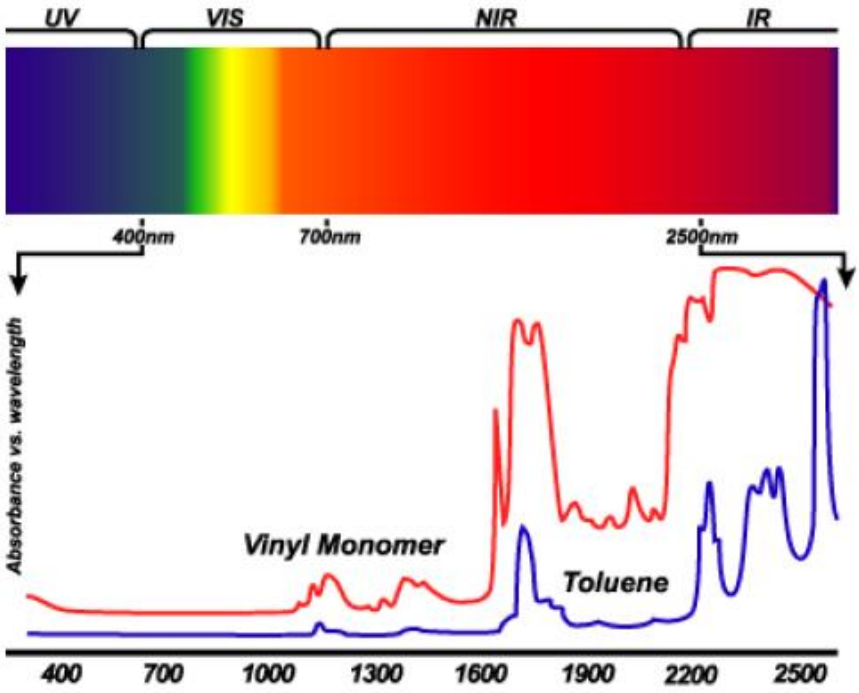

Figure 6-10. Wavelength ranges of UV, VIS, NIR and IR.
(Reference: http://main.nireco.com/jp/prod/nir/index.html)

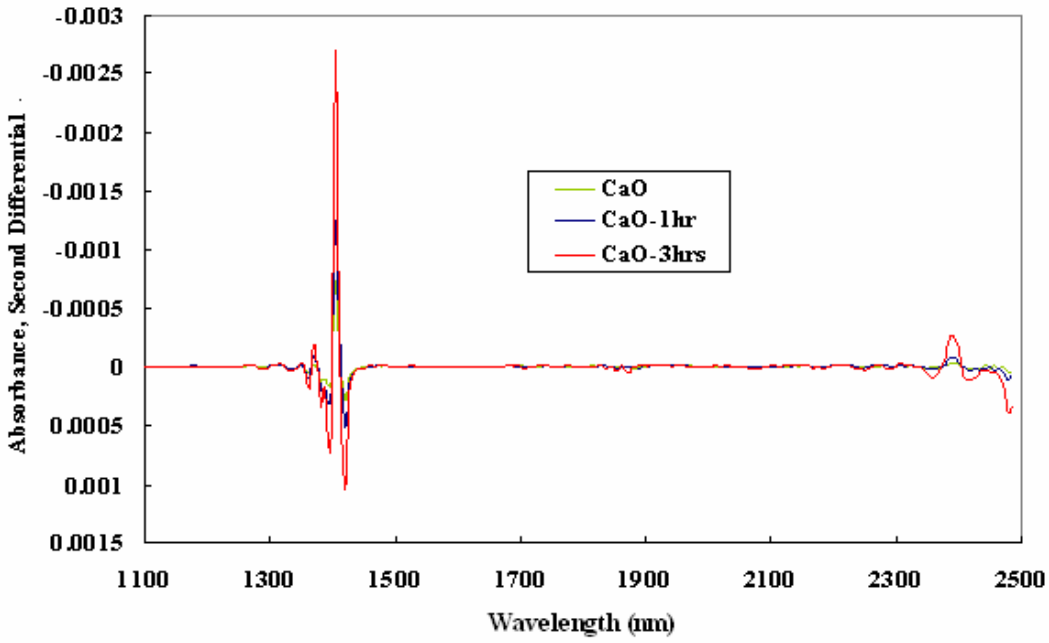

Figure 6-11. Second differential spectrum of CaO testing samples

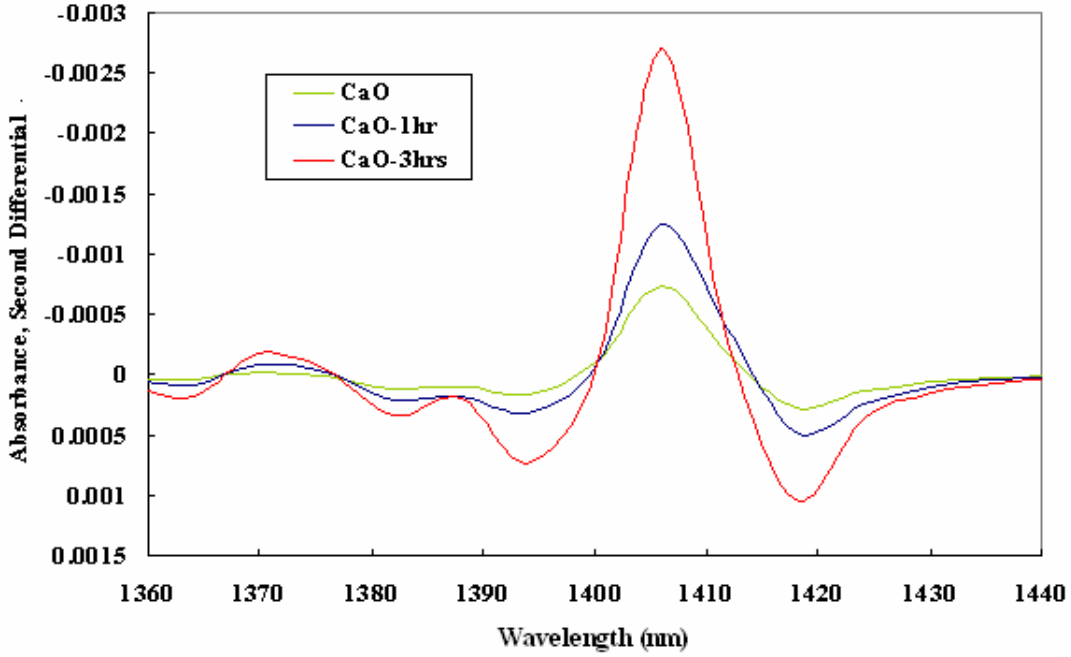

Figure 6-12. Spectrum zoom out from 1360 nm to 1440 nm of Figure 6-11

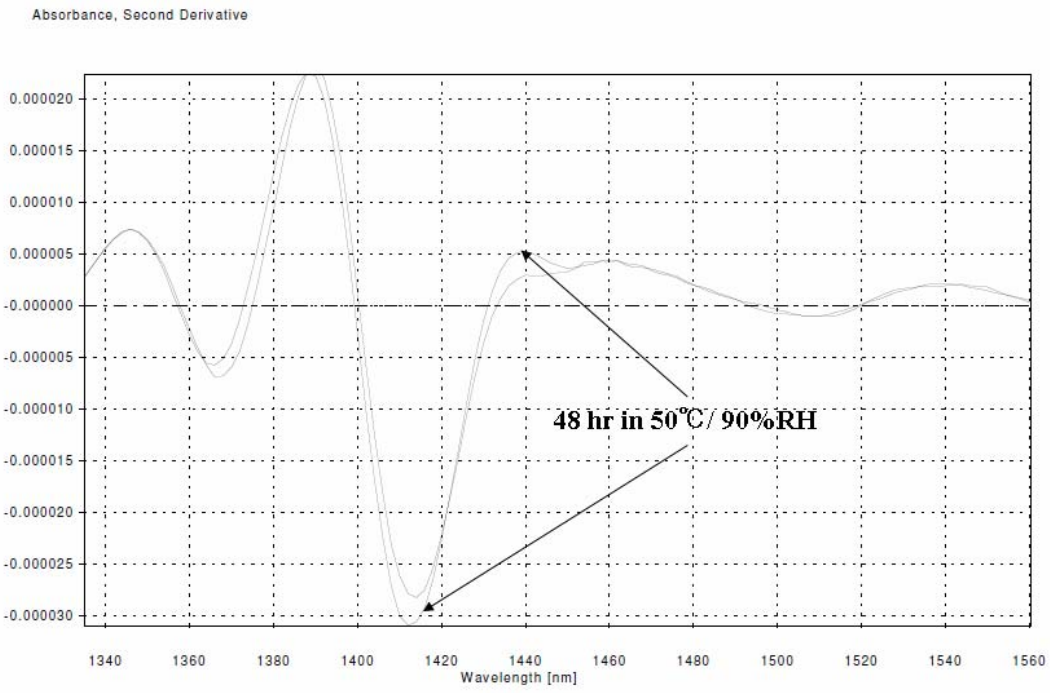

Figure 6-13. Second differential spectrum of samples with and without moisture testing

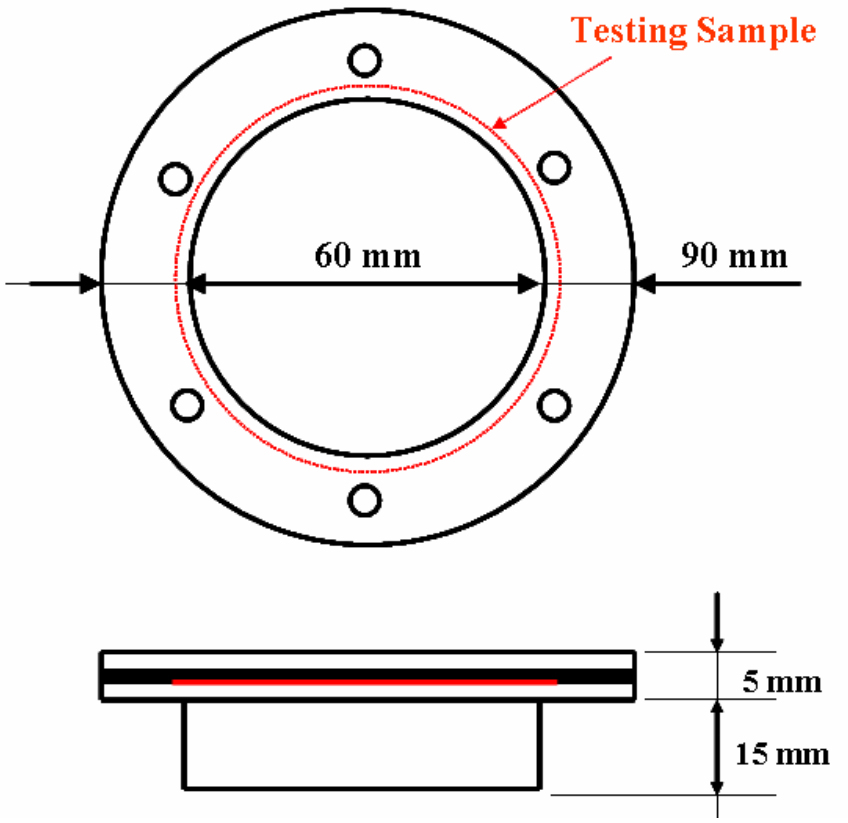

Figure 6-14. Schematic of dish used in water vapor permeation testing

Figure 6-15. Photo of dish used in water vapor permeation testing

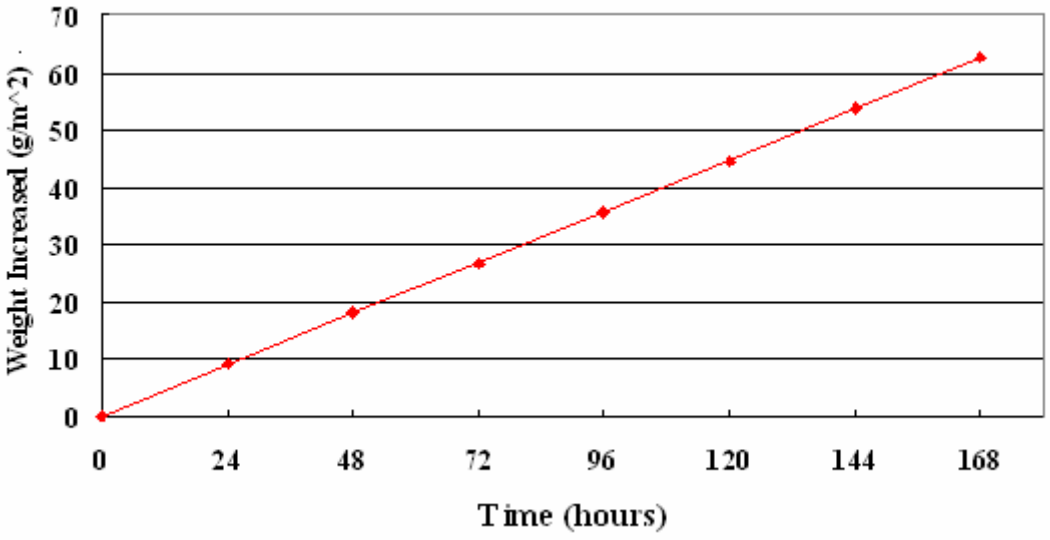

Figure 6-16. Testing sample (PET) weight increased by time at 50℃, 90% RH

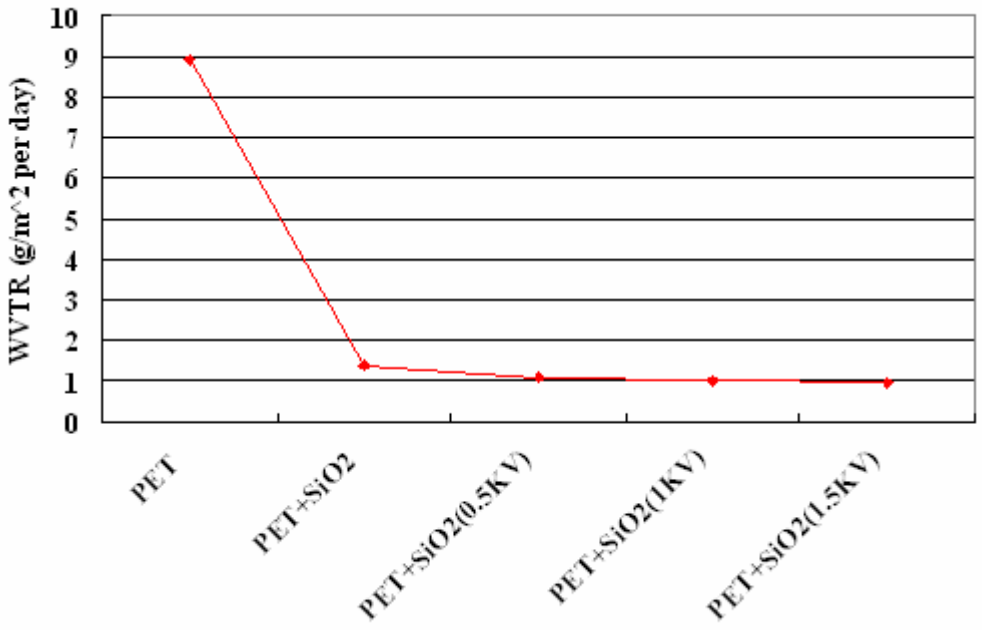

Figure 6-17. Water vapor transmission rate of each sample

Chapter 7

Conclusions and Future outlook

7.1 Conclusions

Flat panel display (FPD) is a dynamic and continuously evolving industry. Improvements of flat panel displays are made rapidly as technology improves and new discoveries are made. The active matrix liquid crystal display (LCD) has recently become the mature product located everywhere. Respectively, the arrival of portable electronic devices has put an increasing premium on durable, lightweight, and inexpensive display components, and the flexible display is expected to be the next generation of the flat panel display [1]. How fast will flexible displays diffuse into the market? That will depend on a variety of factors, but we believe that the identification of key markets will be critical. With only a five-year window to prove itself and gain additional funding, a flexible FPD must attract early adopters of technology to survive. We believe that flexible FPD can create new markets will do that and achieve the critical mass for success, just as monochrome televisions have done [2, 3]. We also believe that flexible FPD for replacement markets will take much longer to diffuse, as in the case of color television [4].

This study has focused on two layers including the transparent conducting electrodes layer and the barrier layer on polymeric substrate used for flexible displays. Moreover, we paid more attention to the ion beam usage on the surface modification by the proper irradiation and ion beam assisted deposition. The new linear ion source system was developed for providing uniform and high quality ion beams for surface modification. In this system, the electron beam evaporation was applied to the deposition process after the surface modification of substrates. For the new system of linear ion source, we measured the irradiation current density and the ion energy at the different discharge voltages. This was compared to the electron cyclotron resonance (ECR) ion source that was used before. The linear ion source provided much higher current density irradiation than the ECR ion source, but the ion energy in our operation range was smaller than the ECR ion source. The ion energy of the linear ion source was approximately 35 % of the discharge voltage. In other words, when we operated the linear ion source at 1500 voltage, the ion energy was about 525 eV. They cannot be compared directly, since they have the different ion emission principles. It was revealed that the different ion energy and irradiated dose distribution contributed to the effect of surface modification.

Polyethylene terephthalate (PET) was used as the flexible substrate in this study. It was a

common polymeric material used in various applications, and it is a good candidate material as flexible display substrate. PET is lightweight and has a good transparency. The critical point of PET is its sensitivity to thermal process with a glass transition point at 78 ℃. It is regarded as a low level temperature for the normal process of deposition, especially for the transparent conductive oxide material. For example, indium tin oxide (ITO) which is commonly used as the premium material for the transparent conducting electrodes currently in the display industry, generally proceed at 300 ℃ or more. This temperature range of deposition processes cannot be applied for PET films. Almost all of the polymeric materials have thermal deformation. In this study, the ITO thin films cannot be successfully formed at room temperature by the electron beam evaporation. Depending on the increasing substrate temperature, the ITO thin films deposited by electron beam evaporation had much better optical and electrical properties. When the ITO was deposited on glass substrate at 280 ℃, the light transmittance and surface resistivity reached over 85 % transmittance and 56 Ω/cm^2. It was very close to the specification expected, but this necessary high substrate temperature cannot be applied at PET substrate. We used the alternative deposition method of the sputtering deposition for the transparent conductive oxide used in this study.

We used the ion beam irradiation to do the surface modification of PET, and expected to improve the surface properties. The argon and oxygen gas were applied in the ion source, and the linear ion source and ECR ion source were operated at 500 V to 1500 discharge. At the beginning of ion irradiation or when the ion energy was less than 500 eV, the ion beam irradiation was mainly experimented as the cleaning effect. With the increase of irradiation dose and ion energy, it has primary effect on sputtering. In the XPS analysis of surface properties after the different kinds of irradiation conditions, the carbon to oxygen concentration increased either by argon ions or oxygen ions irradiations, and it increased more when the irradiated ion energy increased. It was considered a part of oxygen diffused in the vacuum system and carbon remained on surface when the bonding was cut off by the irradiated ions. That was effective when the ion energy is enlarged. The bonding in the PET chemical structure was disconnected and re-bonded during the ion irradiation process, and the phenomenon was a little different depending on the various ions energy irradiated [5, 6]. From the ratio of each peak, represented for the different bonding, comparisons detected by XPS, the oxygen bonded in ester part of PET was detected to increase at low ion energy and become higher gradually. It was considered that the re-bonded phenomenon happened frequently when irradiated ion energy became larger. For argon ions, the carbon and oxygen bonding disconnected and re-bonded occurred, but not completely corresponding to the ion energy.

By increasing the ion irradiated dose, the chemical structure modification was similar when the irradiated ion energy was not changed. It was regarded that the same phenomenon of chemical structure change occurred on the surface. However, it is a little different from atomic force microscopy (AFM) and scanning electron microscopy (SEM) detection. The surface became

smooth and flat at the initial ion irradiation, and it was considered as the cleaning effect or the cutting effect for the sharp parts on the surface. When we extend the irradiation of oxygen ions, the surface became rougher and RMS roughness became larger. From the SEM photo, the convexo-concave topography became clear. This rougher phenomenon cannot be detected in the case of argon ion irradiation. When we compared oxygen ions and argon ions, if they are discharged with the same ion energy, the oxygen ions had a more severe bombing influence, and had a more active chemical reaction to the surface. That was the reason why oxygen ion beam irradiation was more effective in modifying the surface morphology, and it was the main reason why the adhesion improved a little in the scratch testing.

The sputtering deposition is a common deposition process for transparent conductive electrodes in industry. It provides good thin film properties and has the advantage of having thin film composition almost the same as sputtering target. That is the main reason why we used sputtering method for the metal alloy films. In this study, we made the sputtering target by ourselves, and it has a purity of over 99 %. The ITO thin films deposited at room temperature by sputtering method has the premium optical properties near 90 % light transmittance average in visible wavelength and the surface resistivity at 27 Ω/cm^2. It is very close to the specification used in display industry [7, 8]. In this study, we tried to find the substitute material for indium, since it is a rare and expensive metal. It costs about 1200 USD per 1 kilogram of indium oxide [9]. Compared to indium oxide, zinc oxide is much cheaper, and has the wide band gap (about 3.37 eV). It is expected to be the next material for transparent conductive oxide. However, the zinc oxide cannot achieve the proper optical and electrical properties. The zinc oxide deposited at room temperature has good light transmission of an average of over 90 %, but its electrical conductivity was not good enough and was out of the measurement range. The suitable metal oxide doping in zinc oxide was considered to enhance the properties of zinc oxide thin films. The In_2O_3, MgO, Al_2O_3, Ga_2O_3 doping in ZnO at room temperature and 100 ℃ substrate temperature and 150 ℃ post-annealing were applied in this experiment. In the analysis of the thin film properties, we assumed the concentration of each element in thin film is almost the same as the sputtering target. However, the oxygen concentrations are higher in average. We considered that the reason for additional oxygen occurred from impurities like the hydroxide absorbed from the surface during the deposition and transferred to the analysis chamber. In X-ray photoelectron spectroscopy (XPS) analysis, the additional oxygen cannot be completely removed by sputtering and cleaning the surface. Some oxygen in water was absorbed in the thin films. It was considered as the main reason for the deflection in the crystalline structure. X-ray diffraction (XRD) detected that samples deposited at room temperature cannot have the stable crystal structure with lattice spacing d value near the theoretical value 2.603. We cannot find the peak in XRD spectrum for ITO and In_2O_3 doping zinc oxide (IZO), and it was thought as the amorphous structure when these thin films were deposited at room temperature. Other metal oxides

doping in zinc oxide measurement had only one peak close to the theoretical Bragg angle 34.421 degree, so they were considered as the Wurtizite structure with (002) crystal orientation [10].

For the effect of various doping for ZnO, the properties improved depending on the characteristic doping. MgO doping increased the band gap of ZnO, it was observed either in ZnO or AZO. The band gap increase resulted in the light transmittance becoming better at low wavelength range. However, the MgO doping worsened the electrical conductivity. That was the reason why we selected the amount to be as small as possible for MgO doping. Al_2O_3 doping and Ga_2O_3 doping improved the electrical properties of ZnO thin film, and Ga_2O_3 doping appeared to be better than Al_2O_3. The quantities of Al_2O_3 doping and Ga_2O_3 doping were different, so it is difficult to make the conclusion that the Ga_2O_3 doping is better than Al_2O_3. The thermal process of 100 ℃ substrate during deposition made the surface resistivity improve a little, and it also happened at post annealing. However, the thermal effects didn't make the crystalline structure become better in all samples. It was considered that the thermal process used in this study was not high enough. We cannot increase the thermal process over 200 ℃, because the PET substrate cannot endure that range of temperature [11]. In_2O_3 doping has the best optical and electrical properties in all metal oxide doping ZnO sample. Specifically, its surface resistivity of 52 Ω/cm^2 was very close to the ITO used in industry, and it was deposited at room temperature. IZO was considered to substitute for ITO. Except IZO, the electrical properties of other metal oxide doping ZnO deposited at room temperature or low temperature thermal process used in this experiment were not good enough compared to ITO. It needs additional conditional deposition process to improve the property, particularly in the electrical conductivity.

Before the transparent conducting electrode thin films deposited on PET substrate, the barrier layer to protect and enclose the organic luminescent emitting materials was deposited. The organic luminescent emitting materials are usually easily oxidized and degrade faster with water and oxygen permeation. The slight weight increase of calcium oxide to calcium hydrate measured by the precious weighting with 0.01 mg degree of accuracy was used as the detector for the water vapor permeation testing. Before the barrier layer coating, the PET experimented had a water vapor transmission of approximately 10 g/m^2 per day at 50 ℃ and 90 % RH. If the PET was coated with 100 nm SiO_x barrier thin film, the water vapor transmission improved by a lot to 1.5 g/m^2 per day. Moreover, when we used the ion beam assisted deposition process during the SiO_2 deposited by the electron beam evaporation, the water vapor transmission was near 1 g/cm^2 per day. The density of SiO_x thin film, calculated from Rutherford backscattering spectroscopy (RBS) spectrum and SRIM simulation, increased from 2.19 g/cm^3 to 2.4 g/cm^3. Besides the density, the light transmittance also improved 1% in average after the ion beam assisted deposition.

In this study, the ion beams were used to enhance the surface and thin films properties by using ion irradiation and ion beam assisted deposition. The proper condition of ion irradiation contributed

to the improved adhesion between PET and deposited thin film. The ion beam assisted deposition increased the density of barrier thin film and resulted in the lower water vapor transmission.

7.2 Future outlook

Why flexible displays are flexible, compared to other flat panel displays that use rigid glass as the substrate has a lot to do with the lightweight, tough portable and curve display of the advanced applications. The technology of flexible displays includes many components: the flexible substrate, backplane electronics, functional display materials, and the various coating, sealing, and packaging technologies. In most cases, these components cannot be optimized separately. A flexible display is actually a system of linked parts that must be developed in concert for the total product to function.

The substrate is the big challenge and key factor for the development of flexible display. In other words, the substrate material plays the pivotal role in the viability of the flexible display as a competitive product offering [12, 13]. Substrate material is a key to meet the cost, performance, reliability and manufacturing goals for flexible electronics and displays. Two main categories of substrates are under consideration: thin glass and plastic. Each offers a different set of advantages and may be more or less appropriate for a display technology. In the plastic category, besides polyethylene terephthalate (PET) which has been used in this study, another good candidate, polyethylene naphthalate (PEN), is also experimented with and expected to show up in future work. The polymer substrates are flexible and lightweight, but restricted by process temperature and its sensitivity to heat.

Barrier layers are crucial for all types of displays based on a plastic substrate. Compared with glass, plastic is about 10 million times more permeable to water and oxygen. Moisture and oxygen damage liquid crystals, OLED emitters, and other functional display materials. SiO_x was used as the barrier layer, and it made a great improvement for water vapor transmission. The active process of ion beam assisted deposition was applied in this experiment, and it also improved the density of SiO_x and lowered the moisture permeation. For other inorganic compounds used as a barrier layer, Al_2O_3, SiN_x and MgO can be adequate as barrier layers [14]. Moreover, a barrier can be as simple as a single-layer coating or as complex as a multilayer stack. Multilayer barriers tend to be the most robust and forgiving. A defect in one layer does not affect and does not add to a defect in another layer. That is a good approach for the next stage of barrier layers in this study.

For the transparent conducting electrodes and the materials used for it, regardless of whether an inorganic or organic transistor material is to be used, the process of making a transistor array on plastic is nontrivial. Standard process temperature that exceeds 300 ℃ is unacceptably high for most plastic substrate. Process temperature used in this study was room temperature, 100 ℃ and

150 ℃. Only ITO and IZO deposited can achieve the low standard of transparent conductive oxides specification, other metal doping in ZnO and ZnO cannot be used in the manufacturing of active matrix flexible display on plastic. It should be considered to approach by using different processes and methods. Otherwise, it is difficult to use ZnO with the different few metal oxides doping as the alternative substitute for ITO. IZO was only a material experimented with the possibility to be used. In this study, 60 % ZnO and 40 % indium oxide was used as IZO. The different concentrations of zinc oxide to indium oxide are necessary to be experimented, and the optimum ratio for deposition was found at room temperature or low temperature thermal process in the future.

A flexible display panel is considered to be a component, or intermediate product, hence the market for these displays is highly dependent on the market for the end products in which they are to be used. In some cases the flexible display is enabling a new market, and in others it faces competition from nonflexible alternatives. Flexible display is expected as the future product of the flat panel display. Although the flexible display panels are currently available only in sample quantities, it was forecast to reach the market value at $17.8 million in 2010, and it can be widely used in various fields of applications [4]. For example, it can be used in the applications of appliances. Overcoming the barrier of technologies in different fields to manufacture the mature products in market is expected in the coming future.

References

1. N. Savage, Laser Focus World 35, 42-46 (1999).
2. W. E. Howard, Scientific American 290, 76-81 (2004).
3. P. J. Slikkerveer, Information Display 3, 20-24 (2003).
4. G. P. Crawford, “ Flexible Flat Panel Displays”, p512 (2005).
5. J. M. Mayer, E. Rimini, “Ion Beam Handbook for Material Analysis” (1977).
6. J. R. Tesmer, M. Nastasi, “Handbook of modern Ion Beam Materials Analysis”, 37 (1995).
7. G. Frank, H. Kostlin, Applied Phys. A 27, 197-203 (1982).
8. J. R. Bellingham, W. A. Phillips, J. C. Adkins, J Phys.: Condensed Matter 2 (28), 6201 (1990).
9. Kobayakawa, Kyoto University, Master Thesis, (2006).
10. JCPDS, 34-1451 ZnO.
11. W. A. MacDonald, J. Materials Chemistry 14, 4-10 (2004).
12. S, Angiolini, M, Avidano, C. Bracco, C. Barlocco, R. Bracco, J. Bacskay, J. H. Lipian, P. S. Neal, L. S. Rhodes, R. A. Shick, X. M. Zhao, G. Greeeman, SID, Digest of Tech. Papers, 1-4 (2000).
13. S, Angiolini, M, Avidano, C. Bracco, C. Barlocco, N. G. Young, M. Trainor, X. M. Zhao, SID, Digest of Tech. Papers, 1325-1327 (2003).

14. T. Krug, R. Ludwig, G. Steiniger, Society of Vacuum Coaters, 302 (1993).

Appendix 1

X-Ray Photoelectron Spectroscopy (XPS)

X-ray Photoelectron spectroscopy involves the irradiation of a sample with soft X-rays and the energy analysis of photo-emitted electrons which are generated close to the sample surface. An X-ray photoelectron spectrometer therefore consists of a vacuum vessel with its associated pumping system as well as a sample introduction and manipulation system: an X-ray source; an electron energy analyzer, and its associated input electron-optical lens, an electron detection system and a dedicated data base on workstation which both controls the spectrometer operation and provides the means to process the acquired data.

There are two vacuum chambers used in this XPS equipment. One is called the sample treatment chamber (STC), and the other is called the sample analysis chamber (SAC). These two chambers are connected by a gate valve. At STC, the sample is placed on a railway transfer device with the insertion lock at atmospheric pressure. The pumping takes approximately an hour, occurring through opening a gate valve between this chamber (STC) and the second preparation chamber (SAC). In this process, a rotary drive moves the sample into it. The second chamber is continuously pumped with UHV at a base pressure to 10^{-7}～10^{-8} Pa. The sample is transferred using a wobble stick onto a second railway connected similar with the analysis chamber.

X-rays are generated by bombarding a target anode with high energy electrons from a heat filament. The emission consists of characteristic lines, resulting form electronic transitions. There are only two anode materials commonly encountered in XPS; one is aluminum, the other magnesium. These are the only materials which satisfy a number of criteria for X-ray sources. Thus, for Al Kα, the anode potential is usually at 15 KV. In this study, we used it at 14 KV. It is possible to monochromate Al-Kα radiation by means of a quartz crystal monochromator; resulting in the elimination of the Bremsstrahlung, satellite, and ghost radiation. This further allows the characteristic X-ray linewidth to be reduced to below 0.3 eV. In this study, we used the XPS Axis-165 system (Shimadzu / Kratos) with monochromated Al-Kα (1486.6 eV) and a charge neutralizer. The X-rays used in XPS penetrated many microns into the material. X-ray absorption by an atom in the solid lead to the ejection of an electron either from one of the tightly bound core levels or from the more weakly bound valence levels. Some fraction of these electrons emerged from the surface into the vacuum. The photoelectron emission energy is analyzed (as described above) to produce a spectrum of electron intensity as a function of energy. In the case of a conducting sample in electrical contact with the spectrometer, conservation of energy leads to the

equation:

$$E_k = h\nu - E_b \qquad \text{(A1-1)}$$

Where E_k is the measured kinetic energy of the emitted electron, $h\nu$ is the energy of the exciting X-ray photon, E_b is the electron binding energy in the conducting solid relative to the Fermi level. Equation (A1-1) refers to the elastic photoemission process in which the emitted photoelectrons suffer no energy loss during transport through the solid. Therefore, each photon energy in the X-ray source distribution carries a photoelectron spectrum. The peak within the spectrum can be grouped into three classes: those due to photoemission from core levels, those due to photoemission from valence levels, and those due to X-ray excited auger emission.

For the XPS spectrum, quantification of peak intensity data is performed using peak areas. Consequently the form of the background which needs to be subtracted is of major importance, so this is considered first. Then curve fitting is used to find the various bonding energy and shifts in one spectrum. In this study, we used XPSPEAK software to do the curve fitting. Curve fitting, though important, cannot be completed without a detailed interpretation of core level spectra. XPS data analysis, particularly curve fitting and mathematical basis of the techniques used as well as the software allows the generation of line shapes with variable Gauss-Lorentzian ratio and asymmetry. The parameters are varied together with peak FWHM, position and intensity as well as background position during iteration. The ability to freeze certain parameters while varying others, as well as locking certain parameters into some predetermined relative values occurs. In this way, the fitting process can be guided toward a solution.

In XPS analysis, the measurement result is obtained as a spectrum that shows the binding energy distribution of the photoelectron. The position of this spectrum peak to the sample can be calculated for what kind of the element is included within the process. Comparing the intensity of each peak in the spectrum, the composition of elements on surface can be detected. In addition to measuring the shift amount and the intensity of every peak after peak fitting, we can analyze the chemical structure of the same element. From the peak fitting, we can know the properties of the various bonding condition for the same element. Moreover, the detection depth of the XPS analysis can be calculated from the mean free path of the photoelectron λ. When the detection is angle 90°, the detection depth is about d = 3λ. The following equation is referred to as the mean free path of the photoelectron in the organic material:

$$\lambda = \frac{1}{\rho}\left(\frac{49}{E_k^2} + 0.11\sqrt{E_k}\right)\times 10^3 \qquad \text{(A1-2)}$$

Where the photoelectron kinetic energy from a photoelectric effect is E_k, the surface material density is ρ. The detection depth for the material used in this study is approximately 4 nm. It

detected only the thin layer on the surface. In order to remove the effect from the impurity of carbide, the thin etching technique was applied in some cases.

For XPS analysis, it is important to determine the relative concentrations of the various elements. Methods have been developed for quantifying the XPS measurement utilizing peak area and peak height sensitivity factors. The method utilizes peak area sensitivity factors which are typically more accurate, and this approach is satisfactory for quantitative work. For a sample homogeneous in the analysis volume, the number of photoelectrons per second in a spectra peak is given by:

$$I = nf\sigma\theta y\lambda AT \qquad \text{(A1-3)}$$

Where n is the number of atoms of the element per cm^3, f is the x-ray flux in photons / cm^2 sec, σ is the photoelectric cross section for the atomic orbital of interest in cm^2, θ is the angular efficiency factor for the instrumental arrangement based on the angle between the photon path and detected electron, y is the efficiency in the photoelectrons of the normal photoelectron energy, λ is the mean free path of the photoelectrons in the samples, A is the area of the sample from which photoelectrons are detected, and T is the detection efficiency for electron emitted from the sample, we determine the following equation (Axps-m):

$$n = \frac{I}{f\sigma\theta\, y\lambda AT}, \text{ then } \frac{n_1}{n_2} = \frac{I_1 / S_1}{I_2 / S_2} \qquad \text{(A1-4)}$$

This expression may be used for all homogeneous samples, if the ratio S1/S2 is matrix independent for all materials. It is certainly true that such quantities as σ and λ vary somewhat from material to material, but the ratio of each of the two quantities as σ_1/σ_2 and λ_1/λ_2 remains nearly constant. So it is possible to develop a set of relative values of S for all elements. The use of atomic sensitivity factors in the manner described normally provide semi quantitative results, and it cannot be considered as the exact atoms concentration on the surface chemical specific.

Appendix 2

Atomic Force Microscopy (AFM) / Scanning Electron Microscope (SEM)

The atomic force microscopy (AFM) and scanning electron microscopy (SEM) were used in this study to detect the nano and micro scale surface topography roughness.

The AFM is a very high-resolution type of scanning probe microscope, with the demonstrated resolution of fractions of a nanometer, more than 1000 times better than the optical diffraction limit. It is one of the preeminent tools for imaging, measuring, and manipulating matter at the nanoscale. The AFM consists of a microscale cantilever with a sharp probe around 10 nm at its end that is used to scan the specimen surface. The cantilever is silicon or silicon nitride with a tip radius of curvature on the order of nanometers. When the tip is brought into proximity of a sample surface, forces between the tip and the sample lead to a deflection of the cantilever according to Hooke's law. Depending on the situation, forces that are measured in AFM include mechanical contact force, Van der Waals forces, capillary forces, chemical bonding, electrostatic forces, magnetic forces, Casimir forces, solvation forces, etc. Additional quantities may simultaneously be measured through the use of special types of probe. The deflection is measured using a laser spot reflected from the top of the cantilever into an array of photodiodes.

The AFM used in this study can be operated in two modes, one is contact mode, the other is tapping mode. The tapping mode was used in this study. During the tapping mode scanning, the probe was oscillated at its resonant frequency and was positioned above the surface so that it tapped the surface for a very small fraction of its oscillation period and served the lower pressure on the surface. It is especially suitable for the soft polymer films. In the AFM measurement, root mean square (RMS) roughness is employed as an indicator of roughness. The RMS roughness is a simple measure of the height profile roughness and it is defined as:

$$Roughness_{RMS} = \sqrt{\frac{1}{n}\sum_{i=1}^{n}\left(h(x_i)-\bar{h}\right)^2} \qquad \text{(A2-1)}$$

Where n and $h(x_i)$ are the number of lattice points and heights at lattice site x_i, respectively. $\bar{h}$ is the average height of the n number of lattice sites which is given by

$$\bar{h} = \frac{1}{n}\sum_{i=1}^{n} h(x_i) \qquad \text{(A2-2)}$$

The RMS roughness describes the fluctuations of surface heights around an average surface height.

The SEM is a type of electron microscope capable of producing high-resolution images of a sample surface. Due to the manner in which the image is created, SEM images have a characteristic three-dimensional appearance and are useful for judging the surface structure of the sample. In an SEM, electrons are thermionically emitted from a tungsten cathode and are accelerated towards an anode; alternatively, electrons can be emitted via field emission. The electron beam, which has an energy ranging from a few hundred eV to 100 keV, is focused by one or two condenser lenses into a beam with a very fine focal spot sized 0.4 nm to 5 nm. The beam passes through pairs of scanning coils or pairs of deflector plates in the electron optical column which deflect the beam horizontally and vertically so that it scans in a raster fashion over a rectangular area of the sample surface. When the electron beam interacts with the sample, the electrons lose energy by repeated scattering and absorption which extends from less than 100 nm to around 5 um into the surface. The size of the interaction volume depends on the electrons' landing energy, the atomic number of the specimen, and the specimen's density. The energy exchange between the electron beam and the sample resulted in the emission of electrons and electromagnetic radiation which can be detected to produce an image.

When we compare advantages and disadvantage of AFM to SEM. AFM, for instance, produces a true three-dimensional surface profile, compared to the two-dimensional image of a sample in SEM cases. Additionally, samples viewed by AFM do not require any special treatments that would irreversibly change or damage the sample. The polymer material used in this study was coated with Au sputtering before SEM scanning, and it was possible to contribute some modification on the surface. Moreover, while the SEM needed a vacuum environment for proper operation, most AFM modes can work perfectly well in ambient air. Furthermore, AFM can provide a higher resolution than SEM. The disadvantage of AFM, as compared with the SEM, is the image size. The SEM can image an area on the order of mm by mm with a depth of field on the order of mm. The AFM can only image a maximum height on the order of um and a maximum scanning area of 100 um x 100 um. Another inconvenience of AFM is that at high resolution, the quality of an image is limited by the radius of curvature of the probe tip, and an incorrect choice of tip for the required resolution leads to image artifacts.

Appendix 3

Rutherford Backscattering Spectroscopy (RBS)

Rutherford backscattering spectroscopy (RBS) is based on collisions between atomic nuclei, and is derived from its discoverer, Rutherford (1911). It involves measuring the number and energy of those ions in a beam that backscatter after colliding with atoms in the near surface region of a sample. In general, it uses an ion beam with energies in the MeV range to detect the accurate determination of stoichimetry, elemental, areal density, and impurity distributions in thin films. With this information, it is possible to determine atomic mass and elemental concentrations versus depth below the surface. RBS is ideally suited for determining the concentration of trace elements heavier than the major constituents of the substrates.

When a sample is bombarded with a beam of high energy particles, the vast majority of particles are implanted into the material, with the diameter of an atomic nucleus being approximately 1 x 10^{-15} m, with the spacing between nuclei being closer to 2 x 10^{-10} m. A small fraction of the incident particles undergo a direct collision with a nucleus of one of the atoms in the upper few micrometers of the target sample. This "collision" doesn't actually involve direct contact between the projectile ion and target atoms. Rather, energy exchange occurs because of Coulomb forces between nuclei in close proximity to one another. However, the interaction can be modeled accurately as an elastic collision within the context of classical physics. The energy measured for a particle backscattering at a given angle depends on two processes. Particles lose energy while they pass through the sample, both before and after a collision. The amount of energy lost is dependent on that material's stopping power. A particle will also lose energy as a result of the collision. The ratio of the energy of the projectile before and after collision is called the kinematic factor K.

$$K = \frac{E_1}{E_0} = \left(\frac{M_1 \cos\theta + \sqrt{M_2^2 - M_1^2 \sin^2\theta}}{M_1 + M_2}\right)^2 \qquad \text{(A3-1)}$$

Where E_0 is the incident ion kinetic energy, and θ is the angle through which the incident ion is scattered. M_1 and M_2 are the masses of the incident and target atoms, respectively. The kinematic factor of the measured element to He in this study was Zn (0.784), In (0.87), Ga (0.796), O (0.3623), Si (0.5657), Sn (0.8747), Al (0.5525), Mg (0.517) when θ is 170 °.

The number of backscattering events that occur from a given element depend on two factors: the concentration of the element and the effective size of its nucleus. The probability that a material will cause a collision is called its scattering cross section. The areal density $(Nt)_i$ in atoms per unit area is

determined by the *i*th element from the detection of the solid state detector (SSD), the detect solid angle Ω , the integrated peak count A_i for Q incident ions, and the measured and calculated cross section σ_i using:

$$A_i = \sigma_i \cdot \Omega \cdot Q \cdot (Nt)_i$$

Then, $$(Nt)_i = \frac{A_i}{\sigma_i(E,\theta) \times \Omega \times Q} \qquad \text{(A3-2)}$$

Here, Ni is the atomic density (atoms per unit volume) of the ith element and t is the physical film thickness. t , and A is the integrated peak count under the measured spectrum.Cross section σ is then calculated from:

$$\sigma(E,\theta) = \left(\frac{Z_1 Z_2 e^2}{4E}\right)^2 \times \frac{4\left\{\left(M_2{}^2 - M_1{}^2 \sin^2\theta\right)^{1/2} + M_2 \cos\theta\right\}^2}{M_2 \sin^4\theta\left(M_2{}^2 - M_1{}^2 \sin^2\theta\right)^{1/2}} \qquad \text{(A3-3)}$$

Where Z_1 and Z_2 are the atomic numbers of the incident and target ions and M_1 and M_2 are the masses of the incident and target atoms, respectively, and in the equation (A3-3), $e^2 = 1.44 \times 10^{-13}$ MeV. The average concentration of element *x* and *y* in thin film can be calculated from equation (A3-4):

$$\frac{N_x}{N_y} \cong \frac{A_x}{A_y}\frac{\sigma_y}{\sigma_x} \cong \frac{A_x}{A_y}\left(\frac{Z_y}{Z_x}\right)^2 \qquad \text{(A3-4)}$$

From the peak area of measured spectrum for each element, and cross section, the concentration ratio between two elements in thin films is calculated.

To utilize the depth profiling capabilities of backscattering, it is necessary to relate the energy of the scattered particle to the depth in the sample where the scattering occurred. This depends on the energy loss of the analysis ion traversing the sample, the kinematic factor for the scattering, and the orientation of the sample normal relative to both the incident beam and the detector direction. We denote the difference in energy at the detector of a particle scattered at the surface and a particle scattered at a depth x measured. Perpendicular to the sample surface, as

When the ion collide with the solid atoms, the decelerated, and energy loss depends on the depth x as $\frac{dE}{dx}$. When the depth is t, the ion has energy E', then

$$E' = E_0 - \int_0^t \frac{dE}{dx} dx \qquad \text{(A3-5)}$$

And combined with the elastic scattered collision calculated by kinematic factor, the equation is derived as:

$$E'' = KE' = K(E_0 - \int_0^t \frac{dE}{dx}dx) \quad \text{(A3-6)}$$

When a thin film was in several 100 nm range, the depth t is proportional to the energy loss. The stopping power of incident ions can be substituted by $\left.\frac{dE}{dx}\right|_{E_0}$, and one determines the approximate value by the following equation:

$$E'' = KE' = K(E_0 - t \cdot \left.\frac{dE}{dx}\right|_{E_0}) \quad \text{(A3-7)}$$

Using the same way to substitute in escape root $\left.\frac{dE}{dx}\right|_{KE_0}$, then when the incident ions scattered back and out from the surface into vacuum, the energy E is expressed as:

$$E = E'' - \frac{t}{|\cos\phi_1|}\left.\frac{dE}{dx}\right|_{KE_0} = KE_0 - t\left(K\left.\frac{dE}{dx}\right|_{E_0} + \frac{1}{|\cos\phi_1|}\left.\frac{dE}{dx}\right|_{KE_0}\right) \quad \text{(A3-8)}$$

Then, the energy difference between the scattered ions and incident ions for the thickness x is:

$$\Delta E = E_1 - E = x\left(K\left.\frac{dE}{dx}\right|_{E_0} + \frac{1}{|\cos\phi_1|}\left.\frac{dE}{dx}\right|_{KE_0}\right)$$

Then the thickness of a thin film Δt is:

$$\Delta t = \frac{\Delta E}{K\left.\frac{dE}{dx}\right|_{E_0} + \frac{1}{|\cos\phi_1|}\left.\frac{dE}{dx}\right|_{KE_0}} \quad \text{(A3-9)}$$

So the thickness is calculated by RBS spectrum and the stopping power of thin film materials. We used this method to approach the proper density calculated. The stopping power can be calculated from SRIM software with the input of the density, and ΔE is calculated from the FWHM of RBS spectrum for each element Δt is then out from the equation (A3-9). Adjusting the suitable density input makes the calculated Δt gradually approach the real thickness measured. The density of thin film is then obtained.

Appendix 4

X-Ray Diffraction (XRD)

X-ray diffraction (XRD) is a versatile, non-destructive technique for the qualitative and quantitative analysis of the crystalline materials. XRD reveals detailed information about the chemical composition and crystallographic structure of natural and manufactured materials. The most comprehensive description of scattering from crystals is given by the dynamical theory of diffraction. XRD is obtained as the reflection of an X-ray beam from parallel and equally spaced atomic planes. X-rays are beamed on a pair of parallel planes, separated by a spacing d The two parallel incident rays make an angle θ with these planes. When the X-ray beam irradiated in, a reflected beam of maximum intensity results as the difference in path length between related to the mathematically in Bragg's Law as following equation:

$$n\lambda = 2d\sin\theta \qquad \text{(A4-1)}$$

By varying the angle theta, the Bragg's Law conditions are satisfied by different spacing d in polycrystalline materials. Plotting the angular positions and intensities of the resultant diffracted peaks of radiation produces a pattern, which is characteristic of the sample. Where a mixture of different phases is present, the resultant diffraction is formed by addition of the individual patterns. 2θ also constitutes the Bragg angle. Based on the principle of X-ray diffraction, a wealth of structural, physical and chemical information about the material investigated can be obtained.

For the XRD instrument, the mechanical assembly that makes up the sample holder, detector arm and associated gearing is referred to as goniometer. The distance from the X-ray focal spot to the sample is the same as from the sample to the detector. When the sample holder is driven and the detector is in a 1:2 relationship, the reflected or diffracted beam stays focused on the circle of constant radius. The detector moves on this circle. A crystal lattice is a regular three-dimensional distribution of atoms in space. These crystal lattices are arranged so that they form a series of parallel planes separated from one another by a spacing, which varies depending on the material. For any crystal, planes exist in a number of different orientations and each with its own specific spacing d.

The XRD can be used to analyze the several properties of material. Here, we used the θ-2θ method to measure the crystal structure of thin film in this study. We used the θ-2θ method to detect the diffraction spectrum of target thin films. A typical diffraction spectrum consists of a

plot of reflected intensities with the detector angle being 2θ. After the measurement of diffraction spectrum, we compared it to the International Center Diffraction Data (ICDD) as well as the Joint Committee on Powder Diffraction Standards (JCPDS). It is the organization that maintains the data base of inorganic and organic material.

The peak location in the diffraction spectrum determines the crystal orientation and its crystalline stability. Moreover, we can calculate the lattice spacing d by using the Bragg angle 2θ, and Cu Kα wavelength λ 1.5418 Å. The grain size t also can be calculated by the Scherrer equation as following:

$$t = \frac{0.9\lambda}{B\cos\theta} \qquad \text{(A4-2)}$$

And use FWHM of peak angle difference as B.

List of Publications

Publications in international journals/ proceedings and presentations at conferences are listed as followings:

A. Journals/ Proceedings Papers

1. **Shih Hsiu Hsiao**, Tetsuro Yamaguchi, Yoshikazu Tanaka, and Ari Ide-Ektessabi
"Deposition of ITO Film on Ion Beam Treated Polymers"
Materials Research Society Symposium Proceedings
908E, OO14, 06.1 (2006)

2. Tetsuro Yamaguchi, **Shih Hsiu Hsiao**, Yoshikazu Tanaka, and Ari Ide-Ektessabi
"Ion Beam Modification of Polymide with Linear Ion Source"
Materials Research Society Symposium Proceedings
908E, OO14, 07.1 (2006)

3. **Shih Hsiu Hsiao**, Yoshikazu Tanaka, and Ari Ide-Ektessabi
"Adhesion Property of ITO Film on Polymer Treated by Linear Ion Source"
Materials Research Society Symposium Proceedings
936, L05, 27 (2006)

4. Yoshikazu Tanaka, **Shih Hsiu Hsiao**, Yasuhiko Morimoto, Akihiro Nakao, and Ari Ide-Ektessabi
"The Influence of the Properties of Evaporation Source on the Discharge Characteristics of MgO film"
Nuclear Instruments and Methods in Physics Research
B 261, 209-212 (2007)

5. **Shih Hsiu Hsiao**, Yoshikazu Tanaka, and Ari Ide-Ektessabi
"Properties of Transparent Conductive Oxide Films on Flexible Substrates"
Materials Research Society Symposium Proceedings
977, FF04, 20 (2007)

6. **Shih Hsiu Hsiao**, Yoshikazu Tanaka, and Ari Ide-Ektessabi
"Properties of Zinc Oxide Doped Indium, Magnesium and Aluminum Oxide Films used on Flexible Substrates"
Materials Research Society Symposium Proceedings
1035, L05, 03 (2008)

B. Contribution to Conferences

1. "Deposition of ITO Film on Ion Beam Treated Polymers"
Materials Research Society 2005 Fall Meeting
November 28 – December, Boston, USA (2005)

2. "Adhesion Property of ITO Film on Polymer Treated by Linear Ion Source"
Materials Research Society 2006 Spring Meeting
April 17-21, San Francisco, USA (2006)

3. "Mechanical Properties of ITO Film Deposited on Polymers Treated by Linear Ion Source"
International Conference on Metallurgical Coatings and Thin Films 2006
May 1-5, San Diego, USA (2006)

4. "Properties of Transparent Conductive Oxide Films on Flexible Substrates"
Materials Research Society 2006 Fall Meeting
November 27 – Decmeber 1, Boston, USA (2006)

5. "Properties of Zinc Oxide Doped Indium, Magnesium and Aluminum Oxide Films used on Flexible Substrates"
Materials Research Society 2007 Fall Meeting
November 26 – 30, Boston, USA (2007)